# Assessing The Benefits Of Cost-Effective Monitoring Technology On Unstable Slopes Sensitive To Weather

by

Jorge Rodriguez

A thesis submitted in partial fulfillment of the requirements for the degree of

Doctor of Philosophy

in

Geotechnical Engineering

Department of Civil and Environmental Engineering
University of Alberta

# ABSTRACT

Across Canada, the presence of ground hazards, such as rock falls, rock slides, or earth slides, next to transportation corridors, is a potential risk to transport system users, the infrastructure, and traffic operations. Monitoring instrumentation systems tracking unstable slopes are a key aspect of risk management for these transportation corridors. These systems improve our understanding of the landslide motion and help establish limits for trigger-action-response-plans (TARP). One crucial aspect of the monitoring system is to quantify ground deformation. Various techniques exist for monitoring landslide deformation. However, Canada's distribution of transportation infrastructure is extensive, and the high cost of applying high precision monitoring systems becomes unfeasible to monitor all active landslides. Thus, cost/effective monitoring instruments are required to provide precise and timely information to assess the failure mechanisms and mitigation actions, especially when sudden weather changes become trigger factors.

This thesis presents the results from quantifying and validating the benefits of two low-cost monitoring technology to provide accurate, precise, and reliable data to assess complex failure mechanisms of unstable slopes sensitive to weather changes. A slope failure is considered the movement of a soil mass, and the failure mechanism is the physical process that causes to exceed the soil strength. The monitoring technology for this research included the use of low-cost UAV technology and single-frequency dGNSS receivers. These two monitoring systems have an estimated capital cost of less than $4500.oo CAD per unit, based on the equipment cost acquired for this research and other industrial projects. In addition, the capacity for long-term monitoring to track large surficial deformation provides ease adaptability that permits easy reuse of the system on other areas or sites of interest, reducing further the capital cost of the systems. Three sites were considered for low-cost monitoring: the C018 site and the Chin Coulee landslide in Alberta; and

the Ten-mile landslide in British Columbia. The three sites are active, affecting transportation corridors for several years. The analysis of these sites was used to develop a methodology and workflow to apply the monitoring technology.

UAV allows engineers to remotely, safely, and quickly perform site inspections of the ground surface. UAV surveys allowed documenting the C018 site changes with photographic records following two rock fall and rockslide events. Photogrammetry methods using the UAV photographs provided detailed and precise point clouds. The point clouds allowed identifying potentially unstable areas, quantify the magnitude of displacement or loss of soil after a movement occurred, and identify multiple failure mechanisms. The analysis demonstrated the benefits of low-cost UAVs as a monitoring tool to accurately assess the unstable slopes.

The Ten-mile and the Chin Coulee sites were used for the application of low-cost dGNSS receivers to monitor surficial displacement. The Ten-mile permitted testing the system on a sliding mass disaggregated into smaller blocks. The Chin Coulee permitted testing the lower limits of displacement detection on a translational landslide. A network of dGNSS receivers, called Geocube$^{TM}$, installed at each location recorded the ground position in X, Y, Z every 60 seconds between 2017 and 2019. The data allowed calculating displacements and variability in the displacement rates with a ±5 mm precision. Data analysis allowed quantifying the limitations of the Geocube required for early warning systems on landslide deformation.

At the Ten-mile the dGNSS system allowed differentiating the moving blocks and movement sequences in a 3D space of the sliding mass. The sliding mass was discretized in five clusters of moving blocks based on a kinematic analysis using the data from the dGNSS system. These clusters were added to a 3D limit equilibrium back analysis to examine the effect of matric suction

on the landslide stability. The analyses allowed quantifying the average matric suction needed to achieve a meta-stable condition in the clusters of blocks.

This research shows the benefits and limitations of applying two novel low-cost monitoring technologies to assess complex failure mechanisms of ground hazards. A new methodology for the implementation of the Geocube system was developed to monitor landslide movements. The methodology was introduced into the Canadian industry through the application of case studies. The description of the methods used in each case study should provide geotechnical engineers with an adequate understanding to extrapolate the application of these technologies to other ground hazards.

# PREFACE

Chapter 3 of this thesis has been published in the Landslide Journal with the following citation:

Rodriguez, J., Macciotta, R., Hendry, M. T., Roustaei, M., Gräpel, C., & Skirrow, R. (2020). UAVs for monitoring, investigation, and mitigation design of a rock slope with multiple failure mechanisms—a case study. *Landslides*, *April*. doi: 10.1007/s10346-020-01416-4

Chapter 4 of this thesis has been published in the Landslide Journal with the following citation:

Rodriguez J., Deane E., Hendry M. T., Macciotta R.; Evans T., Gräpel C., & Skirrow R. Practical evaluation of single-frequency dGNSS for monitoring slow-moving landslides. Landslides (2021). doi: 10.1007/s10346-021-01737-y

# ACKNOWLEDGEMENTS

I want to acknowledge the support of my supervisor Dr. Michael Hendry who, through these years, provided guidance for the completion of the Ph.D. program. I'm grateful to Dr. Hendry for allowing me to learn unique technical skills in Geotechnical Engineering; he though me to look beyond the numbers and ask the right questions to solve the problems. Also, I want to express my sincere gratitude to my Co-supervisor, Dr. Renato Macciotta, for his mentoring to develop better research practices and for his advice to never lose sight of the broader context of my research. Furthermore, I'm thankful for his time and patience for opening the door to engage in many discussions to improve this work. Also, I express appreciation to Dr. Derek Martin for his advice and information shared relevant to my research.

This research was made possible by the support of (Canadian) Railway Ground Hazard Research Program, NSERC, KCB Engineering Inc., and Alberta Transportation. Special thanks to Mr. Trevor Evans from the Canadian National Railway for providing resources and information during the multiple monitoring campaigns at the Ten-mile landslide. Also, special thanks to Mr. Chris Grapel from Klohn Crippen Berger and Mr. Roger Skirrow from Alberta Transportation to allowed incorporating the C018 site as part of this research and provide access to historical information.

I want to thank colleagues at the department of Civil and Environmental Engineering, many friends, that took the time to share their thoughts and, on occasions, discuss many technical and non-technical topics. Special thanks to Vivian Giang for helping me improve my writing skills; to Lucas Duerksen that help me setting up laboratory testing and solving the problems from implementing the Geocubes; and, thanks to Jennifer Stogowski for her assistance in organizing the many field trips to the sites during this research.

Finally, I wish to acknowledge my friends and family for the support and encouragement during these years that help me move forward and finish this program.

*The time and effort to complete this work is dedicated to my wife Diana*

*and the future of my son Nicolas*

## TABLE OF CONTENTS

# LIST OF TABLES

# LIST OF FIGURES

# CHAPTER ONE. INTRODUCTION

Uninterrupted traffic flow of highways and railways are necessary for a modern Canadian economy. Thirty-eight thousand kilometers of the Canadian highway system integrates between 19% to 53% of Canada's total exporting merchandise (TC, 2018). Similarly, the railway networks' move heavy and bulk merchandise, and containerized cargo over long distances across Canada and into the U.S (TC, 2018). These transportation corridors traverse regions with varying geological and geomorphological characteristics expose the infrastructure to different ground hazards. Studying these ground hazard characteristics next to transportation corridors will aid in assessing the potential impacts of the ground hazards and mitigation actions.

Ground hazards can produce ground displacement that harm users, obstructing trafficability, or otherwise damaging the infrastructure and operations. Approximately 500 geohazard sites have been identified in proximity to Alberta's highway network; 57% of the 213 active cases have been associated with rock and soil slopes (Tappenden and Skirrow 2020). Similarly, studies of railway corridors in Western Canada have shown unstable slopes to be among the most common ground hazards, particularly landslides (Keegan 2007). Enhancing and developing new processes to mitigate landslides' risks has become essential to the industry (Eshraghian 2007; Keegan 2007; Bunce 2008; Macciotta et al. 2020). These processes focus on identifying, analyzing, and evaluating landslides that expose a risk to transportation corridors.

The complexity of taking objective actions to control the hazards and minimize risk exposed by landslides is echoed by the uncertainty associated with assessing the likelihood and consequences of movement. The application of monitoring instruments provides measures to reduce uncertainty, provide early warning, and facilitate the decision-making process to take optimum actions that minimize disruptions on transportation corridors. Recent monitoring technology has provided the opportunity to obtain very detailed characterization of landslides kinematics (Smethurst et al. 2017). Remote sensing techniques such as InSAR, LiDAR, and unmanned air vehicle (UAV) photogrammetry have become useful tools to assess landslide deformation. Using in-place monitoring instruments such as slope inclinometers (SI), ShapeAccelArrays (SAAs), extensometers, and GNSS stations provides a more detailed description of the landslide deformation. The use of these technologies on landslides impacting transportation corridors is starting to provide enough data for engineers to develop early warning systems (Macciotta et al.

2016a; Carlà et al. 2017b; Kromer et al. 2017b). These monitoring technologies have become crucial tools to improve the safety of transportation corridors. However, managing the number of cases, the extent of transportation corridors, and the costs, limits the application of monitoring instruments. Thus, reducing the cost of the monitoring instruments and its application without sacrificing precision has become paramount.

The overall goals of this research program are to: first, quantify the accuracy, precision, and limitations of low-cost surface monitoring technology for unstable slopes sensitive to weather changes through its application; and secondly, testing the benefits of instrumenting multiple locations with low-cost monitoring technologies to assess the failure mechanism of a slow-moving landslide.

The work was undertaken in this research program by: i) reviewing the historical data and monitoring programs from three research sites; ii) monitoring an active site using UAV photos through seasonal changes that allow a detail reconstruction of the ground surface to assess changes and develop an understanding of the failure mechanism; iii) instrumenting two slow-moving landslides next to transportation corridors using a novel single-frequency dGNSS receivers at multiple locations to estimate precise ground positioning and the continuous changes through different seasons; and, iv) evaluating the failure mechanism of a slow-moving landslide based monitoring surface deformation, laboratory evaluation of the effective strength parameters and soil water characteristic curves from materials near the slide plane, and performing 3D limit equilibrium analyses considering the effect of matric suction.

## 1.1 PROBLEM DESCRIPTION

Highways and railway corridors across Canada are exposed to various types of landslides, such as rock falls, rock slides, and earth slides. Activation of landslides next to transportations corridors can potentially damage infrastructure, disrupt traffic operations, and become a safety hazard to users. The extent of these corridors requires timely and precise information to properly consider mitigation actions, particularly if the mechanism of failure (considering failure as movement or deformation of the soil mass and not necessarily to a complete collapse) is associated with sudden weather changes. Advances in monitoring instruments are starting to provide high-rate data collection with extensive spatial coverage at low-cost without sacrificing precision. Thus, the

application of novelty technologies that are cost effective becomes crucial to manage the safety and operability of transportation infrastructure, especially when resources are scarce and need to be allocated at multiple sites. The implementation of low-cost monitoring instruments requires evaluating the extent of the benefits and limitation to assess slopes with complex failure mechanisms that are impacted by weather changes.

Understanding the failure mechanism of a unstable slope next to a transportation corridor allows better assessment of mitigation strategies and reduces its impacts on infrastructure, operations, and users. Monitoring instruments with a high temporal and spatial resolution data provide an opportunity to enhance the assessment of landslides exhibiting a retrogressive displacement process. The increasing interest from the industry into the application of cost/effective monitoring instruments provides an opportunity to develop a methodology to assess landslides' failure mechanisms by incorporating deformation data at multiple locations with advance slope stability analyses.

## 1.2 RESEARCH OBJECTIVES

The main objectives of this research program are:

i) quantify and validate the benefits of low-cost surface-monitoring instrumentation in terms of accuracy, precision, and limitations to assess unstable slopes sensitive to weather changes through the application on real cases. Provide practitioners with orders of magnitude in accuracy, and precision for decision making on instrument selection; and,

ii) test the benefits of instrumenting multiple locations at the Ten-mile landslide to enhance the knowledge on the failure mechanism and provide a workflow that allows examining other unstable slopes.

These objectives provide a framework through real application of case studies to enhance monitoring methods of ground hazards that would provide early warnings and help optimize landslide mitigation actions.

The specific objectives of this thesis are:

1. To evaluate the use of low-cost unmanned aerial vehicle (UAV) and digital photogrammetric techniques for monitoring the surface deformation patterns in unstable slopes with complex mechanisms of failure.

2. To evaluate the effectiveness of new low-cost dGNSS receivers as a surface-monitoring instrument to provide early warning of landslide movement, which is the primary method for risk mitigation of landslides.

3. To assess a landslide's failure mechanism that impacts two transportation corridors by instrumenting multiple locations using low-cost dGNSS receivers with high-frequency displacement monitoring to identify the kinematic sequences of clusters of movement.

## 1.3 OVERVIEW OF METHODOLOGY

Two novel monitoring technologies that have been recently introduced into practice were considered in this research: 1) unmanned aerial vehicles (UAV) and 2) single-frequency dGNSS receivers. The application of these technologies on three active landslides tracked the surface deformations which were then used to interpret the failure mechanism considered as the process by which the soil strength is exceeded. The landslides sites considered in this research have been actively impacting three transportation corridors in Western Canada for decades. A description of the research sites is presented in the next section. The research on real cases provides a framework for implementing and decision-making to apply these technologies by the industry. The following sections describe the methodology for the completion of the specific research objectives.

### 1.3.1 Low-cost unmanned aerial vehicle (UAV) monitoring

This section describes the methodology followed to complete objective 1 through the application of UAV technology. Commercially available UAVs with a cost of less than $2000.oo CAD were used to complete objective 1. Investigation of UAV technology use is mainly focused on monitoring displacement using historical records to describe the failure mechanism. However, the potential benefits of combining low-cost UAV and the implementation of different techniques to assess unstable slopes with complex failure mechanisms impacting transportation corridors need a comprehensive evaluation.

The evaluation of UAV technology to monitor landslides impacting transportation corridors was carried out at the C018 slope. The implementation of UAV allowed assessing a slope with different failure mechanisms and difficult access impacting a highway section. The assessment of the UAV technology required to create a historical registry to evaluate changes by using photogrammetry techniques on the photographs of the slope surface. The historical registry from three UAV surveys between 2017 and 2018 allowed the implementation of different techniques to assess the failure mechanism of the slope using point cloud methods, drainage analysis, and rockfalls simulations.

The investigation of using UAV technology at the C018 slope required to: (1) review past investigations on the site and background information of slope activity that had impacted the highway; (2) perform periodical surveys of the slope by capturing UAV photos of the ground surface; (3) implement photogrammetry techniques to create a point cloud reconstruction of the ground surface; (4) quantify the errors of the point clouds and determine the level of detection from each survey; (5) evaluate the changes of the ground surface between surveys to identify critical areas; (6) assess the relationship between runoff water and the unstable slope at the site by identifying the drainage network using the point cloud of the slope; (7) identify the rock fall trajectories along the slope to quantify the key parameters for decision-making regarding rock fall protection; and, (8) assess the failure mechanisms identified at the C018 based on the analysis and observation.

### 1.3.2 Single-Frequency dGNSS receivers

This section describes the methodology followed to complete objective 2 through the application of single-frequency dGNSS receivers. Slow-moving landslides can experience large deformations with periods of acceleration. Different instruments allow tracking and measuring the deformation occurring from continuous movement on active landslides. GNSS based instruments allow tracking large surface deformation on landslides and can be repurpose for different locations. Obtaining millimeter precision using GNSS is traditionally achieved by using a costly multi-frequency GNSS receiver. In contrast, single-frequency GNSS receiver are a fraction of the cost than its counter part but have low accuracy. Advances in GNSS receivers using single-frequency now permit millimeter precision deformations while maintaining low costs. Assessing the use of single-frequency GNSS receivers with high precision and at multiple locations needs to be

evaluated to better understand the evolution of the failure and determination of the factors affecting the movement (i.e., causal, trigger factors).

The evaluation of single-frequency dGNSS receivers to monitor slow-moving landslides impacting transportation corridors was carried at the Ten-mile landslide and the Chin-Coulee landslide. A network of single-frequency dGNSS receivers, called Geocube, was installed at each location and the change in location of multiple receivers monitored every 60 seconds. The systems recorded measurement for over a year. The effectiveness of this technology was evaluated in terms of the temporal and spatial resolution, the capability to withstand large displacements and the benefits of high-frequency measurements to improve the kinematic interpretation of slow-moving landslides.

The investigation of using single-frequency dGNSS receivers at the Ten-mile and the Chin-Coulee landslides required: (1) installing the network of single-frequency dGNSS, debugging the system, and hardware fixes to make it operational in remote locations; (2) quantifying the displacements and identify the fluctuation in the measurements; (3) evaluate the lower limits of displacement monitoring and reliability; (4) comparing this system's capabilities to other more common high-end GNSS receiver already tested on similar conditions; and, (5) evaluate the interpretive capabilities obtained from high frequency displacement measurements at multiple locations across to assess the failure mechanism and the relationship of displacement to causal factors at a given landslide.

### 1.3.3 Multiple locations monitoring using low-cost dGNSS receivers

This section describes the methodology followed to complete objective 3 through data analysis of displacements records from single-frequency dGNSS receivers installed at the Ten-mile landslide. This methodology employed the application of three-dimensional limit equilibrium analyses. The semi-arid region environment in the area and site investigation have not shown pore water pressure responses within the sliding mass to be associated with the continuous movement. However, the analysis carried for objective 2 suggests that antecedent rainfall might be controlling the displacement rate of an unsaturated landslide without the presence of a phreatic surface within the sliding mass. A hypothesis was developed from site investigation, suggesting that the observed displacement rates are associated with matric suction changes at the sliding surface. The

hypothesis was evaluated by testing unsaturated properties of the sliding mass and back analyzing the Ten-mile's stability while taking into account the measured variance in displacement across the landslide from instrumenting multiple points using low-cost dGNSS receivers.

The investigation of the effect of matric suction on the stability of the Ten-mile landslide was carried by: (1) reviewing background information of the Ten-mile landslide including site investigation reports, geologic studies, past mitigation methods, laboratory testing and site instrumentation; (2) performing a laboratory testing on representative samples of the soil near the shear zone to characterize the material, the shear strength and unsaturated properties; (3) assessing the failure process from a kinematic analysis of the changes in the displacement rates (i.e., acceleration response) to identify clusters of movement displaying similar acceleration response in nearby dGNSS units; (4) quantifying the average matric suction over the shear surface required to maintain a meta-stable condition (i.e., not rapidly accelerating into the river) through back analysis of a 3D LEM model on clusters of movement; and (5) analysing the role of soil's saturation from infiltration has on the factor of safety through simulation of changes in matric suction.

## 1.4 DESCRIPTION OF RESEARCH SITES

### 1.4.1 C018 Slope

The geohazard C018 (as denoted in the AT Geohazard Risk Management Program) is a steep slope in a region of southeastern Alberta known as the Badlands. The region has average temperatures ranging from -18.6 °C in the Winter and 26.7 °C in the Summer, and precipitation averaging 370 mm of combined snow and rainfall per year (Government of Canada 2018). The slope runs parallel for 500 m to Highway 837 and the Red Deer River (Figure 1-1), there is little vegetation cover and the ground surface are highly eroded and weathered. The slope has a history of erosion on river bank slopes, rock falls, rockslides, and debris flow that have blocked traffic. The section of the highway affected by the C018 slope connects local communities between Drumheller to Bleriot Ferry, and serving as a tourist route. Over the past 20 years the provincial ministry of transportation (Alberta Transportation – AT) has been required to increase the frequency of interventions at this site to ensure serviceability and safety.

The C018 slope requires a rapid and accurate assessment of the unstable sections to reduce the risk to the public road users. However, the location and geometry of the site imposed a challenge to observe the location and conditions of the slope high above the highway. The C018 slopes provides an opportunity to assess the effectiveness low-cost UAV to provide detail information of the surface ground conditions, especially on upper areas with difficult access.

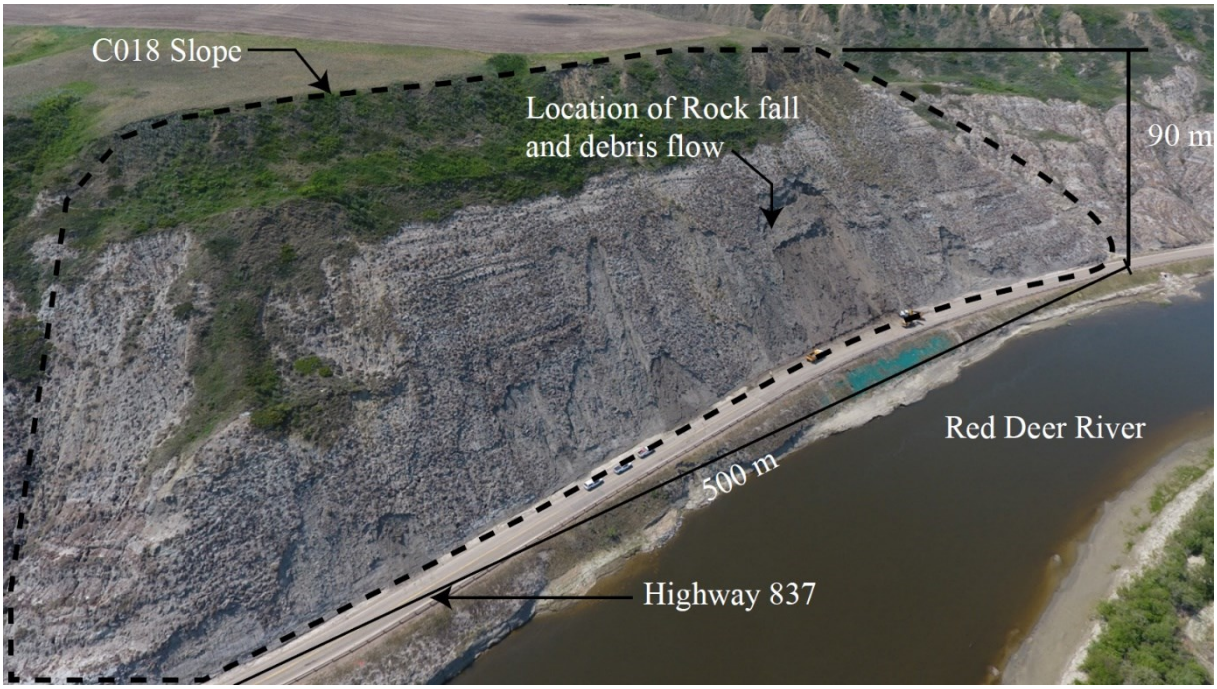


**Figure 1-1 Photograph of the C018 slope taken by UAV inspection following a slope failure on May 23, 2018 (Klohn Crippen Berger 2018a).**

The stratigraphy of the site is part of the Upper Cretaceous Horseshoe Canyon Formation from the Edmonton Group, which is characterized by sub-horizontal interbedded sedimentary rocks mainly composed of fine-grained sandstone, bentonitic mudstone, and carbonaceous mudstone, with coal seams and bentonite beds (Prior et al. 2013). Previous investigations in the area describe the material near the site as highly plastic clay, overlaying sandstones, and shales (Klohn Crippen Berger 2000). The geologic characteristics cause the highway 837 to be susceptible to different failure processes along the riverbank slopes and the slopes above the highway during precipitation events.

### 1.4.2 Ten-mile landslide

The Ten-mile landslide is located in the Fountain Valley approximately 17 km northeast of the town of Lillooet, southeastern BC, adjacent to the Fraser River. The region has an average annual

precipitation of 310 mm, with temperatures ranging from −25 to 39 °C between 2010 and 2018. The vegetation of the landslides is mainly composed of shrubs. The landslide crosses a section of railway track and highway 99, and it presents a hazard to land located in the Xaxli'p Reserve that is of cultural value to the community. The landslide was identified in the early 1970s below the Highway, and it has been retrogressing uphill since the late 1980s (Gaib et al. 2012). The historical displacement rate has increased from 1 mm/day in 2006 to 6 mm/day in 2016 and 12 mm/day (Gaib et al. 2012; BGC Engineering Inc. 2016a). The sliding mass has a volume of approximately 850.000 $m^3$, 200 m wide and 140 m high (Figure 1-2). The Ten-mile landslide provided an opportunity to test the single-frequency dGNSS system in mountainous terrain with limitations on the number of observable satellites, and to observe the movements of various block of soils from a disintegrated sliding mass.

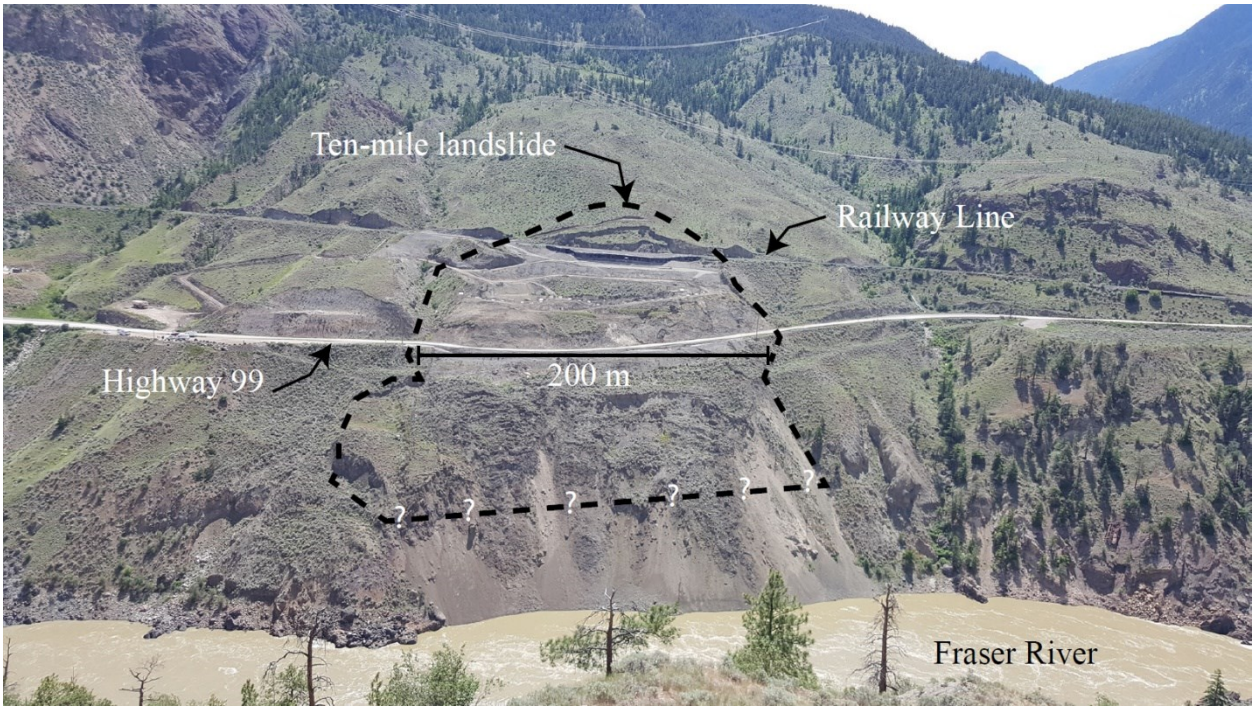


**Figure 1-2 Photograph of the Ten-mile landslide taken across the Fraser River on May 25, 2017.**

The landslide is a reactivation portion of a much larger post-glacial earthflow named Tunnel earthflow with an estimated maximum depth of 30 m (Bovis 1985). Slope inclinometers installed at the site indicate a shear surface at a depth of 18 m. The activity of the past earthflow churned the original soil strata, resulting in complex arraignments of soil types. The soil samples obtained

from landslide have shown that it primarily consists of fine-grained sediment of clay, silt, and sand, with the presence of angular rock fragments that range in size from gravel to boulders. Vibrating wire piezometers have been installed on the landslide on several occasions; and all have indicated that there is not a phreatic surface within the sliding soils. However, slope cuts adjacent to the roadway have shown seepage of water above deposits with high clay contents.

### 1.4.3 Chin-Coulee landslide

The Chin Coulee landslide is located on the northern slope of the valley that contains Chin Lake reservoir, adjacent to Alberta Highway 36 in southern Alberta. Chin Lake is an agricultural water reservoir for the surrounding farmland with a water level that fluctuates seasonally. The region has an average annual precipitation of 360 mm, with temperatures ranging from −14 to 23 °C. The landslide has dense and low vegetation mainly composed of high grass. The landslide impacts a rural two-lane roadway (Alberta Highway 36), which is an important local road and leads to the crossing of Chin lake (Figure 1-3). Historical air photos suggest that initial signs of movement occurred in 1978, following the construction and filling of the reservoir in 1960 and a roadway realignment in 1970 (Golder & Assoc., 1998; Gov. of Canada, 2019; Deane *et al.*, 2020). Formal record keeping and regular site monitoring started after 1997, following the damages of the northbound lane caused by deformations. Since 1998 the landslide has had periods of activity and dormancy, with a maximum average annual displacement rate of only 5 mm/year (AMEC FW 2015). The sliding mass has a volume of approximately 2 $Mm^3$, 350 m wide and 55 m high (Deane et al. 2020). The Chin Coulee landslide provided the opportunity to test the lower limits of detection of the single-frequency dGNSS system and to observe the movements of a translational landslide.

The surficial material at the site is a brown to grey clay till, with low to medium plasticity, silty, very stiff to hard, with traces of fine gravel and sand lenses, some of which conduct water. The till extends from the level terrain surrounding the melt water channel that is now Chin Lake reservoir down 54 m to 12 m below the reservoir's elevation. The local bedrock beneath the till consists of thin and discontinuous layers of grey, low to non-plastic sandstone, grey, clayey, and calcareous siltstone, and brown and grey silty shale of medium to high plasticity, with some coal seams present in some layers (Golders & Assoc., 1998). Borehole logs suggest that blocks of weathered bedrock exist within the clay till material due to glacial overriding. Installed piezometers indicate

that the groundwater depth is 6 m below the head scarp and 2 m near the toe (Golder & Assoc., 1998). Slope inclinometers suggest the presence of a sub-horizontal failure surface within the bedrock unit located approximately 59 m below the elevation of the roadway (AMEC FW 2015).

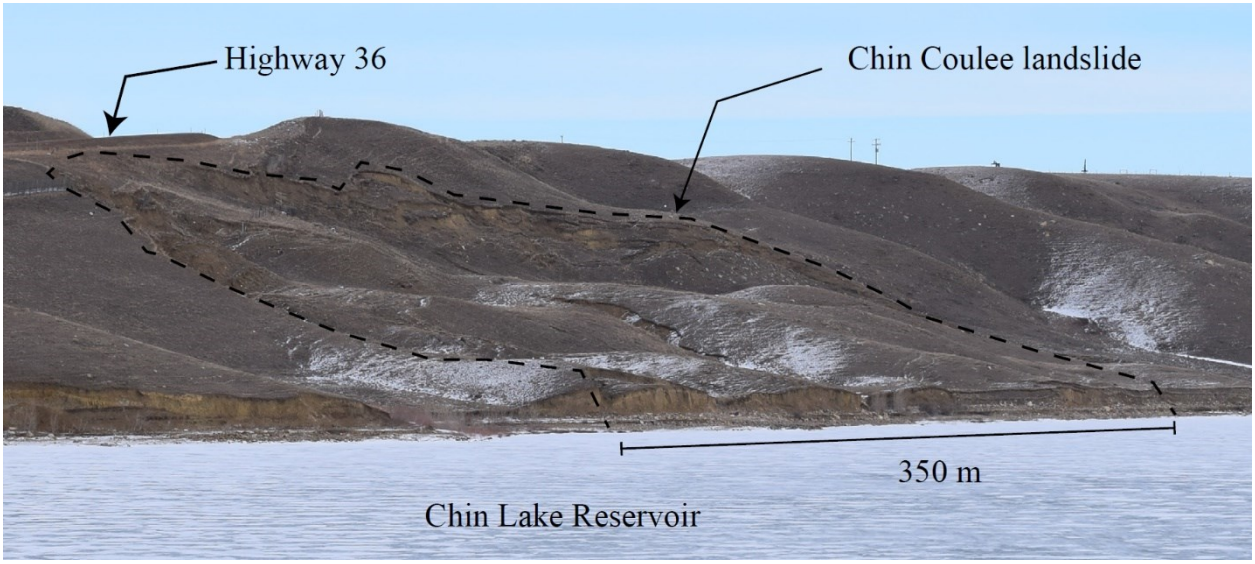


**Figure 1-3 Photograph of the Ten-mile landslide taken across the Chin Lake Reservoir on February 04, 2020.**

## 1.5 Overview of Thesis

The structure of this thesis is in six chapters, which includes this introduction chapter. Chapter Two highlights the relevant literature review to contextualize this study. The next three chapters are written as a paper-based thesis. Chapter Three (Manuscript #1) presents an evaluation of the effectiveness of low-cost UAV (i.e., remote sensing tools) for understanding landslide modes of failure and their relationship with weather conditions. Chapter Four (Manuscript #2) presents an evaluation of low-cost single frequency dGNSS system at two slow moving landslides sensible to weather conditions to provide high precision information with high spatial and temporal resolution that allows quantifying deformation patterns. Chapter Five (Manuscript #3) presents an analysis of the role of matric suction on the stability of a slow-moving landslide with no phreatic surface and under precipitation based on detailed kinematic analysis using multiple dGNSS units to monitor surficial deformation. Finally, Chapter Six provides general conclusions and recommendations for future research.

# CHAPTER TWO. LITERATURE REVIEW

This chapter provides a review of previous work published on the subjects related to this research. The literature review is divided into three topics:

- The importance of kinematic analysis on landslides, and the relation between kinematics and causal factors to estimate the time to failure.
- A review of instruments currently implemented to monitor deformation and provide early warning on landslides next to transportation corridors.
- A review of the potential risks of landslide to transportation corridors.

A detail description of the characteristics of each case study, the instrument and the methods implemented for this research are presented in the manuscripts from Chapter 3, 4, and 5.

- Chapter 3: provides a description the fundamental of unmanned aerial vehicles (UAV) and the processing of point cloud data.
- Chapter 4: provides a description of the fundamentals of the Geocube instrumentation.
- Chapter 5: provides a description of the unsaturated characteristic of an earthflow deposit in the Ten-mile and 3D Limit equilibrium methods.

## 2.1 LANDSLIDE KINEMATICS, CAUSAL FACTORS, AND TIME TO FAILURE

Kinematic analysis of landslides is the study of the ground movement. Such analyses are focused on describing the motion characteristics of the landslide at the surface and depth. These analyses are applied to rock slides (Bednarik et al. 2010; Fan et al. 2017), rock falls (Salvini et al. 2013; Kromer et al. 2015b), earth slides (Rose and Hungr 2007; Handwerger et al. 2015), and debris flows (Cruden and Lu 1992; Jakob and Friele 2010). Landslide displacements can evolve over a short or an extended period, as is the case for active or reactivated landslides. One aspect of these analyses describes the historical changes that allow estimating failure process (Clague and Evans 2003; Kromer et al. 2015b; Intrieri et al. 2019).

The change of a slope from a stable condition to an active landslide is caused by changes in different characteristics that influence the downslope movement (Ansour et al. 2011; Cruden and

VanDine 2013). These changes can be induced by anthropomorphic activities (Clague and Evans 2003; Lacasse and Nadim 2009; Laimer 2017), such as downcutting the toe or increasing the overburden. Other factors include natural conditions (Friele and Clague 2004; Shi 2006; Ansari et al. 2015; Hunter et al. 2016), such as extreme precipitation events or freeze-thaw cycles. One of the primary factors related to changes in movement is water presence (Lacasse and Nadim 2009; Ansour et al. 2011; Ansari et al. 2015). For example, ancient landslides in a dormant state have experienced a partial or complete reactivation from pore water pressure increases (Clague and Evans 2003; Mazzanti et al. 2017). Monitoring deformations provide information that helps identify causal factors (i.e., triggers) that induce continuous deformations or slope failures.

Understanding the kinematics allows evaluating the relationship between the type of movement and the causal factor(s) that could result in failure. Studies of unstable slopes next to transportation corridors help identify the impacts caused by sudden changes in the state of activity (Cruden and VanDine 2013) by assessing the landslides failure mechanisms, identifying trigger factors, the characteristics of the movement (Lan et al. 2010; Wyllie 2014; Jared et al. 2018). For example, an analysis of several slopes next to the railway corridors on the Thompson River Valley has shown to be slow-moving translation slides that change and failed as rapid flow slides due to excessive irrigation above the slopes (Clague and Evans 2003). Understanding the causes that resulting in a slope failure allows stakeholders to implement mitigation actions (Galve et al. 2016) and prevent future failures. Thus, identifying the factor(s) that cause sudden changes on slopes next to transportation corridors provides information to avoid harming users, the trafficability, or damages to the infrastructure and operations.

Kinematic analysis has always been fundamental for designing monitoring strategies. Recently, these analysis are becoming a proactive approach for implementing new methods to forecast potential failures. Forecasting failures is complicated as movement can be related to numerous factors that might be unknown. However, failure prediction is one of the most important issues to assess unstable slopes and plan mitigative actions (Crosta and Agliardi 2003). Several numerical methods have been implemented, such as inverse velocity methods (Dick et al. 2015; Carlà et al. 2017b), empirical correlations to weather (Macciotta et al. 2015), and analysis of precursor slope failures (Kromer et al. 2015b).

## 2.2 LANDSLIDE MONITORING TECHNOLOGIES AND EARLY WARNING SYSTEMS

The presence of numerous unstable slopes next to transportation corridors in Western Canada becomes very challenging to control or mitigate. This challenge requires that the owners of the infrastructure impacted by the instabilities takes a proactive approach towards managing slope hazards. The railway and highway administrations implement different mitigation strategies that improve operational safety (Rodriguez et al. 2017; Macciotta et al. 2020; Tappenden and Skirrow 2020). One of these strategies involves the use of monitoring instruments. The application of monitoring instruments for landslides aims to detect changing slope conditions, characterize material parameters, warn future failures, manage risk to infrastructure, and monitor triggering factors. Railway operators and highway managers in Western Canada have tested several instruments on active landslides to help assess a broad application. The testing has been carried at different sites such as the Ripley landslide located near Ashcroft (Huntley and Bobrowsky 2014; Schafer et al. 2015; Journault et al. 2016); the 10-mile landslide near Lillooet (Guthrie and Nicksiar 2016; Lato et al. 2016; Rodriguez et al. 2017); and the White Canyon in the Thompson Valley (Kromer et al. 2015b; van Veen et al. 2017). The testing has included in-place instrumentation and the use of remote sensing technologies. Testing new monitoring technologies has become primordial to industries impacted by landslides through multiple sites and long distances (Smethurst et al. 2017).

The Ripley landslide has served as a laboratory for landslide research and assessment of novel monitoring technologies (Figure 2-1). Technologies that have been deployed as ground instrumentation includes: acoustic monitoring system, a network of optical fiber to monitor deformations at the retaining wall (Huntley and Bobrowsky 2014; Hendry et al. 2015), ShapeAccelArrays (SAA) (Schafer et al. 2015), and, recently, a new electrical resistivity tomography (ERT) array (Sattler et al. 2018). Remote sensing technologies have included the use of aerial LiDAR scans (ALS), terrestrial LiDAR scans (TLS), and satellite InSAR (Macciotta et al. 2014; Huntley et al. 2019). Other more common instrumentation has included the use of multi-frequency GNSS systems to measure continuous deformation and changes in displacement rates (Macciotta et al. 2016a). Monitoring at the Ripley landslide has provided information on the relationships between weather changes, river elevation, and the impact on the railway corridor

(Hendry et al. 2015) and an analysis of the advantages and limitations of the different installations and the capabilities of diverse technologies.

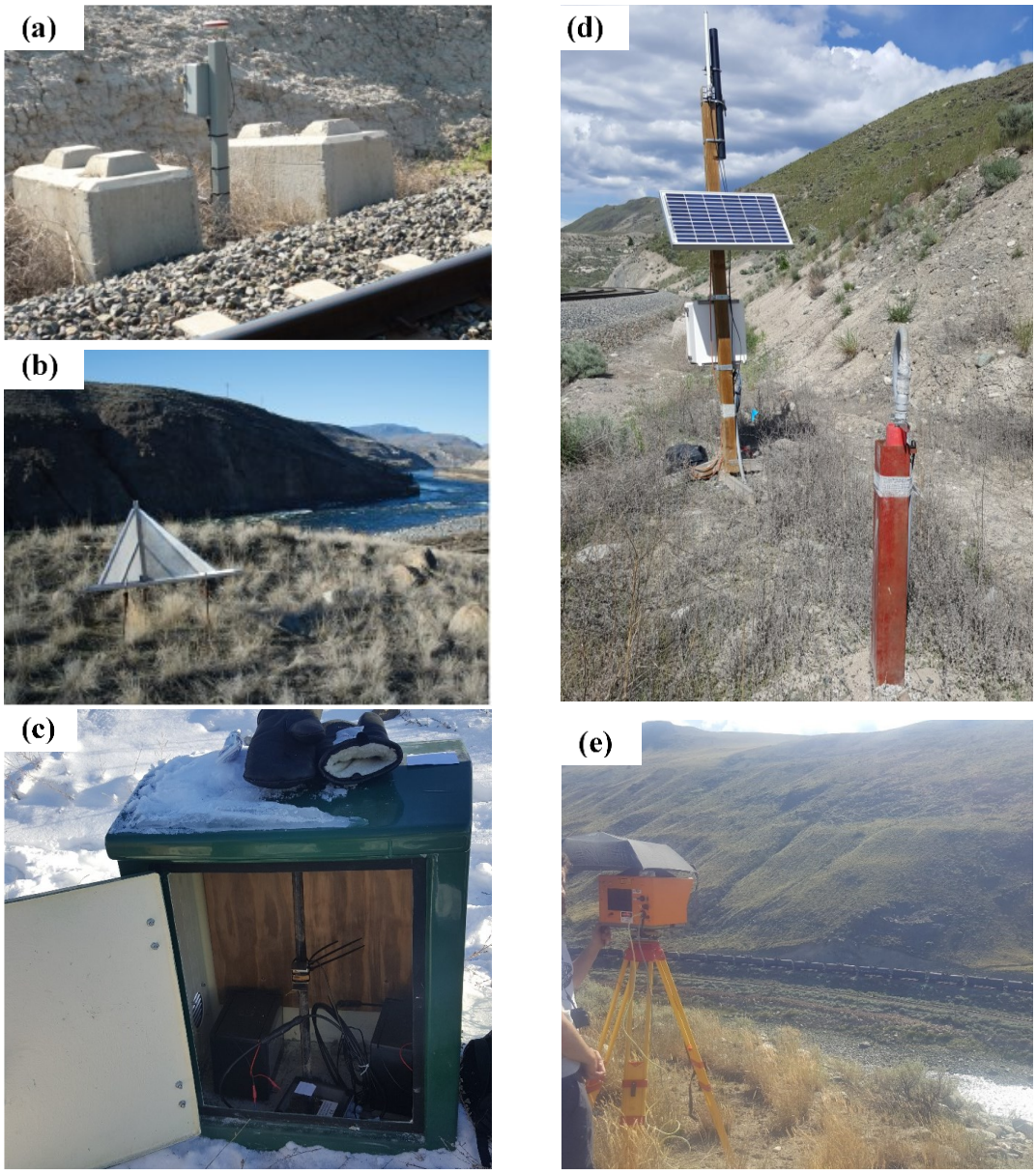


**Figure 2-1 Instrumentation at the Ripley Landslide: a) multi-frequency GNSS receiver; b) reflector for InSAR measures; c) acoustic monitoring system; d) location of piezometer, Shape Accel Array, and data acquisition system; e) terrestrial LiDAR.**

The characteristics of a system deployed to monitor the topography of a landslide can have significant application challenges. Difficulties in the installation and operability processes of the instruments can affect in-place and remote sensing technologies. In-place instruments can be

affected by the remote locations that hinder access to the equipment, increase costs, restrict maintenance service, limit constant power sources, and impede network connectivity for remote monitoring. Although remote sensing technologies aim to facilitate access to remote locations, transport of the equipment can become a challenge (Woods et al. 2019). Generally, the difficulties arising from using different monitoring systems can be resolved if sufficient resources are available.

The application of monitoring systems provides information to understand the characteristic of landslides movements. However, selecting the type of system should consider the spatial and temporal resolution of the data collected. The resolution should meet the requirements of the information expected to be gathered on the landslide. For example, the periodicity between LiDAR scans should be greater than the displacement rate (van Veen et al. 2017; Williams et al. 2017). Thus, implementing monitoring systems that match data's spatial and temporal resolution allows identifying the relevant changes to enhance the kinematics analyses of landslides.

Monitoring system on landslide have been embedded in the risk management programs to act as an alarm system, provide early warning information that helps to inform stakeholders to take mitigation actions, and forecast future failures (Lacasse et al. 2008; Carlà et al. 2017b; Pecoraro et al. 2018; Tappenden and Skirrow 2020). The effectiveness of an early warning system is built upon understanding the failure mechanism and the historical trigger factors, establishing a monitoring program, a decision-making process, a communication system, and action strategies adaptable to changes (Lacasse and Nadim 2009). Measurements of landslide displacements at high frequencies can provide information to estimate potential dangers to transportation corridors. Identifying critical areas from changes in displacements or changes in the trigger factors allows developing hazard management strategies such as hazard maps and hazard threshold criteria (Róbert et al. 2007; Macciotta et al. 2016a). The combination of a pro-active approach to manage risks around landslides and the advances in monitoring technology enhances the ability to obtain reliable information that provides warning and reduces the impacts from unexpected failures (Smethurst et al. 2017).

## 2.3 ASSESSING RISK OF LANDSLIDES IN TRANSPORTATION CORRIDORS

Active landslides near populated areas or near infrastructure can result in life, environmental, and economic losses (Highland and Bobrowsky 2008). Figure 2-2 shows an example of the operational disruption of railway lines in BC due a rock fall and a debris flow reaching the tracks. The rock fall caused a partial blockage, while the debris flow resulted in personal injuries, the derailment of one train, and complete closure of the section. Rockfall are common occurrences along transportation corridors, the first case of a rockfall blocking the tracks occurred on the Yale subdivision. Unfortunately, the second case resulted in the derailment of the locomotive and three cars of a CPR freight train departing from Boston Bar to Vancouver and injured one of the train operators. The Transportation Safety Board report (TSB 2009)showed the slide occurred during a heavy precipitation event, causing a blockage of the track that did not allow enough time for the train operator to stop the train.

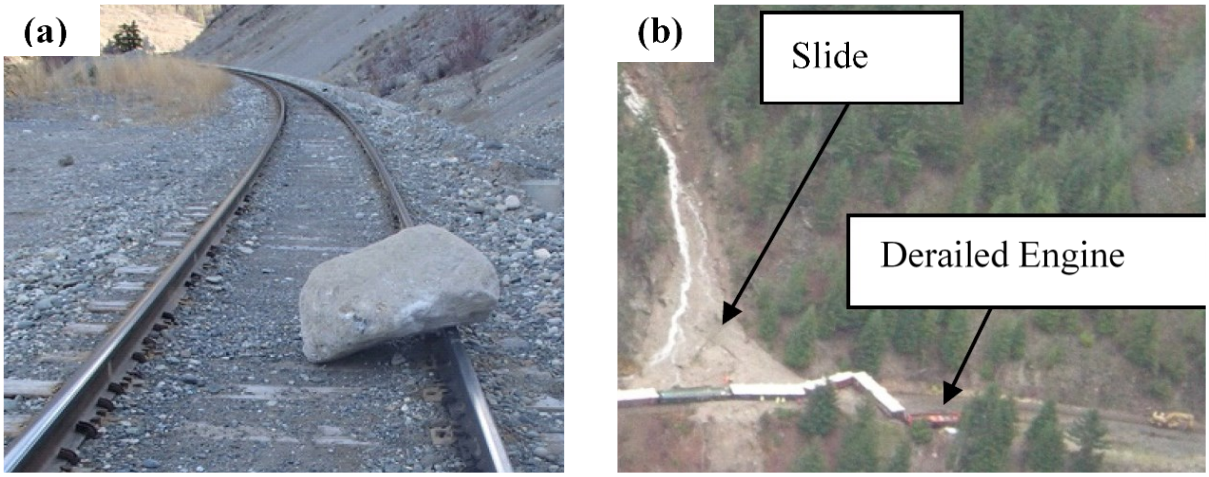


**Figure 2-2. Unstable slopes blocking railway corridors in the BC: (a) rock fall blocking mile 163 of the Lillooet subdivision (photo taken by Mr.Trevor Evans from CN); (b) landslide derailment on mile 7.9 of the Yale subdivision (TSB 2009).**

In Canada, the railway operators and provincial highway administrators are moving to a proactive approach to manage unstable slopes. Since the 1990s, CN has been implementing a grade and slope stabilization protocol as part of its safety management system (TSB 2009). Also, the concern of transportation of dangerous goods has required the railway industry to implement risk management strategies (Transport Canada 2012). The ministry of transportation in Alberta has been implementing a Geohazard risk management program since 1999 for the highway network

(Tappenden and Skirrow 2020). Risk management programs establish a framework for managing ground hazards from identifying to mitigating and reviewing processes related to the hazard. These processes are common for assessing the impact of unstable slopes on transportation corridors around the world, including Asia (Jaiswal and van Westen 2013; Hsu et al. 2016), Europe (Bednarik et al. 2010; Voumard et al. 2018), Oceania (Michael-Leiba et al. 2003; Otto et al. 2019), and North America (Jakob and Friele 2010; Macciotta et al. 2016b). Lacasse (2016) suggests that the objective is to achieve risk management practices that involve all coordinated activities that identify, assess, and control the exposed risks. Thus, transportation industries have been developing a holistic approach to manage unstable slopes and their impacts. This approach looks at integrating the risks at all levels of an organization to the institution's business functions; in the U.S., this goal has been a focus since 2012 (American Association of State Highway and Transportation 2018).

Risk management programs require to be adaptable to the changes (Fell et al. 2005). Real time monitoring instruments can provide information on the changing landslides displacements and trigger factors. The application of monitoring techniques with frequent measurement intervals allows assessing changes in the risk factor remains constant or if the likelihood of occurrence increases or decreases (American Association of State Highway and Transportation 2018). Collecting information that helps identify landslides' characteristics, especially with complex failure mechanisms, allows applying more objective risk assessment methodologies.

Different methodologies have been proposed to analyze the impact of unstable slopes, particularly on landslides (Fell et al. 2005; Porter and Morgenstern 2013; Lacasse 2016). Current methodologies aim to achieve a quantitative evaluation of the landslide risk, such as quantitative risk analysis (QRA). QRA methods provide an objective approach that can be compared and communicated across different cases and scenarios (Morgenstern 1995; Fell et al. 2005; Macciotta 2013; Porter and Morgenstern 2013; Lacasse 2016). QRA features a numeric assessment of the probability, vulnerability, and consequences of hazards by obtaining a numeric value of risk (Fell et al. 2005). Quantifying the risk from landslides becomes a function of different variables, such as annual loss of property value, probability of occurrence, the likelihood of the landslide reaching the element at risk, the likelihood the element at risk is present, the vulnerability of the element at risk, and value of the element at risk. However, QRA methods can grow in complexity and become

very limited by the availability of information for each factor (Fell et al. 2005). Thus, monitoring becomes an essential asset to assess the potential impacts of landslides on transportation corridors and the risk management processes.

# CHAPTER THREE. UAVs FOR MONITORING, INVESTIGATION AND MITIGATION DESIGN OF A ROCK SLOPE WITH MULTIPLE FAILURE MECHANISMS – A CASE STUDY

**Contribution of the Ph.D. candidate**

The work presented in this chapter, that includes literature review, site investigation from 2018, investigation methodology, analysis and discussion of the results and writing of the text was carried out by the Ph.D. candidate.

The supervisors Dr. Michael Hendry and Dr. Renato Macciotta have reviewed all parts of the work. This chapter has been published in the Landslide Journal with the following citation:

Rodriguez, J., Macciotta, R., Hendry, M. T., Roustaei, M., Gräpel, C., & Skirrow, R. (2020). UAVs for monitoring, investigation, and mitigation design of a rock slope with multiple failure mechanisms—a case study. *Landslides*, *April*. doi: 10.1007/s10346-020-01416-4

**Contribution of this chapter to the overall study**

The province of Alberta has various unstable slopes that could become a hazard to the infrastructure, the land, the environment, the users, the communities, or all of the above. Managing the risk of unstable slopes near transportation corridors requires information that helps to characterize the type of failure and potential consequences. However, extensive highway infrastructure exposed to multiple hazardous sites would limit the allocated resources required to assess mitigation actions effectively. Thus, the development of low-cost remote sensing techniques such as unmanned aerial vehicles (UAV) have become a useful tool to assess landslide deformation, especially in areas with difficult access.

The photos collected through UAV monitoring can provide a detailed and precise point cloud of the ground elevation using numerical algorithms. Also, novel analysis techniques historical records on point cloud allows identifying the changes of ground deformation that allows quantifying the magnitude and extent of the unstable slope. The following manuscript presents the benefits and application of low-cost UAV technology for assessing a slope with difficult access and limited resources impacting a 500 m section of a highway in Alberta. An analysis of the slope using the data from three UAV surveys between 2017 and 2018 allowed the implementation of different

techniques to assess the slope with different failure mechanisms using point cloud methods. The manuscript shows the methods used to assess the slope failure and propose mitigation action by identifying the areas deformation, the characteristic of the drainage network, and the rock fall trajectories based on UAV data. The combination of site inspection and the analysis using UAV technology in the slope allowed identifying three potential modes of failure related to weather conditions.

***Abstract***

Slope instabilities adjacent to transportation corridors require timely and precise assessment to determine the risk to road users, particularly when weather changes trigger these instabilities. In southern Alberta, Canada, near the town of Drumheller, a 500 m long, 60 m high slope adjacent to Highway 837 has a history of slope instabilities that includes rock falls, frozen soil falls, and debris flows. The slope failures have blocked the road which increases user and maintenance costs. Due to unsafe conditions and the steepness of the slope (1H:1V inclination) it was only possible to undertake visual assessments of the slope conditions from the road. Advances in unmanned aerial vehicle (UAV) technology has resulted in a quick and safe tool for collecting detailed photographic records of the slope conditions. The combination of UAV data and photogrammetry methods allows engineers to remotely, safely and quickly perform a precise assessment of the slope instabilities. The paper demonstrates the use of UAV derived data to evaluate: critical unstable areas in practice; the magnitude of unstable events; the relationship between the drainage network and slope instabilities, and; models for rock fall trajectory analyses. The paper also provides a methodology that can be implemented on other slope instabilities to support the decision making process to define mitigation action(s) that are practical and minimize associated risks.

**Keywords**:

Ground Hazards, Highway, Change detection, Rock falls, Unmanned air vehicle, Digital Elevation Model

**Abbreviations**:

AT: Alberta Transportation.

C2C: Closest Point Method.

GCP: Ground Control Points.

GSD: Ground Sampling Distance.

GSI: Ground Strength Index.

INSAR: Interferometric Synthetic Aperture Radar.

M3C2: Multiscale Model to Model Cloud Comparison.

RMSE: Root Means Square Error.

RTK GNSS: Real-Time Kinematic Global Navigation Satellite Systems

SFM: Structure from Motion.

SOR: Statistical Outlier Removal.

UAV: Unmanned Aerial Vehicle.

## 3.1 INTRODUCTION

Geohazard monitoring technologies continue to develop, allowing users to increase the frequency, repeatability, accuracy and extent of displacement measurements (Hendry et al. 2015; Carlà et al. 2017a; Macciotta et al. 2017b; Smethurst et al. 2017; Williams et al. 2017). Remote sensing methods are now implemented as part of routine geohazard monitoring programs (Carlà et al. 2017b; Kromer et al. 2017a; Riquelme et al. 2017; Cucchiaro et al. 2018; Rodriguez and Hendry 2018). Methods include technologies such as Interferometric Synthetic Aperture Radar (InSAR), Light Detection and Ranging (LiDAR), and unmanned aerial vehicle (UAV) photogrammetry. These methods have been applied on a variety of geohazards affecting cut slopes (Sousa et al. 2016; Beregovoi et al. 2017; Vanneschi et al. 2017), and natural slopes (Petschko et al. 2016; Fey and Wichmann 2017; Roque et al. 2018). These technologies allow collection of data over large areas with high spatial resolution, as opposed to only at discrete locations (e.g., slope inclinometers, survey monuments). The use of UAVs to assess geohazard kinematics is becoming more common around the world; examples of this can be found from southeast Spain (Agüera-Vega et al. 2018; Martínez-Carricondo et al. 2018), China (Fan et al. 2017; Huang et al. 2018), Italy (Mazzanti et al. 2017; Allasia et al. 2019), and North America (Al-Rawabdeh et al. 2017; Solazzo et al. 2018).

UAVs provide multiple perspectives of the geohazard from photographic or video records. Each photographic record from the UAV is stored with geotags (coordinates and orientation information) that allows for georeferentiation of a point cloud obtained from digital photogrammetry reconstruction algorithms. The point clouds can result in highly detailed topographic information to enhance conventional investigation methods. Current UAVs and UAV software, such as Pix4Dcapture by (Pix4D S.A. 2018a) or DroneDeploy by (DroneDeploy Inc. f.k.a. Infatics Inc. 2020), allow defining automatic flight patterns to collect information easily, quickly, and at relatively low cost from a safe distance. This encourages more frequent data collection which can be very useful for rapidly evolving site conditions. The increased monitoring frequency enables the collected data to provide earlier warning of changing conditions, assessment of triggering factors, as well as integration into a geotechnical asset management program.

This paper presents a case study illustrating the use of UAVs and digital photogrammetry to monitor an unstable slope adjacent to a section of a transportation corridor. The study site is a 90 m high, 520 m wide slope located in Highway 837 adjacent to the south bank of the Red Deer River approximately 10 km northwest of the town of Drumheller, Alberta (Canada). The section of interest had a history of rock fall and rockslides events that have impacted the highway at the toe of the slope. The analysis presented in this paper corresponds to two events that occurred in December 2017 and May 2018. The use of digital photogrammetry provided detailed information to assess the rock falls and debris flow failure mechanisms observed at the site. The collection of data before and after one of the recorded failures allowed insight into the stability of sensitive areas on the steep slope. A change detection analysis on the point clouds derived from digital photogrammetry indicated sources of failure and the magnitude of the event. Since erosion processes from precipitation and surface water run-off had been associated with the occurrence of instabilities at the site (Klohn Crippen Berger 2000), a digital elevation model (DEM) derived from the point cloud were utilized to investigate the drainage network of the slope. Lastly, the point clouds and the analysis of the source of failure provided information to conduct rock fall analysis in 2D (although 3D analysis would also be possible). The results presented in this paper show the effectiveness of UAVs to enhance the understanding of these instabilities, monitor, and aid in decision-making about the optimal mitigation at landslide prone areas.

### 3.1.1 Alberta Transportation's C018 Rock Slope

The study site is in a region of southeastern Alberta known as the Badlands. The Badlands are an arid to semiarid region with average temperatures ranging from -18.6 °C in the Winter and 26.7 °C in the Summer, and precipitation averaging 370 mm of combined snow and rainfall per year (Government of Canada 2018). The landscape along the Red Deer River has little vegetation cover and is highly eroded and weathered. Highway 837 carries an average of 340 vehicles per day (Alberta Transportation 2017), connecting local communities between Drumheller to Bleriot Ferry, and serving as a tourist route, which provides access to a large paleontology museum, the Midland Provincial Park, and the Badlands area. This 6 km section of highway was constructed adjacent to steep valley slopes (1:1 or steeper) up to 90 m high. A 500 m section of these slopes directly adjacent to the highway (Figure 3-1) has a history of erosion on river bank slopes, rock falls, rockslides, and debris flows that have blocked traffic is known by the provincial ministry of transportation (Alberta Transportation – AT) as geohazard site C018 (as denoted in the AT Geohazard Risk Management Program). AT has been required to increase the frequency of interventions at this site over the past 20 years to ensure serviceability and safety.

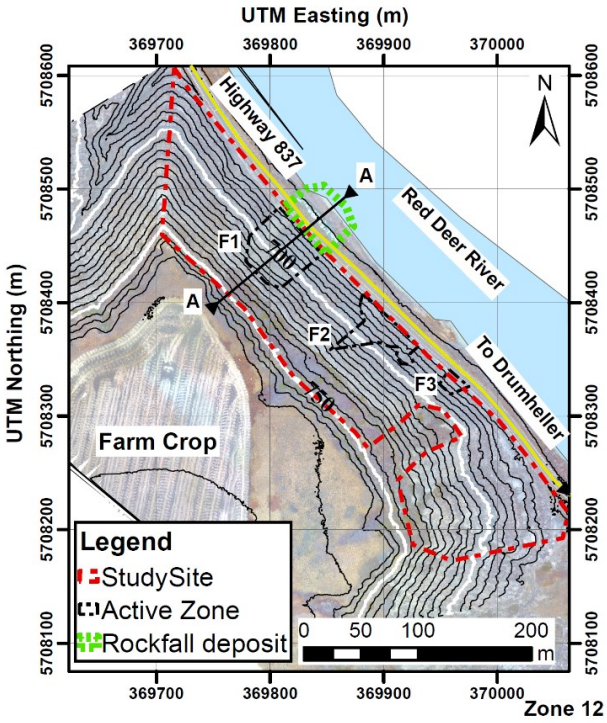


**Figure 3-1 Plan view of the site located next to highway 837 near Drumheller, Alberta. The red dash line shows the extent of the study site. Black dash lines show the three current active zones in the slope (F1, F2, and F3).**

The stratigraphy of the site is part of the Upper Cretaceous Horseshoe Canyon Formation from the Edmonton Group (Figure 3-2), which is characterized by interbedded sedimentary rocks mainly composed of fine-grained sandstone, bentonitic mudstone, and carbonaceous mudstone, with coal seams and bentonite beds (Prior et al. 2013). The terrain in this region is the result of glaciation deposition followed by erosion from meltwater from creeks and the Red Deer River (Borneuf 1972; Stalker 1973). The exposed bedding planes are visible in the valley slopes due to the variations of color, texture, and slope (Figure 3-2), these structures have an approximately sub-horizontal inclination (Allan 1921) of 10˚. The Horseshoe formation is weak to extremely weak bedrock with a UCS of less than 5 MPa and GSI of 20 to 25 (Marinos and Hoek 2000). Previous investigations in the area describe the material near the site as highly plastic clay, overlaying sandstones, and shales (Klohn Crippen Berger 2000). These geologic characteristics cause the highway 837 to be susceptible to different unstable processes along the riverbank slopes and the slopes above the highway during precipitation events.

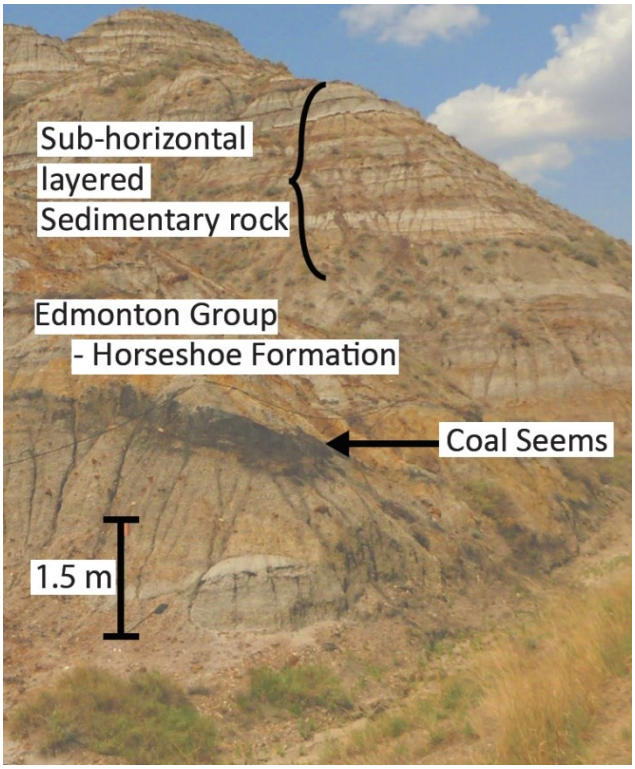


**Figure 3-2 Slopes exposing the horseshoe formation in the vicinity of the study site.**

Weathering of exposed bedrock and surficial material exhibit a soft soil-like behavior, with discontinuous blocks of more indurated bedrock which remains as intact blocks (Klohn Crippen

Berger 2018a). Rock layers composed mainly of sand-size particles present a higher susceptibility to the weathering process; however, these layers appeared to be mixed with fine soil particles. The mixture of sand-size and fine soil particles allows the erosion process to vary throughout the slope. Analyses on moisture susceptibility from different materials in the slope resulted in a deterioration of the material structure (i.e., dispersive material). The bonding of coarse grain particles decays during the saturation process changing their behavior to a weaker rock by destroying its internal structure. The degradation of the materials in the presence of water further suggests swelling potential, a likely key factor for the release of rock blocks into the highway.

During the summer of 2017, two large debris flows of approximately 1,300 $m^3$ occurred in the northern section of the study site. These two large events were preceded by rainfall events of approximately 30 mm and 8 mm in 24 hours, two days before failure. Later, on December 18, 2017, approximately 120 $m^3$ of blocks were estimated to have been released from 5 to 30 m above the highway in a similar location to the previous events (Klohn Crippen Berger 2018a). Further site inspections revealed that during winter 2017-2018, clumps of frozen soil and bedrock had fallen (Klohn Crippen Berger 2018b). During this freezing event, rock blocks were released from the slope, bounce to the highway, and reached the frozen surface of Red Deer River shore (Figure 3-3a).

On May 23, 2018, a large rock fall and debris flow at this location again blocked the highway. The event was preceded by a 15 mm rainfall event in 48 hours, that occurred six days prior to failure. This latest slide exposed a large rock outcrop approximately 40 m high and 50 m wide above the highway, on the northern side of the slope (Klohn Crippen Berger 2018a). After the later event, a variety of rock block sizes were found on the roadbed, from 4 mm gravel size to cobbles of 0.5 m in equivalent diameter (Figure 3-3b). Some of these larger particles appear to disaggregate while falling or upon impact with the roadbed. Following the May 2018 event, AT partially closed one lane section and temporarily installed concrete barriers to stop material from reaching the road. The barriers were Jersey Barriers approximately 80 cm in height (Figure 3-3c). The barrier extended for 90 m along the highway.

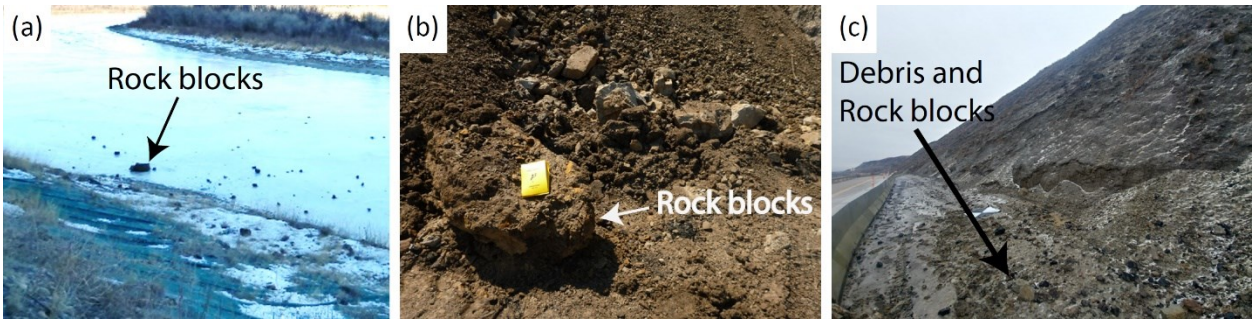


**Figure 3-3 Slope failures at the C018 slope; (a) rock blocks found on the frozen Red Deer River on December 2017; (b) rock blocks found across the Highway on May 2018; (c) accumulation rock falls and debris slide behind jersey barrier on November 2018.**

According to Cruden and VanDine (2013) classification system, the study site appears to show a complex failure mode that is weather-dependent. During spring, summer, and fall, the erosion process triggers rock falls. In addition, preceding precipitation events weaken the slope materials and increase the susceptibility for debris flows (Figure 3-3c). During the winter, the materials harden, and rock falls become the predominant mode of failure.

## 3.2 Application of UAV technology at the Study Site – Methods

The study site required a rapid and accurate assessment of the slope instabilities to reduce the risk to the public road users. However, the location and geometry of the site imposed a challenge to observe the location and conditions of the slope high above the highway. UAVs are equipped with a digital camera to capture photos along a flight path. The application UAV technology at the study site allowed to capture images of the slope not achievable from the highway. UAV data used in this paper was provided by AT (December 2017 and May 2018, after the slope failure events). Moreover, a third survey was done in November 2018 by the authors to continue monitoring the slope. The sequence of surveys allowed assessing the progressive erosion process that is deteriorating the slope surface through change detection techniques (comparing the surface of successive UAV surveys allows quantifying the changes of the surface over time). The information collected from the three UAV surveys was analyzed following six steps, as shown in Figure 3-4. This methodology derived from processes recommended by Pix4D (Pix4D S.A. 2018b) and LiDAR processing (Lague et al. 2013; Esposito et al. 2017).

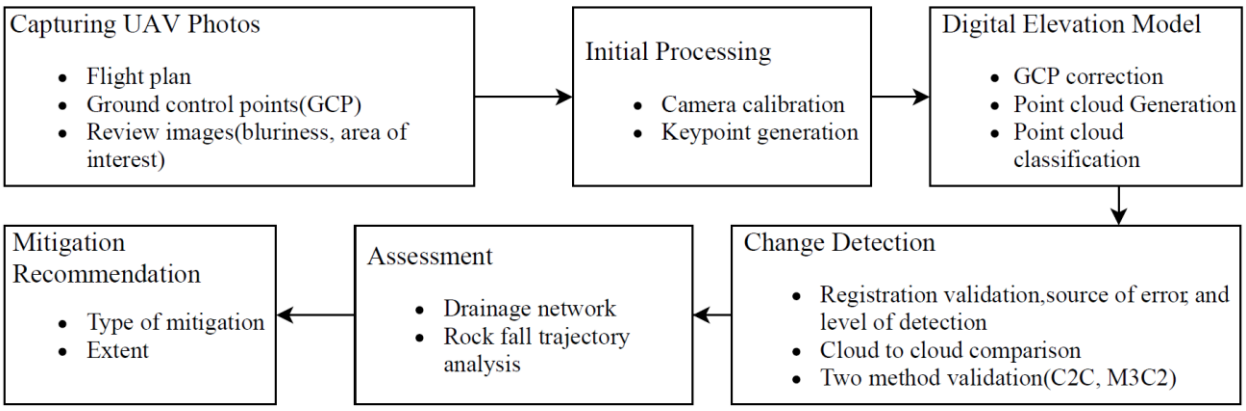


**Figure 3-4 Methodology followed with UAV data collected on three surveys at the study site.**

This section describes the fundamentals of the first five steps for the implementation of UAVs at the study site.

### 3.2.1 Capturing UAV Photos

The use of digital photogrammetric algorithms requires a set of pictures with enough overlap to reconstruct the terrain and to produce a point cloud with a resolution that captures the scale of significant features. This is achieved by allowing a minimum overlap of 60% between images, collecting at least three photos per feature, and using high-resolution cameras. The UAVs used in the surveys had a 12 MP camera for the first and third flight, and 17 MP camera for the second flight. The 12 MP camera had a sensor 1/2.3" CMOS (6.3 mm width and 4.7 mm height), a 94° field of view, a 20 mm focal length, and aperture f 1:2.8. The 17 MP camera had a sensor 1/2.3" CMOS (6.3 mm width and 4.7 mm height), an 82° field of view, a 44 mm focal length, and aperture f 1:3.3. The photos were stabilized using a gimbal attached to the camera to reduce the vibrations.

UAV systems are a quick and easy tool to deploy for surveying slope instabilities with difficult access. The UAVs were equipped with an internal GPS+GLONASS dual positioning module to allow precise control of the location during the flight. The internal GNSS has a hovering accuracy of ±1.5 m. Different software allows creating automatic flight plans to optimize collecting photos using UAVs, for this analysis the flight path was created using Pix4DCapture (Pix4D S.A. 2018b). An example of the flight path and photo locations is available as supplementary material to this paper. The automatic survey is established for different drone parameters such as (i) grid pattern,

(ii) flight height, (iii) flight speed, and (iv) camera angle. These parameters facilitate the collection of multiple photo records covering the study site.

The first two photogrammetry surveys were captured using a step stair sequence (different elevation) with a ground base elevation between 50 m and 90 m from the highway, with over 600 photos collected per survey. The third survey was performed at a single elevation of approximately 50 m measured from the crest of the slope, with 900 photos. The resulting GSD was between 1 and 3 cm per pixel. The UAVs used on the surveys are light quadcopters (less than 1.5 kg) that can reach speeds up to 20 m/s. Although, high speeds reduce the flight time and battery consumption; the speed was kept below 7.2 m/s to avoid capturing blurry images during the survey. Lastly, the camera angle can provide oblique images to capture more details on very steep slopes. Capturing photos at oblique angles allows adequate coverage of steep slopes. Care should be taken to avoid angles and orientations that result in direct sunlight on the lens that may result in the overexposure of the images. This can be mitigated through proper flight planning (time of the day and flight path). The photos from the surveys were captured at an angle between 0 to 10 degrees from the vertical. During the surveys, the internal GNSS and gimbal provide the location and orientation of each photo taken during the survey (also known as *geotags*). The geotag collected on each photo allows having local precision within a few meters. This information allows determining the position, orientation, and scale of the capture objects to generate a point cloud in each survey. Nevertheless, the low precision of the internal UAV GNSS required to have ground control points (GCP) whose coordinates are measured.

The use of GCPs allows to optimize the absolute accuracy of the point cloud georeferentiation obtained from the geotags, this resulted in a georeferentiation with root mean square error between 0.01 m and 0.06 m. The coordinates of the GCP were measured with an RTK GNSS (traditional survey methods). The site conditions limited the distribution of the GCPs due to the steepness of the slope. The GCPs were distributed along the highway and crest of the slope. The first two surveys had 5 GCPs near the highway with a precision of ±2 cm in the horizontal direction and ±2 cm in the vertical direction; while the last survey used 10 GCPs near the highway and the crest of the slope with a precision of ±10 cm in the horizontal direction and ±10 cm in the vertical direction. Finally, a visual inspection of the captured photos from the site was made to remove low-quality

photos reducing errors in the point cloud reconstruction (as suggested by the software manufactures such as Pix4D and Adam Technology).

### 3.2.2 Digital Photogrammetric Reconstruction

The photos from each survey are used to generate point clouds. The point cloud requires having a resolution that captures the surficial details to allow analyzing the changes of relevant features. The events that occurred prior to the UAV surveys are over 10 m wide, with a depth between 30 cm to 2.0 m. The process to reconstruct the topography at the study site using UAV photos was fully automated with commercial software (Pix4Dmapper, Pix4D S.A. 2018). This software uses *Structure From Motion* (SFM) algorithms (Westoby et al. 2012), in combination with the camera correction process, photographic georeferencing, and private algorithm processes to find common points (*key points*) between photos. The key points have known coordinates in X, Y, and Z axis that allows reconstructing the topographic ground surface through point clouds (Küng et al. 2012a). Pix4D mapper divides the reconstruction process of the point cloud in two steps; the first step consists in the calibration of camera internal and external parameters. The internal camera parameters are the temperature, vibrations, focal length, and shutter mode (Vautherin et al. 2016) to reduce distortion and noise in the photos. The external parameters are the orientation and position of the photos (Vallet et al. 2011). Next, sample key points are automatically generated in each photo and matched to other overlapping photos. At the study site between 40,000 to 60,000 points were extracted per photo and matched between 17% to 23% of points per photo. The coordinates of the key points are calibrated based on the GCPs. The calibration required manual selection of key points on 8 to 15 photos per GCP. The calibration using GCP improves georeferencing and scale of the point cloud. The relative difference between the initial position and the corrected position from the three surveys was between 2 cm to 6 cm. The second step is a densification of the point cloud based on the key points from the first step. Pix4D mapper uses key points as input to apply a clustering multi-view stereo algorithm (CMVS) and patch-based multi-video stereo algorithm (PMVS) to densify the point cloud (Furukawa and Ponce 2009; Küng et al. 2012b). The size of the original photo was reduced to one half of its original size to increases computational efficiency while maintaining an optimal point cloud density that reflects the roughness different features (Pix4D S.A. 2018b). Reducing the scale allowed to compute one 3D point every 8 pixels. The validity of each 3D point was defined by having 3 or more re-projections

into the photos. In the third survey, 5 or more re-projections were required due to the homogeneity of the ground surface of the farm field above the slope. Details of point cloud processing of each UAV survey is presented on Table 3-1.

**Table 3-1 Hardware characterist, processing time, and points from densification.**

| UAV Flight | December 2017 | May 2018 | November 2018 |
|---|---|---|---|
| **Photos** | 655 | 600 | 910 |
| **CPU** | Intel(R) Xeon(R) CPU E5-1620 0 @ 3.60GHz | Intel(R) Xeon(R) CPU E5-1620 v4 @ 3.50GHz | Intel(R) Core(TM) i7-6700 CPU @ 3.40GHz |
| **RAM** | 32GB | 64GB | 16GB |
| **GPU** | NVIDIA Quadro 4000 (Driver: 21.21.13.7748) | NVIDIA GeForce GTX 1080 (Driver: 24.21.13.9731) | Intel(R) HD Graphics 530 (Driver: 23.20.16.4849), NVIDIA GeForce GTX 745 (Driver: 23.21.13.8813) |
| **Processing time** | 5 hours and 30 min | 3 hours and 40 min | 33 hours and 20 min |
| **Number of key points** | 2,461,994 | 1,641,029 | 4,008,579 |
| **Number of densified points** | 39,069,202 | 54,014,157 | 116,255,113 |

Following the densification of each point cloud, outlier points were filtered without altering the overall roughness of the point cloud. The filter was done using open source software CloudCompare V2.9 (LGPL 2011). Outlier points are identified as those outside the confidence interval defined by the average distance to a common point of 10 neighboring points plus “n” standard deviations of the distance. This was achieved in a two-step process using the Statistical Outlier Removal (SOR) tool in the software. The first step removed points outside with “n” of 3 standard deviations, followed by “n” of 2. This process ensures a precise outlier filter.

### 3.2.3 Change Detection

Change detection analyses using point clouds require accurate alignment between clouds from different surveys. The UAV surveys had different precisions associated with the GSD; the geotags and GCPs that translates into point cloud precision. Variability in the location of the points is referred to as registration error. Aligning the point clouds reduces this registration error. The fine alignment of the point clouds is achieved by using known stable areas outside of the area of analysis. This process was performed using the first survey as a reference for alignment for the other two. The alignment areas were selected to the north and south side of the study site, shown in Figure 3-1. The fine alignment iterates to create a transformation matrix of 10,000 points randomly sampled until a maximum root means square error (RMSE) of 1.0e-5 m is achieved. The final transformation matrix is applied to the entire point cloud to proceed with the cloud to cloud

comparison. The alignment and cloud to cloud comparison were computed using CloudCompare V2.9 (LGPL 2011).

There are multiple methods available to evaluate the differences between point clouds (Lague et al. 2013; Kromer et al. 2015a). The two methods used in this paper are: the closest point method (C2C) to provide a first estimate with lower computational requirements (Girardeau-Montaut et al. 2005); and, the multiscale model to model cloud comparison (M3C2) based on a more robust statistical analysis (Lague et al. 2013). This methodology is based on Esposito et al. (2017) that also used C2C to quantify the registration error and M3C2 to assess landslides on a coastal region in Italy. The registration error was quantified by selecting three zones outside the study site and assumed to be unaltered.

The C2C method computes change as the absolute distance between a point on the first point cloud to the nearest point on the subsequent point cloud; this method is limited as it is affected by the point cloud roughness (Girardeau-Montaut et al. 2005). The reader should be aware that the roughness is affected by the density of points in the point cloud. Consequently, variation in density would induce errors in the implementation of the C2C method. The computation of the distance using the C2C method was computed using a quadratic regression on the reference cloud for points within a 0.3 m radius.

The M3C2 method allows computing the total displacement of two point cloud in a positive (material gain) or negative (material loss) direction. The direction of the displacement is quantified based on the calculation of normal vector on the reference cloud (i.e., December 2017 survey) using a triangulation model build on the software. The total displacement is measured by selecting a point cloud as a reference and calculating the average distance of each point to a second point cloud. The points selected from the second point cloud are those points located within a circular projection from the reference point. In the analysis, a circular projection of 0.3 m in diameter was used. The orientation of the projection from the reference point is with respect to the normal vector of the original cloud, calculated within the 0.3 m diameter circle.

Also, the algorithm in the M3C2 method computes the level of detection (minimum distance change that can be measured) within a 95% confidence interval by accounting the roughness of the reference point cloud (also calculated within the algorithm) and the registration error from the

cloud determined using the C2C method. Details of the procedure can be found in Lague et al. (2013).

### 3.2.4 Drainage Network

Site observations have shown that unstable slope events at the study site have been preceded by precipitation events. In addition, the slope maps from the third survey showed that the farm land (Figure 3-1) above the slope drains towards the study site. An analysis of the drainage network (watershed) of the ground surface allows to determine the preferential path runoff water takes from the top of the slope to the highway. The paths allow assessing the relationship between runoff water and the unstable slopes at the site. In addition, this analysis allows quantifying the contributing area for water to flow through the preferential paths of the slope surface. The drainage network was calculated using ArcGIS Desktop V10.5 (Environmental Systems Research Institute Inc. 2016).

The drainage network was estimated based on the changes in elevation of the ground surface. The process proposed by Jenson and Domingue (Jenson and Domingue 1988) was used to derive the accumulated flow path of a DEM generated from the third survey. The resolution achieved with the UAV point clouds provides the opportunity to analyze the influence of preferential drainage paths (watershed) on the active zones at a small scale. Then, the point cloud was transformed into a DEM with a cell size of 20 cm by 20 cm using a rasterize tool in CloudCompare V2.9 (LGPL 2011) from the May 2018 point cloud. The direction of flow is calculated in each cell by comparing the elevation difference to the surrounding eight cells. Next, the cumulative flow is calculated for each cell by summing the number of contributing cells. The cumulative flow is transformed into a contributing area by multiplying the quantity of contributing cells on each cell by the cell size. The result is a dense drainage network that accounts for any difference elevation at the scale size. The main drainage lines were determined by filtering the drainage network. The filter was applied to remove drainage lines with less than 125 $m^2$ of contributing area. The minimum value accounts for 0.78% of the total contributing area in the DEM. This process has shown to be scale dependent (Tarboton et al. 1991); a larger extension of the DEM could increase the values of the contributing area.

### 3.2.5 Rock fall Trajectory Modelling

Using the surface reconstruction from the UAV, 2-dimensional rock fall simulations were used to estimate the run-out distance, bouncing height and kinetic energy generated by falling, bouncing and rolling blocks. The rock fall hazard was predominantly located on the northern active zone of the study site. The rock fall simulations were conducted using Rocscience's RocFall (Rocscience Inc. 2018), using a Monte-Carlo based method to derive a statistical distribution from 1000 rock fall events. RocFall simulates the rocks as solid blocks with parabolic trajectories and notes the modeled location impacts, subsequent rebounds and rolling. Energy losses during impacts are modeled using coefficients of restitution which range from 0 if all of the kinetic energy is lost and 1 if no energy lost.

The trajectory of rock falls from the rock outcrop on the northern side of the study site (Figure 3-1, F1) was modeled using the cross-section A-A. The source of rock falls has a length of 50 m equal to 10% of the entire section of the study site. The cross section was generated from the point cloud of the second UAV survey following the rock fall and debris flow. The rock outcrop exposed after the rockslide became a concern to the highway due to the susceptibility of eroding the base layer and release other large blocks into the highway. A 2.5-dimensional (2.5D) rock fall trajectory simulation was conducted to evaluate if the geometry of the slope results in rock fall trajectories that deviate significantly from those represented from a 2D analysis. A lower density DEM with cell size of 1 m by 1 m from the May 2018 point cloud was generated for the 2.5D analysis. Rockfall Analyst (Lan et al. 2007, 2010), an addon for ArcGIS Desktop V10.5, was used for modeling the 2.5 D rockfall trajectories (Macciotta and Martin 2019). The analysis used a lumped mass approach, which models the blocks as points without considering the shape and volume of the blocks. The rock fall seeders (location of rock fall initiation) were located at the crest of the slope at the elevation of material observed to result in rockfalls which consists of stronger materials overlying erosion features. The higher potential corresponded to the layer of stronger materials overlying eroded areas. Initial velocity was set at 0.1m/s.

Initial input parameters for the models in Rockfall Analyst and RocFall were estimated based on field measurements and observation of the predominant size of blocks and location after falling. The initiation of the rock fall trajectory models in RocFall was distributed between 32 m and 46 m upslope from the highway, consistent with the observed rock fall source areas on site. The

analysis assumes an initial horizontal velocity of 0.1 m/s, no initial vertical and angular velocity at three starting points within the observable source area. This reflects the observations on site where blocks tend to reach the road and approximate the river. Also, these low initial velocities reflect what is expected at the initial movements of the fall after the block detaches from the slope. The size of the blocks assumed a 0.5 m diameter block with a mass of 896 kg released 1 m above ground. The rock fall modeling followed the rigid-body methodology that accounts for the shape of the block. The shape was simulated as a cube with rounded edges and specified in the software model as a "superellipse of the fourth order". The modeling was not capable of accounting for the disaggregation of the blocks and was made with the largest sizes found on the highway.

Typical coefficients of energy restitution for the slope materials (talus, uniform debris, sedimentary rock, and asphalt) were used initially and then modified such that the simulated rock fall fit with the distribution of material observed on the highway (Pfeiffer and Bowen 1989; Giani 1992; Hoek 2018). The final coefficient of restitution parameters are presented in Table 3-2 and are similar to values from the literature for similar areas (Pfeiffer and Bowen 1989; Giani 1992; Hoek 2018).

**Table 3-2 Input surface parameters used in the 2D rock fall simulations**

| Input Parameter | | Asphalt Surface | | Sedimentary Rock Surface | |
|---|---|---|---|---|---|
| | | Mean | Standard Deviation | Mean | Standard Deviation |
| Surface parameters | Normal Coefficient of Restitution, Rn | 0.40 | 0.04 | 0.30 | 0.04 |
| | Tangential Coefficient of Restitution, Rt | 0.85 | 0.04 | 0.70 | 0.04 |
| | Dynamic Friction | 0.5 | - | 0.56 | - |
| | Rolling Friction | 0.1 | 0 | 0.05 | 0 |

## 3.3 RESULTS

### 3.3.1 Digital Photogrammetric Reconstruction

The use of digital photogrammetric techniques had several sources of errors from the collected data and post-processing methods. The resulting point cloud density of the first survey was an average of 60 3D points per cubic meter; the second survey resulted in an average density of 100 3D points per cubic meter, and the third resulted in 280 3D points per cubic meter. The height and

slope of the study area resulted in a lower resolution at the bottom of the slope. This variability can result in a lower accuracy near the toe of the slope. An example of the changes in GSD in cross section from the study for a flight path 50 m above the crest of the slope used in November 2018 is shown in Figure 3-5.

The change in accuracy from the UAV surveys allowed to reach an average GSD between 2.0 cm/pixel and 6.0 cm/pixel, being highest at the base of the slope. The point cloud scale and global position were improved using different GCPs targets on the area. The RMSE of the GCP coordinates respect to the 3D point cloud reconstruction is 0.02 m, 0.01 m, 0.06 m for December 2017, May 2018, and November 2018 respectively.

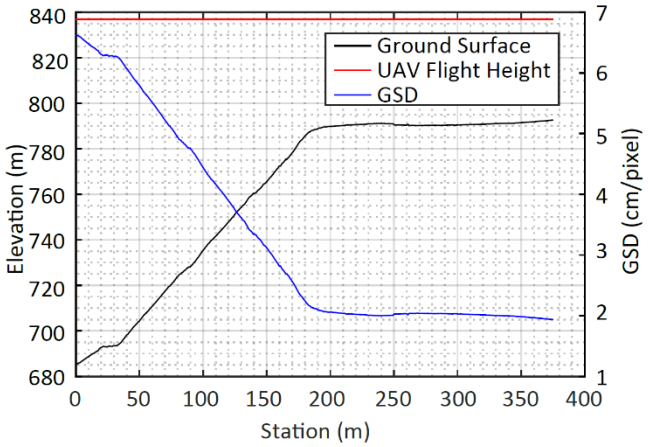


**Figure 3-5 Changes in GSD from a single flight path along the slope surface in the November UAV flight.**

Fine alignment of the two 2018 point clouds to the reference point cloud from 2017 allowed reducing the relatively local and global uncertainty of the point cloud with respect to each other. The alignment of 10 thousand random points at each side of the slope and three registration zones with a maximum RMSE of 1.0e-5 m resulted in a maximum distance frequency of 0.05 m for May and November 2018. The registration error for May and November point cloud resulted in 0.08 m and 0.13 m respectively, based on the alignment of the cloud and registration zone analysis. This local variability is also increased by vegetation cover, snow cover, and the slope deterioration between each point cloud. The removal of points associated with the small coverage of snow and vegetation, predominantly located on the upper section of the slope, were not considered in the point cloud. However, the SOR filter allowed to smooth the point cloud, reducing the point density

from 13 to 11 million for December 2017, from 7.5 to 6 million for May 2018, and from 27 to 23 million for November 2018.

The point clouds from the three surveys were used to measure the dimension and obtain a closer perspective of the slope instabilities. Figure 3-6 shows the three point clouds for the largest active zone on the slope and the extent of the failure zone. The rock outcrop is approximately 50 m wide and located 30 m above the highway. The extent has not changed between December 2017 and November 2018; however, the upper scarp is becoming steeper as the material erodes. The material that is being deposited on the highway is the result of further erosion within the active zone limits. The erosion is more pronounced to the northern side of the active zone than the southern side.

The photograph from the second survey (Figure 3-6a) shows the areas of rock falls and debris being generated from the upper section, near the scarp. The December 2017 point cloud (T1, Figure 3-6b) shows the initial conditions of the rock fall zone from the start of the analysis presented in this paper. The point cloud from May 2018 shows the progressive erosion process towards the northern side (T2, Figure 3-6c). On the third survey, it was noticeable that the southern side of the active zone continues to release debris to the highway (T3, Figure 3-6d).

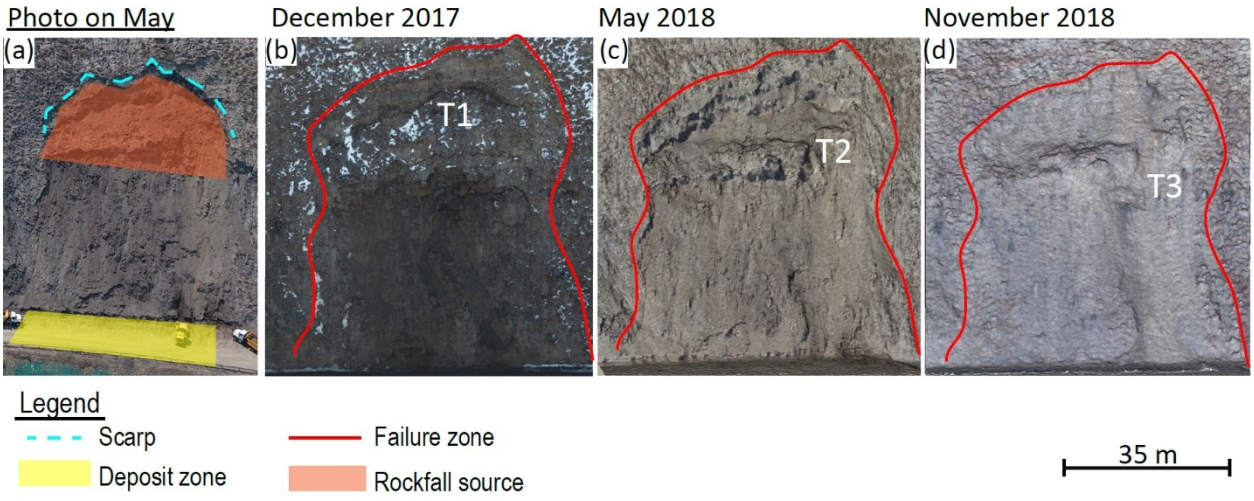


**Figure 3-6 Point cloud on the largest active zone F1 Northen side of the study site;(a) shows the photo taken from the UAV after the May event; (b) shows the point cloud from first UAV survey; (c) shows the point cloud from the second UAV survey; (d) shows the point cloud from the third UAV survey.**

### 3.3.2 Change Detection

Use of historical point cloud data allowed to estimate the changes on the surface between December 2017 and November 2018. The change detection analysis of the first survey with respect to the second and third surveys shows the progressive erosion process that occurred at the surface. The analysis using the M3C2 method resulted in 8.5% of the points in the reference point cloud had a significant change (movement greater than the level of detection) at 95% confidence level (Figure 3-7). Areas with significant change showed a small cluster located in the active zone.

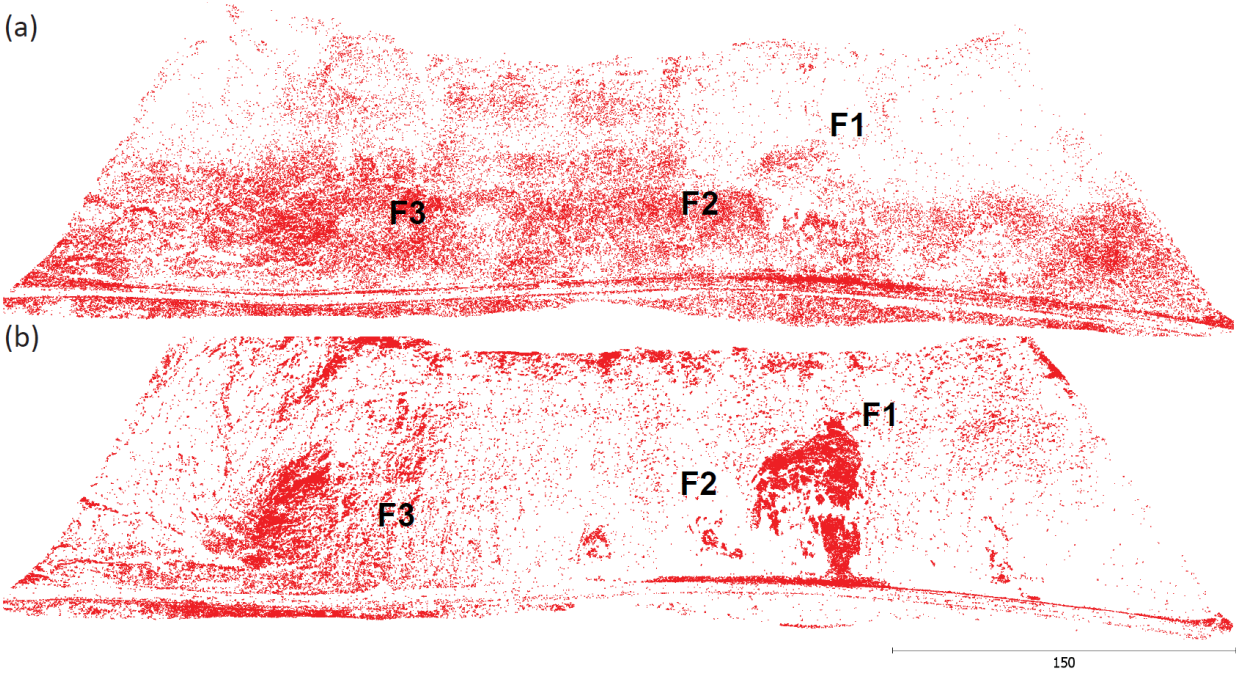


**Figure 3-7 Zones of significant change (red points) derived from the change detection analyses using the M3C2 method; (a) show the comparison between the first and second surveys; (b) show the comparison between the first and third surveys.**

The comparison between December 2017 point cloud and May 2018 point cloud resulted in an average level of detection of 0.2 m. The comparison between December 2017 point cloud and November 2018 point cloud resulted in an average level of detection of 0.3 m. After filtering the points with movement lower than the level of detection from both slope analyses, the results provide the magnitude and direction (i.e., material gain or loss) of the areas with measurable topographic change (Figure 3-8). Assessing the cumulative slope changes from December 2017 to

November 2018 in a two-step process required to homogenize the level of detection of both change detection analyses, which resulted in a minimum resolution of 0.3 m.

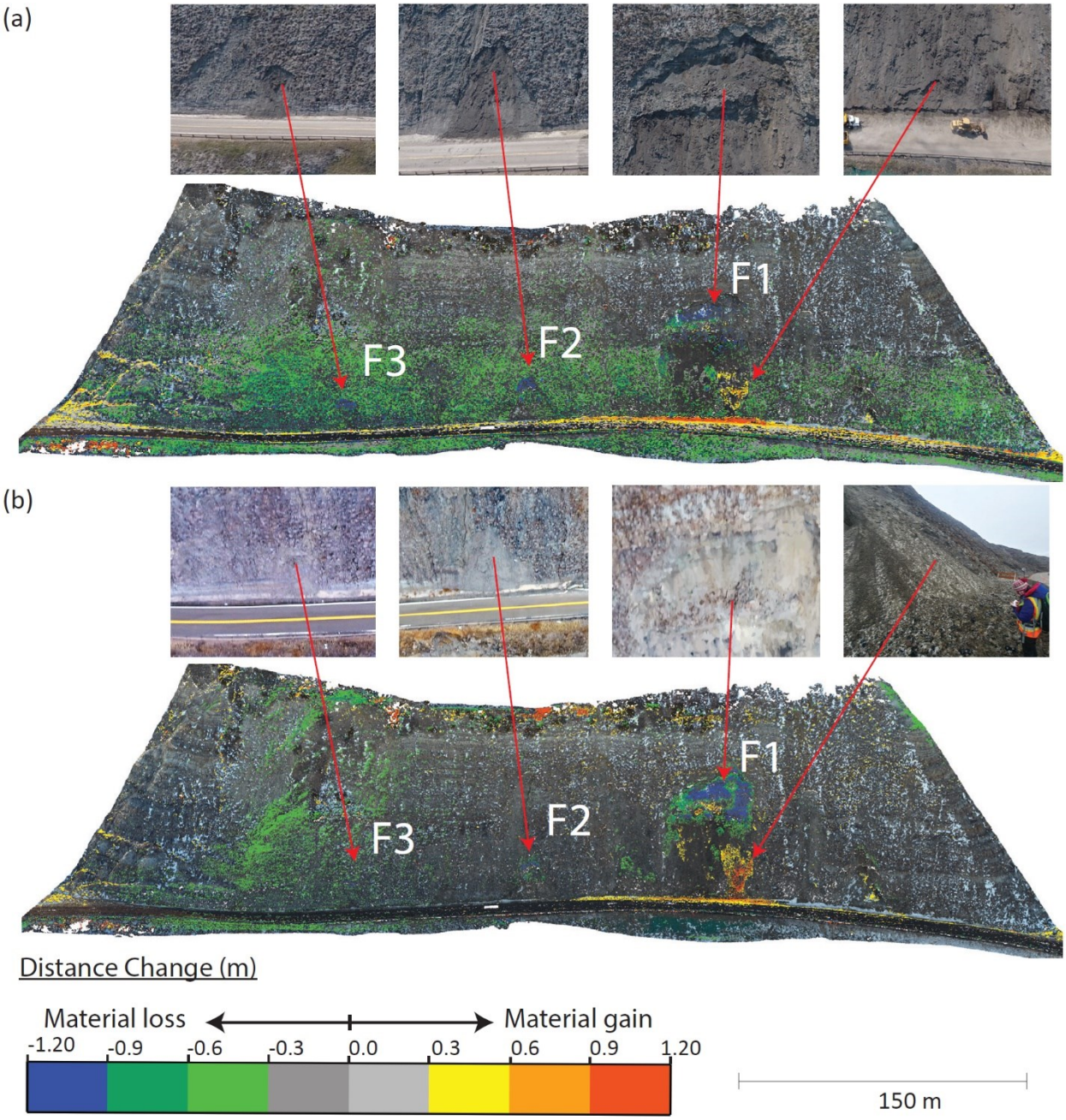


**Figure 3-8 Change detection analysis from the three UAV surveys using M3C2 method; (a) shows the comparison between the first and second surveys; (b) show the comparison between the first and third surveys. Warmer colors indicating a gain in material and cooler colors are indicating a material loss.**

The estimated distance change from the three point clouds shows the highest material loss to be located in the northern area (Figure 3-8a, F1). This area of the slope also indicates the accumulation of material near the base of the slope and along the ditch of the highway. The results also show additional movements in the same area in November (Figure 3-8b, F1). The analysis shows more material accumulation along the ditch between December 2017 and May 2018 than between December 2017 and November 2018, which is associated with highway maintenance and cleanup operations, following recommendations by KCB (Klohn Crippen Berger 2018b). Minor movements were measured near the road on other sections of the slope towards the south. This movement on the bottom sections of the slope agreed with the field observation.

The analysis reveals contrasting movements along the slope, increasing towards the center and northern side of the slope. Conversely, fewer movements are found near the crest of the slope. The change detection analysis shows several zones on the upper and middle sections of the slope with an average material loss from 0.18 m to 0.58 m in depth. The loss of material occurred in May 2018, accompanied by an average accumulation of material along the ditch of the highway from 0.09 m to 0.69m. In November, less material is shown to be loss on the upper and middle sections of the slope. These changes correspond to a loss of 738 $m^3$ of material and a gain of 323 $m^3$ at the toe of the slope in the northern area (Figure 3-8b, F1). The difference in volume (loss and gain) corresponds to material being removed from the ditch along the highway prior the UAV flight in December 2017. At the center and eastern side of the slope the two smaller instabilities had a loss of material of 25 $m^3$ (Figure 3-8b, F2 and F3).

Lastly, a comparison of the cross-section A-A extracted from the December 2017 point cloud and May 2018 point cloud allowed to visually assess if the rock outcrop had moved between the two UAV surveys (Figure 3-9). The cross-section revealed zone of material loss after the rock slide, and the remaining material deposited on the ditch of the road; unfortunately, the scan on May 2018 was made one day after the clearing of the highway. Thus, the collection of the total deposition zone is not complete.

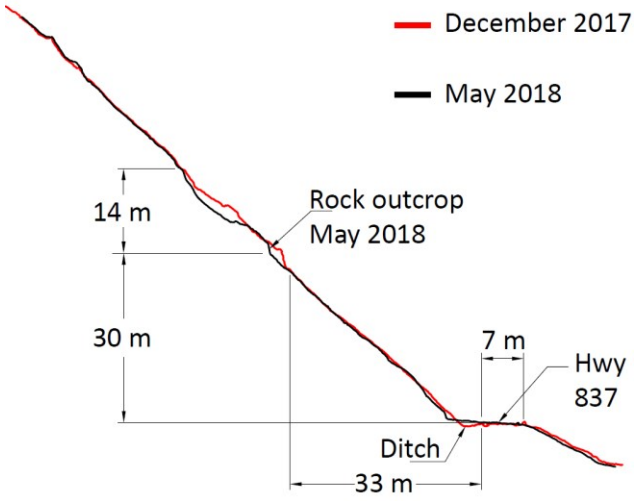


**Figure 3-9 Cross-section A-A for the Rock fall trajectory analysis at the study site .**

### 3.3.3 Drainage Network

The computation of the drainage network using the raster generated from the November 2018 point cloud allowed to quantify the drainage above and at the face of the slope. Figure 3-10 shows the location of the preferential drainage lines from the farm crop to the toe of the slope. The figure shows the drainage network classified in 10 classes ranging from 125 $m^2$ to 15,800 $m^2$ of contributing area. The lines are color-coded to indicate the amount of contributing area along the drainage lines. Thus, it's expected higher values are located near the toe of the slope. Still, one drainage line at the top of the farmland reached 10,800 $m^2$ of contributing area, equal to 38% of the total mapped area of the farm crop. This drainage line flows to the face of the slope in between zone F1, and F2, the largest active zones in the slope (Figure 3-10). This distribution could be related to the higher activities located to the center and the northern section of the study area.

The three active zones (F1, F2, and F3, shown in Figure 3-10) have drainage lines distributed on the surface. Active zone A shows drainage lines with up to 1100 $m^2$ of contributing area at the center of the active zone. The exposed outcrop on May 2018 generated a small bench at the middle of the active zone that increased the contributing area to approximately 800 $m^2$. This increment in zone A coincides with the material loss between the point cloud from May and November 2018, as shown in point T1, T2, and T3 in Figure 3-6.

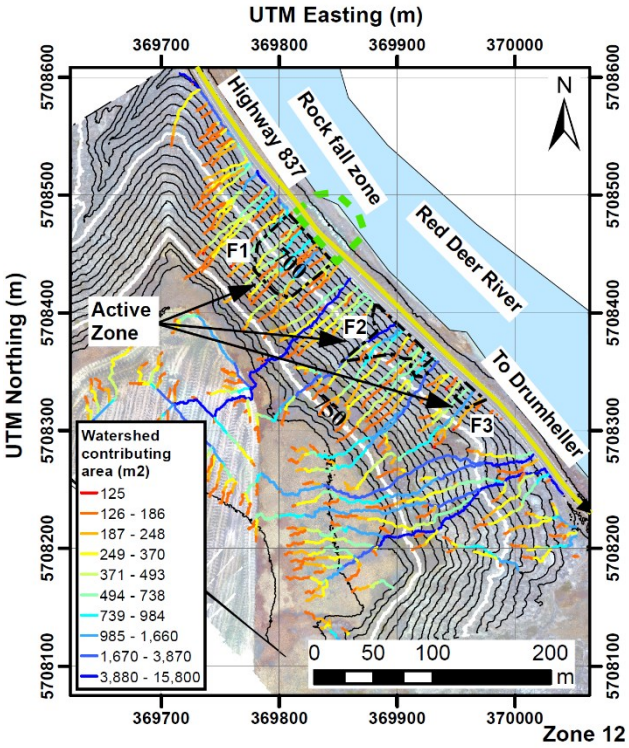


**Figure 3-10 Drainage Network of the study site using DEM from point cloud from the November 2018 UAV survey.**

Active zone F2 (Figure 3-10) has a high drainage line of approximately 3000 $m^2$ of contributing area starting from the upper section of the slope. This high-intensity drainage line has eroded the upper section of the slope. In the southern area of the active zone F2, there is another high-intensity drainage line with approximately 800 $m^2$ of contributing area. This area in zone F2 started to increase the border of the erosion process similarly to active zone F3 (Figure 3-10).

The analysis of the drainage network allows assessing runoff water as one contributing factor to the erosion process at the study site. High-intensity drainage lines are converging south of active zone F3 (Figure 3-10) which could suggest future stability problems. The result gives an indication of the relationship between runoff water and the active zones. However, this analysis does not account for water infiltration or evaporation. Although not conclusive at this site, the analysis provides important insight into drainage factors of the slope as they relate to the activity observed.

### 3.3.4 Modeled Rock Fall Trajectories

The results from the 2.5-dimensional rock fall analysis were not used to calculate the length of the rock fall trajectories or to compare the kinetic energies from both techniques, but to evaluate if the geometry of the slope results in rock fall trajectories that deviate significantly from those represented from a 2D analysis. The results confirm that the trajectories along the slope do not notably deviated from an idealized 2-dimensional trajectory, and therefore the critical block in the northern side of the slope can be analysed with a 2-dimensional approach, as shown in Figure 3-11, F1. The 2-dimensional simulation of rock fall trajectories considered blocks of equivalent diameter to 0.05 m, 0.1 m, 0.2 m, 0.3 m, 0.4 m, and 0.5 m. The corresponding masses are shown in Figure 3-12. The analysis of the trajectory of potential rock falls estimates rock blocks reaching the highway, resting on the side berm of the highway, and crossing the road towards the Red Deer River. The simulation of 1000 possible falling blocks can reach a height of approximately 5 m (Figure 3-12b) at the edge of the highway with a total kinetic energy of up to 110 kJ (Figure 3-12). Figure 3-12 shows the overall distribution of trajectories and how all block size trajectories overlap.

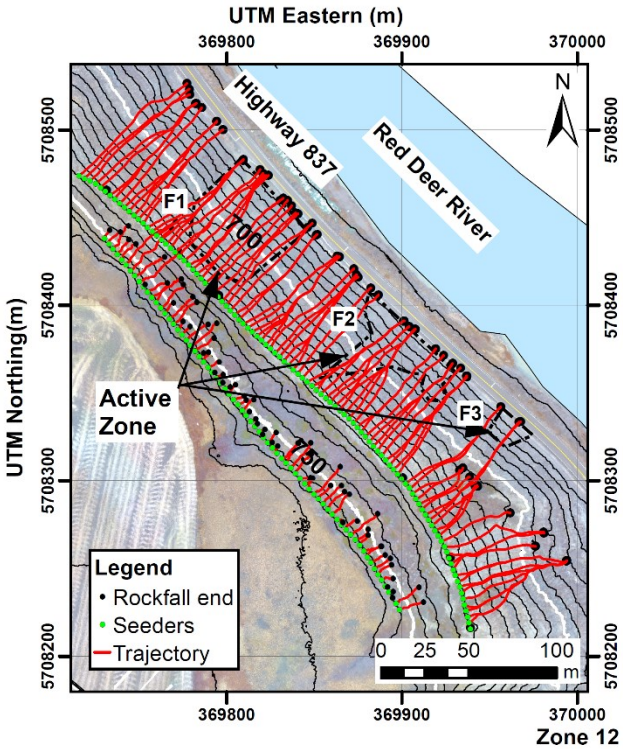


**Figure 3-11 2.5 D Rock fall simulation for trajectory of blocks generated with two lines of seeders located at the crest of the slope.**

The calibration of the coefficients of restitution resulted in trajectories with similar characteristics to those observed during the site visits. These modelled trajectories resting near the highway and near the river bank matched these observations. These sizes resemble cube blocks with a side length of 0.08m, 0.16m, 0.32m, 0.6m, 0.65m, 0.8m as measured during the site visits. The detachment locations for falling blocks were modelled as a continuous line, located between the head scarp and the location of the large block (also according to observed rock fall scars with the higher potential energies).

The simulation using RocFall (Rocscience Inc. 2018) showed modelled trajectories of the different rock block sizes identified from the May 2018 survey. The simulation shows the impact of different block sizes and sources on the energy of the block and bouncing height when reaching the ditch adjacent to the road. These are key parameters for decision-making regarding rock fall protection (e.g., height of lock block walls) (Macciotta and Martin, 2019).

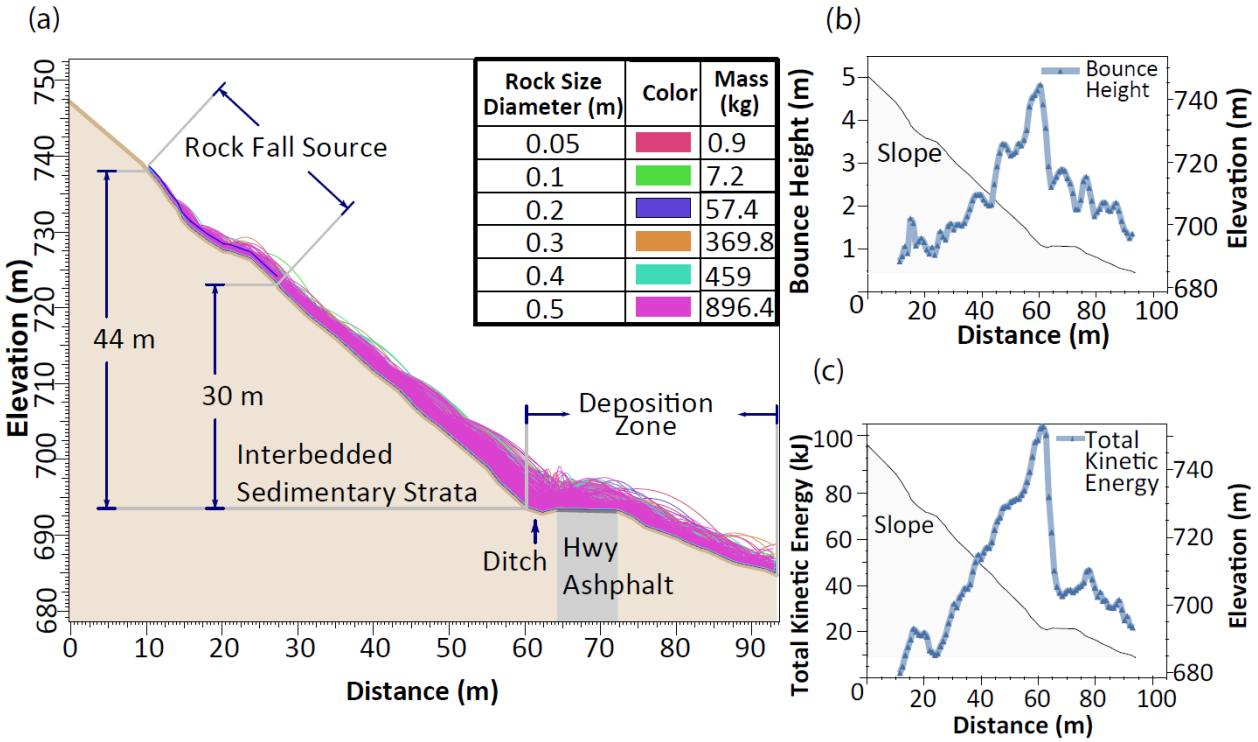


**Figure 3-12 2D Rock fall simulation on section A-A (a) Trajectories from 1000 blocks using Monte Carlo Method; (b) bounce height from 95% percentile of rock fall trajectories; (c) total kinetic energy from 95% percentile of rock fall trajectories.**

## 3.4 DISCUSSION

### 3.4.1 Rock Slope Failure Processes and their Relationship with Weather Conditions

The geology of the slope contributes to a differential erosion process and variability in the weathering of the materials on the slope. The formation of preferential flow paths tends to be developed in areas with a higher content of sand-size particles. The different geological layers are distributed horizontally and the perpendicular direction of the preferential flow paths cross all different rock layers. Consequently, the flow paths intensify the erosion processes in the vicinity of these channels resulting in areas with more susceptibility to failure. This erosion process increases near the base of the slope as sedimentary layers are less distinctive and layers are a mixture of sand-size particles with different levels of fine particles.

The results from the change detection analysis in Figure 3-8 and site observations resulted in the identification of the following three modes of failure.

The first mode of failure is the development of debris flows. This is postulated to be the result of layers of the argillaceous rocks rapidly eroding with seasonal precipitation, and freeze-thaw cycles. This erosion generates a layer of loose clayey soil that is prone to flowing down the slope once it has a high enough moisture content to sufficiently lower its strength. These events are more probable during the spring due to melting snow and higher levels of precipitation. The event in May 2018 was an example of the mode of failure (Figure 3-8a, F1).

The second mode of failure is rock falls. This was observed to be a result of the differential weathering of the sedimentary rock. Layers of sedimentary rock more prone to weathering are eroded from beneath more competent rock layers, leaving the competent rock unsupported (Figure 3-8, F1), leading to rock detachment and rock fall events. The rock fall events shown in Figure 3-3b were an example of the mode of failure after the exposure of the large rock blocks following the debris flow in May 2018.

The third mode of failure is the detachment and falling of blocks of frozen soil from the surface of the slope. This mode of failure was identified from the observation of frozen blocks of soil and bedrock over the highway and the frozen river and the identification of the source of the frozen material on the slope (Figure 3-3a).

### 3.4.2 Mitigation Strategies

The susceptibility of the slope to generate rock falls after precipitation events, and particularly after the large event on May 2018 that exposed a large outcrop with the potential to release large blocks to the highway, requires a detailed analysis of the rock fall hazard that users are exposed to. The point cloud derived from the UAV survey provided the necessary means to identify and analyze in detail the critical area of the slope prone to rock falls. Rock fall trajectories can be better estimated by extracting detailed topographic information in a point cloud. The rock fall trajectory analysis provided the information on which to base decisions and design for rock fall hazard mitigation. Nonetheless, this information must be integrated with field observations to adjust and calibrate the characteristics of the event such as block size and shapes, location, deposition zone, and surface conditions.

The use of sequential topographic reconstructions, field observations and the comparison of two cross sections from the two UAV surveys in December 2017 and May 2018 (Figure 3-9) allowed for an informed assessment of the potential hazards associated with this slope. The information gained in this analysis lead to proposing a combination of a catchment net near the base of the slope and slope maintenance (e.g. scaling) to decrease the risk to highway users from rock falls on the northern side of the slope (Klohn Crippen Berger 2018a). This catchment net was selected to provide retention of 95% of the blocks with a total dissipation energy of 150 kJ as indicated by the model. Options to manage the risk to debris flows included weather-based hazard notifications and detection fences that, when triggered, alert the users about a potential blocked section of highway. These last are still under development at this site (Klohn Crippen Berger 2018a).

## 3.5 CONCLUSION

UAV and digital photogrammetric techniques are very useful to characterize inaccessible areas. Creating a historical registry through point clouds becomes a useful methodology for monitoring purposes and assess changes, as well as to obtain comparison maps from 3D points clouds or section profiles. Other sub products like DEM in raster format may be used for drainage analysis or rockfalls simulations.

The analysis of rock failure process and the mitigation strategies have taken advantage of UAV photos and digital photogrammetry. Risk management of ground hazards on large extents of linear

infrastructure limits the resources that specific problems might require. The use of low-cost UAV becomes a useful tool that provided detail information of the surface ground conditions, especially on sites with difficult access. At the C018 site, the slope inclination and height became an obstacle for visual inspection after the sliding events; however, the use of low-cost point cloud during several inspections provides a new perspective that can optimize the ground hazard assessment. The use of digital photogrammetric techniques based on pictures obtained with UAV devices allows quantifying the magnitude and extent of the slope instabilities.

The low-cost point cloud provides the opportunity to generate historical records that show different perspectives on the rock fall hazards at the study site. The use of change detection analysis in combination with visual inspections provided the information to determine the location of critical zones, magnitude, and extend for the implementation of mitigation strategies.

Ultimately, the use of digital photogrammetric techniques based on pictures acquired with UAV became a tool that helped in the risk management process on the C018 site after the latest events. The information gathered from the UAV survey would continue to influence future decisions on the site as it captured a larger picture of the processes that otherwise might be difficult or not viable to obtain.

The geologic characteristics of the slope at the study site in combination with water have always been the driven factor of the historical failure process that has impacted the highway. Analysis of the drainage network has given an indication of the potential critical areas that can be impacted during a period of heavy rainfall.

The geometry of the slope made access difficult to the active zone source and other weathered features upslope. The implementation of UAV technology to assess the conditions of the slope allowed having a large perspective on the conditions during each survey. Monitoring and investigation of the C018 slope have provided insight into the use of low-cost UAV for monitoring and assessing rock slopes with multiple failure mechanisms associated with weather conditions. This tool provides the engineer with multiple perspectives of ground hazards with complex modes of failure and difficult access, that translates in more information to improve the assessment of the slope and optimized mitigation strategies. The point cloud in combination with the change detection analyses allowed to quantify the dimensions and show the evolution of the erosion

process at the study site. Low-cost UAV surveys should not replace or undermine the importance of site inspections; rather, it enhances the information to make better decisions.

## 3.6 ACKNOWLEDGMENTS

This research was made possible by the (Canadian) Railway Ground Hazard Research Program, which is funded by the Natural Sciences and Engineering Research Council of Canada (NSERC), Canadian Pacific Railway (CR), Canadian National Railway Company (CN); and Transport Canada.

## 3.7 REFERENCES

Agüera-Vega F, Carvajal-Ramírez F, Martínez-Carricondo P, et al (2018) Reconstruction of extreme topography from UAV structure from motion photogrammetry. Meas J Int Meas Confed 121:127–138. doi: 10.1016/j.measurement.2018.02.062

Al-Rawabdeh A, Moussa A, Foroutan M, et al (2017) Time series UAV image-based point clouds for landslide progression evaluation applications. Sensors (Switzerland) 17:. doi: 10.3390/s17102378

Alberta Transportation (2017) Traffic Counts Reference No. 106230 2016. http://www.transportation.alberta.ca/mapping/. Accessed 17 Oct 2018

Allan JA (1921) Geology of Drumheller Coal Field , Alberta. J.W. Jeffery, Kings's Printer, Edmonton

Allasia P, Baldo M, Giordan D, et al (2019) Near Real Time Monitoring Systems and Periodic Surveys Using a Multi Sensors UAV: The Case of Ponzano Landslide. IAEG/AEG Annu Meet Proceedings, San Fr California, 2018 - Vol 1 1:303–310. doi: 10.1007/978-3-319-93124-1_37

Beregovoi D V., Younes JA, Mustafin MG (2017) Monitoring of Quarry Slope Deformations with the Use of Satellite Positioning Technology and Unmanned Aerial Vehicles. Procedia Eng 189:737–743. doi: 10.1016/j.proeng.2017.05.116

Borneuf D (1972) Hydrogeology of the Drumheller Area, Alberta, Report 72-1. Edmonton

Bowen TJ, Pfeiffer TD (1989) Computer Simulation of Rockfalls. Environ Eng Geosci xxvi:135–146. doi: https://doi-org.login.ezproxy.library.ualberta.ca/10.2113/gseegeosci.xxvi.1.135

Carlà T, Farina P, Intrieri E, et al (2017a) On the monitoring and early-warning of brittle slope failures in hard rock masses: Examples from an open-pit mine. Eng Geol 228:71–81. doi: 10.1016/j.enggeo.2017.08.007

Carlà T, Macciotta R, Hendry M, et al (2017b) Displacement of a landslide retaining wall and application of an enhanced failure forecasting approach. Landslides 15:489–505. doi: 10.1007/s10346-017-0887-7

Cucchiaro S, Cavalli M, Vericat D, et al (2018) Monitoring topographic changes through 4D-structure-from-motion photogrammetry: application to a debris-flow channel. Environ Earth

Sci 77:1–21. doi: 10.1007/s12665-018-7817-4

DroneDeploy Inc. f.k.a. Infatics Inc. (2020) Drone Deploy

Environmental Systems Research Institute Inc. (2016) ArcGIS Desktop [Software]

Esposito G, Salvini R, Matano F, et al (2017) Multitemporal monitoring of a coastal landslide through SfM-derived point cloud comparison. Photogramm Rec 32:459–479. doi: 10.1111/phor.12218

Fan X, Xu Q, Scaringi G, et al (2017) Failure mechanism and kinematics of the deadly June 24th 2017 Xinmo landslide, Maoxian, Sichuan, China. Landslides 14:2129–2146. doi: 10.1007/s10346-017-0907-7

Fey C, Wichmann V (2017) Long-range terrestrial laser scanning for geomorphological change detection in alpine terrain – handling uncertainties. Earth Surf Process Landforms 42:789–802. doi: 10.1002/esp.4022

Furukawa Y, Ponce J (2009) Accurate Camera Calibration from Multi-View Stereo and Bundle Adjustment - Furukawa, Team - Unknown.pdf. Int J Comput Vis 84:257– 268

Giani GP (1992) Rock slope stability analysis. Rotterdam : Balkema

Girardeau-Montaut D, Roux M (2005) Change detection on points cloud data acquired with a ground laser scanner. Int Arch Photogramm Remote Sens Spat Inf Sci 36:W19. doi: 10.1.1.221.8313

Government of Canada (2018) Historical Weather Data from Drumheller. http://climate.weather.gc.ca/. Accessed 20 Aug 2018

Hendry M, Macciotta R, Martin CD, Reich B (2015) Effect of Thompson River elevation on velocity and instability of Ripley Slide. Can Geotech J 52:257–267. doi: 10.1139/cgj-2013-0364

Hoek E (2018) Unpublished notes. In: Rocscience. https://www.rocscience.com/help/rocfall/baggage/rn_rt_table.htm. Accessed 27 May 2018

Huang H, Song K, Yi W, et al (2018) Use of multi-source remote sensing images to describe the sudden Shanshucao landslide in the Three Gorges Reservoir, China. Bull Eng Geol Environ 1–20. doi: 10.1007/s10064-018-1261-2

Jenson SK, Domingue JO (1988) Extracting topographic structure from digital elevation data for geographic information system analysis. Photogrammetric Engineering and Remote. Photogramm Eng Remote Sensing 54:1593–1600. doi: 0099-1112/88/5411-1593$02.25/0

Klohn Crippen Berger (2000) Central Region Landslide Assessment SH837:02 River Scour @ km 1.9 Emergency Geotechnical Inspection Report, July 25, 2000

Klohn Crippen Berger (2018a) CON0017608 Central Region GRMP – Call-Out Report C018 Hwy 837:02 Call-Out Report Revision 1 July 13, 2018. Red Deer

Klohn Crippen Berger (2018b) CON0017608 Central Region GRMP – Call-Out Report C018 Hwy 837:02 Call-Out Report January 19, 2018. Red Deer

Kromer R, Lato M, Hutchinson DJ, et al (2017) Managing rockfall risk through baseline monitoring of precursors using a terrestrial laser scanner. Can Geotech J 54:953–967. doi:

10.1139/cgj-2016-0178

Kromer RA, Abellán A, Hutchinson DJ, et al (2015) A 4D filtering and calibration technique for small-scale point cloud change detection with a terrestrial laser scanner. Remote Sens 7:13029–13058. doi: 10.3390/rs71013029

Küng O, Strecha C, Beyeler A, et al (2012a) The Accuracy of Automatic Photogrammetric Techniques on Ultra-Light Uav Imagery. ISPRS - Int Arch Photogramm Remote Sens Spat Inf Sci XXXVIII-1/:125–130. doi: 10.5194/isprsarchives-XXXVIII-1-C22-125-2011

Küng O, Strecha C, Fua P, et al (2012b) Simplified Building Models Extraction From Ultra-Light Uav Imagery. ISPRS - Int Arch Photogramm Remote Sens Spat Inf Sci XXXVIII-1/:217–222. doi: 10.5194/isprsarchives-XXXVIII-1-C22-217-2011

Lague D, Brodu N, Leroux J (2013) Accurate 3D comparison of complex topography with terrestrial laser scanner: Application to the Rangitikei canyon (N-Z). ISPRS J Photogramm Remote Sens 82:10–26. doi: 10.1016/j.isprsjprs.2013.04.009

Lan H, Derek Martin C, Lim CH (2007) RockFall analyst: A GIS extension for three-dimensional and spatially distributed rockfall hazard modeling. Comput Geosci 33:262–279. doi: 10.1016/j.cageo.2006.05.013

Lan H, Martin CD, Zhou C, Lim CH (2010) Rockfall hazard analysis using LiDAR and spatial modeling. Geomorphology 118:213–223. doi: 10.1016/j.geomorph.2010.01.002

LGPL (2011) CloudCompare [GPL software]

Macciotta R, Martin CD (2019) Preliminary approach for prioritizing resource allocation for rock fall hazard investigations based on susceptibility mapping and efficient three-dimensional trajectory modelling. Bull Eng Geol Environ 78:2803–2815. doi: 10.1007/s10064-018-1279-5

Macciotta R, Rodriguez J, Hendry M, et al (2017) The 10-mile Slide North of Lillooet , British Columbia – History , Characteristics and Monitoring. In: 3rd North American Symposium on Landslides. Roanoke, Virginia

Marinos PG, Hoek E (2000) GSI: A geologically friendly tool for rock mass strength estimation. In: Proc. GeoEng2000 Conference. pp 1422–1442

Martínez-Carricondo P, Agüera-Vega F, Carvajal-Ramírez F, et al (2018) Assessment of UAV-photogrammetric mapping accuracy based on variation of ground control points. Int J Appl Earth Obs Geoinf 72:1–10. doi: 10.1016/j.jag.2018.05.015

Mazzanti P, Bozzano F, Brunetti A, et al (2017) Experimental Landslide Monitoring Site of Poggio Baldi Landslide (Santa Sofia, N-Apennine, Italy). In: Advancing Culture of Living with Landslides. Springer International Publishing, Ljubljana, Slovenia, pp 259–260

Petschko H, Bell R, Glade T (2016) Effectiveness of visually analyzing LiDAR DTM derivatives for earth and debris slide inventory mapping for statistical susceptibility modeling. Landslides 13:857–872. doi: 10.1007/s10346-015-0622-1

Pix4D S.A. (2018a) Pix4DCapture

Pix4D S.A. (2018b) Pix4Dmapper Pro

Prior GJ, Hathway B, Glombick PM, et al (2013) Bedrock Geology of Alberta, AER/AGS Map

600, scale 1:1,000,000. To accompany AGS Open File Report 2013-02.

Riquelme A, Cano M, Tomás R, Abellán A (2017) Identification of Rock Slope Discontinuity Sets from Laser Scanner and Photogrammetric Point Clouds: A Comparative Analysis. Procedia Eng 191:838–845. doi: 10.1016/j.proeng.2017.05.251

Rocscience Inc. (2018) Rocfall

Rodriguez J, Hendry M (2018) Cost-effective Landslide Monitoring GPS System : Characteristics , Implementation and Results. In: Geohazards7. Canmore, Alberta

Roque D, Perissin D, Falcão AP, et al (2018) Analysis of InSAR displacements for the slopes around Odelouca reservoir. Procedia Comput Sci 138:338–345. doi: 10.1016/j.procs.2018.10.048

Smethurst JA, Smith A, Uhlemann S, et al (2017) Current and future role of instrumentation and monitoring in the performance of transport infrastructure slopes. Q J Eng Geol Hydrogeol 50:271–286. doi: 10.1144/qjegh2016-080

Solazzo D, Sankey JB, Sankey TT, Munson SM (2018) Mapping and measuring aeolian sand dunes with photogrammetry and LiDAR from unmanned aerial vehicles (UAV) and multispectral satellite imagery on the Paria Plateau, AZ, USA. Geomorphology 319:174–185. doi: 10.1016/j.geomorph.2018.07.023

Sousa JJ, Ruiz AM, Bakoň M, et al (2016) Potential of C-Band SAR Interferometry for Dam Monitoring. Procedia Comput Sci 100:1103–1114. doi: 10.1016/j.procs.2016.09.258

Stalker AM (1973) Memoir 370 Surficial Geology of the Drumheller area, Alberta. Ottawa

Tarboton DG, Bras RL, Rodriguez-Iturbe I (1991) Tarboton_et_al-1991-Hydrological_Processes. Hydrol Process 5:81–100. doi: 10.1002/hyp.3360050107

Vallet J, Panissod F, Strecha C, Tracol M (2011) PHOTOGRAMMETRIC PERFORMANCE OF AN ULTRA LIGHT WEIGHT SWINGLET "UAV." Int Arch Photogramm Remote Sens Spat Inf Sci. doi: 10.5194/isprsarchives-XXXVIII-1-C22-253-2011

Vanneschi C, Eyre M, Francioni M, Coggan J (2017) The Use of Remote Sensing Techniques for Monitoring and Characterization of Slope Instability. Procedia Eng 191:150–157. doi: 10.1016/j.proeng.2017.05.166

Vautherin J, Rutishauser S, Schneider-Zapp K, et al (2016) Photogrammetric accuracy and modeling of rolling shutter cameras. ISPRS Ann Photogramm Remote Sens Spat Inf Sci 3:

Westoby MJJ, Brasington J, Glasser NFF, et al (2012) 'Structure-from-Motion' photogrammetry: A low-cost, effective tool for geoscience applications. Geomorphology 179:300–314. doi: 10.1016/j.geomorph.2012.08.021

Williams JG, Rosser NJ, Hardy RJ, et al (2017) Optimising 4D Approaches to Surface Change Detection: Improving Understanding of Rockfall Magnitude-Frequency. Earth Surf Dyn Discuss 1–36. doi: 10.5194/esurf-2017-43

# CHAPTER FOUR. PRACTICAL EVALUATION OF SINGLE-FREQUENCY DGNSS FOR MONITORING SLOW-MOVING LANDSLIDES

**Contribution of the Ph.D. candidate**

The work presented in this chapter, that includes literature review, instrument installation, investigation methodology, analysis and discussion of the results and writing of the text was carried out by the Ph.D. candidate.

The supervisors Dr. Michael Hendry and Dr. Renato Macciotta have reviewed all parts of the work. This chapter has been published in the Landslide Journal with the following citation:

Rodriguez J., Deane E., Hendry M. T., Macciotta R.; Evans T., Gräpel C., & Skirrow R. Practical evaluation of single-frequency dGNSS for monitoring slow-moving landslides. Landslides (2021). doi: 10.1007/s10346-021-01737-y

**Contribution of this chapter to the overall study**

In 2016 the University of Alberta, in partnership with the Canadian National Railway through the *Railway Ground Hazard Research Program* acquired a novel monitoring system named Geocubes™ to assess landslides in an active state (i.e., moving landslide). The Geocubes are low-cost differential Global navigation satellite system (dGNSS) units with single-frequency signal capability that monitor surficial deformation at multiple locations. This manuscript presents the first application of a network of Geocube units in Canada, installed in 2016 at the Ten-mile landslide in British Columbia, and a second installation in 2018 at the Chin-Coulee landslide in Alberta. The dGNSS units at the Ten-mile continuously recorded the ground position for 536 days between 2017 and 2018, while the Chin-Coulee recorded the ground position for 436 days between 2018 and 2019. The data was used to quantify the surficial deformation on different areas of the landslide. The precision of the recorded data from the Geocube at the two sites is presented and compared against the measurements of a multi-frequency GNSS installed at the Ripley landslide in British Columbia. Installation of multiple units across the landslides allowed the interpretation of the magnitude and inclination of displacement as an alternative to slope inclinometers (SI) or ShapeAccelArrays (SAA). The continuous monitoring of displacement allowed evaluating weather-based changes as causal factors of the changes in the displacement rates at each site. This manuscript highlights the benefits, limitations and application of low-cost single-frequency

dGNSS units with precise spatial and temporal resolution to measure deformations of the ground surface, and identify mechanisms of failure for slow-moving landslides.

***Abstract***

Assessing the risk of a landslide requires an understanding of the kinematics and triggers. These are best evaluated with higher frequency displacement measurements at multiple measurement locations across the sliding mass; to allow for the evaluation of the impact of meteorological events and the displacement of different portions of the landslide. Installing a monitoring system that provides suitable higher-frequency displacement data from multiple locations on a landslide can be expensive and thus not commonly used. Single-frequency dGNSS provide a relatively 'low-cost' alternative to provide long term monitoring for landslides at multiple locations with a high data collection rate and precision. A network of single-frequency dGNSS, called Geocube, was installed at two slow-moving landslides, at the Ten-mile landslide near Lillooet, B.C. and the Chin-Coulee landslide near Taber, AB. The Geocube system allowed monitoring surficial deformation every 60 seconds with a precision of ± 5 mm at each site for the duration of the monitoring program, over 500 days. The quality of the collected data was compared to the GMX 910 Leica GNSS, a high-end multi-frequency GNSS, installed at the Ripley landslide near Ashcroft, BC. The data collected from the monitoring system at the two sites showed the variability in displacements and displacement rates of the sliding mass. The application of multiple monitoring points provided an alternative for evaluating the shape of the sliding shear surface and the causal factor driving movement at each site. The paper demonstrates the application of single-frequency dGNSS in the Canadian environment with exposure to seasonal weather. The paper also evaluates the monitoring system application to provide reliable information required for the development of early warning systems on landslide deformation.

***Keywords:***

Single-frequency dGNSS, Geocubes, Ten-mile, Chin Coulee, Landslide, Monitoring

## 4.1 INTRODUCTION

Measurements of landslide displacements at high frequencies are necessary for early warning systems; and, regular displacement measurements at frequencies in the order of days have proven useful for assessing mechanisms associated with changing the rates of displacement.

Instrumentation installed within the ground, such as in-place slope inclinometers (SI), ShapeAccelArrays (SAAs), and extensometers can be effective at providing high frequency data collection. However, these come with limitations in that they are: (1) expensive to install as they require drilling, and thus these are often only used in limited numbers with low spatial resolution; (2) the measurements of displacement are limited in directions that can be observed. In-plane two-dimensional displacement for inclinometers and SAAs, and one dimensional for extensometers; (3) the measurements are relative to a point on the instrument itself; and, (4) continued deformations will eventually result in the loss of the instruments and the need to purchase and install replacements (Smethurst et al. 2017; Hendry et al. 2019).

The use of differential Global navigation satellite system (dGNSS) based monitoring systems has allowed for high frequency measurements without the loss of functionality with displacements. The precision of survey quality instruments has proven to be high enough to develop early warning systems (Vaziri et al. 2010; Intrieri et al. 2012; Macciotta et al. 2016a). However, high equipment costs and power requirements have still limited the locations at which these can be used and the spatial resolution of installations (Hendry et al. 2015; Woods et al. 2020). Continued advancements in both hardware and processing of GNSS radio signals have been driven by the incorporation of positioning technology in consumer electronics (Rodriguez et al. 2020). This has resulted in less expensive (and less capable) hardware being used to provide precise and repeatable location measurements.

Lower cost dGNSS systems for landslide monitoring are becoming available commercially, an example of which is the Geocube from Ophelia Sensors, which was originally developed by the French Institut Géographique National (Benoit et al. 2015a, b). The system was initially tested at the Super-Sauze landslide and the Glacier d'Argentière both in the French Alps (Benoit et al. 2015a, b). This system, inclusive of processing methods, has resulted in the capability to obtain high frequency and high precision measurements at lower costs; and, is configured with the required communications and coordination to develop a network of many sensors across a site (Benoit et al. 2015a; Odolinski and Teunissen 2017; Romero-Andrade et al. 2019; Zhang et al. 2019).

These lower cost dGNSS systems, with lower power requirements, have the potential to greatly expand the use of GNSS monitoring of landslide to new sites, which were not feasible due to

budget constraints and available power (Benoit et al. 2015a, b). As all of the sensors remain on the surface, these systems can be installed by two people without heavy equipment and can be redeployed to other sites as needed. The lower costs allow for multiple dGNSS units to be "seeded" across a landslide to evaluate displacements and provide more information as to the mechanism of failure and the kinematics of a land movement (Benoit et al. 2015a).

This paper presents a study that was undertaken to evaluate a dGNSS system (Geocube) to determine if current technology provides measurements with high enough precision to develop early warning systems, evaluate the lower limits of displacement monitoring, and the interpretive capabilities obtained from high frequency displacement measurements at multiple locations across a given landslide. This study was undertaken by installing single-frequency dGNSS systems at two active landslides: the Ten-mile landslide near Lillooet, British Columbia Canada, and the Chin Coulee landslide adjacent to the Chin reservoir in southern Alberta, Canada; these are a slow and an extremely slow landslides, respectively (Cruden and VanDine 2013). The Ten-mile landslide provided an opportunity to test the system in mountainous terrain with limitations on the number of observable satellites, and to observe the displacement of various block of soils from a disintegrated sliding mass. The Chin Coulee landslide provided the opportunity to test the lower limits of detection of the system and to observe the displacements of a translational landslide. The qualities of the resulting measured displacements are compared to those obtained from a traditional GNSS (GMX 910 Leica multi-frequency GNSS receivers) previously presented in Macciotta *et al.* (2016). The Leica GNSS at the Ripley landslide has provided detailed surficial deformation since 2004, and it has been part of the Railway Ground Hazard Research Program for testing multiple instruments (Macciotta et al. 2014; Journault et al. 2016; Huntley et al. 2019).

### 4.2 DESCRIPTION OF SITES AND INSTRUMENTS

The following is a description of the two testing sites for the dGNSS system, the Ten-mile landslide and the Chin Coulee landslide, and the characteristic of the dGNSS system and installation.

### 4.2.1 The Ten-mile landslide

The Ten-mile landslide is located approximately 17 km northeast of the town of Lillooet, southeastern BC, adjacent to the Fraser River (50°44'49.3"N 121°50'56.0"W). The Ten-mile landslide is approximately 200 m wide and 140 m high, oriented to the North-West, with 850.000 $m^3$ of active material. This landslide is a concern as both a railway and critical local roadway cross over it, and there are no other route options for this infrastructure due to the steep terrain (Figure 4-1a).

The landslide is at the toe of a much larger post-glacial earthflow named Tunnel earthflow with an estimated maximum depth of 30 m (Bovis 1985). As a past earthflow, the original soil strata have been churned, resulting in complex arraignments of soil types (Figure 4-1b). The soil samples obtained from landslide have shown that it primarily consists of fine-grained sediment of clay, silt, and sand, with the presence of angular rock fragments that range in size from gravel to boulders. Vibrating wire piezometers have been installed on the landslide on several occasions; however, all have indicated that there is not a phreatic surface within the sliding soils. Cuts made adjacent to the roadway (Figure 4-1b) have shown the slow seepage of water above deposits with high clay contents, and the underlying moist clay was found to be soft enough to press one's thumb into easily.

The landslide was identified in the early 1970s below the Highway, and it has been retrogressing uphill since the late 1980s (Gaib et al. 2012). The historical displacement rate has increased from 1 mm/day in 2006 to 6 mm/day in 2016 and 12 mm/day (Gaib et al. 2012; BGC Engineering Inc. 2016a). The total displacements of portions of the landslide exceeded 20 m between 2009 and 2015. Over this time, the sliding mass has broken up into many blocks of soil (Figure 4-1c) (Lato et al. 2016). Slope inclinometers installed at the site were rarely able to be read more than twice due to the high rate of movement, the available readings indicate a shear surface at a depth of 18 m. Core retrieved from sonic drilling indicated that the shear surface is located near the base of the soil displaced from the tunnel earthflow.

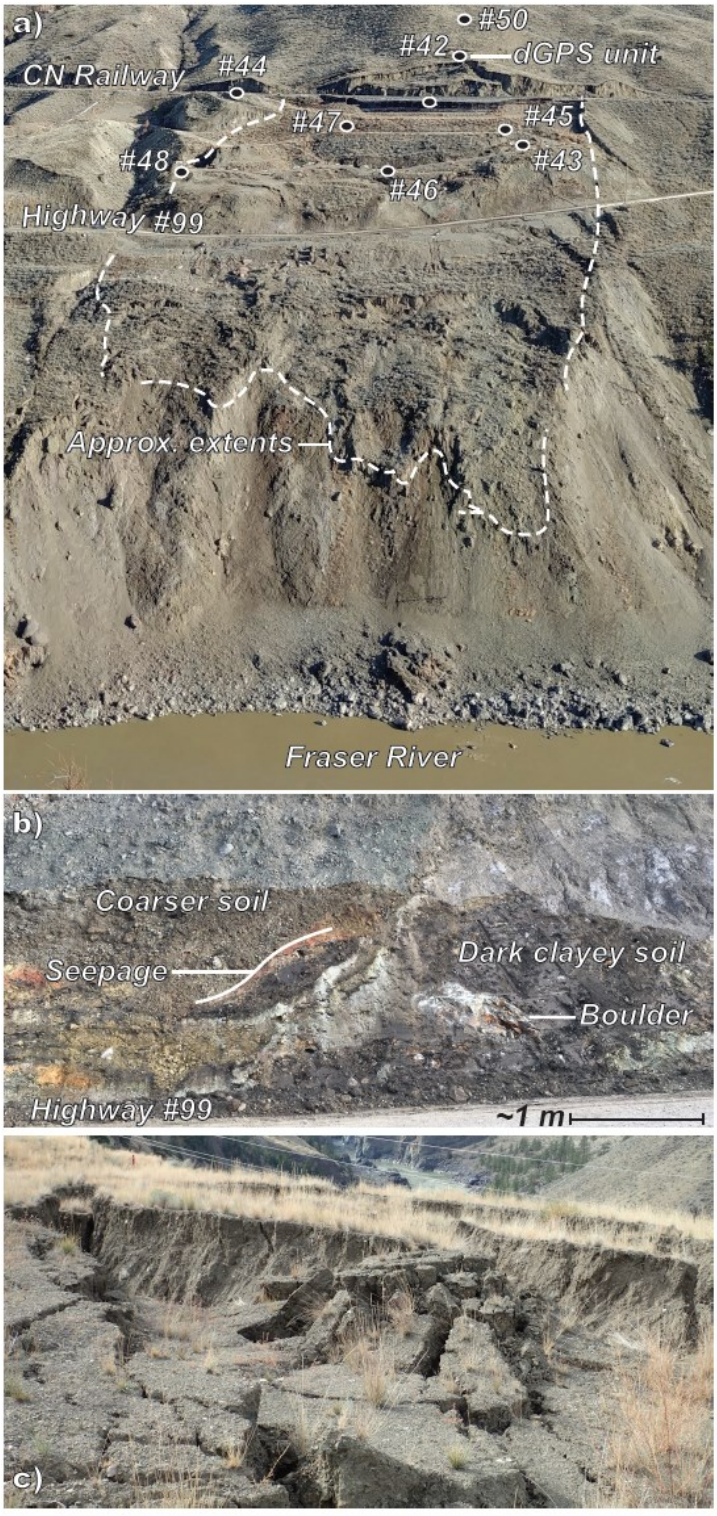


**Figure 4-1 Photographs of the Ten-mile (a) from across the Fraser river showing the extents and locations of road and railway (Mar. 2018); (b) a cut adjacent to the road showing the churned strata (Oct. 2016); and, (c) from the surface of the landslide showing the sliding mass having broken into blocks of varying sizes (Oct. 2015).**

Canadian National Railway (CN) and the British Columbia Ministry of Transportation and Infrastructure (MoTI) have taken measures to maintain their right of way. The retrogression of the landslide required since 2004: realignment of the railway track in 2004, install lock blocks below the track in 2005, and construct a shotcrete soil anchor wall in 2006. Following the reappearance of tension cracks below the tracks in early 2008, ballast and lock blocks were added to the retaining wall for additional support. In the summer of 2008, the shotcrete wall was replaced with an 18 m length H-pile retaining wall with timber lagging and soil anchors. The loss of soils in front of the wall between 2008 and 2010 required extending the height and length by adding lagging to newly exposed lower portions of the H-Piles. Near the Highway, the MoTI has realignment of the road and to cut into the slope to keep it passable. The MoTI trialed a soil-cement shear key wall with an orientation perpendicular to the slide movement over a small portion of the slope in 2011 to increase the resistance of the soil and reduce the movement (Gaib et al. 2012). In 2012 and 2014, excessive deformation and loss of material in the front of the H-pile retaining wall required reinforcement by welding steel plates. Subsequent retrogression of the landslide above the railway track was controlled by installing 253 steel shear piles in 2016, the piles were 364 mm in diameter and up to 21 m in length, and located downslope of the H-pile retaining wall. These shear piles effectively slowed the displacement rate of the track and H-pile wall from 12 mm/day to less than 1 mm/day. However, these shear piles only slowed the upper portions of the landslide. As a result, the MoTI started in 2017 mitigation measures by installing 32 steel strands anchors with thrust blocks on the first slope bench above the Highway.

### 4.2.2 The Chin Coulee landslide

The Chin Coulee landslide is located on the northern slope of the valley that contains Chin Lake reservoir, adjacent to Alberta Highway 36 in southern Alberta (49°36'17.0"N 112°10'45.9"W). Chin Lake is an agricultural water reservoir for the surrounding farmland with a water level that fluctuates seasonally. The Chin Coulee landslide is approximately 350 m wide at the reservoir and 55 m high above the reservoir, with an average slope angle of 13° and an estimated volume of 2 $Mm^3$ (Deane et al. 2020) (Figure 4-2).

The surficial material at the site is a brown to grey clay till, with low to medium plasticity, silty, very stiff to hard, with traces of fine gravel and sand lenses, some of which conduct water. The till extends from the level terrain surrounding the melt water channel that is now Chin Lake reservoir

down 54 m to 12 m below the reservoir's elevation. The local bedrock beneath the till consists of thin and discontinuous layers of grey, low to non-plastic sandstone; grey, clayey, and calcareous siltstone, and brown and grey silty shale of medium to high plasticity, with some coal seams present in some layers (Golder and Associates 1998). Past borehole logs suggest that blocks of weathered bedrock exist within the clay till material and suggest glacial overriding. Additionally, slickensides were also found within the till layer (Golder and Associates 1998). Installed piezometers indicate that the groundwater depth is 6 m below the head scarp and 2 m near the toe (Golder and Associates 1998). Information on the shear surface from slope inclinometers has been limited by the accessibility and installation issues (Amec FW 2015). Slope inclinometers installed near the head scarp suggest the presence of a sub-horizontal failure surface within the bedrock unit. The failure surface is approximately 59 m below the elevation of the roadway and within a clay shale layer with a coal seam inclined 1.5° upwards to the reservoir (Amec FW 2015). The intact clay shale has a tested effective strength of $\phi' = 30°$ and a back calculated residual effective strength of $\phi'_r = 8°$ (Amec FW 2015).

The landslide impacts a rural two-lane roadway (Alberta Highway 36), which is an important local road and leads to the crossing of Chin lake. Prior to 1998, there was little formal record keeping of the landslide movements, and the following timeline has been reconstructed from air photos retrieved from the National Air photo Library and other reports (Deane et al. 2020). The roadway was realigned from the base of the valley to the crest prior to 1960 with the construction of the dam and filling of the Chin Lake reservoir. A subsequent realignment of the road occurred prior to 1970, requiring the additional fill material and grading of the roadway. Significant displacements occurred during the autumn of 1978, extending to the shoulder of the road, and thus developing the current extents of the landslide (Golder and Associates 1998) (Figure 4-2). Displacements appeared to continued based on observed tension cracks beneath guard rails and road structures. However, regular monitoring started after 1997, following the damages of the northbound lane caused by deformations. Since 1998 the landslide has had periods of activity and dormancy, with a maximum average annual displacement rate of only 5 mm/year (Amec FW 2015).


**Figure 4-2 Photographs of the Chin Coulee landslide (a) showing the extents of the landslide and locations of the dGNSS units (Photo from 2015 Google Earth); and, (b) the backscarp of the landslide (Photo by Evan Deane).**

### 4.2.3 Single-frequency dGNSS system

Global navigation satellite system (GNSS) receivers process the signal information from four or more satellites to determine the geographical location. The geographical location is determined by the distance from satellites within the line of sight to the receiver. The distance is calculated based on the time it takes for the satellite signal to reach the GNSS receiver, and the velocity of the signal (i.e., the speed of light). The satellite signal is transmitted at various L-band frequencies (such as 1575.42 MHz or L1 and 1227.60 MHz or L2), providing information on the satellite location, the system time, satellite clock corrections, and other codes (Doberstein 2012). Typically, a high precision GNSS receiver uses multiple frequencies, using L1 and L2, to obtain the geographical

location (Doberstein 2012; Miller et al. 2015). However, different factors contribute to error in the satellite signal, such as signal reflection (multipath), the earth atmosphere, satellite location (ephemeris), satellite clock, and the GNSS receiver (Doberstein 2012; Miller et al. 2015). The use of L2 frequency by a GNSS receiver provides a more reliable signal with less interference than L1 (Doberstein 2012). Thus, multi-frequency GNSS receivers were developed to use two frequencies to calculate the errors, correct the signal, and collect accurate geographical locations within a few millimeters. Other single-frequency GNSS receivers that only use the L1 frequencies required additional information to correct the signal and compute an accurate geographical location. Using two or more single-frequency GNSS receivers can be used to improve and correct the geographical location. The use of one single-frequency GNSS as a base station allows calculating the difference in the arrival time of the satellite signal. GNSS receivers relying on a differential correction of the satellite signal are referred to as dGNSS, like the Geocube.

The Geocube dGNSS units have an integrated LEA-6 T GNSS chip and an SL1206 antenna for differential positioning (Benoit et al. 2014). The Geocube network uses a base station unit installed on stable ground to perform a differential correction of the location of the units installed on an area being monitored to achieve a centimeter level accuracy (Benoit et al. 2015a). The integration of multiple dGNSS units in a network allows additional distance correction from the multiple measurements (Benoit et al. 2014). The system is compatible with satellite signals from GPS, BeiDou, GLONASS, and Galileo constellations (Ophelia Sensors 2019). Also, each unit has a radio frequency antenna that allows communication with other units and a data collector. The communications systems allow for unobstructed ranges of up to 200 m with an internal antenna or 1000 m with an external antenna. The data can be directly transmitted from each GNSS unit to the data collector or relayed through other GNSS units to the data collector if the distance is too far or the signal is obstructed. The capability of the dGNSS units to connect remotely to a data collector allows centralizing and processing the information to provide near real-time positioning or RTK (Benoit et al. 2014). Benoit *et al.* (2014) provided significant detail regarding the computation process of the Geocube.

The installation of Geocubes at the Ten-mile landslide was the first use in North America. The novelty of the technology, and the early adoption of this system for this research program, resulted in multiple difficulties in implementation. The difficulties included software bugs, the replacement

of faulty parts, and other site-specific challenges. These issues were addressed in collaboration with the manufacturer to allow for the improvement of subsequent systems.

The initial installation of the system at the Ten-mile landslide was in July 2016 but was not reliably operational until March 2017. Five dGNSS units were installed on the larger blocks of moving soil, one on the H-pile wall which was regularly surveyed by CN, three more up slope of the railway track to monitor for retrogression and one was installed on stable ground to act as a base station (unit # 39) (Figure 4-1a). Each unit was mounted on a galvanized U-channel post driven 1.0 m into the ground with 0.3 m to 1.5 m above the ground (Figure 4-3). The dGNSS units were powered independently by a 10-Watt solar panel paired with two 12-volt, 100 Ah batteries. The data collector was mounted on an electricity pole near the road with a continuous AC power supply. The system was set to collect the geographical location from each dGNSS units every 60 s.

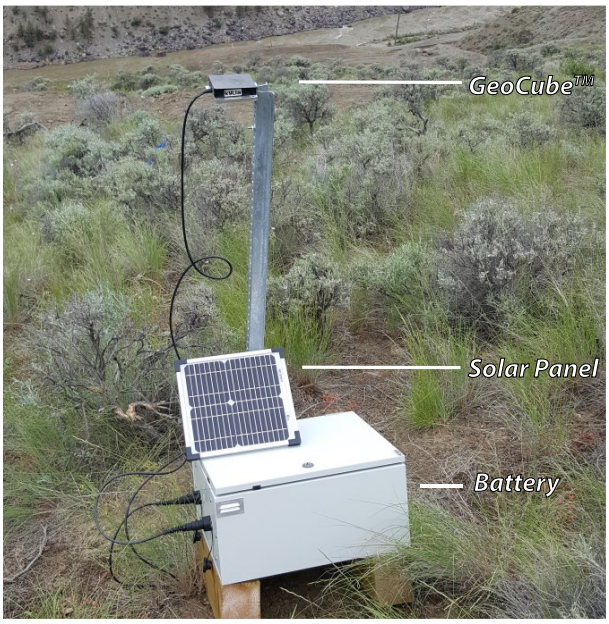


**Figure 4-3 Photograph of a dGNSS unit installed on the Ten-mile landslide (May 2017).**

At the Chin Coulee landslide, four dGNSS units were installed on the moving landslide, five additional units were installed around the periphery of the landslide adjacent to the scarps to monitor for retrogression of the landslide, and one was installed on stable ground away from the landslide (unit # 175) as a base unit (Figure 4-3). Each unit was mounted on helical piles, commonly used for residential decks, which were embedded approximately 1 m into the ground.

The power for the dGNSS units was the same as that used at Ten-mile. The data collector was mounted on an electricity pole across the reservoir with a hard-wired AC power supply. The geographical locations were recorded at 1 minute intervals.

### 4.3 PRESENTATION OF RESULTS

The Geocube dGNSS units collected continuous data for 536 days between March 30, 2017, to September 18, 2018, at the Ten-mile landslide, and for 436 days between July 11, 2018, to September 19, 2019, at the Chin Coulee landslide. These systems recorded the UTM coordinates of each dGNSS unit relative to the fixed point. Examples of the unfiltered data from the Ten-mile landslide are presented in Figure 4-4 for a dGNSS unit recording very small displacements (unit # 44) outside of the sliding mass of the landslide and a dGNSS unit in the center of the landslide with the largest recorded displacements (unit # 46). This data is similar to that collected at the Chin Coulee landslide. Appendix B shows the detailed collected data from the dGNSS units at Ten-mile and Chin Coulee landslides.

Gaps visible in the example data (Figure 4-4) are primarily due to the steep valley and the north orientation, which limited the number of visible satellites. The number of satellites observed by the dGNSS units ranged from none to ten, with most measurements taken with signals from five satellites. Less than four satellite signals resulted in a *null* value being recorded. Gaps of more than three days were related to continued hardware issues (example December 22, 2017, to January 5,2018). Longer gaps in data at the Chin Coulee site were due to vandalism and tampering with the equipment near the roadway.

From Figure 4-4a and 4b, there is variability in the measurement consisting of both occasional or continuous large peaks, which were well over the average measurement. The data collected from the Ten-mile reached up to 2099 mm peak differences to the average measurement and up to 254 mm from data collected at Chin Coulee. However, the peaks represent less than 3% of the recorded data with a maximum continuous duration of 57 minutes at the Ten-mile and 17 minutes at the Chin Coulee. The short duration and prominence of this erroneous data allow it to be easily identified such that it can be removed, while still allowing for the identification of real large rapid changes in location due to landslide displacements after multiples of the longest duration of peaks at that site.

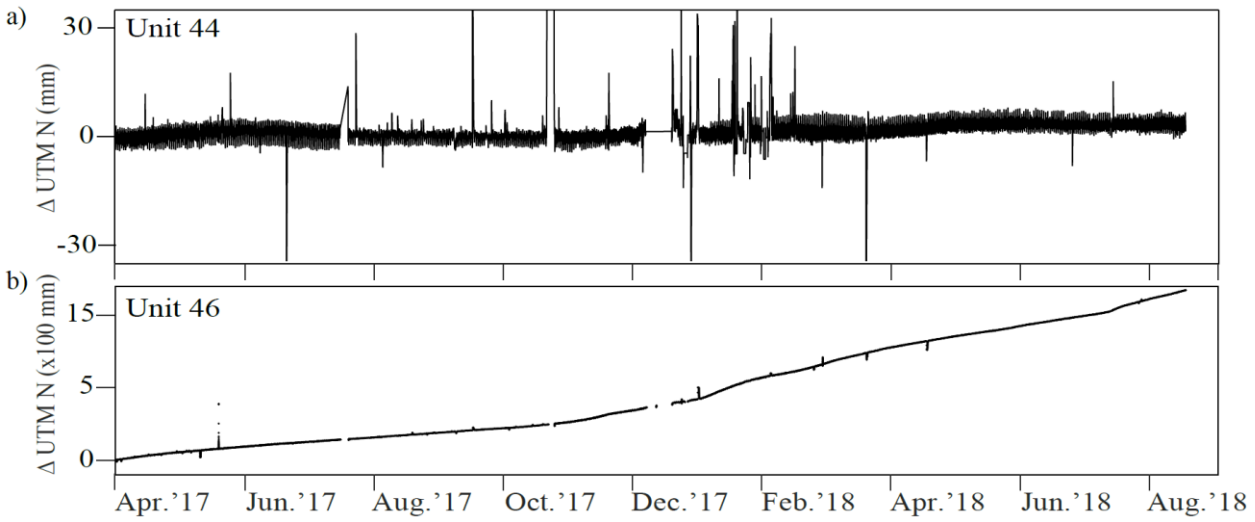


**Figure 4-4 Displacement measurements from the Ten-mile landslide in the north direction from UTM coordinates recorded by of (a) dGNSS unit # 44 and (b) dGNSS unit # 46 from April 2017 to October 2018.**

The pattern of daily fluctuations changes with atmospheric conditions and probably the reflections of the satellite signals. Most units installed at the two sites did not have significant surroundings obstructions that could cause a multipath error in the satellite signal; however, at the Ten-mile, the depth of the valley and the relative location with respect to the signal angle from satellites can cause reflection of the satellite signal, such as unit #48 and #42 located closed to steep slope, or unit #49 near the railway track. Figure 4-5 shows the daily fluctuations of the measured displacement. From Figure 4-5a and 5b, a repeating pattern is visible in the data and is the result of the daily change in the satellite signals observable by the dGNSS units, this is a known and commonly observed phenomenon within dGNSS data (Kintner et al. 2007). Thus, any corrections of the dGNSS signal are site specific and transient.

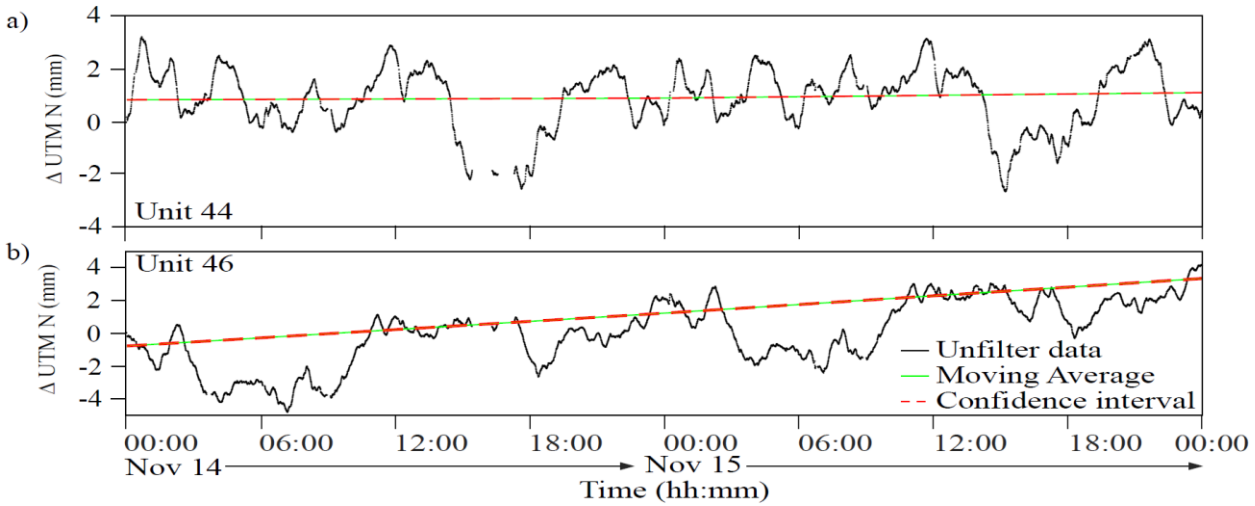


**Figure 4-5 Displacement measurements from the Ten-mile landslide in the north direction from UTM coordinates recorded by of (a) dGNSS unit # 44 and (b) dGNSS unit 46 # for Nov. 14-16, 2017 showing the daily fluctuations of the measured location.**

The data from all dGNSS units were processed further to improve interpretation. The processing included the removal of peaks that exceeded two standard deviations of the data recorded within 24 hours to create a clear trendline. Figure 4-6 and Figure 4-7 show the direction and magnitude of the horizontal displacement discretized by months for the Ten-mile and the Chin-Coulee, respectively (Appendix B). At the Ten-mile (Figure 4-6**),** the largest displacements were measured on units # 46, # 47, and # 48 located on the left and central areas of the landslide. Although, recorded displacement on unit # 46 (1500 mm approx.) was three times larger than the other two. On the opposite side from unit # 48, the units # 43 and # 45 showed displacement lower than 50 mm. Above the H-pile remediation structure, the dGNSS units near the railway showed displacements below 10 mm orientated towards the center of the landslide. The system also showed an irregular increment of approximately 5 mm in the displacement for units located outside the sliding mass (unit # 44, # 50, and # 69). These irregular displacements are probably related to an external movement of the post in these dGNSS units.

At the Chin-Coulee (Figure 4-7), the highest magnitude of displacement measured within the sliding mass of the landslide was 107 mm by unit # 176, located near the reservoir. The other three units within the sliding mass (unit # 151, # 154, and # 172) showed displacement between 17 mm and 54 mm. The five units located outside the sliding mass and near the edge of the landslide recorded displacements ranging between 16 mm and 21 mm on the east side (i.e., units # 153 and

# 173); and, between 10 mm and 36 mm near the crest of the landslide (i.e., units # 152, # 174, and # 177). The units at the Chin-Coulee showed more irregular displacement measurements than the Ten-mile system. These abnormalities are reflected in a sudden increment of displacement of 10 mm in the initial seven days of monitoring; unit # 176 showed an increment of 54 mm on September that shifted the direction of displacement; other units (i.e., # 153, # 172, and # 173) experience approximately 5 mm to 10 mm increments in displacement in the first eight to ten days in the opposite direction of movement.

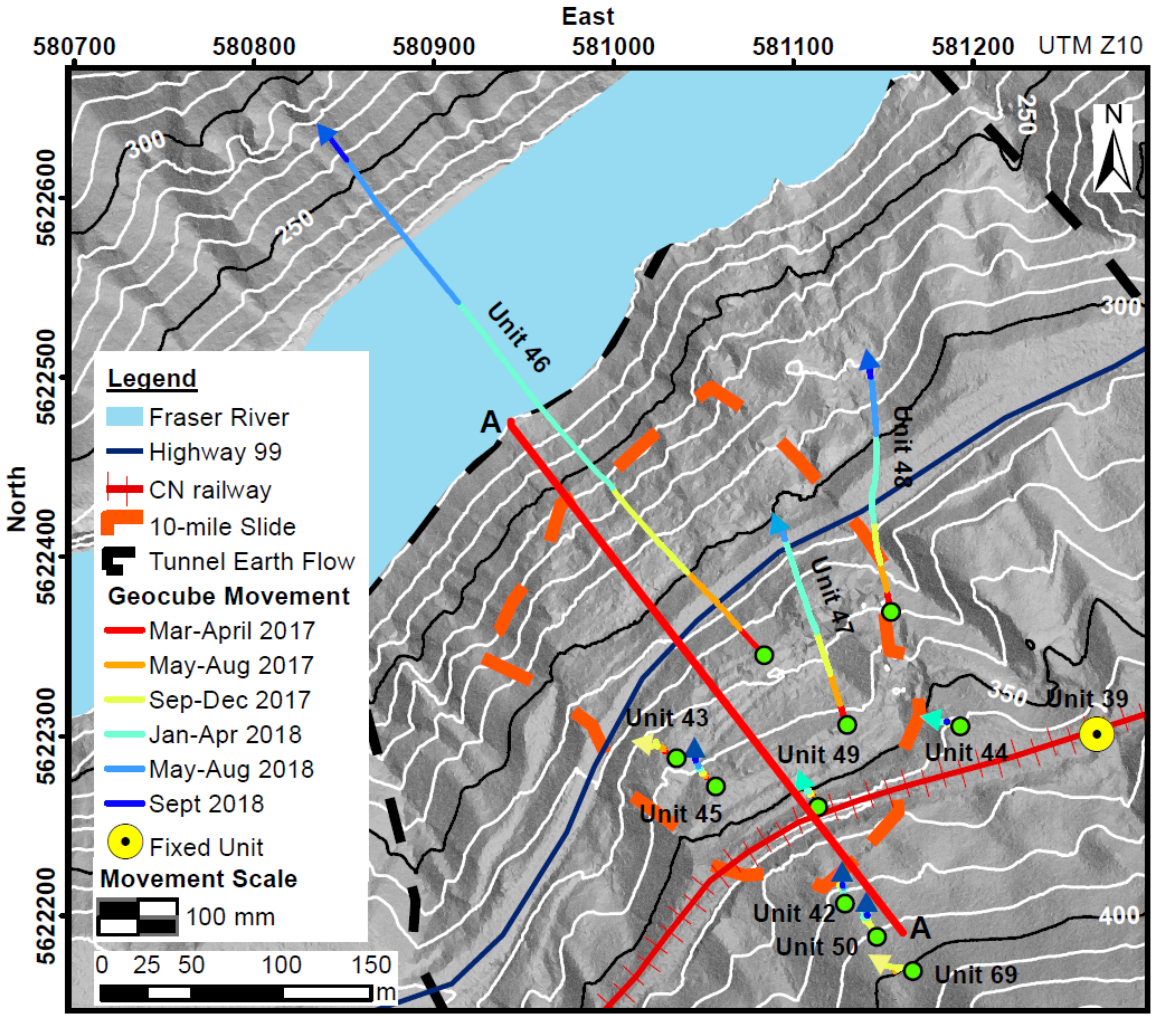


**Figure 4-6 Map showing the measured displacements at the Ten-mile landslide between March 30, 2017, to September 18, 2018. Note: data was filtered with a 24-hour moving average to remove variance in data.**

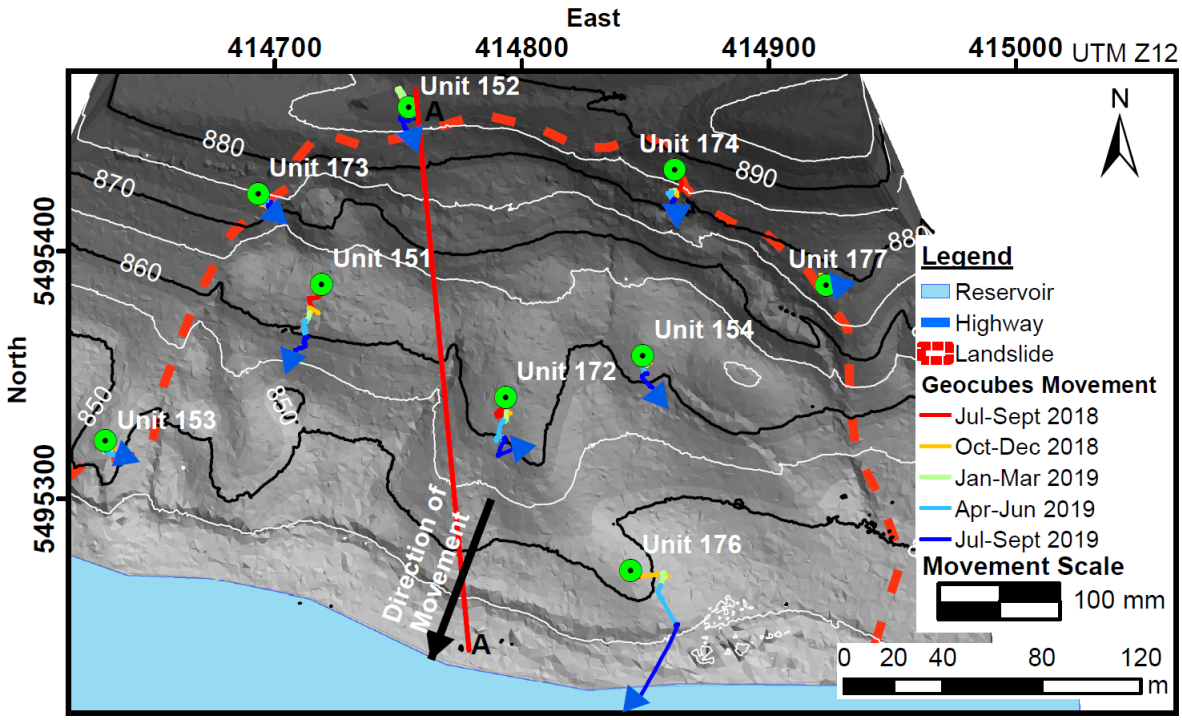


**Figure 4-7 Map showing the measured displacements at the Chin Coulee landslide between July 11, 2018, and September 19, 2019. Note: data was filtered with a 24-hour moving average to remove variance in data.**

## 4.4 DISCUSSION

This section discusses the benefits of a single-frequency dGNSS system for monitoring slow-moving landslides deformation. The discussion presents a qualitative comparison of the data recorded from single-frequency dGNSS units on the sites with the multi-frequency GNSS used at Ripley landslide (Macciotta et al. 2014). Also, a discussion is presented of the advantages of having multiple monitoring points and the high frequency in data collection to develop a better understanding of the shear surface and assess the potential causal factor of displacement.

### 4.4.1 Comparison of single-frequency DGNSS and conventional GNSS for monitoring Landslide deformation

A comparative analysis of fluctuations in location measurements between the Geocubes single-frequency dGNSS against a high precision multi-frequency GNSS allows assessing the effectiveness and limitations to monitor landslide deformations. The data recorded from the dGNSS receivers have shown millimeters changes like other more expensive high-end GNSS

systems, such as the Leica multi-frequency GNSS receivers installed at the Ripley landslide (Macciotta et al. 2014). The Leica GNSS monitoring installation at Ripley has three units taking measurements every 1-hour. Similarly, to Figure 4-4 and Figure 4-5, the Leica GNSS is exposed to signal interference that generates noise and fluctuations in the measurement (Macciotta et al. 2016a). The data fluctuation on both systems deviates from the true location during the monitoring period as noise sources intensify or diminish.

The deviation of data records is calculated as the difference between raw recorded location (i.e., Figure 4-4) to the 24-hr moving average trendline (i.e., green line in Figure 4-5) in each coordinate direction. The data samples of measurements from the Ripley, the Ten-mile, and the Chin Coulee provided information on the dispersion in fluctuations over seasonal weather variations. Analysis of the deviation in data shows the magnitude of peak measurement and the duration of fluctuation exceeding a maximum threshold. A statistical test for the Leica GNSS and the Geocubes dGNSS shows that data deviations described a normal distribution shape at a 95% confidence level. Figure 4-8 shows the frequency distribution of deviation measurements for the three coordinate components at the three sites.

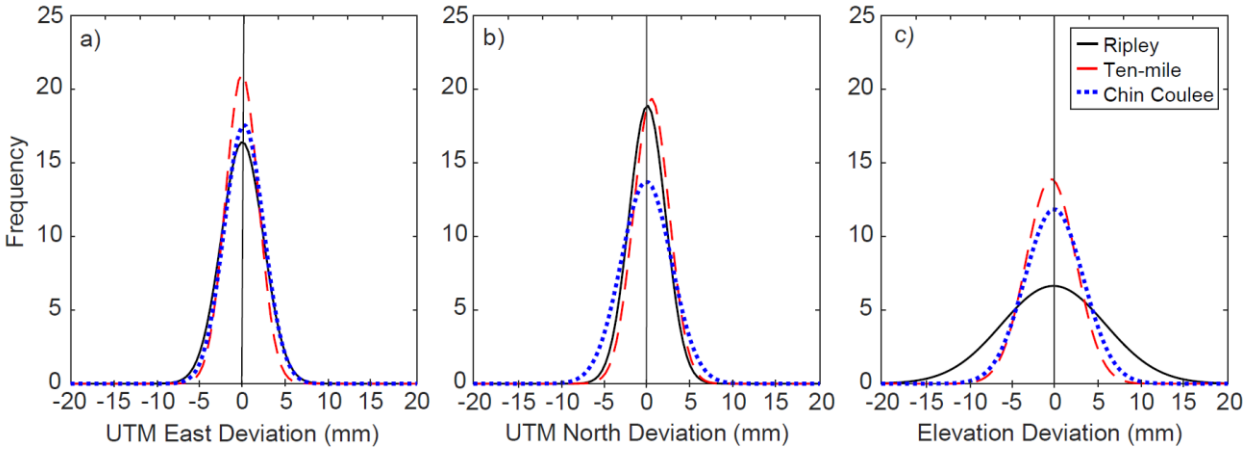


**Figure 4-8 Dispersion of the raw measurements with respect to the trendline for the eastern UTM (a), northern UTM (b), and elevation (c) from GNSS 1, 2 and 3 at the Ripley; the Geocube units #42 to #49 at the Ten-mile; and Geocubes units #151 to #174, #176 and #177 at the Chin Coulee landslide.**

The deviation distributions for the Leica GNSS and Geocubes dGNSS have a median of less than 1 mm with a 5$^{th}$ and 95$^{th}$ percentiles less than ±5 mm, indicating most measurement approximating the trendline. The maximum frequency in deviation measures varies between 14% and 21% for

the East and North coordinates, while the elevation measures have frequencies between 6% and 14%. The results show the Geocubes dGNSS had similar deviations results to the Leica GNSS, the dispersion in the horizontal coordinates (Figure 4-8a and Figure 4-8b) is lower than the elevation measurement (Figure 4-8c). However, Figure 4-8c shows that the Leica GNSS had a higher dispersion and lower frequency in elevation than the Geocubes dGNSS. The distributions on both systems have deviations extending beyond 100 mm and varying with each monitoring unit. Table 4-1 shows a detailed comparison of the data sample size, the deviation, and peak deviations from each monitoring unit for the Leica GNSS and the Geocubes dGNSS.

Both systems had missing data points during the monitoring periods despite having constant intervals for data recordings. Error in signals, hardware, or quality in measurements impacted the data records with an average loss of 45% in the Leica GNSS, while the Geocubes dGNSS had an average of 20% at the Ten-mile and 34% at the Chin Coulee. Although the missing data points are not necessarily continuous, this comparison shows the limitations of the Geocubes dGNSS to provide early warning. The Geocubes are reliable in collecting data with high precision measurement from all units, as shown in Table 4-1. Thus, the errors measured on dGNSS unit #69 at the Ten-mile can be considered outliers from the rest of the system, leaving nine additional monitoring points to assess the landslide deformation. Lastly, peak deviations from false displacement vary from each location in magnitude and duration. The peak deviations recorded from Leica GNSS reached magnitudes approximately 200x higher than the average maximums from the Geocubes dGNSS. Also, the duration of the peak measurement had a longer duration for the Leica GNSS than the Geocubes dGNSS. Table 4-1 shows measures deviated above 100 mm lasted between 60 min and 1060 min through continuous measures with the Leica GNSS, while the Geocubes dGNSS showed continuous deviated measures between 2 min and 57 min.

Ultimately, monitoring system used for early warning of landslide deformation should have precise measures at a high rate of data recording. Detecting continuous changes over a long period can enhance the use of advanced trend analysis like inverse velocity plots to assess the potential collapse of a landslide. These characteristics would provide information on time to take action against future deformations and accelerations. The data recorded from the Geocubes dGNSS at the Ten-mile and Chin Coulee landslide displayed similar performance to the Leica GNSS, and some characteristics were showing a better response.

**Table 4-1 Comparison of the deviation of raw data recorded from single-frequency and multi-frequency receivers from monitoring active landslides in western Canada.**

| Unit | Data points | | Deviation Distribution of the North UTM, East UTM and Elevation (mm) | | | Max. Peak (mm) | Max. duration of peak > 100 mm (min) |
|---|---|---|---|---|---|---|---|
| | Recorded | % missing | Percentile 5th | Percentile 95th | Median | | |
| **Ripley landslide Leica GNSS** | | | | | | | |
| #1* | 23726 | 43% | -7.76 | 7.92 | -0.08 | 42821 | 1060 |
| #2* | 20478 | 51% | -8.12 | 8.12 | -0.04 | 5498 | 120 |
| #3* | 24133 | 42% | -7.60 | 6.39 | -1.0E-07 | 8541 | 60 |
| **Ten-mile landslide dGNSS** | | | | | | | |
| #42 | 658908 | 15% | -2.76 | 2.87 | 0.01 | 1019 | 26 |
| #43 | 325964 | 17% | -2.81 | 2.94 | -0.03 | 612 | 23 |
| #44 | 638242 | 18% | -3.17 | 3.40 | 0.09 | 754 | 13 |
| #45 | 494262 | 36% | -3.71 | 3.46 | 0.04 | 92 | N/A |
| #46 | 650718 | 16% | -5.16 | 4.08 | -0.67 | 240 | 9 |
| #47 | 512728 | 15% | -2.72 | 2.62 | 0.11 | 1013 | 14 |
| #48 | 659267 | 15% | -2.99 | 2.69 | 0.10 | 744 | 8 |
| #49 | 341558 | 25% | -3.88 | 4.33 | 0.10 | 2099 | 57 |
| #50 | 553720 | 20% | -3.51 | 3.88 | 0.07 | 794 | 46 |
| #69** | 83623 | 78% | -29.44 | 32.76 | 0.01 | 3336 | 71 |
| **Chin Coulee landslide dGNSS** | | | | | | | |
| #151 | 410931 | 33% | -4.64 | 4.26 | -4.0E-07 | 134 | 2 |
| #152 | 410932 | 33% | -4.85 | 4.87 | -1.0E-06 | 141 | 3 |
| #153 | 408020 | 34% | -3.86 | 3.76 | -2.0E-06 | 157 | 4 |
| #154 | 407943 | 34% | -4.60 | 4.26 | -2.0E-06 | 133 | 3 |
| #172 | 410932 | 33% | -4.86 | 4.69 | -3.0E-06 | 139 | 3 |
| #173 | 410932 | 33% | -5.08 | 4.57 | 7.0E-05 | 254 | 17 |
| #174 | 410872 | 33% | -4.76 | 4.87 | -4.0E-06 | 129 | 3 |
| #176 | 401552 | 35% | -4.38 | 4.02 | 2.0E-06 | 115 | 2 |
| #177 | 410932 | 33% | -4.78 | 4.88 | -6.0E-05 | 159 | 4 |

* Records used for the analysis were taken between September 2004, and January 2010.

** The results from dGNSS-69 are outliers associated to external movement and hardware errors that shorten the recording duration and increase errors.

### 4.4.2 Evaluation of inclination of shear surface(s)

Interpreting the shape of the shear surface from SIs or SAAs is costly, and it can have restricted applications. The SI instruments can be sheared quickly from excessive deformation, as it occurred at the Ten-mile, or its location can be constrained by limited accessibility for installation, as Chin-Coulee. The use of dGNSS units provides an indirect estimation of the sliding angle of the shear surface on different areas of the landslide while overcoming the limitation of excessive deformation and accessibility. The ratio between the vertical displacement and horizontal displacement measured from dGNSS units allows estimating the shear surface inclination and the changes in time. Figure 4-9 shows the interpretation of the inclination and magnitude of displacement from multiple dGNSS units for a cross section of the Ten-mile and the Chin-Coulee.

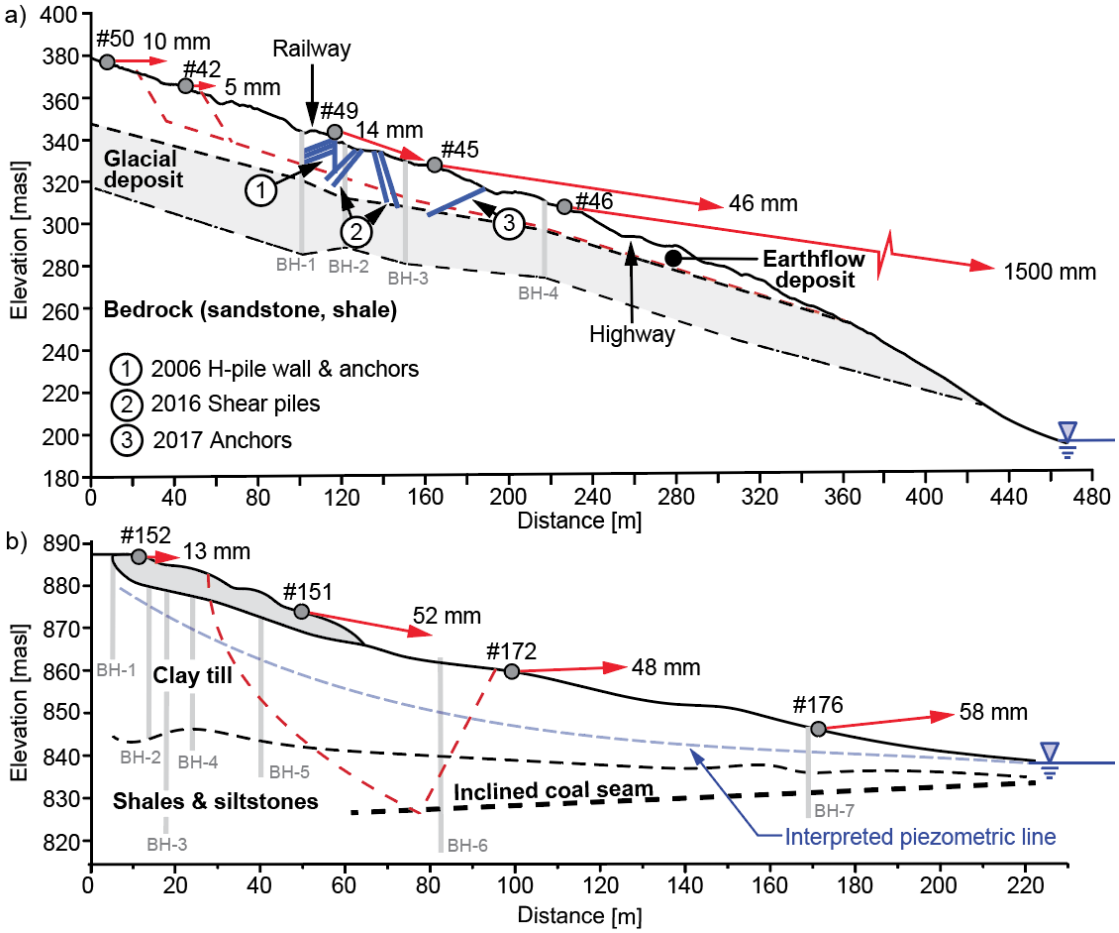


**Figure 4-9 Cross-sections A-A of (a) the Ten-mile landslide (location of section shown in Figure 4-6), and (b) the Chin Coulee (location of section shown in Figure 4-7) derived from LiDAR obtained from these sites and showing the inclination of the measured displacements.**

The dGNSS units allowed a continuous estimation of the sliding angle even after large displacement were recorded in different areas of the Ten-mile. The interpretation of SIs data at the Ten-mile suggested that the shear surface had a sliding angle of approximately 22° (Gaib et al. 2012). However, the dGNSS system shows a variation of cumulative displacement and the sliding angle for different sections of the landslide (Figure 4-9a), similar to previous LiDAR interpretations (Lato et al. 2016). The dGNSS units show variations below the railway track from 30° to 45°. In contrast, the angles near the crest of the landslide vary from 15° to 30°. The inclination from the dGNSS units suggests a complex mode of failure with displacement variations of the different blocks of failure.

Previous site investigation at the Chin-Coulee had suggested a failure process either by a rotational or a translational movement (Amec FW 2015). However, the distribution of the dGNSS units on the sliding mass and the data interpretation provides evidence of a complex failure mechanism that combines a rotational and translation movement. Figure 4-9b shows that units located in the upper section of the landslide, unit 151, describe a downward displacement along a back-scarp failure plane. While units located in the toe region, unit 172 and 176, displayed a horizontal displacement. The implementation of dGNSS units at the Chin-Coulee recorded information in areas of difficult access for SI or SAA to improve the interpretation of the failure mechanism.

The use of the dGNSS system provides a unique characterization of the shape of the shear surface, which can be discretized spatially from multiple units. The capability of dGNSS system for continuous positional measurements provides a clear description of the evolution of the shape shear surface from complex landslide failure. This temporal capability of continuous monitoring regardless of large deformation (Figure 4-6) also provides the opportunity to assess changes external factors that would be driving movement.

### 4.4.3 Evaluation of causal factors from higher frequency data collection

Changes in the stability of a landslide are usually associated with natural factors, human activities, or a combination of both (Highland and Bobrowsky 2008). Determining the factor(s) that could be related changes on slow-moving landslides is often challenging. Although water-related events are among the most common factor for impacting stability (Schulz et al. 2009), these events can have periods of acceleration and deceleration associated with the seasonal weather (Macciotta et al.

2017a; Pratt et al. 2019). Determining causal factors that are time-dependent requires monitoring instruments that detect continuous changes over a long period. Thus, the implementation of the dGNSS units detailed the changes in displacement every 60 s to evaluate the effect of causal factors in different seasons at each site.

The dGNSS data at the Ten-mile allowed assessing the relationship between antecedent precipitation events and changes in the displacement rates. The MoTI had installed a weather station collecting data every hour approximately 1 km Southwest from the site. Figure 4-10 shows the comparison between the displacement rate and the 1-, 30-, and 60-day antecedent precipitation between April 2017 and August 2018 for unit #46. The antecedent precipitation during the monitoring period shows three peaks, the first occurring in the spring months between April and May 2017, a second event between fall and winter from October 2017 to February 2018, and a third event in the summer of 2018. A visual comparison between precipitation peaks and the displacement rate shows an increment in the displacement rate that occurred after the precipitation peaks. Evidence of a correlation between displacement rates and antecedent precipitations is evaluated by calculating the "Spearman rank correlation coefficient" (SCC). The SCC values resulted in a high positive correlation for antecedent precipitations above 60 days in the areas with the largest displacement. For example, unit #46 shows SCC values of 0.65 at a 95% confidence level for 60-day antecedent precipitation (See Appendix E for detailed statistical correlation analysis). The dGNSS system at the Ten-mile provided clarity between landslide displacement and water as a driving factor, although past instruments had not been able to detect a phreatic surface within the sliding soils. The variability on cumulative displacement and inclination of the shear surface shown by the dGNSS units suggest that antecedent precipitation impact on the landslide displacement varies across the sliding mass.

The changes in the reservoir elevation at the Chin-coulee were compared with changes in displacement rates. The comparison allows assessing the influence of the changes in the reservoir elevations and the stability of the landslide. Figure 4-11 shows the changes in displacement rate for unit #151 and the reservoir elevation between July 2018 and September 2019. During the winter period between October 28, 2018, and April 08, 2019, there were no records of the reservoir elevation. Changes in displacement rate appeared to be affected by the periods of drawdown and the rise of the reservoir levels. A calculation of the SCC shows a strong negative correlation of -

0.64 at a 95% confidence level for unit #151 for the first drawdown and rise of the reservoir. This correlation would suggest that decrease in the water table or, more likely, the loss of buttressing increases the displacement rate of the landslide.

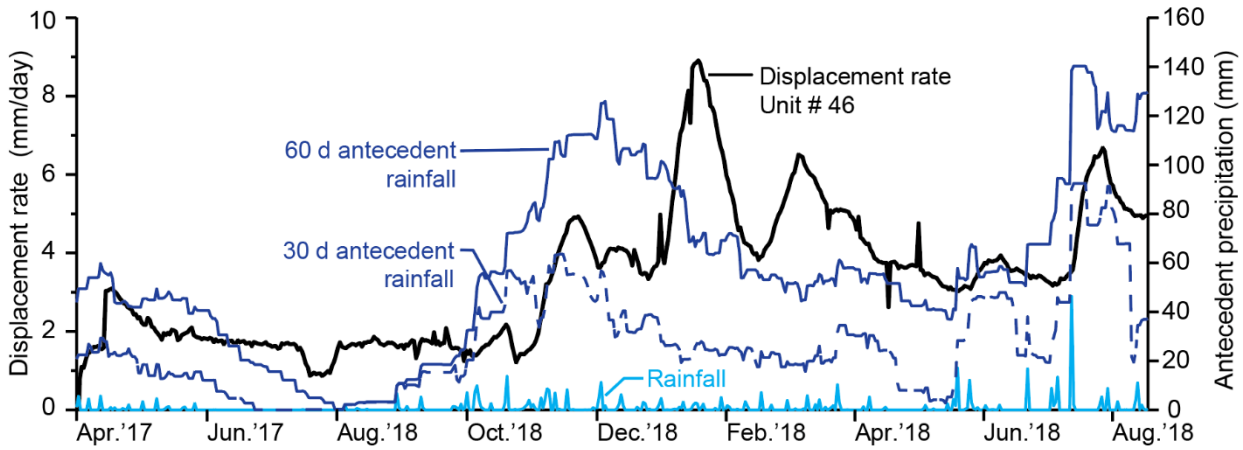


**Figure 4-10 Comparison of the 30-day and 60-day antecedent rainfall at Ten-mile landslide with displacement rate of the landslide as measured by unit # 46.**

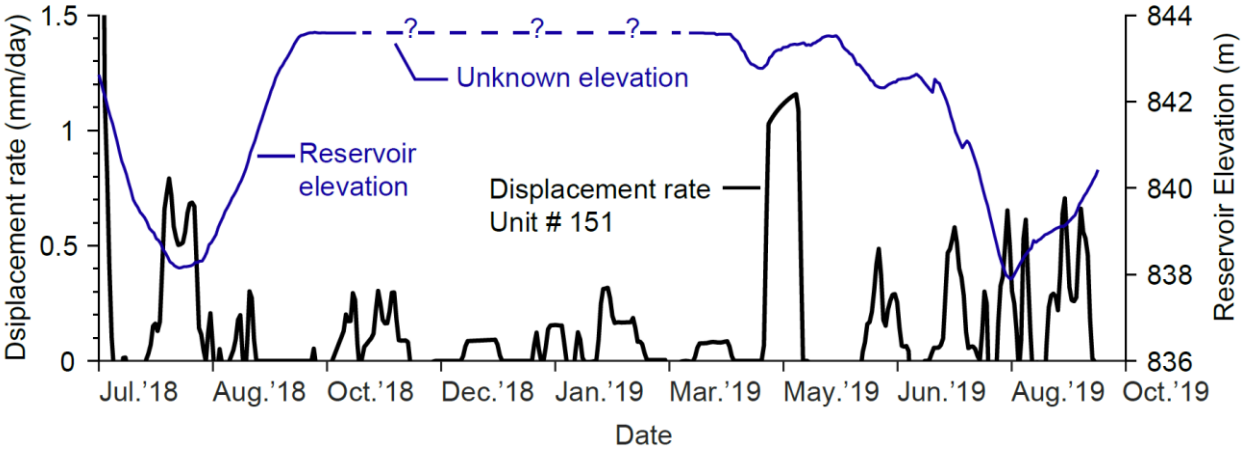


**Figure 4-11 Comparison of the elevation of the Chin reservoir to the displacement rates of the Chin Coulee landslide as measured by unit # 151.**

The network of Geocube installed at the two slow-moving landslides provided a unique opportunity to evaluate potential triggering factor(s). The two monitored sites have shown hints of the relationship of water-related factors and the continuous displacement of the sliding mass. Systems that provide a high temporal resolution allows for an interpretation of the factor(s)

involved in displacement changes over short and long intervals. Evaluating the relationship between the kinematics of the landslide and trigger factor(s) allows developing tools to provide early warning against future movements.

## 4.5 CONCLUSIONS

The use of single-frequency dGNSS with high precision provides an opportunity to enhance monitoring programs of landslides. The application of the Geocube at the Ten-mile and Chin-Coulee showed high precision measurements with a ±5 mm deviation that allows determining continuous displacement and changes in displacement rates. The single-frequency dGNSS had comparable reliability in precision to the multi-frequency Leica GNSS. The high rate in data collection and the high precision of the Geocube resulted in short data deviations from the trendline of measurements. The capability of achieving high precision measurement using a lower cost of single-frequency GNSS to multi-frequency GNSS allows achieving better spatial coverage of a landslide within similar costs. Also, multiple dGNSS units makes the operability of a monitoring instruments more reliable for implementation. The exposure of monitoring instruments to extreme weather conditions can impact the data collection by damaging the hardware or generating noise. The Geocube systems had up to 34% missing data through different seasons at both sites. However, the gaps in data are not uniform on all dGNSS units. Thus, monitoring of the landslides with multiple dGNSS units would continue even though external sources might impact the data collection from some dGNSS units.

Measurements from multiple locations allowed assessing complex failure mechanisms and the causal factors that drive changes in the kinematics of a landslide. This paper has demonstrated the implementation of single-frequency dGNSS to monitor multiple locations at two landslides with complex failure mechanisms. The Geocube systems provided information on the changes in the displacement and displacement rates. The collected data allowed estimating the sliding angle of the landslide and evaluating the causal factors driving the movement. The variability in displacements (Figure 4-6) and sliding angles (Figure 4-9a) at the Ten-mile suggest that the movement as discrete blocks of failure is potentially triggered by antecedent precipitation (Figure 4-10). At Chin-Coulee, multiple dGNSS units have shown the increase in displacement at the toe area of the slide (Figure 4-7) cause a small rotational movement near the Highway (Figure 4-9b),

which is being controlled by changes in the reservoir elevation (Figure 4-11). The data recorded exposed critical areas in each site that would require additional geotechnical investigation to help distinct causal factor(s) from the sliding mass. Thus, single-frequency dGNSS at multiple locations becomes an enhanced monitoring instrument for landslides with complex kinematic.

Finally, the implementation of the Geocube system at the two sites show the potential for developing an early warning system with high confidence. The Geocube system can be set up to provide warning against continuous displacement or accelerations at multiple locations. A multiple monitoring point capability allows monitoring different elements at risk with distinct thresholds of displacement and orientation related to tolerance criteria. Warning systems exposed to extreme weather or tampering that damages the instrument are enhanced by the discretization of the monitoring system and providing operational reliability. The operability of multiple dGNSS units as a warning system is supported by the high precision and low frequency of peak measures. The data collected suggest that few false positive and false negatives would result from implementing the Geocube system as a warning system.

## 4.6 ACKNOWLEDGEMENTS

The research at the Ten-mile landslide was completed through the (Canadian) Railway Ground Hazard Research Program, which is funded by the Natural Sciences and Engineering Research Council of Canada (NSERC, Alliance Grant # CRDPJ 470162-14), Canadian Pacific Railway (CP), Canada National Railway (CN), and Transport Canada. The authors would like to thank CN for providing access to the site and for purchasing the Geocubes. The research at the Chin Coulee landslide was completed through a collaboration with KCB Engineering Inc. and Alberta Transportation. NSERC funded the research at the Chin Coulee site (Engage Grant # EGP 521877-17; KCB CRD # CRDPJ 543429-19) and KCB Engineering Inc.

## 4.7 REFERENCES

AMEC Foster Wheeler (2015) Southern Region Geohazard Assessment 2015 Annual Inspection Report Site S5: Highway 36:02, Chin Coulee. Calgary, Alberta

Benoit L, Briole P, Martin O, et al (2015a) Monitoring landslide displacements with the Geocube wireless network of low-cost GPS. Eng Geol 195:111–121

Benoit L, Briole P, Martin O, Thom C (2014) Real-time deformation monitoring by a wireless network of low-cost GPS. J Appl Geod 8:119–128. doi: 10.1515/jag-2013-0023

Benoit L, Dehecq A, Pham HT, et al (2015b) Multi-method monitoring of Glacier d'Argentière dynamics. Ann Glaciol 56:118–128. doi: 10.3189/2015AoG70A985

BGC Engineering Inc. (2016) Ten mile slide 2016 site investigation data report. Victoria, British Columbia

Bovis MJ (1985) Earthflows in the Interior Plateau, southwest British Columbia. Can Geotech J 22:313–334

Cruden D, VanDine DF (2013) Classification, Description, Causes and Indirect Effects - Canadian Technical Guidelines and Best Practices Related to Landslides: A National Initiative For Loss Reduction

Deane E, Macciotta R, Hendry MT, et al (2020) Leveraging historical aerial photographs and digital photogrammetry techniques for landslide investigation—a practical perspective. Landslides. doi: 10.1007/s10346-020-01437-z

Doberstein D (2012) Fundamentals of GPS Receivers. Springer, Nipomo, CA, USA

Gaib S, Wilson B, Lapointe E (2012) Design, Construction and Monitoring of a Test Section for the stabilization of an Active Slide Area Utilizing Soil Mixed Shear Keys Installed Using Cutter Soil Mixing. In: ISSMGE - TC 211 International Symposium on Ground Improvement IS-GI. Brussels

Golder and Associates (1998) Geotechnical Investigation – Site S5: Highway 36:02 – November 1998 Report Geotechnical Risk Management Plan

Hendry MT, Chalcroft D, Zaidi H, Iqbal MJ (2019) Instrumentation Data Review and Long-Term Trends of Displacement at the Oldman River Dam: A Case Study. In: Proceedings Canadian Dam Association Annual Conference,. Calgary, Alberta

Hendry MT, Macciotta R, Martin CD, Reich B (2015) Effect of Thompson River elevation on velocity and instability of Ripley Slide. Can Geotech J 52:257–267. doi: 10.1139/cgj-2013-0364

Highland LM, Bobrowsky P (2008) The Landslide Handbook — A Guide to Understanding Landslides, Circular 1. U.S. Geological Survey, Reston, Virginia

Huntley D, Bobrowsky P, Hendry MT, et al (2019) Multi-technique Geophysical Investigation of a Very Slow-moving Landslide near Ashcroft, British Columbia, Canada. J Environ Eng Geophys 24:87–110. doi: 10.2113/JEEG24.1.87

Intrieri E, Gigli G, Mugnai F, et al (2012) Design and implementation of a landslide early warning system. Eng Geol 147–148:124–136. doi: 10.1016/j.enggeo.2012.07.017

Journault J, Macciotta R, Hendry MT, et al (2016) Identification and Quantification of Concentrate Movement Zones within the Thompson River Valley using Satellite InSAR. Proc 2016 11th Int Pipeline Conf

Kintner PM, Ledvina BM, De Paula ER (2007) GPS and Ionospheric Scintillations. Sp Weather 5:1–23. doi: 10.1029/2006SW000260

Lato M, Porter M, Henshold G, et al (2016) Understanding Landslide Movement and Kinematics with Airborne Lidar. Proc 69th Can Geotech Soc Conf GeoVancouver 2016. doi: 10.1007/s12013-010-9150-8

Macciotta R, Hendry MT, Cruden DM, et al (2017) Quantifying rock fall probabilities and their temporal distribution associated with weather seasonality. Landslides 14:2025–2039. doi: 10.1007/s10346-017-0834-7

Macciotta R, Hendry MT, Martin CD (2016) Developing an early warning system for a very slow landslide based on displacement monitoring. Nat Hazards 81:887–907. doi: 10.1007/s11069-015-2110-2

Macciotta R, Hendry MT, Martin CD, et al (2014) Monitoring of the Ripley Landslide in the Thompson River Valley , B . C . Geohazards 6 8. doi: 10.13140/2.1.2811.7125

Miller S, Zhang X, Spanias A (2015) Multipath effects in GPS receivers

Odolinski R, Teunissen PJG (2017) Low-cost, high-precision, single-frequency GPS–BDS RTK positioning. GPS Solut 21:1315–1330. doi: 10.1007/s10291-017-0613-x

Ophelia Sensors (2019) Geocube Applications. https://ophelia-sensors.com/applications. Accessed 26 Aug 2019

Pratt C, Macciotta R, Hendry MT (2019) Quantitative relationship between weather seasonality and rock fall occurrences north of Hope, BC, Canada. Bull Eng Geol Environ 78:3239–3251. doi: 10.1007/s10064-018-1358-7

Rodriguez J, Macciotta R, Hendry MT, et al (2020) UAVs for monitoring, investigation, and mitigation design of a rock slope with multiple failure mechanisms—a case study. Landslides. doi: 10.1007/s10346-020-01416-4

Romero-Andrade R, Zamora-Maciel A, Uriarte-Adrián J de J, et al (2019) Comparative analysis of precise point positioning processing technique with GPS low-cost in different technologies with academic software. Meas J Int Meas Confed 136:337–344. doi: 10.1016/j.measurement.2018.12.100

Schulz WH, McKenna JP, Kibler JD, Biavati G (2009) Relations between hydrology and velocity of a continuously moving landslide-evidence of pore-pressure feedback regulating landslide motion? Landslides 6:181–190. doi: 10.1007/s10346-009-0157-4

Smethurst JA, Smith A, Uhlemann S, et al (2017) Current and future role of instrumentation and monitoring in the performance of transport infrastructure slopes. Q J Eng Geol Hydrogeol 50:271–286. doi: 10.1144/qjegh2016-080

Vaziri A, Moore L, Ali H (2010) Monitoring systems for warning impending failures in slopes and open pit mines. Nat Hazards 55:501–512. doi: 10.1007/s11069-010-9542-5

Woods A, Hendry MT, Macciotta R, et al (2020) GB-InSAR monitoring of vegetated and snow-covered slopes in remote mountainous environments. Landslides. doi: 10.1007/s10346-020-01408-4

Zhang Y, Yu W, Han Y, et al (2019) Static and kinematic positioning performance of a low-cost real-time kinematic navigation system module. Adv Sp Res 63:3029–3042. doi: 10.1016/j.asr.2018.10.048

# CHAPTER FIVE. ASSESSING THE EFFECT OF MATRIC SUCTION ON THE STABILITY OF A REACTIVATED EARTHFLOW

**Contribution of the Ph.D. candidate**

The work presented in this chapter, that includes literature review, laboratory testing, investigation methodology, analysis and discussion of the results and writing of the text was carried out by the Ph.D. candidate. Sections of this chapter is intended to be submitted as a journal publication.

**Contribution of this chapter to the overall study**

The dry conditions (310 mm/year of precipitation) of the region in which the Ten-mile landslide is located, and the results from previous site investigation suggest that the shear surface is unsaturated. The implementation and data collection from 10 dGNSS units situated at multiple locations at the Ten-mile landslide described in Chapter 4 shows that precipitation is correlated with the landslide rate of displacement. This manuscript is focus on the main objective ii) to assess the mechanism of failure of the Ten-mile by linking the monitoring data of the dGNSS units at multiple locations with back analysing the magnitude of matric suction on the shear surface. This manuscript also shows the results from laboratory testing performed on the earthflow deposit to characterize grain size distribution, the residual strength, and the unsaturated properties (i.e., SWCC). A methodology to identify clusters that move together based on changes in displacement rate measured by the dGNSS units. These clusters were incorporated into a limit equilibrium model by discretizing the model in different areas using numerical methods in a 3D space and back analyze the average matric suction required in the clusters to maintain a meta-stable condition. The back analysis was used to assess two possible mechanisms of failure, one based on the loss of support from the displacement of adjacent block, and the second based on the continuous loss of matric suction. Further, numerical simulations are used to show a relationship between matric suction and the factor of safety. The comparison on the displacement from a cluster following one another (i.e., successive movement) allows assessing the change stability induced by water infiltrating and increasing the degree of saturation.

***Abstract***

The Ten-mile landslide is located in a semi-arid region of British Columbia that receives approximately 310 mm/y of precipitation. The landslide is comprised of 850,000 $m^3$ of a reactivated portion of an ancient earthflow exhibiting displacement rates of up to 10 mm/d. Site investigations have not indicated the presence of a phreatic surface or temporal buildup of pore water pressure. However, seepage on slope cuts has been observed after precipitation periods, and increasing displacement rates have been correlated with antecedent precipitation periods. The low to none pore pressure at the shear surface and laboratory characterization of the shear surface soils suggests unsaturated conditions. This paper tests the hypothesis that matric suction controls displacement rates at the sliding surface and analyzes the effect of matric suction on the stability of the landslide and the relationship with the failure mechanism. A methodology is presented to discretize the translational movement of the sliding mass into clusters of blocks and determine the corresponding sequence of movement in a 3D space based on monitoring the displacement rates. The discretization of the Ten-mile landslide into five clusters was combined in a three-dimensional limit equilibrium model to assess the effect of changes of matric suction on the factor of safety. The results suggest the sliding mass requires an average of 80 kPa of matric suction across the shear surface to maintain a meta-stable condition of the initial moving cluster and up to 200 kPa for the successive movement of all clusters. Finally, the effect of changes in the factor of safety from a variation of matric suction is analyzed through three-dimensional limit equilibrium simulations and compared with changes in the saturation of the sliding mass impacted by precipitation.

## 5.1 INTRODUCTION

Studies of slope failures around the world have found that over 30% of landslides are triggered by water-related events, such as rainfall, snowmelt, or seepage (Eshraghian et al. 2007; Lacasse and Nadim 2009; Ansari et al. 2015; Klose 2015). Water infiltration in soils increases saturation and pore water pressure (PWP), which causes either a decrease in shear strength that can lead to slope failures or changes in the displacement rates for slow-moving slopes (Al-Homoud et al. 1995; Porter et al. 2001; Schulz et al. 2009; Ansari et al. 2015; Zhang et al. 2015). The infiltration process through a porous soil is a function of the hydraulic conductivity of the soil, precipitation rate, evaporation, transpiration, and runoff. At low saturation, water only infiltrates through connected

channels of water created (Richards 1931; Horton and Hawkins 1965). As the soil dries, the increment of matric suction reduces the hydraulic conductivity, limiting the infiltration rate and depth. However, the development of cracks on active landslides provides a path for water to easily infiltrate and reduces the matric suction (Novák et al. 2000; Cao et al. 2016). In unsaturated slopes, the slope shear strength is controlled by the effective stress and the matric suction acting on the failure surface. Thus, a loss of matric suction by water infiltrating and filling the air voids can reduce the shear strength to unstable conditions on unsaturated slopes.

The Ten-mile slide, in central British Columbia, is a reactivated earthflow with a translational movement. The landslide has retrogressed up to 26 m at different displacement rates over the last decade. A study of historical lidar images has identify 17 distinct blocks of movement (Lato et al. 2016). The landslide is located in a semi-arid environment, and site investigations have not detected pore water pressure responses within the sliding mass. Also, pore water pressure has not being associated with the different changes in displacement rates. However, recent surface displacement measurements collected at 1-min intervals and at multiple locations with a network of differential GNSS (dGNSS) suggest antecedent rainfall is associated with increasing displacement rates (Appendix E). Although laboratory testing of the sliding soil shows a hydraulic conductivity as low as $10^{-8}$ m/d (see Figure C-7b in Appendix C) which would impede a water front from reaching the shear surface at 17 m depth within a reasonable time; the open fissures and cracks that have been increasing (Macciotta et al. 2017; Rodriguez and Hendry 2018; Donati et al. 2020) provide a high permeability path for infiltration. Infiltration up to the sliding surface would increase the volumetric water content (VWC), decrease the soil's matric suction, and decrease the shear strength. This paper tests the hypothesis that the observed displacement rate is a result of changes in matric suction at the sliding surface. The influence of unsaturated soil behavior on this landslide is considered by: (1) assessing the failure process from displacement measurements, the measurements of the dGNSS units was used to identify clusters of blocks with similar changes in the displacement rate and determine the movement sequence, and (2) calculating the average matric suction in the shear surface required to maintain a meta-stable condition, defined by a factor of safety (FoS) of one, using a three-dimensional limit equilibrium (3D LEM) model. The quantification of matric suction is focus on the shear surface within each cluster of blocks, relation of the failure mechanism to the loss of matric suction, and effect of changes in soil saturation due to infiltration on the FoS.

## 5.2 THE TEN-MILE LANDSLIDE

The Ten-mile landslide is located along the Fraser River valley, approximately 15 km northeast of the town of Lillooet, British Columbia, Canada (Figure 5-1). The valley's average annual precipitation is approximately 310 mm, with temperatures ranging from −25 to 39 °C between 2010 and 2018.

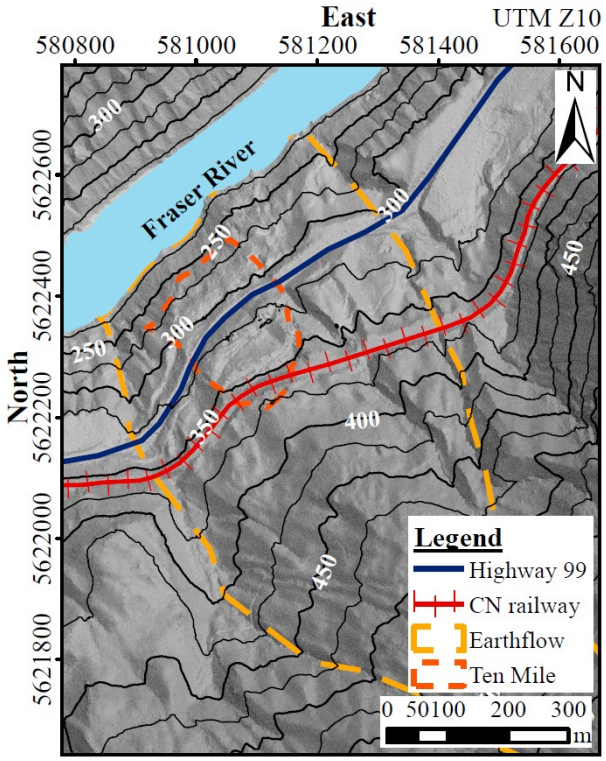


**Figure 5-1 Location of the active zone of the earthflow deposit named the Ten-mile landslide in British Columbia. Aerial LiDAR image was taken in 2015, showing the location of the highway and railway section affected by the landslide.**

The landslide was initially identified in the early 1970s below Highway 99. Since the late 1980s, the movement has been retrogressing uphill with displacement rates that have increased from 1 mm/d (Gaib et al. 2012) in 2006 to 6 mm/d in 2016, with peak accelerations of 10 mm/d (BGC, 2016a). These displacement rates increased the length of cracks and fissures to up to 5000 m between 2006 and 2017 (Donati et al. 2020), and displacements below the highway reached 17 m between 2006 and 2016 (Lato et al. 2016). The continuously deteriorating ground surface has negatively impacted a 110-m section of railway track operated by Canadian National Railway (CN) and a 200-m section of Highway 99 managed by the British Columbia Ministry of

Transportation and Infrastructure (MoTI), reaching the upper slope of the railway track (Figure 5-1) (JCL Consulting 2006; Wilson and Lapointe 2013; Macciotta et al. 2017). The landslide also presents a hazard to land located in the Xaxli'p First Nations reserve that is of cultural value to the community.

### 5.2.1 Geology and stratigraphy

The landslide is at the toe of a much larger post-glacial earthflow named the Tunnel earthflow (Bovis, 1985). The activation of the Tunnel earthflow churned the original soil strata, resulting in complex arrangements of soil types (Figure 5-2). Site investigations carried out in 2015 and 2016 by CN and MoTI provide a detailed stratigraphic description of seven boreholes distributed over the sliding mass (BGC 2016a,b). The earthflow deposit is up to 35 m thick in the middle of the active area and decreases in thickness towards the Fraser River. The earthflow primarily consists of layers of fine-grained clay, silt, and sand with the presence of angular rock fragments that range in size from gravel to boulders. Sieve analysis of earthflow soil samples shows a 56 to 74% fines content with up to 19% attributed to clay; the remainder is composed of fine to coarse sand. Surface observations show the presence of angular boulders over 3 m in diameter embedded within the earthflow. The materials immediately below are glaciofluvial deposits consisting of gravel and sand with a thickness of approximately 10 m (BGC 2016a). At greater depth is bedrock of volcanic and sedimentary origin made up of basalt, andesite, sandstone, and shales from the Jackass Mountain group (Bovis 1985).

### 5.2.2 Past mitigation methods

Different mitigation actions over the last two decades have been carried out by CN and MoTI to improve the stability and maintain their right of way for the transportation corridors. In 2004, a realignment of the corridor was conducted after the landslide retrogression reached the railway tracks. In 2005, CN installed concrete blocks below the track to preserve the alignment of the track, but in 2006 the construction of a shotcrete soil anchor wall was required (Figure 5-3a). Following the reappearance of tension cracks below the tracks in early 2008, ballast and lock blocks were added to the retaining wall for additional support. Later in 2008, an 18-m deep H-pile retaining wall with timber lagging and soil anchors was added to replace the shotcrete soil anchor wall. In

2010, the loss of soils in the lower portions of the H-piles required extending the length with additional lagging at the base of the wall. Similarly, the highway has required realignments and cuts into the slope to maintain the two road lanes. In 2011, the MoTI trialed soil-cement shear keys over a small section of the highway (Gaib et al. 2012). Steel plates were welded in the front of the H-pile retaining wall from 2012 to 2014 to reinforce, limit deformation, and limit loss of the backfill material (Figure 5-3b). In 2016, a tension crack appeared 60 m upslope from the railway track leading to installation of 253 steel shear piles near the toe of the H-pile retaining wall (Figure 5-3b). These shear piles are 364 mm in diameter and approximately 21 m in length. The shear piles slowed the displacement rate of the track and H-pile wall from 12 mm/d to less than 1 mm/d. However, they were designed to only stabilize the upper portion of the landslide and the railway. In February of 2017, MoTI installed 32 steel strands anchors on the first slope bench above the highway (Figure 5-3c). Finally, in 2019, MoTI initiated a mitigation plan to slow down the displacement below the shear piles by installing over 400 soil anchors and a tied-back pile wall with 180 piles.

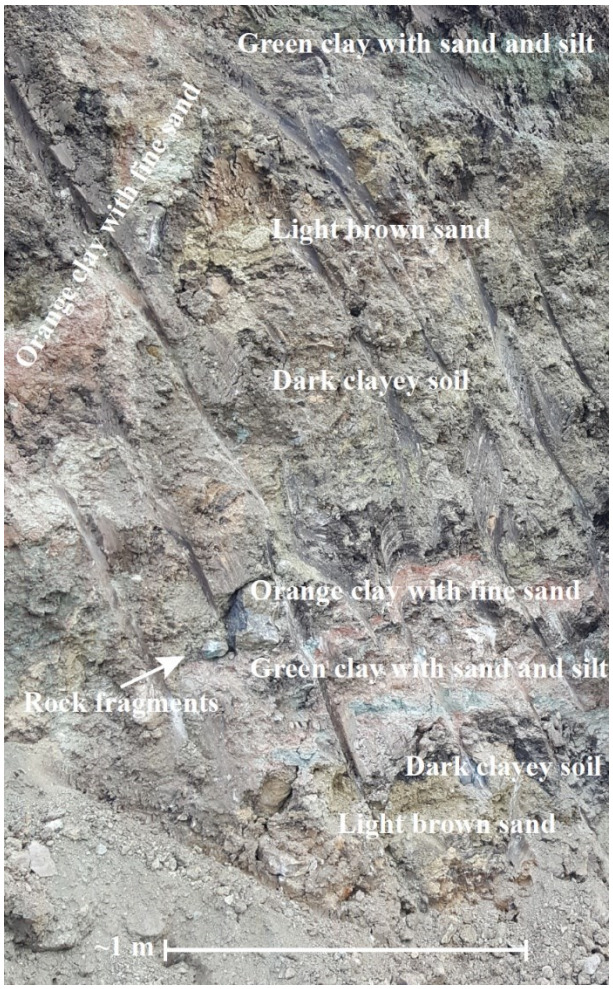


**Figure 5-2 Photographs of the earthflow showing the churned strata from a cut adjacent to the access road located between the highway and the railway at the Ten-mile landslide (October 2016).**

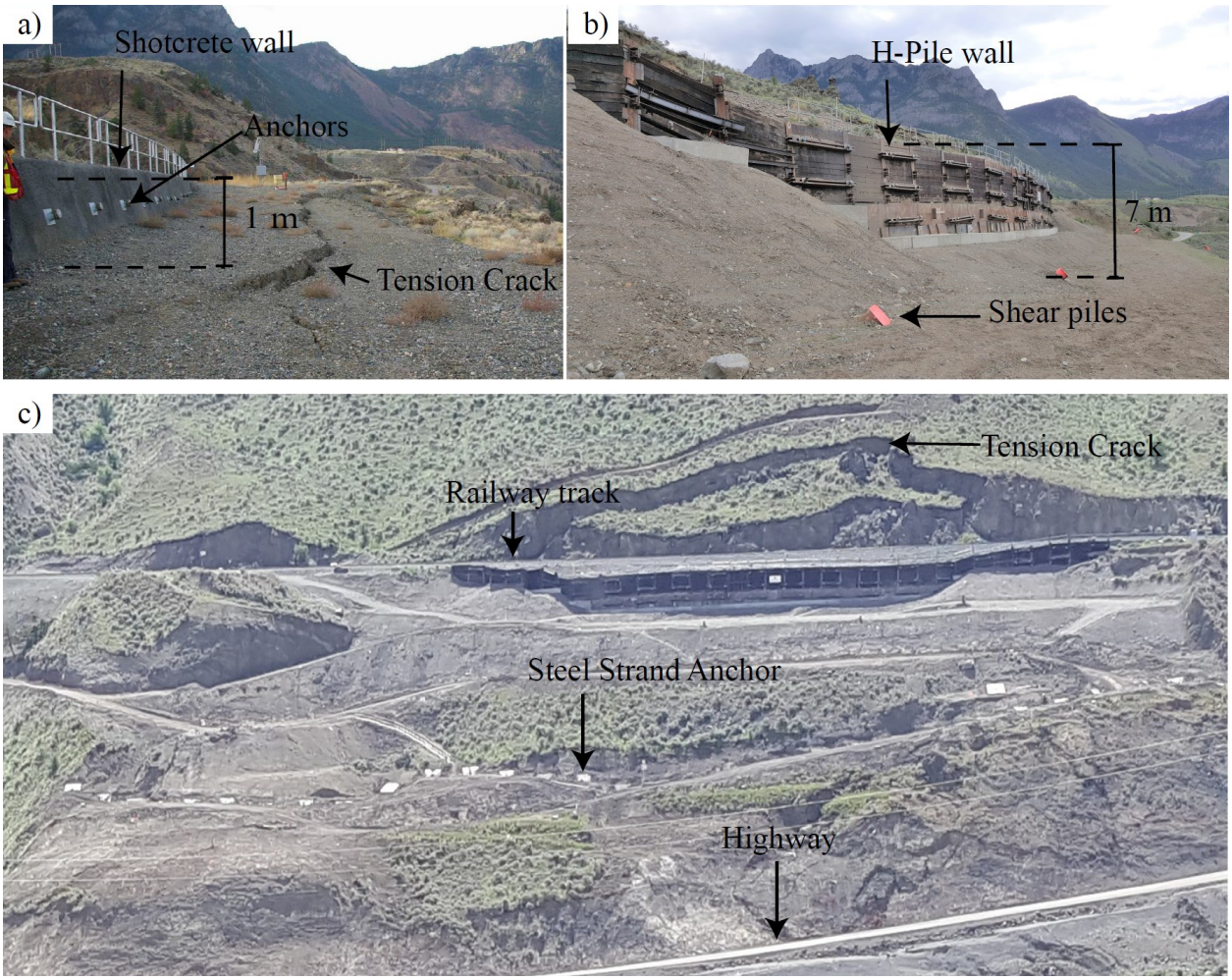


**Figure 5-3 Photographs of mitigation actions at the Ten-mile landslide: (a) next to the railway showing the shotcrete and anchor wall (taken by T. Evans, Oct. 2019); (b) below the railway showing the H-pile wall and the shear piles (May 2017); and (c) from across the Fraser River showing the location of the steel strand anchors and the road and railway (May 2017).**

### 5.2.3 Instrumentation and monitoring

Surface displacement monitoring of the Ten-mile landslide has been carried out using aerial photography (manned and unmanned aircraft), manual surveys of ground stations, and aerial and terrestrial LiDAR. Appendix H shows the change detection analysis of the Ten-mile with changes in displacement, similar to the analysis presented in Chapter 3. In the summer of 2016, a network of 10 single-frequency dGNSS systems (Geocube units, Ophelia Sensors, France) installed across different sections of the landslide recorded the latitude, longitude, and elevation at 1-min intervals (Rodriguez and Hendry 2018) (Appendix B); the dGNSS units recorded data within ±5 mm

accuracy, as presented in Chapter 4. Measuring displacement at the surface using multiple dGNSS units show variation across the landslide (Figure 5-4). The largest displacement occurred on the lower side of the slope near the highway, between April 2017 to November 2018 the dGNSS #46 recorded 1500 mm of displacement; the magnitude of displacement decreases uphill from the highway and the 2016 shear piles (Figure 5-4a). Above the railway track displacement measurements were less than 10 mm. The displacement measures allowed to quantify the displacement rate in each dGNSS units between April 2017 to November 2018 (Figure 5-4b). A comparison of displacement rates between dGNSS units allow identifying the blocks (Lato et al. 2016) that exhibit similar changes in displacement.

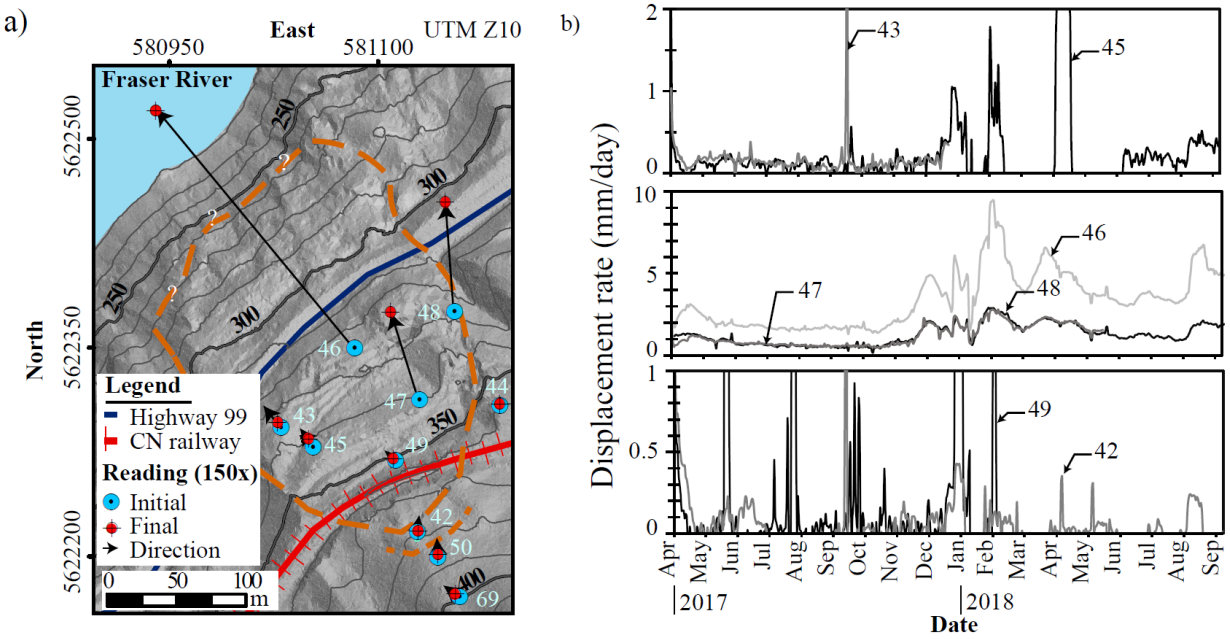


**Figure 5-4 dGNSS measurements of landslide displacement from ten Geocube units scattered across the site. (a) Vector plot showing the trend in horizontal orientation of each dGNSS unit based on initial and final readings scaled 150×. (b) 15-d moving average of the displacement rates between April 2017 and November 2018 from dGNSS units within the sliding mass.**

Effort to measure pore water pressures in the sliding mass has been made through site investigation that included the installation of eight vibrating wire piezometers (VWP) and cone penetration tests with pore water pressure measurement (CPTu) between the highway and railway. The VWPs were installed at different elevations between the ground surface and shear surface. However, multiple VWP readings between 2016 and 2019 showed very low positive pore water pressures fluctuating

from 0 to 1.5 m between 12 to 20 m below ground surface (BGC 2016a, 2019). Positive pore water pressures from five VWPs installed in 2016 were related to the drilling process and summer precipitation (BGC 2016a); unfortunately, two VWPs near the shear surface only recorded information for three months before the landslide movement destroyed the piezometer casing (BGC 2016a). CPTu tests carried out up to a depth of 23 m showed a pore water pressure build up to 4.3 m at 13 m below ground surface (Figure 5-5); however, zones of refusal were advances through sonic drilling to continue the CPTu test which can impact pore pressure readings (BGC 2016a). Historical pore pressure measurements have near the shear surface have fluctuated from 0 to 2.6 m (BGC 2016a). The low pore water pressure measurements can indicate that there isn't a phreatic surface within the sliding mass. Therefore, the analysis of the Ten-mile in this research should consider the mechanical properties of the earthflow deposit as an unsaturated soil that influences the mechanism of failure.

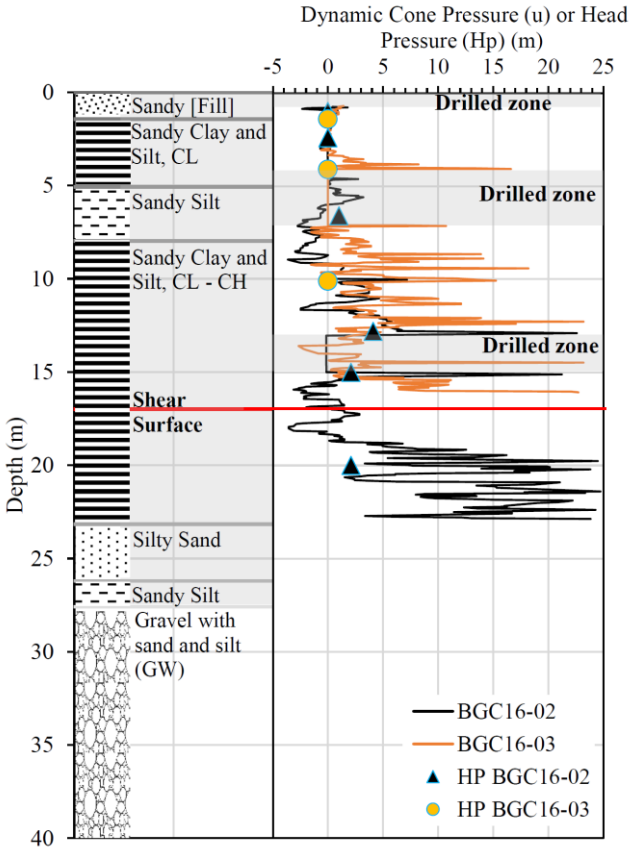


**Figure 5-5 Dynamic cone pressure and head pressure from CPTu and dissipation test (BGC Eng. 2016a).**

Despite being very dry, slow seepage of water has been observed after precipitation periods on the slope cuts adjacent to the roadway (see Chapter 4). This suggests that after water infiltration, water seepage reaches the clay layers and travels on top of it. The increase in moisture sufficiently softens the clay so that it can be easily pressed with one's thumb. A comparison of antecedent rainfall with displacement rates from the dGNSS network indicates strong correlations of the movement to weather changes (see Chapter 4 and Appendix E). The presence of seepage and relationship between precipitation with displacement rate indicates that water is infiltrating the soil, causing an increment in water content and a decrease in matric suction and strength.

Lastly, slope inclinometers (SIs), borehole logs, and observation of surficial features have allowed for a delineation of the extent of the landslide and depth of the shear surface (Figure 5-6a) (BGC 2016a,b, 2019). The shear surface is located at a depth of 17 m below the railway tracks (BGC 2016b) and becomes shallower near the highway with an approximate depth of 12 m from the surface (BGC 2016a). The shear surface is sub-parallel to the surface of the slope, with a back scarp that extends upwards to the uppermost tension crack 60 m upslope from the railway tracks (Figure 5-6b). Before the installation of the 2016 shear piles, four SIs were sheared off within a month of installation (BGC 2016a,b). These SIs located between the highway and CN's retaining wall recorded displacement rates between 6 and 8 mm/d and sheared at a depth of 12 to 17 m from the surface. After 2017, the installation of one SI between the railway tracks and the highest tension crack has provided information for three years with recorded displacement rates between 0.8 and 4.8 mm/y and deformation at a depth of approximately 17 m (BGC, 2019).

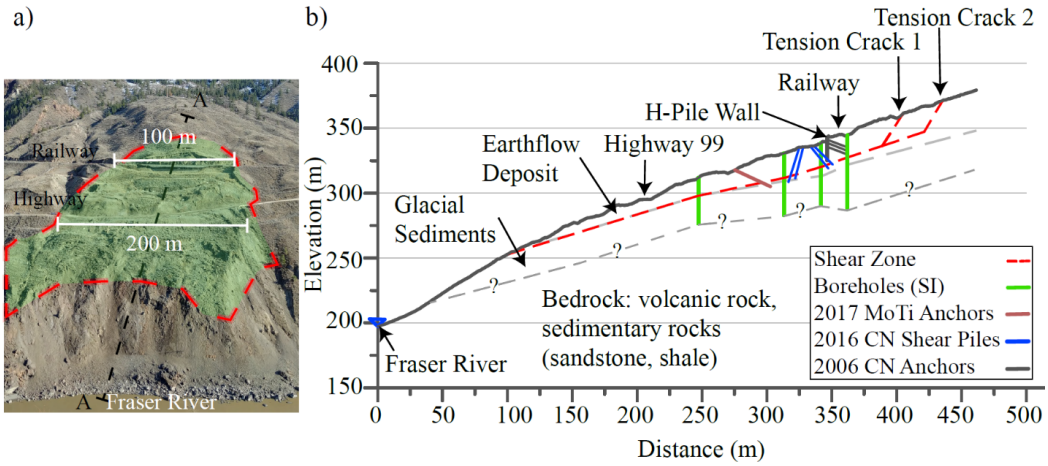


**Figure 5-6 Active zone at the Ten-mile landslide: (a) frontal view from March 2018; (b) typical cross-section A-A. The width of the glacial sediments is inferred from previous site investigations.**

## 5.3 UNSATURATED CHARACTERISTICS OF THE EARTHFLOW DEPOSIT

The unsaturated properties of the earthflow were measured on samples recovered from a sonic drilling (BH-BGC15-01), located adjacent to the railway (BGC 2015). Testing of VWC from earthflow samples ranged from 12 to 45% above the shear surface and from 21 and 30% near the shear surface. Figure 5-7 shows the profile comparison of soil description, the changes in VWC with depth, and the CPTu test results. Soil water characteristic curves (SWCCs) (Fredlund and Xing 1994) were measured from representative samples of the earthflow deposit within sliding mass (Appendix C). Three samples were taken at 10 m and 17 m below ground surface. The samples are a clayey sand, medium to high plastic and very stiff, with some silt and traces of gravel, and a dark brown color. The three samples had an initial VWC between 0.25 and 0.35, porosity between 0.3 and 0.49, and a void ratio between 0.43 and 0.96. The SWCCs were measured on a Tempe cell (Fredlund et al. 2012) for two samples (samples 1 and 2) and with a Hyprop 2 meter (METER Group AG 2018) (sample 3) through the drying process. Figure 5-8 shows the SWCC measurement and the fitting curve using Fredlund and Xing (1994)'s model.

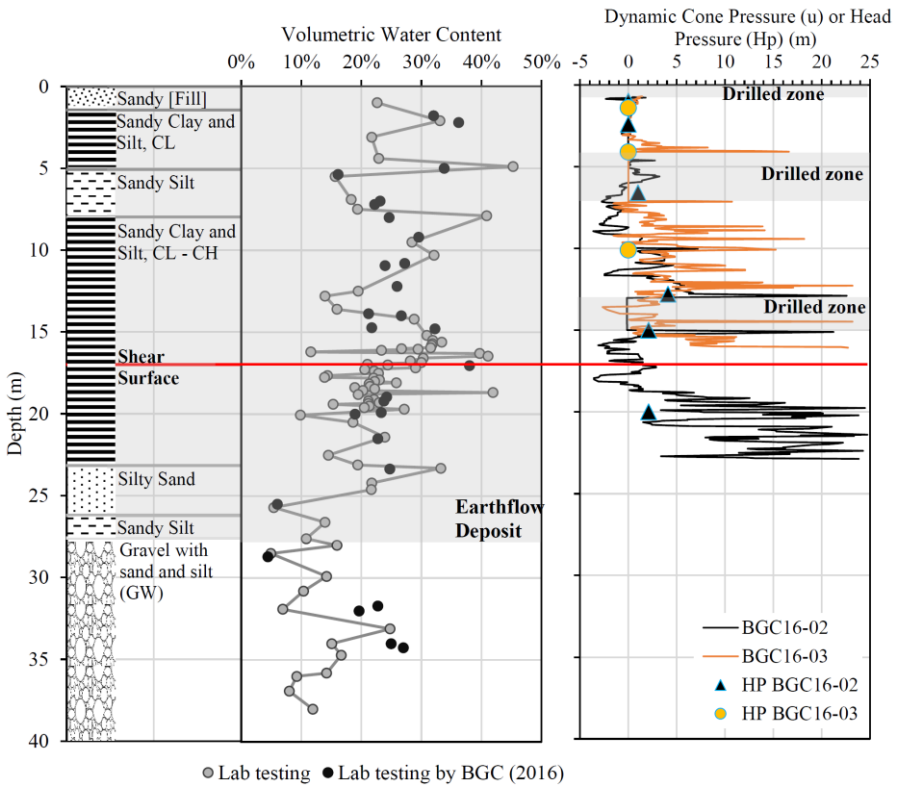


**Figure 5-7 Changes in the volumetric water content from earthflow deposit samples at the Ten-mile landslide (including testing carried out by BGC Eng. 2016a); and, dynamic cone pressure and head pressure from CPTu and dissipation test (BGC Eng. 2016a).**

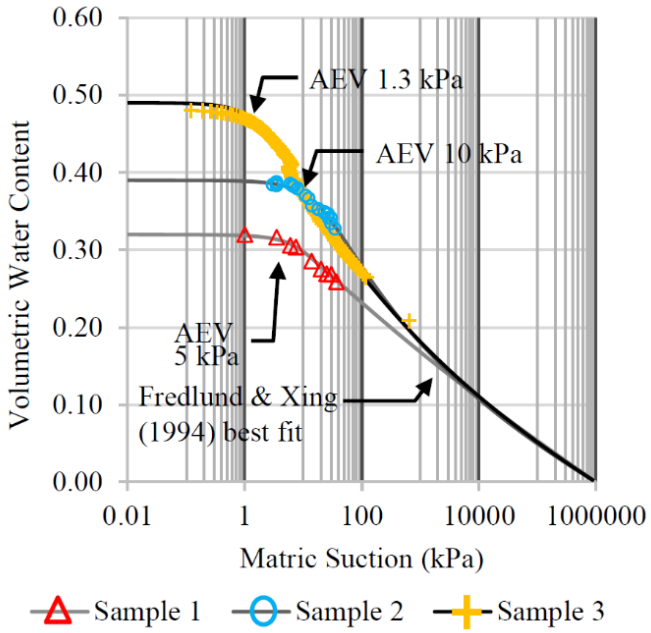


**Figure 5-8 SWCC and curve fitting using Fredlund and Xing (1994)'s model for three earthflow samples at the Ten-mile landslide.**

The shear strength of the earthflow has a non-linear relation to matric suction as the soil's air-entry value (AEV) is exceeded in unsaturated conditions (Fredlund et al. 2012). However, the available laboratory apparatus did not allow for control of the matric suction while measuring the shear strength. The simplified linear form proposed by Fredlund et al. (1978) [Eq.1] is used in this paper to evaluate the effects of matric suction on shear strength ($\tau'$).

$$\tau' = c' + (\sigma_n - u_a)\tan\phi' + (u_a - u_w)\tan\phi_b\ , \qquad [1]$$

where c' is the cohesion, $(\sigma_n - u_a)$ is the effective stress, $\sigma_n$ is the normal stress, $u_a$ is the pore-air pressure, $(u_a - u_w)$ is the matric suction, $u_w$ is the pore water pressure, $\phi$' is the angle of internal friction, and the angle $\phi_b$ indicates the increased rate of shear strength with an increase in matric suction and is equal to or less than $\phi$ (Fredlund et al. 2012). Eq. 1 provides reasonable results at matric suction values close to the AEV and where changes in the soil's VWC do not reach the residual suction (Fredlund et al. 2012).

The large displacement of the sliding mass can reduce the shear strength to residual (Skempton 1985; Stark and Eid 1994; Mesri and Huvaj-Sarihan 2012), as is the case for the reactivation of the earthflow deposit at the Ten-mile site. Eight samples selected from BH-BGC15-01 at 10 m, 16

m, 16.5 m (two samples), 17 m (two samples), 18 m, and 19 m below ground surface were use to measure the effective angle of friction ($\phi$') through direct shear testing (ASTM International 2011)(Appendix C). The samples are a clayey sand, medium to high plastic and very stiff, with some silt and traces of gravel, and a dark brown color. The initial VWC of the samples ranged from 0.2 to 0.4 (Appendix C). The samples were initially submerged until saturation and tested in drained conditions. The $\phi$' ranged from 15 to 24°, with an apparent cohesion between 38 and 49 kPa. The residual angle of internal friction ($\phi_r$') was estimated by multiple reversals of drained direct shear tests on each sample. The tests showed that $\phi_r$' vary at similar normal stress (Appendix C). The $\phi_r$' ranged between 15 and 29° while assuming that the soil had lost any apparent cohesion. The earthflow had a clay and silt content ranging from 56 to 74% (Appendix C) that would cause variability in $\phi_r$' as discussed by Stark and Eid (1994). Thus, the magnitude of $\phi_b$ at residual ranges between 6 and 10°, approximately 40% lower than the friction angle (Fredlund et al. 2012). The unsaturated soil model using Eq. 1 indicates a significant increase in matric suction should affect the shear strength based on the earthflow's residual condition.

### 5.4 KINEMATICS OF THE LANDSLIDE MOVEMENT

A comparison of two point clouds (Appendix H) and previous research (Lato et al. 2016) shows a large variability in displacement across the sliding mass. Lato et al. (2016) discretized the sliding mass in 18 intact blocks of soil, named A to S (block C was outside the sliding mass). These blocks were delineated based on the uniform displacement and does coincide in occasion with the location of tension cracks and scarps. The location of the dGNSS network on the landslide allowed to monitor the characteristics of the displacement in the identified blocks. The changes in the displacement rates (i.e., accelerations) measured from the dGNSS units were used to identify the blocks that are moving in clusters (i.e., moving together) and differentiate the movement sequence (i.e. successive movement). Specifically, correlation analysis of the displacement rates (Figure 5-4b) between two dGNSS units was used to differentiate between clusters. The correlations between displacement rate of two dGNSS units was evaluated using Spearman's rank correlation coefficient (SCC):

$$SCC = 1 - \frac{6}{n(n^2-1)} \sum (RA - RB)_i^2 \, , \qquad [2]$$

where n is the number of observations from the displacement rate in each dGNSS unit, RA and RB are the ranks of the displacement rates from two dGNSS units at $i$ (Appendix F). SCC varies from −1 to +1, indicative of strong negative and positive correlations, respectively. The Spearman correlation allows for a determination of whether the displacement rates from two dGNSS units describe a nonincreasing or nondecreasing relation (i.e., monotonic function). A strong SCC between two dGNSS units indicates a similar change in displacement rates (Table 5-1). Also, SCC values with confidence level of the statistical relationship below 95% (or P-value < 5%) are discarded, assuming a normal distribution.

**Table 5-1 Correlation coefficients between changes in displacement rate measured with dGNSS within the active zone between April 2017 and November 2018.**

| Unit | 42 | 43 | 45 | 46 | 47 | 48 | 49 |
|---|---|---|---|---|---|---|---|
| 42 | 1.00 | | | | | | |
| 43 | 0.52 | 1.00 | | | | | |
| 45 | 0.26 | 0.37 | 1.00 | | Symmetric Matrix | | |
| 46 | 0.00 | 0.28 | 0.44 | 1.00 | | | |
| 47 | | 0.44 | 0.31 | **0.92** | 1.00 | | |
| 48 | 0.06 | 0.40 | 0.44 | **0.95** | **0.94** | 1.00 | |
| 49 | 0.56 | 0.30 | 0.42 | 0.23 | 0.26 | 0.34 | 1.00 |

The dGNSS units recorded over 500 d of displacement. The recorded displacements varied in magnitude, exhibiting different acceleration and deceleration periods (Figure 5-4a). The extent of each cluster was determined based on a logical spatial location. The dGNSS units required to be located on adjacent blocks to have a logical correlation regardless of having a strong SCC; thus, a cluster can be defined by a strong correlation between dGNSS units close to one another. Weak correlations were considered an indication of another cluster of movement. Table 5-1 shows the correlation coefficients between dGNSS units determined from Eq. 2. at a 95% confidence level; blank cells indicate coefficients below the confidence level and not considered in the analysis (Appendix F).

The correlation analysis indicates that dGNSS units 46, 47, and 48 are strongly correlated (Figure 5-9) and suggests the northeast section of the landslide moves as a cluster of blocks. The weak correlations between dGNSS units within the sliding mass (42, 43, 45, and 49) could be related to

the small movements recorded. The correlations indicate a relationship of movement with a confidence level above 95%, but other unknown variables could improve the correlation. The results from these correlations allowed to discretize the movement of the Ten-mile landslide into five clusters, named "I" to "V", as shown in Figure 5-10.

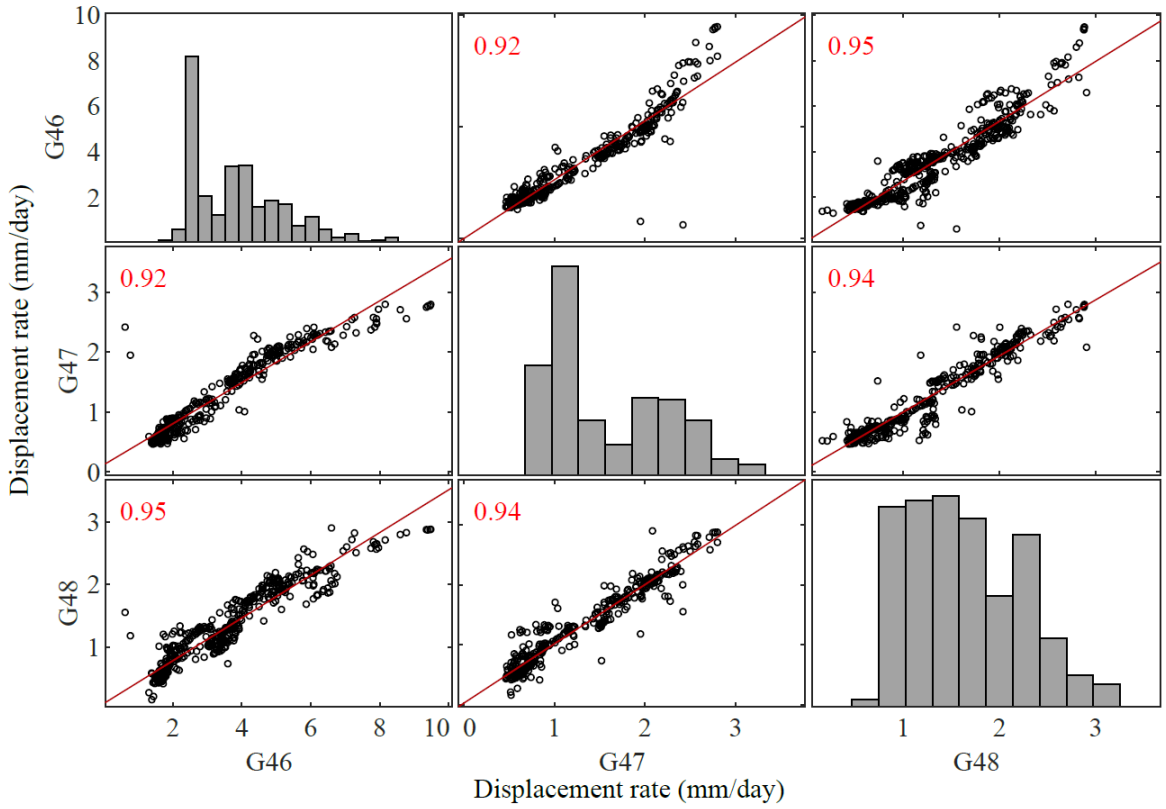


**Figure 5-9 Correlation matrix between displacement rate of dGNSS units 46, 47, and 48 and frequency of histogram displacement rate along matrix diagonal. Red values indicating the Spearman correlation coefficient.**

The sequence of movement of each cluster was analyzed through a sliding correlation (SSCC) of the displacement rate using Eq. 3. In this method, a correlation is determined between two dGNSS units with a temporal offset of D. The sliding correlation was evaluated for D equal to 0 d (i.e., synchronized time), 1, 2, 3, 7, and 15 d (Appendix F).

$$SSCC = 1 - \frac{6}{n(n^2-1)}\sum(RA_i - RB_{i-D})^2 \text{ , D= 0, 1, 2, 3, 7 and 15 days} \quad [3]$$

The sliding correlation provides two correlation coefficients from the two-way approach between two dGNSS units (i.e., $RA_i - RB_{i-D}$ or $RB_i - RA_{i-D}$). The sequence is defined based on the

sliding time that results in a maximum correlation coefficient for the displacement rates. The correlation coefficients are calculated for dGNSS units within the active zone. This analysis was conducted for the period exhibiting the highest rates of movement (October 2017 to March 2018). Table 5-2 shows the correlation coefficients resulting from changing the time offset (i.e., D) of dGNSS unit 43. Appendix F shows the sliding correlation coefficients for all dGNSS units.

**Table 5-2 Sliding correlation coefficient between the displacement rate of unit 43 and other dGNSS units. Results are for sliding windows of 0, 1, 2, 3, 7, and 15 d between October 2017 and March 2018.**

| Unit | Days after registering acceleration in unit 43 | | | | | |
|---|---|---|---|---|---|---|
| | 0 | 1 | 2 | 3 | 7 | 15 |
| 42 | 0.54 | 0.53 | 0.57 | 0.49 | 0.53 | 0.23 |
| 45 | | | | | | |
| 46 | 0.39 | 0.40 | 0.37 | 0.33 | 0.25 | |
| 47 | 0.57 | 0.48 | 0.45 | 0.46 | 0.29 | |
| 48 | 0.43 | 0.44 | 0.42 | 0.41 | 0.32 | |
| 49 | | | | | | |

The sliding correlation for the displacement rate of dGNSS unit 43 indicates the correlation coefficient with unit 42 is the highest after a time offset of 2 d. Similarly, dGNSS unit 46 has a stronger correlation a time offset of 1 d, unit 47 at 0 d, and unit 48 at 1 d. Lastly, dGNSS units 45 and 49 do not correlate with other units at a confidence level above 95%. Table 5-3 presents a summary of the results from each sliding correlation.

**Table 5-3 Days of successive acceleration experienced by a dGNSS unit after the initial acceleration of another dGNSS unit.**

| Initial acceleration | Successive acceleration | | | | | | |
|---|---|---|---|---|---|---|---|
| | 42 | 43 | 45 | 46 | 47 | 48 | 49 |
| 42 | 0 | | | | | | |
| 43 | 2 | 0 | | | | | |
| 45 | 15 | 15 | 0 | | | | |
| 46 | 7 | 7 | 7 | 0 | | | |
| 47 | 3 | 1 | 0 | 0 | 0 | | |
| 48 | 7 | 3 | 0 | 0 | 0 | 0 | |
| 49 | 2 | | | | | | 0 |

Asymmetric Matrix

The sliding correlation indicates movement starts in Cluster I (Figure 5-10), with dGNSS units 46, 47, and 48 moving together. The second movement is in dGNSS unit 45 (Cluster II), moving after unit dGNSS 46. The third movement is experienced by dGNSS unit 43 (Cluster III) after units 45, 46, 47, and 48. The fourth movement is in dGNSS unit 49 (Cluster IV), followed by unit 42 (Cluster V).

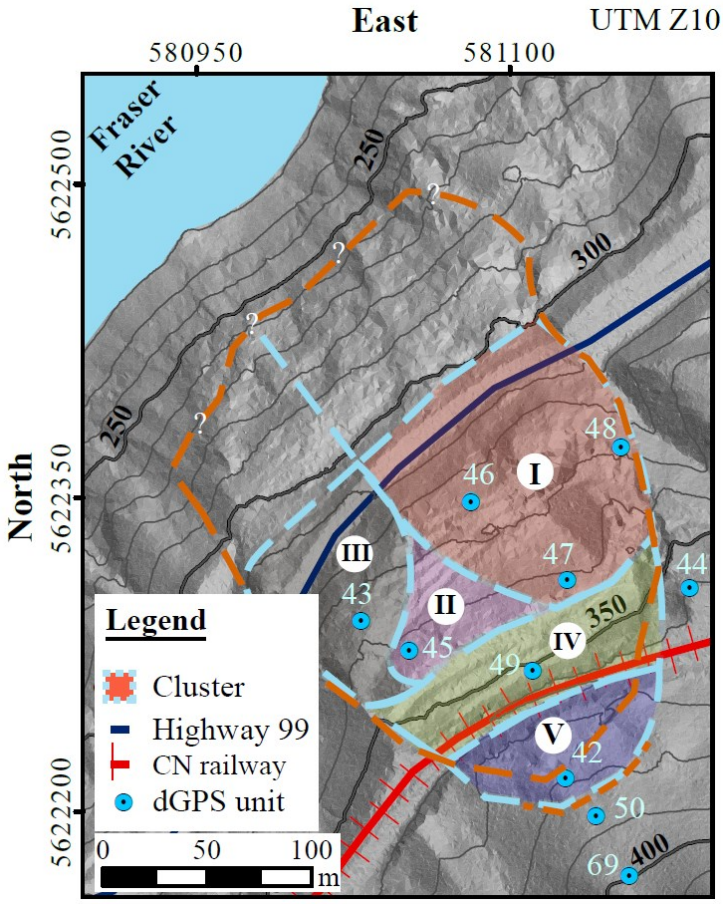


**Figure 5-10 Cluster of moving blocks at the Ten-mile landslide. Ascending order of cluster label (i.e I to V) indicates the sequence of movemen. Dashed lines with interrogation marks indicate the estimated extent of the movement zone.**

The measurement of displacement from all dGNSS units suggests that the block movement is in clusters. The movement of cluster I in the sliding mass would be follow by the movement of cluster I and II. Afterwards, the sliding mass below the shear pile moves with cluster I, II, and III. Thereafter, the sliding mass from cluster I to IV, and finally the entire sliding mass moves (cluster I to V).

## 5.5 ESTIMATING THE EFFECT OF MATRIC SUCTION ON THE STABILITY OF THE TEN-MILE LANDSLIDE

The 3D LEM model of the landslide was solved using the generalized Morgenstern and Price method using SvSlope (The SoilVision Systems Ltd. Team 2019) for a fully specified shear surface. The first analysis of the model evaluated the FoS using the extreme values of $\phi_r$' (i.e., 15 and 29°) with zero matric suction to determine if matric suction is required to explain the meta stable condition of the landslide. The $\phi_r$' resulting in unstable conditions (FoS<1) allows determining the matric suction required to achieve a meta stable condition (FoS=1) through back-analysis of the shear surface. A back-analysis was carried on the shear surface representing the successive movement of the five clusters.

The surface geometry for the numerical model was generated from a point cloud using 3D digital photogrammetric reconstruction from photos collected using an unmanned aerial vehicle (UAV) on November 5, 2017 (Rodriguez et al. 2020). The 3D stratigraphy was extruded from a 2D profile (Figure 5-6b). Figure 5-11 shows the 3D LEM model and the shear surface geometry used for analysis based on the sequences of movement. A shear surface representing each cluster was estimated based on the SI data (Figure 5-6b) and the delineated clusters (Figure 5-10). The shear surface inclination on the sides was set to 56° from horizontal (i.e., the average angle from $45°+\phi/2$ for a $\phi_r$' of 15 and 29°). The movement of a cluster after another increases the sliding mass volume, starting from 330,000 $m^3$ for cluster I, to 360,000 $m^3$ for cluster I and II, to 570,000 $m^3$ for cluster I to III, to 700,000 $m^3$ for cluster I to IV, until it reaches 850,000 $m^3$ for cluster I to V (Figure 5-11c and 10d). The soil below the shear surfaces was assumed to be stable. SvSlope discretized the fully specified shear surfaces into a grid of columns with an average of three columns per $m^2$; software assumptions are provided in the theory manual (The SoilVision Systems Ltd. Team 2019). Also, four case-specific assumptions were made: (1) the analysis does not take into account the active forces from retaining structures or ground improvements (i.e., pre-remediation conditions); (2) the boundary of the landslide is assumed in specific zones where tension cracks are not visible on the ground, especially in the southeast border (Figure 5-4a); (3) the matric suction estimated from the analysis is representative of the average across the shear surface; and (4) the samples tested to determine the strength of the earthflow are representative of the material over the shear surface.

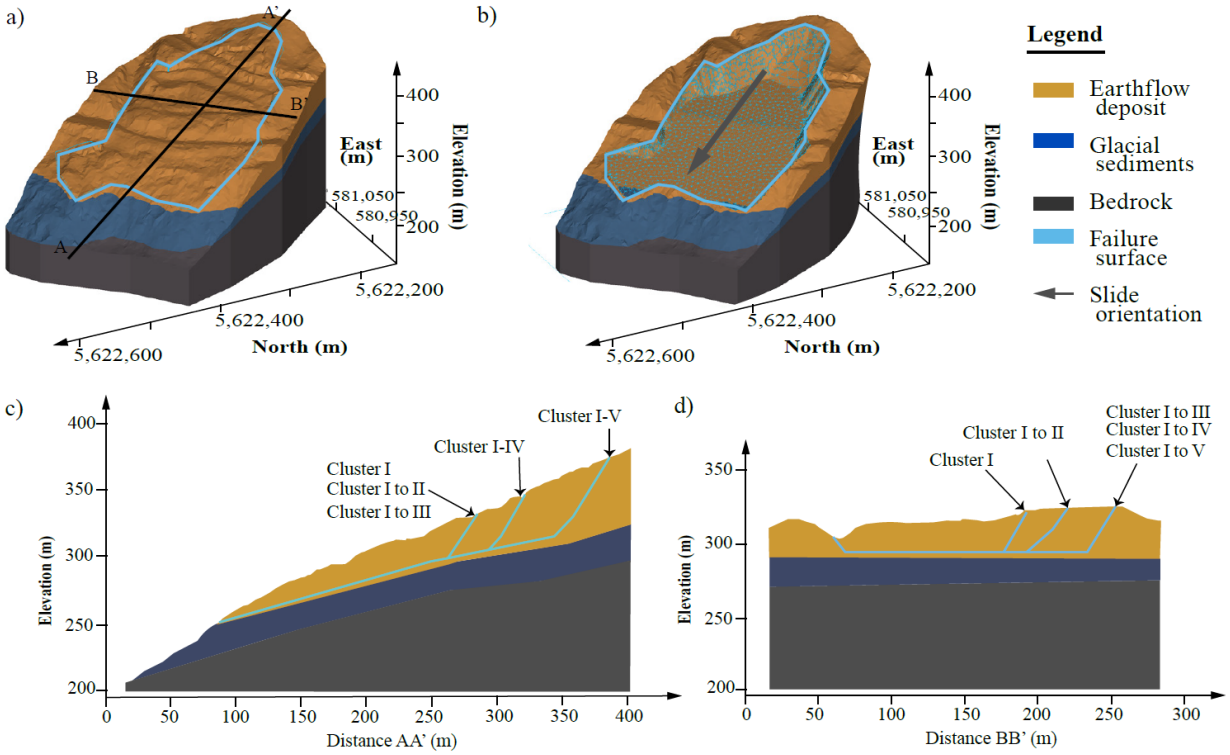


**Figure 5-11 3D limit equilibrium model of the Ten-mile landslide: (a) an oblique view of the model of the ground surface, (b) oblique view of the global shear surface, (c) cross section AA' parallel to slope movement, and (d) cross section BB' across the slope movement.**

The FoS for the extreme values of $\phi_r$' with zero matric suction are 0.80 for $\phi_r$' of 15° and 1.4 for $\phi_r$' of 24°. The results show that a $\phi_r$' of 15° is representative of a weak material with increased clay content that would be affecting the shear surface. It is assumed the sliding surfaces followed zones of increased clay content, which is consistent with observation from core samples near the shear surface's depth.

A $\phi_r$' of 15° and $\phi_b$ of 6° were considered a reasonable base case to back-analyze the effect of matric suction. Back-analysing clusters within the shear piles and above the railway track (i.e., cluster IV and V) shows what would have existed before installing the shear piles and does not represent the current state. Table 5-4 shows the FoS at zero matric suction and the average matric suction for a FoS=1.0 at the shear surface from the successive movement of each cluster.

**Table 5-4 Back analysis result for clusters of movement at the Ten-mile landslide.**

| Cluster | FoS without matric suction | Average matric suction at the shear zone for a FoS of 1.0 (kPa) |
|---|---|---|
| I | 0.89 | 80 |
| I-II | 0.89 | 82 |
| I- III | 0.84 | 130 |
| I-IV | 0.81 | 180 |
| I-V | 0.80 | 200 |

The back-analysis shows unsaturated soil conditions may impact the stability. An average matric suction from approximately 80 to 200 kPa reflects the meta stable condition of the five clusters. These matric suction values are reasonable based on VWC between17% and 28% as measured in earthflow samples (Figure 5-7 and Figure 5-8). The relation of the back-analysis results (Table 5-4) and the AEV indicates the earthflow is unsaturated and that increments in the VWC would decrease the stability of the sliding mass by reducing the matric suction. The magnitudes in matric suctions shown in Table 5-4 suggests that the initial block would require less increments in VWC to results in unstable conditions.

A detailed discretization of the sliding mass allowed to estimate the average matric suction at the shear surface within each cluster to maintain meta-stable conditions. Therefore, the back-analysis of only cluster II shows a 100 kPa matric suction (i.e., a VWC of less than 26% in the earthflow at the shear zone to reach 100 kPa of matric suction), assuming the matric suction in cluster I is 80 kPa (Table 5-4). Similarly, the back-analysis of only cluster III shows a 300 kPa matric suction (i.e., a VWC of less than 22% in the earthflow at the shear zone to reach 300 kPa of matric suction), while assuming the matric suction in both clusters I and II is 82 kPa (Table 5-4). These matric suction values are reasonable considering the variability of the VWC measured on the earthflow deposit, as shown in Figure 5-7. The variance of matric suction on the shear surface suggests each cluster has a different effect on global stability (i.e., movement of all five clusters). The back-analysis of clusters I, II, and III indicates the average matric suction at the shear surface during the time measurements were taken with the dGNSS units.

The successive movement of clusters I to V described by the dGNSS unit data is considered to be related to three possible failure mechanisms. The first failure mechanism is related to a loss of support; after matric suction is lost in the initial cluster (I) and subsequent movement occurs, other

clusters move due to the loss in support. The second failure mechanism is related to a successive loss of suction from water infiltration and increases in the VWC at the shear zone at different times. A third failure mechanism is a combination of the former two.

Analyzing loss of support in the global shear surface was carried out by removing cluster I from the model. The results show the FoS is reduced to 0.9 on clusters II to V. Similarly, a successive loss of matric suction decreases the FoS in the global shear surface. Table 5-5 shows the reduction in FoS and the relative mobilized shear strength through the successive loss of 200 kPa of matric suction (i.e., the meta-stable condition) that the shear surface of the earthflow can reached with increments of the VWC above 17% .

**Table 5-5 Impact of successive loss of matric suction on the FoS and mobilized shear strength**

| Cluster | FoS of global shear surface | Reduced mobilized shear strength (%) |
|---|---|---|
| I | 0.92 | 9% |
| I-II | 0.91 | 10% |
| I- III | 0.86 | 15% |
| I-IV | 0.83 | 17% |
| I-V | 0.80 | 20% |

The mobilized shear strength on the sliding mass can decrease up to 20% when matric suction is lost in all clusters. The results suggest the loss of matric suction in cluster I would significantly impact the global stability by reducing the mobilized shear strength of the sliding mass by up to 9%. Cluster III has second highest reduction of 5%, then cluster V with 3%, cluster IV with 2%, and finally cluster II with 1%. The loss in matric suction for larger portions of the sliding mass substantially reduces the mobilized shear strength. The successive loss of matric suction can occur from variabilities in the earthflow properties and the distribution of preferential flow paths to facilitate infiltration (Appendix G). Controlling infiltration to limit saturation at key areas could minimize the weakening of the shear strength and reduce the FoS of the sliding mass for the three possible failure mechanisms.

## 5.6 Impact of Changes in the Degree of Saturation on the Stability of the Ten-mile Landslide

A simulation of changes in matric suction of the five clusters allowed for an assessment of the effect on the FoS due to changes in saturation, similar to a methodology proposed by Fredlund et al. (2012). Simulating changes in matric suction on the different clusters provides insights into the role of precipitation, as water is stored in the soil and changes the saturation. The saturation curve is calculated based on the measured VWC changes and the porosity of the SWCC samples shown in Figure 5-8. The saturation curves from two samples with the measured SWCC (sample 1 and 3) provide upper and lower bounds of changes in the saturation of the earthflow relative to the matric suction. The sensitivity of the FoS and changes in the earthflow's saturation with matric suction are summarized in Figure 5-12. The curves show the limits of saturation required to reduce the FoS and increase the movement of the sliding mass. Conversely, the plotted curves indicate a decrease in saturation would increase the FoS.

Identifying the movement sequence of the clusters allows a comparison of the effect of changes in earthflow saturation on the FoS with respect the successive movements. A comparison of the curves shows that the smaller soil masses (e.g., cluster I or I-II) requires a saturation below 65% to achieve a FoS above 1.0. In contrast, the largest soil mass of the global shear surface (cluster I-V) requires a saturation below 60% to achieve a FoS above 1.0. Thus, controlling the infiltration rate to maintain the saturation of the earthflow below 60% can reduce the continuous movement of the sliding mass. Figure 5-12 thus becomes a tool for engineers to plan mitigation strategies that focus on different sections of the sliding mass; for example, curve I-III provides the saturation magnitude that needs to be controlled after stabilizing the upper section of the sliding mass with the installation of shear piles.

The FoS of the sliding mass changes with seasonal weather and fluctuations of the VWC in the earthflow as the amount of water stored changes in each cluster. Comparing the saturation curves of the earthflow and the changes in the FoS with matric suction illustrates the consequence of water fluctuation on the five clusters. Figure 5-12provides a measure of the degree of saturation to increase or reduce the FoS below meta-stable conditions. Thus, precipitation rates that cause a saturation increase at the shear surface above 60% would result in a potential failure or increase the displacement rate; conversely, a decrease in saturation would result in a higher FoS and

increase stability. This relationship helps to define a hazard level based on the effect of weather factors that alter the earthflow saturation and stability of the sliding mass, as suggested by Fredlund et al. (2012).

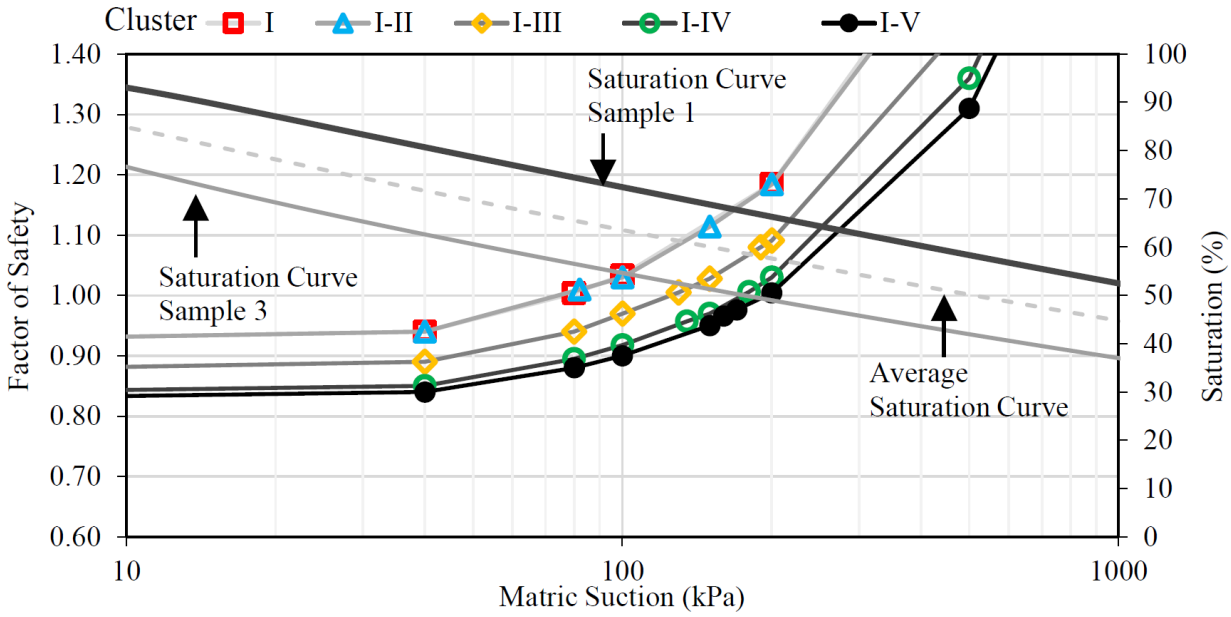


**Figure 5-12 Simulation of the change in FoS with matric suction for the sucessive movement of the five clusters and the saturation curve of the earthflow.**

## 5.7 CONCLUSIONS

Piezometer readings and CPTu tests have shown low to zero positive water pressure or a phreatic surface within the sliding mass at the Ten-mile landslide. The low range of VWC from 21% to 30% from earthflow samples near the shear zone indicated the sliding surface is unsaturated when compared to the measured SWCC. Although obtaining *in situ* measures of matric suction or VWC at the site was not possible, laboratory results supported the hypothesis that matric suction may be impacting the stability of the landslide. The detailed description of movements and laboratory testing enhanced the numerical model and the ability to analyze the effect of matric suction on the failure mechanism of the Ten-mile landslide.

The intensive monitoring and laboratory testing at the Ten-mile landslide provided insights into the mechanism of failure and the relation to the unsaturated characteristics of the soil. The monitoring data from the dGNSS system has allowed for a measurement of displacement rates at

multiple locations. The use of correlation analysis of displacement rates from the multiple dGNSS units identified five clusters. Analyzing the displacement of the clusters indicated the movement sequence starts on the northeast side of the sliding mass near the highway, propagates to the northwest side, and uphill to the highest tension crack.

The movement sequence was back-analyzed using 3D LEM to determine the magnitude of the average matric suction required to maintain a meta-stable condition of the sliding mass. The methodology implemented in the study helped to estimate the average matric suction for each cluster with respect to successive movement and as required to maintain meta-stable conditions assuming a $\phi$r' of 15°. The analysis shows a matric suction above 80 kPa at the shear surface for cluster I and above 200 kPa for the global shear surface (cluster I-V) are required to maintain meta-stable conditions. These matric suctions values are reasonable for an unsaturated earthflow deposit that in which dry conditions reduced the VWC between between17% and 28%. Water infiltration causing an increase of saturation above 60% at the shear surface would decrease the matric suction below a FoS of 1.0. A complete loss of matric suction in the clusters can reduce the FoS by 20%. The results presented supports the hypothesis that changes in matric suction at the sliding surface have an influence in the meta stable condition of the Ten-mile that would results in changes in the displacements rates.

This case study illustrates the important role of matric suction on the stability of a landslide with a deep, partially saturated failure surface. The analysis highlighted the importance of characterizing in detail the kinematics of active landslides to better understand the mechanism of failure.

## 5.8 ACKNOWLEDGMENTS

The research at the Ten-mile landslide was completed through the (Canadian) Railway Ground Hazard Research Program, which is funded by the Natural Sciences and Engineering Research Council of Canada (NSERC), Canadian Pacific Railway, CN, and Transport Canada. The authors thank CN for providing access to the site and for purchasing the Geocubes. The authors also thank MoTI and BGC for providing access to site investigation reports from the Ten-mile landslide.

## 5.9 REFERENCES


Al-Homoud AS, Taqieddin S, Saket S (1995) Investigation on the geological and geotechnical factors leading to a major slope failure at a selected site on a Jordanian highway. Nat Hazards 12:203–224. doi: https://doi-org.login.ezproxy.library.ualberta.ca/10.1007/BF00596221

Ansari MK, Ahmed M, Rajesh Singh TN, Ghalayani I (2015) Rainfall, A Major Cause for Rockfall Hazard along the Roadways, Highways and Railways on Hilly Terrains in India. In: Engineering Geology for Society and Territory - Volume 1. Springer International Publishing, Cham, pp 457–460

ASTM International (2011) ASTM D3080 / D3080M-11, Standard Test Method for Direct Shear Test of Soils Under Consolidated Drained Conditions

BGC Engineering Inc. (2016a) Ten mile slide 2016 site investigation data report. Victoria, British Columbia

BGC Engineering Inc. (2016b) CN Lillooet Sub. M. 167.7 (Ten Mile Slide) April 2016 Drilling and Instrumentation. Kamloops, British Columbia

BGC Engineering Inc. (2019) Ten Mile Slide Monitoring Update – January 10, 2019. Victoria, British Columbia

BGC Engineering Inc. (2015) CN Lillooet Sub. M. 167.7 (Fountain Slide) September 2015 Drilling and Instrumentation. Kamloops, British Columbia

Bovis MJ (1985) Earthflows in the Interior Plateau, southwest British Columbia. Can Geotech J 22:313–334

Cao L, Wang Z, Chen Y (2016) Unsaturated Seepage Analysis of Cracked Soil including Development Process of Cracks. Adv Mater Sci Eng 2016:. doi: 10.1155/2016/2684297

Carlà T, Macciotta R, Hendry MT, et al (2017) Displacement of a landslide retaining wall and application of an enhanced failure forecasting approach. Landslides 15:489–505. doi: 10.1007/s10346-017-0887-7

Donati D, Stead D, Lato M, Gaib S (2020) Spatio-temporal characterization of slope damage: insights from the Ten Mile Slide, British Columbia, Canada. Landslides. doi: 10.1007/s10346-020-01352-3

Eshraghian A, Martin CD, Morgenstern NR (2008) Hazard analysis of an active slide in the Thompson River Valley, Ashcroft, British Columbia, Canada. Can Geotech J 45:297–313. doi: 10.1139/T07-085

Eshraghian A, Martin CD, Morgenstern NR (2007) A Review of Pore-Pressure-Induced Reactivation of Translational Earth. In: 60th Canadian Geotechnical Conference. Ottawa, pp 2245–2251

Fredlund DG, Morgenstern NR, Widger RA (1978) The shear strength of unsaturated soils. Can Geotech J 15:313–321

Fredlund DG, Rahardjo H, Fredlund MD (2012) Unsaturated Soil Mechanics in Engineering Practice, 2nd edn. John Wiley & Sons, Inc., Hoboken, NJ, USA

Fredlund DG, Xing A (1994) Equations for the Soil-water Characteristic Curve. Can Geotech J

31:521–532

Gaib S, Wilson B, Lapointe E (2012) Design, Construction and Monitoring of a Test Section for the stabilization of an Active Slide Area Utilizing Soil Mixed Shear Keys Installed Using Cutter Soil Mixing. In: ISSMGE - TC 211 International Symposium on Ground Improvement IS-GI. Brussels

Horton JH, Hawkins RH (1965) Flow Path of Rain From The Soil Surface To The Water Table. Soil Sci 100:377–383

JCL Consulting (2006) Highway 99 , Fountain Slide Value Analysis Report. Kamloops, British Columbia

Klose M (2015) Landslide Databases as Tools for Integrated Assessment of Landslide Risk. Springer International Publishing, Cham

Lacasse S, Nadim F (2009) Landslide Risk Assessment and Mitigation Strategy. Landslides – Disaster Risk Reduct 31–61. doi: 10.1007/978-3-540-69970-5_3

Lato M, Porter M, Henshold G, et al (2016) Understanding Landslide Movement and Kinematics with Airborne Lidar. Proc 69th Can Geotech Soc Conf GeoVancouver 2016. doi: 10.1007/s12013-010-9150-8

Macciotta R, Rodriguez J, Hendry MT, et al (2017) The 10-mile Slide North of Lillooet , British Columbia – History , Characteristics and Monitoring. In: 3rd North American Symposium on Landslides. Roanoke, Virginia

Mesri G, Huvaj-Sarihan N (2012) Residual Shear Strength Measured by Laboratory Tests and Mobilized in Landslides. J Geotech Geoenvironmental Eng 138:585–593. doi: 10.1061/(ASCE)GT.1943-5606.0000624

METER Group AG (2018) HYPROP User Manual

Mualem Y (1976) A new model for predicting the hydraulic conductivity of unsaturated porous media. Water Resour Res 12:513–522. doi: 10.1029/WR012i003p00513

Novák V, Šimůnek J, Van Genuchten MT (2000) Infiltration of water into soil with cracks. J Irrig Drain Eng 126:41–47. doi: 10.1061/(ASCE)0733-9437(2000)126:1(41)

Pertassek T, Peters A, Durner W (2011) HYPROP Data Evaluation Software User's Manual. 1–47

Porter MJ, Savigny KW, Keegan TR, et al (2001) Controls on stability of the Thompson River landslides. 55th Can Geotech Conf 1393–1400

Richards LA (1931) Capillary conduction of liquids through porous mediums. J Appl Phys 1:318–333. doi: 10.1063/1.1745010

Rodriguez J, Hendry MT (2018) Cost-effective Landslide Monitoring GPS System : Characteristics, Implementation and Results. In: Geohazards7. Canmore, Alberta

Rodriguez J, Macciotta R, Hendry MT, et al (2020) UAVs for monitoring, investigation, and mitigation design of a rock slope with multiple failure mechanisms—a case study. Landslides. doi: 10.1007/s10346-020-01416-4

Schulz WH, McKenna JP, Kibler JD, Biavati G (2009) Relations between hydrology and velocity

of a continuously moving landslide-evidence of pore-pressure feedback regulating landslide motion? Landslides 6:181–190. doi: 10.1007/s10346-009-0157-4

Skempton AW (1985) Residual strength of clays in landslides, folded strata and the laboratory. Geotechnique 35:3–18. doi: 10.1680/geot.1985.35.1.3

Stark TD, Eid HT (1994) Drained Residual Strength of Cohesive Soils. J Geotech Geoenvironmental Eng 120:856–871

The SoilVision Systems Ltd. Team (2019) SvSlope Theory Manual

Wilson B, Lapointe E (2013) Partial Stabilization of an Active Slide Area Utilizing Soil Mixed Shear Keys installed Using Cutter Soil Mixing Results of a Test Section. Proc Found Eng Face Uncertain 2170–2183

Zhang LL, Fredlund MD, Fredlund DG, et al (2015) The influence of the unsaturated soil zone on 2-D and 3-D slope stability analyses. Eng Geol 193:374–383. doi: 10.1016/j.enggeo.2015.05.011

# CHAPTER SIX. CONCLUSION AND FUTURE RESEARCH

## 6.1 GENERAL CONCLUSIONS

The research goals presented in this thesis were to quantify and validate the benefits of low-cost monitoring instrumentation in terms of accuracy, precision, and limitations to assess unstable slopes sensitive to weather changes through its application on real cases; and test the benefits of instrumenting multiple locations at the Ten-mile landslide to enhance the knowledge on the failure mechanism and provide a workflow that allows examining other unstable slopes.

Low-cost unmanned air vehicles (UAV) and single-frequency GNSS monitoring instruments were used to address these objectives through three case studies. First, the presence of multiple ground hazards next to transportation corridors requires evaluating cost/effective monitoring technology, such as UAV, that can be quickly allocated at different sites while gathering precise information to assess complex failure mechanisms. Second, precise GNSS receivers that effectively monitor slow-moving landslides and provide early warning to transportation corridors have limited application due to its high cost; therefore, evaluating GNSS receivers that are low cost without sacrificing precision and its effectiveness to provide early warning had to be evaluated. Finally, the development of low-cost receivers provides an opportunity to evaluate the benefits of collecting continuous data on multiple units to assess the complex failure mechanism of two landslides affecting two transportation corridors.

The following sections provides the general conclusion from each study conducted in this research.

### 6.1.1 Assessing unstable slopes sensitive to changes in weather using Low-cost UAV monitoring technology

UAV technology's advances is becoming an important monitoring tool for ground hazards by collecting high resolution photos of the ground surface. The use of photogrammetry processes such as *Structure From Motion* algorithms that can be applied to photographs taken from a low-cost UAV (i.e. having a price ranged of less than $2000.oo CAD) has enhanced the capabilities to analyze ground hazards failure mechanisms. The potential benefits of using low-cost UAV on unstable slopes with difficult access next to a transportation corridor need to be evaluated. The analysis presented in Chapter 3 (Manuscript #1) showed the application of low-cost UAV and

digital photogrammetric techniques to assess the failure mechanisms of the geohazard site C018 (as denoted in the AT Geohazard Risk Management Program), near Drumheller (Alberta). The site located next to Highway 837 has required monitoring and serviceability for over two decades, with increasing frequency. A history of rock fall and rockslides events has caused damage and blockage of the corridor, hindering the local commute and a touristic route in Alberta. The analysis carried by implementing UAV technology reflects the characteristics of two events that occurred in December 2017 and Many 2018. The first event was 130 $m^3$ of clumps of frozen soil and bedrock that fell on to the highway and reached the river shore. The second event was characterized by the release of rock falls and debris flow that blocked the highway and exposed a rock outcrop 30 m above the highway. Three inspections using low-cost UAV, one following each event and one in November 2018, provided the information to analyze the failure mechanism.

UAV photogrammetry added an important component to the landslide monitoring program of the C018 site by giving a different perspective of the erosion process in the slope. The proposed methodology (Figure 3-4) on over 600 hundred UAV photos from each survey allowed generating precise point clouds of the entire ground surface. The application of low-cost UAV with multiple GCPs worked as a reliable alternative to other remote sensing techniques, such as LiDAR or InSAR, to obtain precise ground surface information. A UAV's capability to reach high altitudes became essential for collecting data in the high zones with difficult access to the slope. UAV technology's adaptability to reach areas with difficult access and to identify concerns allows geotechnical engineers to have a broader visualization and minimize overlooking at crucial characteristics of ground hazards next to transportation corridors.

The data collected from the three surveys allowed identifying the critical unstable areas and determined the magnitude of the unstable events. The detailed representation of the ground surface allowed to track changes of features developing over time in different sections. The point clouds reflected the loss of material after the first UAV inspection and the variability of the erosion process at the slope surface. The data collected on the upper zones of the slope showed that the rock falls source is approximately between 30 m and 44 m from the toe of the slope. The data analysis also indicated that the event in May 2018 activated approximately 738 $m^3$ of material deposited on the highway. Although the exposed rock outcrop was an initial concern, the detailed comparison from each survey allowed to discard a pre-sheared surface.

The detailed point cloud of the ground surface allowed evaluating the relationship between the drainage network and unstable sections of the slope. The change detection analysis from the different inspection revealed that the erosion process is not uniform along the slope, despite being composed of a uniform stratigraphy with horizontal bedding planes. An analysis of the runoff water on the ground surface provided information about the variability of the erosion process and the location of active zones. The drainage network showed flow lines with the highest contribution area being located primarily near the largest active zones. The drainage network results provided initial information for understanding water's role in the stability of highly erodible materials present on multiple roads in the Badlands region.

The analysis of the C018 site allowed identifying three failure modes associated with weather changes. Debris flows occurring from seasonal precipitation and freeze-thaw cycles. Rock falls from differential weathering in the sedimentary rock. And detachment and falling of frozen soil during the winter period. The UAV data became useful to provided models for rock fall trajectory analyses. The results from the analysis allowed making informed suggestions on mitigation actions that maintain the corridor's safety.

Slopes susceptible to weather changes that become a hazard to transportation corridors require performing periodical monitoring flights to evaluate the relation of weather changes and surface changes. The presence of multiple types of ground hazards affecting the highway network in Alberta and budget constraints typically present for managing ground hazards requires implementing cost/effective monitoring tools. With a commercial cost of less than US$1500[1] for one UAV and processing software of less than US$400[1]/month between 2017 and 2019, the application of UAV technology on extensive highway network systems provides a versatile low-cost monitoring tool that can be deployed quickly and collect precise information that enhances mitigations actions. It is not expected that these costs should be considered for budgeting the use of UAV technology. The low costs enable to increase the frequency to collect data, which is useful for monitoring rapidly evolving site conditions, such as highly erodible soils. The increased monitoring frequency at different weather conditions allows developing earlier warning systems through data revealing the relation of causal factors and the ground changing conditions. Thus,

[1] It is not expected that these costs should be considered for budgeting installations.

geotechnical asset management programs can be enhanced by integrating methodologies involving low-cost UAV.

### 6.1.2 Assessing unstable slopes sensitive to changes in weather using single-frequency dGNSS to monitor landslide in Canada

Current in-place instrumentations for measuring landslides displacements can continuously track continuous changes while providing high-frequency data collection. In-place slope inclinometers (SI), ShapeAccelArrays (SAAs), extensometers, or multi-frequency GNSS receivers have been used to measure continuous deformation with high precision. However, the high cost of these instruments and its installations, and the potential risk of losing them due to excessive deformation, limits the application. Low-cost GNSS receivers that could overcome the limitations of in-place monitoring instruments while maintaining a high precision measurement required evaluation. The analysis presented in Chapter 4 (Manuscript #2) explored the effectiveness of using single-frequency dGNSS receivers to monitor slow-moving landslides while having a relatively lower cost than multi-frequency GNSS receivers. The analyses of single-frequency dGNSS receivers were carried through installing a novel network of Geocubes$^{TM}$ at two sites. The Geocube network requirement to have a minimum fixed unit to provide the differential correction that allowed achieving a ±5 mm precision. This precision was achieved installing single-frequency dGNSS with an approximate capital cost of US$4500 per unit between 2016 and 2021. The installation at the Ten-mile landslide in British Columbia and the Chin Coulee landslide in Alberta allowed tracking the sliding mass movement and monitoring the retrogression at multiple locations.

Monitoring the landslide movement using the Geocube network had initial challenges related to the ability to record data by the system, especially at remote locations. The orientation of the landslide at the Ten-mile facing the south slope of the Fountain valley and the high mountain surroundings limited the satellite signal at each Geocube, ranging from 4 to 9. Similarly, the landslide location limited the amount of sunlight during the winter required by the solar panels to charge the unit's batteries. Addressing the operational requirements and environmental factors allowed recording over 500 days of data in a 60 seconds interval. On the other hand, the installation at the Chin Coulee landslide exposed the Geocube to vandalism and tampering. It was not possible to corroborate the source of the damages during the site visits; however, the units were visible and had easy access for people and animals to manipulate. The system's ability for remote access

allowed identifying the time the units were damaged and required maintenance. Different sites might present implementation challenges for in-place GNSS monitoring systems. Thus, assessing the exposure of GNSS-based systems to external factors that could result in noise or loss data improves installation procedures and planned mitigation actions, such as periodical maintenance. Mitigating or reducing external noise becomes essential for including the Geocube in an early warning system.

Early warning systems for landslides impacting transportation corridors require precise measures with a high rate of data recording. The data recorded have shown the effectiveness of low-cost GNSS to provide precise information on continuous deformation at the two sites. A comparison of the deviation of measurement for each cartesian coordinate has shown the Geocube with similar or better distributions than the high-end multi-frequency GNSS at the Ripley landslide (Figure 4-8). Similarly, loss in data records during the monitoring period was lower in the Geocube, between 20% to 34% missing data, while the GNSS at the Ripley had an average of 45% missing data (Table 4-1). The fluctuation from the true location on GNSS based systems are to be expected as noise sources intensify or diminish during the monitoring period. However, the lower cost of single-frequency GNSS provides an opportunity to install multiple units that validate the measurements and enhance reliability as an early warning system.

Monitoring multiple locations within the same network enhances the capability of describing the movement of a sliding mass. The Geocube network allows covering large monitoring areas while each unit communicates and transfers data to the datalogger separately. Multiple monitoring locations allow identifying areas of the largest movement and direction trends over time. The data recorded allowed to identify displacements of up to 1500 mm within the Ten-mile sliding mass, while units above remediation structures only recorded displacement below 10 mm within the same monitoring period (Figure 4-6). Monitoring multiple points allows assessing the impact of implementing mitigations structures and its area of influence on the unstable slope.

Moreover, the measurements at multiple locations provide a low-cost alternative to interpret the inclination of shear surfaces. The Geocube measurements at Chin Coulee showed that the failure mechanism combines a rotational movement in the upper section and translational movement at the middle section from two sliding masses (Figure 4-9b). Installing cost/effective dGNSS receivers at multiple locations of landslides enhanced the kinematic characterization at each site.

Monitoring the sites with a high rate of data measures allowed identifying changes in the kinematic characteristic and assessing causal factors.

Identifying the causal factor(s) that affect slow-moving landslides is critical for characterizing the failure mechanism and planning mitigation actions. Analysis of changes in displacement rates in multiple units allowed evaluating the effect of weather changes in the movement. The antecedent precipitation was identified as a potential precursor factor of increment displacements at the Ten-mile based on Geocube measurements (Figure 4-10 and Appendix E). In contrast, the changes in displacement rates are influenced by the reservoir elevation at the Chin Coulee (Figure 4-11). Thus, single-frequency dGNSS with high precision is an effective and reliable alternative at low cost for monitoring landslides and provide early warning.

### 6.1.3 Assessing the Ten-mile landslide by instrumenting multiple locations

At the Ten-mile landslide, movements have continued despite multiple mitigation measures and structures built in the last two decades to mitigate the highway and railway infrastructure damages. The analysis presented in Chapter 5 (Manuscript #3) assess the effect of matric suction in the Ten-mile failure mechanism based on deformation monitoring at multiple locations and stability analysis. An analysis of the measurements from the Geocube network provided insight into the kinematic characteristics of the sliding mass. The methodology for a detailed characterization of the Ten-mile movement using multiple monitoring points allowed clustering areas of movement and identify the movement sequence. 3D limit equilibrium methods allowed to investigate the average matric suction at the shear surface to achieve a meta-stable condition (i.e., a safety factor of one) based on the successive movement of the clusters.

Displacement and displacement rates measurement based on the dGNSS units vary across the landslides. These variances occurred from the fluctuation of the displacement rates during the monitoring campaign. Correlation analyses of these fluctuations allowed for the identification of dGNSS units that moved together or in sequence. The correlation results exposed a translational movement divided into five clusters that moved from the north side up to the crest of the landslide (Figure 5-10, Appendix F). The use of the Geocube network provided a detailed description of the translational movement of the Ten-mile.

The kinematic analysis of the sliding mass at the Ten-mile allowed the back analysis required to estimate the magnitude of matric suction for a meta-stable condition. The results showed matric suction values above 80 kPa were required. The laboratory testing of the VWC and SWCC from earthflow samples supported these results. The earthflow required having a VWC of less than 28% for a shear strength that maintains meta-stable conditions. The results presented in Chapter 5 supports the hypothesis that changes in matric suction at the sliding surface have an influence in the meta stable condition of the Ten-mile that would results in changes in the displacements rates. The susceptibility of the sliding surface to increase saturation from infiltration or other source results in the loss of matric suction and the shear strength, translating into movement.

## 6.2 IMPLICATIONS OF THE STUDY

In relation to the first objective, this research allowed to quantify and validate the benefits of low-cost monitoring instrumentation in terms of accuracy, precision, and limitations to assess complex failure mechanisms in ground hazards next to transportation corridors. The application of low-cost UAV and GNSS receivers provided detailed information to assess the failure mechanisms in three active landslides next to transportation corridors. This was achieved with instruments with a lower cost (less than $4500.oo per unit) than other alternative instruments with similar advantages and limitations to measure surface deformation.

The C018 site analysis demonstrated the advantages of using a low-cost UAV as a remote sensing technique to inspect landslides next to transportation corridors. The application of low-cost UAV proved to be a quick and safe tool for collecting information on unstable slopes susceptible to weather changes, difficult access, and limited resources. Risk management programs that deal with multiple presence ground hazards next to transportation corridors can use low-cost UAV during inspections to create historical registries and characterize the slope failure through the methods presented in Chapter 3 (Manuscript #1). The analysis presents a methodology that can be extrapolated to other unstable slopes to identify critical areas, magnitudes of unstable events, evaluate trigger factors, and perform stability analyses.

In this research a new methodology for the implementation of single-frequency dGNSS receivers, called Geocube, was develop to monitor landslide movements. The methodology was introduced for the first time into to the Canadian industry through the application in two case studies impacting

transportation corridors in Western Canada. The Geocube instrument show the advantages of in-placed monitoring instruments that are low cost. Instrumenting the Ten-mile and Chin Coulee landslides using single-frequency dGNSS receivers allowed assessing the effectiveness and limitations to monitor surficial deformation (Chapter 4, Manuscript #2). The results demonstrated that the recorded data from the dGNSS receivers could achieve similar precision to the multi-frequency Leica GNSS while reducing the instrument's cost. The low-cost of dGNSS receivers with high precision allow having access to more monitoring points. Multiple monitoring points at each site allowed provide a methodology to identify variances of movement across the landslides and assessing causal factors in the movements. Low-cost technologies allow geotechnical engineers to strengthen landslide monitoring, leading to factual decision processes focused on mitigating possible risks.

In relation to the second objective, this research allowed to test the benefits of instrumenting multiple locations at the Ten-mile landslide to enhance the knowledge on the failure mechanism and provide a workflow that allows examining other unstable slopes. A new statistical methodology in Chapter 5 (Manuscript #3) is proposed to discretize the movement areas of a landslide in clusters and determine the sequence of movement between clusters. The analysis using the network of dGNSS receivers provided adequate spatial and temporal resolution data to enhance the characterization of the translational movement at the Ten-mile.

The advances in 3D LEM allowed developing a methodology that correlates the factor of safety associated to the displacement of different clusters of movement. At the Ten-mile this methodology was incorporated to evaluate the magnitude of matric suction at the shear surface to maintain a meta stable conditions on five clusters of movement. In addition, the Ten-mile analysis helps to understand the relation between the stability and the water within the earthflow. This relation provides the information to stakeholders to define hazard level criteria based on weather factors and the successive movement of different zones in the landslides.

## 6.3 FUTURE RESEARCH

The research presented in this thesis provided detail understanding in the benefits and methodologies of applying specific monitoring technologies. The thesis also shows the implication of having low-cost monitoring technology with precise spatial and temporal resolution to assess

complex failure mechanisms of landslides sensitive to changes in weathers for transportation corridors. The following task are recommended to continue investigation the potential application of these technologies and the study sites:

- The analysis of C018 site gave an indication of the relationship of runoff water and the active zones. However, obtaining more conclusive evidence of the relation of water as a causal factor would require to investigate the role of water infiltration and evaporation. Future research could investigate the seepage process from precipitation and the irrigation effect from farming above the slope.

- High moisture was identified during the inspection on the different materials of the C018 site following rainfall events. However, the inclination and heigh of the slope limited the access to evaluate variances in moisture at different elevations. Future research could take advantage of developing UAV technology with thermal cameras to monitor moisture zone on landslides exhibiting surficial weathering.

- The susceptibility to high erosion processes from rainfall events of slopes next to transportation corridors has resulted in initiation or propagation of ground hazards. The study presented of the C018 site shows the erosion processes varying along the slope, initiation different magnitude events and different location. An initial analysis of the drainage network showed the variances in eroded channels impacted the distribution of runoff water in the slope. Future research should be focussed on analysing continuous weathering on highly erodible slopes, such as C018 site, as a causal factor for initiating landslides. The analysis could implement numerical simulation, using software that models erosion and the geomorphological evolution of the ground surface to forecast future instabilities.

- Single-frequency GNSS receivers have shown to be effective for monitoring slow-moving landslide during different season and limited signal areas. However, the application of the system should explore the potential application on different types of failure mechanisms. Future research could focus on installing a network of GNSS receivers on different types of geohazards or earth structures, such as checkerboard rockslide failure in Revelstoke, BC or on a mining embankment.

- The data recorded from the single-frequency GNSS receivers have shown to have the potential for developing a warning system based on measurements at multiple locations. However, the investigation of presented on this thesis did not present an actual use of this system to provide early warning from displacements. Future research should explore the implementation of single-frequency GNSS receivers as an early warning system for transportation corridors, as described in Appendix I.

- The use of surficial deformation data at multiple locations has provided detail on the shape of the shear surface from interpreting the direction of movement. However, interpreting the inclination of the shear surface from surficial deformation does not replace the use of SIs or SAAs. Landslides exhibiting complex failure mechanism and triggered by weather changes could have different impact with depth. Future research of active landslides impacted by precipitation can explore the effect of infiltration in the differences of surficial deformation measures and deformation measures at the shear zone to characterize complex failure mechanism.

- The detailed data at the Ten-mile of surface deformation, material testing, and analysis presented in this research provides an opportunity to implement other advanced numerical analyses, such as finite element methods, to better replicate the mechanisms and observed kinematics.

# BIBLIOGRAPHY


Agüera-Vega F, Carvajal-Ramírez F, Martínez-Carricondo P, et al (2018) Reconstruction of extreme topography from UAV structure from motion photogrammetry. Meas J Int Meas Confed 121:127–138. doi: 10.1016/j.measurement.2018.02.062

Al-Homoud AS, Taqieddin S, Saket S (1995) Investigation on the geological and geotechnical factors leading to a major slope failure at a selected site on a Jordanian highway. Nat Hazards 12:203–224. doi: https://doi-org.login.ezproxy.library.ualberta.ca/10.1007/BF00596221

Al-Rawabdeh A, Moussa A, Foroutan M, et al (2017) Time series UAV image-based point clouds for landslide progression evaluation applications. Sensors (Switzerland) 17:. doi: 10.3390/s17102378

Alberta Transportation (2017) Traffic Counts Reference No. 106230 2016. http://www.transportation.alberta.ca/mapping/. Accessed 17 Oct 2018

Allan JA (1921) Geology of Drumheller Coal Field , Alberta. J.W. Jeffery, Kings's Printer, Edmonton

Allasia P, Baldo M, Giordan D, et al (2019) Near Real Time Monitoring Systems and Periodic Surveys Using a Multi Sensors UAV: The Case of Ponzano Landslide. IAEG/AEG Annu Meet Proceedings, San Fr California, 2018 - Vol 1 1:303–310. doi: 10.1007/978-3-319-93124-1_37

AMEC Foster Wheeler (2015) Southern Region Geohazard Assessment 2015 Annual Inspection Report Site S5: Highway 36:02, Chin Coulee. Calgary, Alberta

American Association of State Highway and Transportation (2018) AASHTO Guide for Enterprise Risk Management. American Association of State Highway and Transportation Officials

Ansari MK, Ahmed M, Rajesh Singh TN, Ghalayani I (2015) Rainfall, A Major Cause for Rockfall Hazard along the Roadways, Highways and Railways on Hilly Terrains in India. In: Engineering Geology for Society and Territory - Volume 1. Springer International Publishing, Cham, pp 457–460

Ansour MF, Morgenstern NR, Martin CD (2011) Expected damage from displacement of slow-moving slides. Landslides 8:117–131. doi: https://doi.org/10.1007/s10346-010-0227-7

ASTM International (2011) ASTM D3080 / D3080M-11, Standard Test Method for Direct Shear Test of Soils Under Consolidated Drained Conditions

Bednarik M, Magulová B, Matys M, Marschalko M (2010) Landslide susceptibility assessment of the Kraľovany-Liptovský Mikuláš railway case study. Phys Chem Earth 35:162–171. doi: 10.1016/j.pce.2009.12.002

Benoit L, Briole P, Martin O, et al (2015a) Monitoring landslide displacements with the Geocube wireless network of low-cost GPS. Eng Geol 195:111–121

Benoit L, Briole P, Martin O, Thom C (2014) Real-time deformation monitoring by a wireless network of low-cost GPS. J Appl Geod 8:119–128. doi: 10.1515/jag-2013-0023

Benoit L, Dehecq A, Pham HT, et al (2015b) Multi-method monitoring of Glacier d'Argentière dynamics. Ann Glaciol 56:118–128. doi: 10.3189/2015AoG70A985

Beregovoi D V., Younes JA, Mustafin MG (2017) Monitoring of Quarry Slope Deformations with the Use of Satellite Positioning Technology and Unmanned Aerial Vehicles. Procedia Eng 189:737–743. doi: 10.1016/j.proeng.2017.05.116

BGC Engineering Inc. (2016a) Ten mile slide 2016 site investigation data report. Victoria, British Columbia

BGC Engineering Inc. (2016b) CN Lillooet Sub. M. 167.7 (Ten Mile Slide) April 2016 Drilling and Instrumentation. Kamloops, British Columbia

BGC Engineering Inc. (2019) Ten Mile Slide Monitoring Update – January 10, 2019. Victoria, British Columbia

BGC Engineering Inc. (2015) CN Lillooet Sub. M. 167.7 (Fountain Slide) September 2015 Drilling and Instrumentation. Kamloops, British Columbia

Borneuf D (1972) Hydrogeology of the Drumheller Area, Alberta, Report 72-1. Edmonton

Bovis MJ (1985) Earthflows in the Interior Plateau, southwest British Columbia. Can Geotech J 22:313–334

Bunce CM (2008) Risk estimation for railways exposed to landslides. University of Alberta

Cao L, Wang Z, Chen Y (2016) Unsaturated Seepage Analysis of Cracked Soil including Development Process of Cracks. Adv Mater Sci Eng 2016:. doi: 10.1155/2016/2684297

Carlà T, Farina P, Intrieri E, et al (2017a) On the monitoring and early-warning of brittle slope failures in hard rock masses: Examples from an open-pit mine. Eng Geol 228:71–81. doi: 10.1016/j.enggeo.2017.08.007

Carlà T, Macciotta R, Hendry MT, et al (2017b) Displacement of a landslide retaining wall and application of an enhanced failure forecasting approach. Landslides 15:489–505. doi: 10.1007/s10346-017-0887-7

Clague JJ, Evans SG (2003) Geologic Framework of Large Historic Landslides in Thompson River Valley, British Columbia. Environ Eng Geosci 9:201–212. doi: 10.2113/9.3.201

Crosta GB, Agliardi F (2003) Failure Forecast for Large Rock Slides by Surface Displacement Measurements. Can Geotech J 40:176–191. doi: 10.1139/t02-085

Cruden D, VanDine DF (2013) Classification, Description, Causes and Indirect Effects - Canadian Technical Guidelines and Best Practices Related to Landslides: A National Initiative For Loss Reduction

Cruden DM, Lu ZY (1992) The rockslide and debris flow from Mount Cayley, BC, in June 1984. Can Geotech J 29:614–626. doi: 10.1139/t92-069

Cucchiaro S, Cavalli M, Vericat D, et al (2018) Monitoring topographic changes through 4D-structure-from-motion photogrammetry: application to a debris-flow channel. Environ Earth Sci 77:1–21. doi: 10.1007/s12665-018-7817-4

Deane E (2019) The Application of Emerging Monitoring Technologies on Very Slow Vegetated Landslides by. University of Alberta

Deane E, Macciotta R, Hendry MT, et al (2020) Leveraging historical aerial photographs and digital photogrammetry techniques for landslide investigation—a practical perspective.

Landslides. doi: 10.1007/s10346-020-01437-z

Dick GJ, Eberhardt E, Cabrejo-Liévano AG, et al (2015) Development of an early-warning time-of-failure analysis methodology for open-pit mine slopes utilizing ground-based slope stability radar monitoring data. Can Geotech J 52:515–529. doi: 10.1139/cgj-2014-0028

Doberstein D (2012) Fundamentals of GPS Receivers. Springer, Nipomo, CA, USA

Donati D, Stead D, Lato M, Gaib S (2020) Spatio-temporal characterization of slope damage: insights from the Ten Mile Slide, British Columbia, Canada. Landslides. doi: 10.1007/s10346-020-01352-3

DroneDeploy Inc. f.k.a. Infatics Inc. (2020) Drone Deploy

Environmental Systems Research Institute Inc. (2016) ArcGIS Desktop [Software]

Eshraghian A (2007) Hazard Analysis of Reactivated Earth Slides in the Thompson River Valley, Ashcroft, British Columbia. University of Alberta

Eshraghian A, Martin CD, Morgenstern NR (2008) Hazard analysis of an active slide in the Thompson River Valley, Ashcroft, British Columbia, Canada. Can Geotech J 45:297–313. doi: 10.1139/T07-085

Eshraghian A, Martin CD, Morgenstern NR (2007) A Review of Pore-Pressure-Induced Reactivation of Translational Earth. In: 60th Canadian Geotechnical Conference. Ottawa, pp 2245–2251

Esposito G, Salvini R, Matano F, et al (2017) Multitemporal monitoring of a coastal landslide through SfM-derived point cloud comparison. Photogramm Rec 32:459–479. doi: 10.1111/phor.12218

Fan X, Xu Q, Scaringi G, et al (2017) Failure mechanism and kinematics of the deadly June 24th 2017 Xinmo landslide, Maoxian, Sichuan, China. Landslides 14:2129–2146. doi: 10.1007/s10346-017-0907-7

Fell R, Ho KKS, Lacasse S, Leroi E (2005) State of the Art Paper 1 A framework for landslide risk assessment and management. 23

Fey C, Wichmann V (2017) Long-range terrestrial laser scanning for geomorphological change detection in alpine terrain – handling uncertainties. Earth Surf Process Landforms 42:789–802. doi: 10.1002/esp.4022

Fredlund DG, Morgenstern NR, Widger RA (1978) The shear strength of unsaturated soils. Can Geotech J 15:313–321

Fredlund DG, Rahardjo H, Fredlund MD (2012) Unsaturated Soil Mechanics in Engineering Practice, 2nd edn. John Wiley & Sons, Inc., Hoboken, NJ, USA

Fredlund DG, Xing A (1994) Equations for the Soil-water Characteristic Curve. Can Geotech J 31:521–532

Friele P a, Clague JJ (2004) Large Holocene Landslides from Pylon Peak, Southwestern British Columbia. Can J Earth Sci 41:165–182. doi: 10.1139/e03-089

Furukawa Y, Ponce J (2009) Accurate Camera Calibration from Multi-View Stereo and Bundle Adjustment - Furukawa, Team - Unknown.pdf. Int J Comput Vis 84:257– 268

Gaib S, Wilson B, Lapointe E (2012) Design, Construction and Monitoring of a Test Section for the stabilization of an Active Slide Area Utilizing Soil Mixed Shear Keys Installed Using Cutter Soil Mixing. In: ISSMGE - TC 211 International Symposium on Ground Improvement IS-GI. Brussels

Galve JP, Cevasco A, Brandolini P, et al (2016) Cost-based Analysis of Mitigation Measures for Shallow-Landslide Risk Reduction Strategies. Eng Geol 213:142–157. doi: 10.1016/j.enggeo.2016.09.002

Giani GP (1992) Rock Slope Stability Analysis. Rotterdam: A.A. Balkema

Girardeau-Montaut D, Roux M, Marc R, Thibault G (2005) Change Detection on Points Cloud Data Acquired with a Ground Laser Scanner. In: Vosselman G, Brenner C (eds) International Society for Photogrammetry and Remote Sensing (ISPRS) Workshop Laser scanning 2005. Enschede, Netherlands, pp 30–35

Golder and Associates (1998) Geotechnical Investigation – Site S5: Highway 36:02 – November 1998 Report Geotechnical Risk Management Plan

Government of Canada (2018) Historical Weather Data from Drumheller. http://climate.weather.gc.ca/. Accessed 20 Aug 2018

Guthrie RH, Nicksiar M (2016) Time to Failure – Practical Improvements of an Analytical Tool. GeoVancouver - 69th Can Geotech Conf CD-Rom. doi: 10.1037/13755-000

Handwerger AL, Roering JJ, Schmidt DA, Rempel AW (2015) Kinematics of earthflows in the Northern California Coast Ranges using satellite interferometry. Geomorphology 246:321–333. doi: 10.1016/j.geomorph.2015.06.003

Hendry MT, Chalcroft D, Zaidi H, Iqbal MJ (2019) Instrumentation Data Review and Long-Term Trends of Displacement at the Oldman River Dam: A Case Study. In: Proceedings Canadian Dam Association Annual Conference,. Calgary, Alberta

Hendry MT, Macciotta R, Martin CD, Reich B (2015) Effect of Thompson River elevation on velocity and instability of Ripley Slide. Can Geotech J 52:257–267. doi: 10.1139/cgj-2013-0364

Highland LM, Bobrowsky P (2008) The Landslide Handbook — A Guide to Understanding Landslides, Circular 1. U.S. Geological Survey, Reston, Virginia

Hoek E (2018) Unpublished notes. In: Rocscience. https://www.rocscience.com/help/rocfall/baggage/rn_rt_table.htm. Accessed 27 May 2018

Horton JH, Hawkins RH (1965) Flow Path of Rain From The Soil Surface To The Water Table. Soil Sci 100:377–383

Hsu CH, Tsao TC, Huang CM, et al (2016) Using Remote Sensing Techniques to Identify the Landslide Hazard Prone Sections along the South Link Railway in Taiwan. Procedia Eng 143:708–716. doi: 10.1016/j.proeng.2016.06.107

Huang H, Song K, Yi W, et al (2018) Use of multi-source remote sensing images to describe the sudden Shanshucao landslide in the Three Gorges Reservoir, China. Bull Eng Geol Environ 1–20. doi: 10.1007/s10064-018-1261-2

Hunter E, Hendry MT, Cruden D (2016) Effects of Extreme Rainfall on Geotechnical Hazards in

the Canadian Rocky Mountains. In: Proceedings of the 17th Nordic Geotechnical Meeting Challenges in Nordic Geotechnic. Reykjavik, pp 1163–1172

Huntley D, Bobrowsky P, Hendry MT, et al (2019) Multi-technique Geophysical Investigation of a Very Slow-moving Landslide near Ashcroft, British Columbia, Canada. J Environ Eng Geophys 24:87–110. doi: 10.2113/JEEG24.1.87

Huntley DH, Bobrowsky PT (2014) Surficial geology and monitoring of the Ripley Slide, near Ashcroft, British Columbia, Canada

Intrieri E, Carlà T, Gigli G (2019) Forecasting the time of failure of landslides at slope-scale: A literature review. Earth-Science Rev 193:333–349. doi: 10.1016/j.earscirev.2019.03.019

Intrieri E, Gigli G, Mugnai F, et al (2012) Design and implementation of a landslide early warning system. Eng Geol 147–148:124–136. doi: 10.1016/j.enggeo.2012.07.017

Jaiswal P, van Westen CJ (2013) Use of Quantitative Landslide Hazard and Risk Information for Local Disaster Risk Reduction Along a Transportation Corridor: A Case Study from Nilgiri District, India. Nat Hazards 65:887–913. doi: 10.1007/s11069-012-0404-1

Jakob M, Friele P (2010) Frequency and magnitude of debris flows on Cheekye River, British Columbia. Geomorphology 114:382–395. doi: 10.1016/j.geomorph.2009.08.013

Jared M., Dupuis ST., Goguen P., Parsons R. (2018) Development of a Geotechnical Asset Management Program for the New Brunswick of Transportation and Infrastructure. In: 2018 Annual Conference of the Transportation Association of Canada. Saskatoon, SK

JCL Consulting (2006) Highway 99 , Fountain Slide Value Analysis Report. Kamloops, British Columbia

Jenson SK, Domingue JO (1988) Extracting Topographic Structure from Digital Elevation Data for Geographic Information System Analysis. Photogramm Eng Remote Sensing 54:1593–1600. doi: 0099-1112/88/5411-1593

Journault J, Macciotta R, Hendry MT, et al (2016) Identification and Quantification of Concentrate Movement Zones within the Thompson River Valley using Satellite InSAR. Proc 2016 11th Int Pipeline Conf

Keegan TR (2007) Methodology for Risk Analysis of Railway Ground Hazards. UNIVERSITY OF ALBERTA

Kintner PM, Ledvina BM, De Paula ER (2007) GPS and Ionospheric Scintillations. Sp Weather 5:1–23. doi: 10.1029/2006SW000260

Klohn Crippen Berger (2018a) CON0017608 Central Region GRMP – Call-Out Report C018 Hwy 837:02 Call-Out Report Revision 1 July 13, 2018. Red Deer

Klohn Crippen Berger (2000) Central Region Landslide Assessment SH837:02 River Scour @ km 1.9 Emergency Geotechnical Inspection Report, July 25, 2000

Klohn Crippen Berger (2018b) CON0017608 Central Region GRMP – Call-Out Report C018 Hwy 837:02 Call-Out Report January 19, 2018. Red Deer

Klose M (2015) Landslide Databases as Tools for Integrated Assessment of Landslide Risk. Springer International Publishing, Cham

Kromer R, Lato M, Hutchinson DJ, et al (2017a) Managing rockfall risk through baseline monitoring of precursors using a terrestrial laser scanner. Can Geotech J 54:953–967. doi: 10.1139/cgj-2016-0178

Kromer RA, Abellán A, Hutchinson DJ, et al (2017b) Automated terrestrial laser scanning with near-real-time change detection - Monitoring of the Séchilienne landslide. Earth Surf Dyn 5:293–310. doi: 10.5194/esurf-5-293-2017

Kromer RA, Abellán A, Hutchinson DJ, et al (2015a) A 4D filtering and calibration technique for small-scale point cloud change detection with a terrestrial laser scanner. Remote Sens 7:13029–13058. doi: 10.3390/rs71013029

Kromer RA, Hutchinson DJ, Lato MJ, et al (2015b) Identifying rock slope failure precursors using LiDAR for transportation corridor hazard management. Eng Geol 195:93–103. doi: 10.1016/j.enggeo.2015.05.012

Küng O, Strecha C, Beyeler A, et al (2012a) The Accuracy of Automatic Photogrammetric Techniques on Ultra-Light Uav Imagery. ISPRS - Int Arch Photogramm Remote Sens Spat Inf Sci XXXVIII-1/:125–130. doi: 10.5194/isprsarchives-XXXVIII-1-C22-125-2011

Küng O, Strecha C, Fua P, et al (2012b) Simplified Building Models Extraction From Ultra-Light Uav Imagery. ISPRS - Int Arch Photogramm Remote Sens Spat Inf Sci XXXVIII-1/:217–222. doi: 10.5194/isprsarchives-XXXVIII-1-C22-217-2011

Lacasse S (2016) Hazard, Reliability and Risk Assessment -Research and Practice for Increased Safety. NGM 2016 Reykjavik Proc 17th Nord Geotech Meet Challenges Nord Geotech 25th – 28th May 18–42

Lacasse S, Eidsvig U, Nadim F, et al (2008) Event Tree Analysis of Åknes Rock Slide Hazard. In: Geohazards 4. Quebec

Lacasse S, Nadim F (2009) Landslide Risk Assessment and Mitigation Strategy. Landslides – Disaster Risk Reduct 31–61. doi: 10.1007/978-3-540-69970-5_3

Lague D, Brodu N, Leroux J (2013) Accurate 3D comparison of complex topography with terrestrial laser scanner: Application to the Rangitikei canyon (N-Z). ISPRS J Photogramm Remote Sens 82:10–26. doi: 10.1016/j.isprsjprs.2013.04.009

Laimer HJ (2017) Anthropogenically Induced Landslides – A challenge for Railway Infrastructure in Mountainous Regions. Eng Geol 222:92–101. doi: 10.1016/j.enggeo.2017.03.015

Lan H, Derek Martin C, Lim CH (2007) RockFall analyst: A GIS extension for three-dimensional and spatially distributed rockfall hazard modeling. Comput Geosci 33:262–279. doi: 10.1016/j.cageo.2006.05.013

Lan H, Martin CD, Zhou C, Lim CH (2010) Rockfall hazard analysis using LiDAR and spatial modeling. Geomorphology 118:213–223. doi: 10.1016/j.geomorph.2010.01.002

Lato M, Porter M, Henshold G, et al (2016) Understanding Landslide Movement and Kinematics with Airborne Lidar. Proc 69th Can Geotech Soc Conf GeoVancouver 2016. doi: 10.1007/s12013-010-9150-8

LGPL (2011) CloudCompare [GNU GPL software]

Macciotta R (2013) Quantitative Risk Assessment of Natural and Cut Slopes: Measuring

Uncertainty in the Estimated Risks and Proposed Framework for Developing Risk Evaluation Criteria. University of Alberta

Macciotta R, Edwards T, Hendry MT, et al (2015) Weather-based rockfall hazard criteria along a railway corridor in the Canadian Cordillera. Proc 2015 Int Heavy Haul Assoc Conf

Macciotta R, Gräpel C, Keegan T, et al (2020) Quantitative risk assessment of rock slope instabilities that threaten a highway near Canmore, Alberta, Canada: Managing risk calculation uncertainty in practice. Can Geotech J 57:337–353. doi: 10.1139/cgj-2018-0739

Macciotta R, Hendry MT, Cruden DM, et al (2017a) Quantifying rock fall probabilities and their temporal distribution associated with weather seasonality. Landslides 14:2025–2039. doi: 10.1007/s10346-017-0834-7

Macciotta R, Hendry MT, Martin CD (2016a) Developing an early warning system for a very slow landslide based on displacement monitoring. Nat Hazards 81:887–907. doi: 10.1007/s11069-015-2110-2

Macciotta R, Hendry MT, Martin CD, et al (2014) Monitoring of the Ripley Landslide in the Thompson River Valley , B . C . Geohazards 6 8. doi: 10.13140/2.1.2811.7125

Macciotta R, Hendry MT, Roghani A (2016b) Developing Hazard Management Strategies based on Tolerable Risk to Railway Operations. 1–16. doi: 10.4203/ccp.110.282

Macciotta R, Martin CD (2019) Preliminary approach for prioritizing resource allocation for rock fall hazard investigations based on susceptibility mapping and efficient three-dimensional trajectory modelling. Bull Eng Geol Environ 78:2803–2815. doi: 10.1007/s10064-018-1279-5

Macciotta R, Rodriguez J, Hendry MT, et al (2017b) The 10-mile Slide North of Lillooet , British Columbia – History , Characteristics and Monitoring. In: 3rd North American Symposium on Landslides. Roanoke, Virginia

Marinos PG, Hoek E (2000) GSI: A geologically friendly tool for rock mass strength estimation. In: Proc. GeoEng2000 Conference. pp 1422–1442

Martínez-Carricondo P, Agüera-Vega F, Carvajal-Ramírez F, et al (2018) Assessment of UAV-photogrammetric mapping accuracy based on variation of ground control points. Int J Appl Earth Obs Geoinf 72:1–10. doi: 10.1016/j.jag.2018.05.015

Mazzanti P, Bozzano F, Brunetti A, et al (2017) Experimental Landslide Monitoring Site of Poggio Baldi Landslide (Santa Sofia, N-Apennine, Italy). In: Advancing Culture of Living with Landslides. Springer International Publishing, Ljubljana, Slovenia, pp 259–266

Mesri G, Huvaj-Sarihan N (2012) Residual Shear Strength Measured by Laboratory Tests and Mobilized in Landslides. J Geotech Geoenvironmental Eng 138:585–593. doi: 10.1061/(ASCE)GT.1943-5606.0000624

METER Group AG (2018) HYPROP User Manual

Michael-Leiba M, Baynes F, Scott G, Granger K (2003) Regional Landslide Risk to the Cairns Community. Nat Hazards 30:233–249. doi: 10.1023/A:1026122518661

Miller S, Zhang X, Spanias A (2015) Multipath effects in GPS receivers

Morgenstern NR (1995) Managing Risk in Geotechnical Engineering. In: The 3rd Casagrande

Lecture. Proceedings 10th Pan-American Conference on Soil Mechanics and Founda- tion Engineering. Guadalajara, Mexico, pp 102–126

Mualem Y (1976) A new model for predicting the hydraulic conductivity of unsaturated porous media. Water Resour Res 12:513–522. doi: 10.1029/WR012i003p00513

Novák V, Šimůnek J, Van Genuchten MT (2000) Infiltration of water into soil with cracks. J Irrig Drain Eng 126:41–47. doi: 10.1061/(ASCE)0733-9437(2000)126:1(41)

Odolinski R, Teunissen PJG (2017) Low-cost, high-precision, single-frequency GPS–BDS RTK positioning. GPS Solut 21:1315–1330. doi: 10.1007/s10291-017-0613-x

Ophelia Sensors (2019) Geocube Applications. https://ophelia-sensors.com/applications. Accessed 26 Aug 2019

Otto A, Kellermann P, Thieken AH, et al (2019) Risk Reduction Partnerships in Railway Transport Infrastructure in an Alpine Environment. Int J Disaster Risk Reduct 33:385–397. doi: 10.1016/j.ijdrr.2018.10.025

Pecoraro G, Calvello M, Piciullo L (2018) Monitoring strategies for local landslide early warning systems. Landslides. doi: 10.1007/s10346-018-1068-z

Pertassek T, Peters A, Durner W (2011) HYPROP Data Evaluation Software User's Manual. 1–47

Petschko H, Bell R, Glade T (2016) Effectiveness of visually analyzing LiDAR DTM derivatives for earth and debris slide inventory mapping for statistical susceptibility modeling. Landslides 13:857–872. doi: 10.1007/s10346-015-0622-1

Pfeiffer TJ, Bowen TD (1989) Computer Simulation of Rockfalls. Environ Eng Geosci xxvi:135–146. doi: 10.2113/gseegeosci.xxvi.1.135

Pix4D S.A. (2018a) Pix4DCapture

Pix4D S.A. (2018b) Pix4Dmapper Pro

Porter M, Morgenstern NR (2013) Landslide Risk Evaluation Canadian technical guidelines and best practices related to landslides: A national initiative for loss reduction

Porter MJ, Savigny KW, Keegan TR, et al (2001) Controls on stability of the Thompson River landslides. 55th Can Geotech Conf 1393–1400

Pratt C, Macciotta R, Hendry MT (2019) Quantitative relationship between weather seasonality and rock fall occurrences north of Hope, BC, Canada. Bull Eng Geol Environ 78:3239–3251. doi: 10.1007/s10064-018-1358-7

Prior GJ, Hathway B, Glombick PM, et al (2013) Bedrock Geology of Alberta, AER/AGS Map 600, scale 1:1,000,000. To accompany AGS Open File Report 2013-02.

Richards LA (1931) Capillary conduction of liquids through porous mediums. J Appl Phys 1:318–333. doi: 10.1063/1.1745010

Riquelme A, Cano M, Tomás R, Abellán A (2017) Identification of Rock Slope Discontinuity Sets from Laser Scanner and Photogrammetric Point Clouds: A Comparative Analysis. Procedia Eng 191:838–845. doi: 10.1016/j.proeng.2017.05.251

Róbert J, Hervás J, Maureen W (2007) Risk Mapping of Flood Hazards in New Member States.

Luxembourg

Rocscience Inc. (2018) Rocfall

Rodriguez J, Hendry MT (2018) Cost-effective Landslide Monitoring GPS System : Characteristics, Implementation and Results. In: Geohazards7. Canmore, Alberta

Rodriguez J, Macciotta R, Hendry MT, et al (2017) Slope hazards and risk engineering in the Canadian railway network through the Cordillera. In: Transport Infrastructure and Systems: Proceedings of the AIIT International Congress on Transport Infrastructure and Systems. CRC Press /Balkema, Rome, pp 163–168

Rodriguez J, Macciotta R, Hendry MT, et al (2020) UAVs for monitoring, investigation, and mitigation design of a rock slope with multiple failure mechanisms—a case study. Landslides. doi: 10.1007/s10346-020-01416-4

Romero-Andrade R, Zamora-Maciel A, Uriarte-Adrián J de J, et al (2019) Comparative analysis of precise point positioning processing technique with GPS low-cost in different technologies with academic software. Meas J Int Meas Confed 136:337–344. doi: 10.1016/j.measurement.2018.12.100

Roque D, Perissin D, Falcão AP, et al (2018) Analysis of InSAR displacements for the slopes around Odelouca reservoir. Procedia Comput Sci 138:338–345. doi: 10.1016/j.procs.2018.10.048

Rose ND, Hungr O (2007) Forecasting potential rock slope failure in open pit mines using the inverse-velocity method. Int J Rock Mech Min Sci 44:308–320. doi: 10.1016/j.ijrmms.2006.07.014

Salvini R, Francioni M, Riccucci S, et al (2013) Photogrammetry and laser scanning for analyzing slope stability and rock fall runout along the Domodossola-Iselle railway, the Italian Alps. Geomorphology 185:110–122. doi: 10.1016/j.geomorph.2012.12.020

Sattler K., Elwood D., Hendry MT., et al (2018) Real-time Monitoring of Soil Water Content and Suction within a Slow Moving Landslide. In: Geoedmonton 2018. Edmonton, Alberta

Schafer M, Macciotta R, Hendry MT, et al (2015) Instrumenting and Monitoring a Slow Moving Landslide. 68th Can Geotech Conf

Schulz WH, McKenna JP, Kibler JD, Biavati G (2009) Relations between hydrology and velocity of a continuously moving landslide-evidence of pore-pressure feedback regulating landslide motion? Landslides 6:181–190. doi: 10.1007/s10346-009-0157-4

Shi R (2006) A Methodology for Evaluating Rainfall-induced Railway Ground Hazards Encountered at Port Douglas , June 1998. University of Alberta

Skempton AW (1985) Residual strength of clays in landslides, folded strata and the laboratory. Geotechnique 35:3–18. doi: 10.1680/geot.1985.35.1.3

Smethurst JA, Smith A, Uhlemann S, et al (2017) Current and future role of instrumentation and monitoring in the performance of transport infrastructure slopes. Q J Eng Geol Hydrogeol 50:271–286. doi: 10.1144/qjegh2016-080

Solazzo D, Sankey JB, Sankey TT, Munson SM (2018) Mapping and measuring aeolian sand dunes with photogrammetry and LiDAR from unmanned aerial vehicles (UAV) and

multispectral satellite imagery on the Paria Plateau, AZ, USA. Geomorphology 319:174–185. doi: 10.1016/j.geomorph.2018.07.023

Sousa JJ, Ruiz AM, Bakoň M, et al (2016) Potential of C-Band SAR Interferometry for Dam Monitoring. Procedia Comput Sci 100:1103–1114. doi: 10.1016/j.procs.2016.09.258

Stalker AM (1973) Memoir 370 Surficial Geology of the Drumheller area, Alberta. Ottawa

Stark TD, Eid HT (1994) Drained Residual Strength of Cohesive Soils. J Geotech Geoenvironmental Eng 120:856–871

Tappenden KM, Skirrow RK (2020) Vision for Geotechnical Asset Management at Alberta Transportation. In: GeoVirtual 2020. Edmonton, Alberta

Tarboton DG, Bras RL, Rodriguez-Iturbe I (1991) Tarboton_et_al-1991-Hydrological_Processes. Hydrol Process 5:81–100. doi: 10.1002/hyp.3360050107

The SoilVision Systems Ltd. Team (2019) SvSlope Theory Manual

Transport Canada (2018) Transportation in Canada Overview Repor

Transport Canada (2012) Transportation in Canada, Comprehensive Review. Canada

Transportation Safety Board of Canada (2009) RAILWAY INVESTIGATION REPORT R09V0235

Vallet J, Panissod F, Strecha C, Tracol M (2011) PHOTOGRAMMETRIC PERFORMANCE OF AN ULTRA LIGHT WEIGHT SWINGLET "UAV." Int Arch Photogramm Remote Sens Spat Inf Sci. doi: 10.5194/isprsarchives-XXXVIII-1-C22-253-2011

van Veen M, Hutchinson DJ, Kromer R, et al (2017) Effects of Sampling Interval on the Frequency - Magnitude Relationship of Rockfalls Detected from Terrestrial Laser Scanning Using Semi-automated Methods. Landslides 14:1579–1592. doi: 10.1007/s10346-017-0801-3

Vanneschi C, Eyre M, Francioni M, Coggan J (2017) The Use of Remote Sensing Techniques for Monitoring and Characterization of Slope Instability. Procedia Eng 191:150–157. doi: 10.1016/j.proeng.2017.05.166

Vautherin J, Rutishauser S, Schneider-Zapp K, et al (2016) Photogrammetric Accuracy and Modeling of Rolling Shutter Cameras. ISPRS Ann Photogramm Remote Sens Spat Inf Sci III–3:139–146. doi: 10.5194/isprsannals-III-3-139-2016

Vaziri A, Moore L, Ali H (2010) Monitoring systems for warning impending failures in slopes and open pit mines. Nat Hazards 55:501–512. doi: 10.1007/s11069-010-9542-5

Voumard J, Derron MH, Jaboyedoff M (2018) Natural Hazard Events Affecting Transportation Networks in Switzerland from 2012 to 2016. Nat Hazards Earth Syst Sci 18:2093–2109. doi: 10.5194/nhess-18-2093-2018

Westoby MJJ, Brasington J, Glasser NFF, et al (2012) "Structure-from-Motion" photogrammetry: A low-cost, effective tool for geoscience applications. Geomorphology 179:300–314. doi: 10.1016/j.geomorph.2012.08.021

Williams JG, Rosser NJ, Hardy RJ, et al (2017) Optimising 4D Approaches to Surface Change Detection: Improving Understanding of Rockfall Magnitude-Frequency. Earth Surf Dyn Discuss 1–36. doi: 10.5194/esurf-2017-43

Wilson B, Lapointe E (2013) Partial Stabilization of an Active Slide Area Utilizing Soil Mixed Shear Keys installed Using Cutter Soil Mixing Results of a Test Section. Proc Found Eng Face Uncertain 2170–2183

Woods A, Hendry MT, Macciotta R, et al (2020) GB-InSAR monitoring of vegetated and snow-covered slopes in remote mountainous environments. Landslides. doi: 10.1007/s10346-020-01408-4

Woods A, Hendry MT, Macciotta R, et al (2019) Application Of Ground-Based Interferometry For Reservoir Slope Monitoring At Checkerboard Creek Rock Slope In Revelstoke, Bc. In: CDA 2019 Annual Conference. Calgary, AB, Canad

Wyllie DC (2014) Rock fall engineering: development and calibration of an improved model for analysis of rock fall hazards on highways and railways. UNIVERSITY OF BRITISH COLUMBIA

Zhang LL, Fredlund MD, Fredlund DG, et al (2015) The influence of the unsaturated soil zone on 2-D and 3-D slope stability analyses. Eng Geol 193:374–383. doi: 10.1016/j.enggeo.2015.05.011

Zhang Y, Yu W, Han Y, et al (2019) Static and kinematic positioning performance of a low-cost real-time kinematic navigation system module. Adv Sp Res 63:3029–3042. doi: 10.1016/j.asr.2018.10.048

## APPENDIX A: DIGITAL PHOTOGRAMMETRY RECONSTRUCTION AT C018

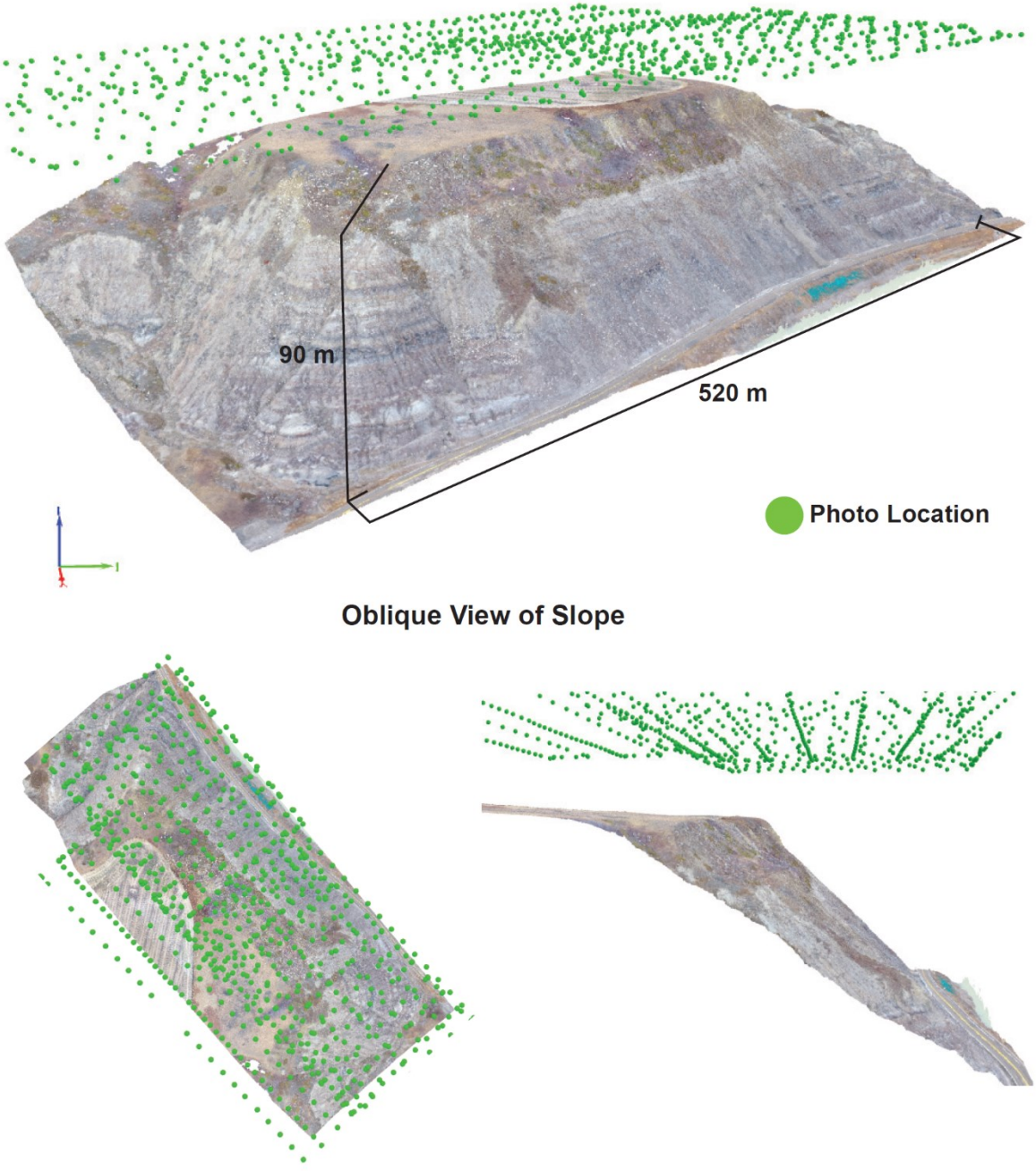


**Figure A-1 Photo location from November 2018 UAV Flight at C018 site**

## APPENDIX B: RESULTS FROM GEOCUBE INSTRUMENTATION

This appendix provides the recorded data collected for this research from the Geocube system at the Ten-mile landslide and Chin Coulee landslide during the monitoring campaign between 2017 and 2019. Evan Deane collected the Geocube data from the Chin Coulee landslide for his M.Sc. thesis (Deane 2019). The discussion of the results from monitoring the two landslides is presented in Chapter 4.

**Ten-mile**

- Changes in the East UTM Coordinates:

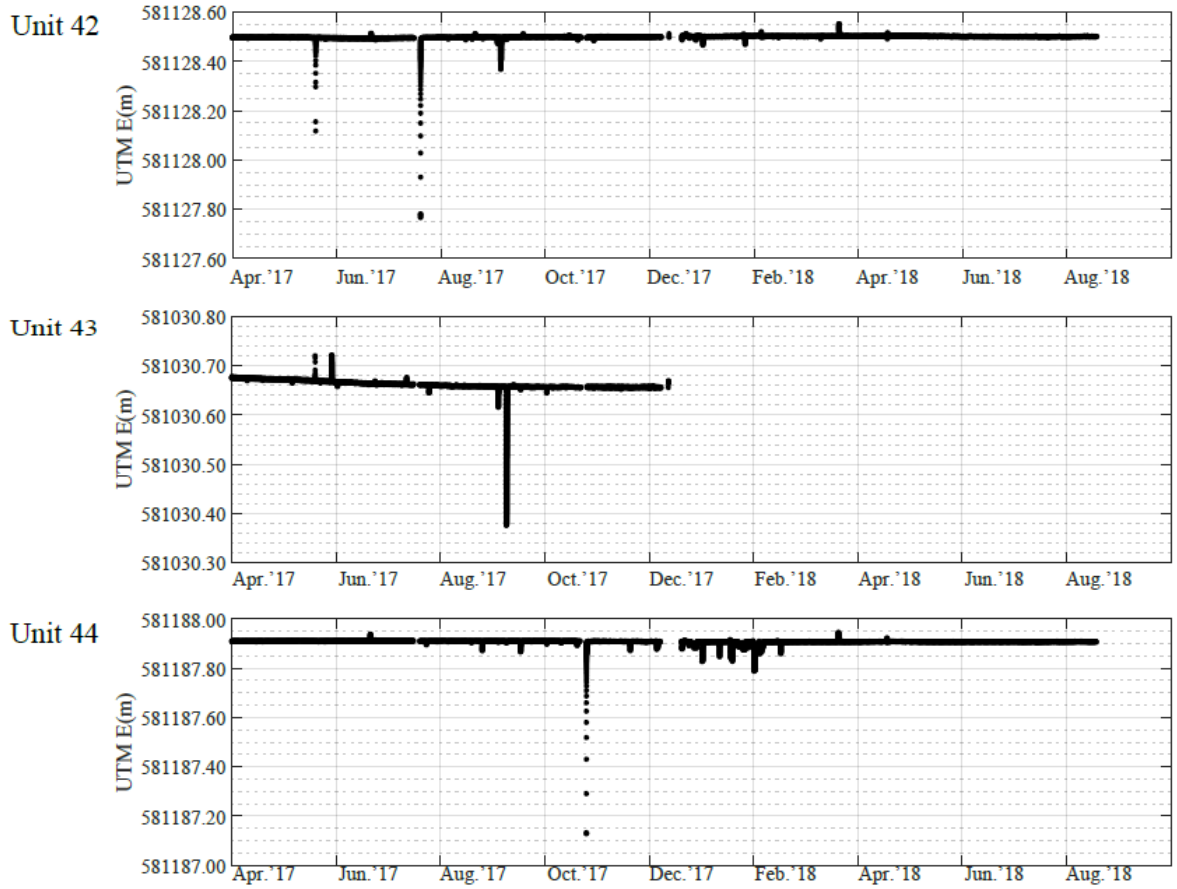


**Figure B-1 Raw data recorded of the changes in the East UTM format for units #42, #43, #44 at the Ten-mile landslide.**

## Appendix B: Results from Geocube instrumentation

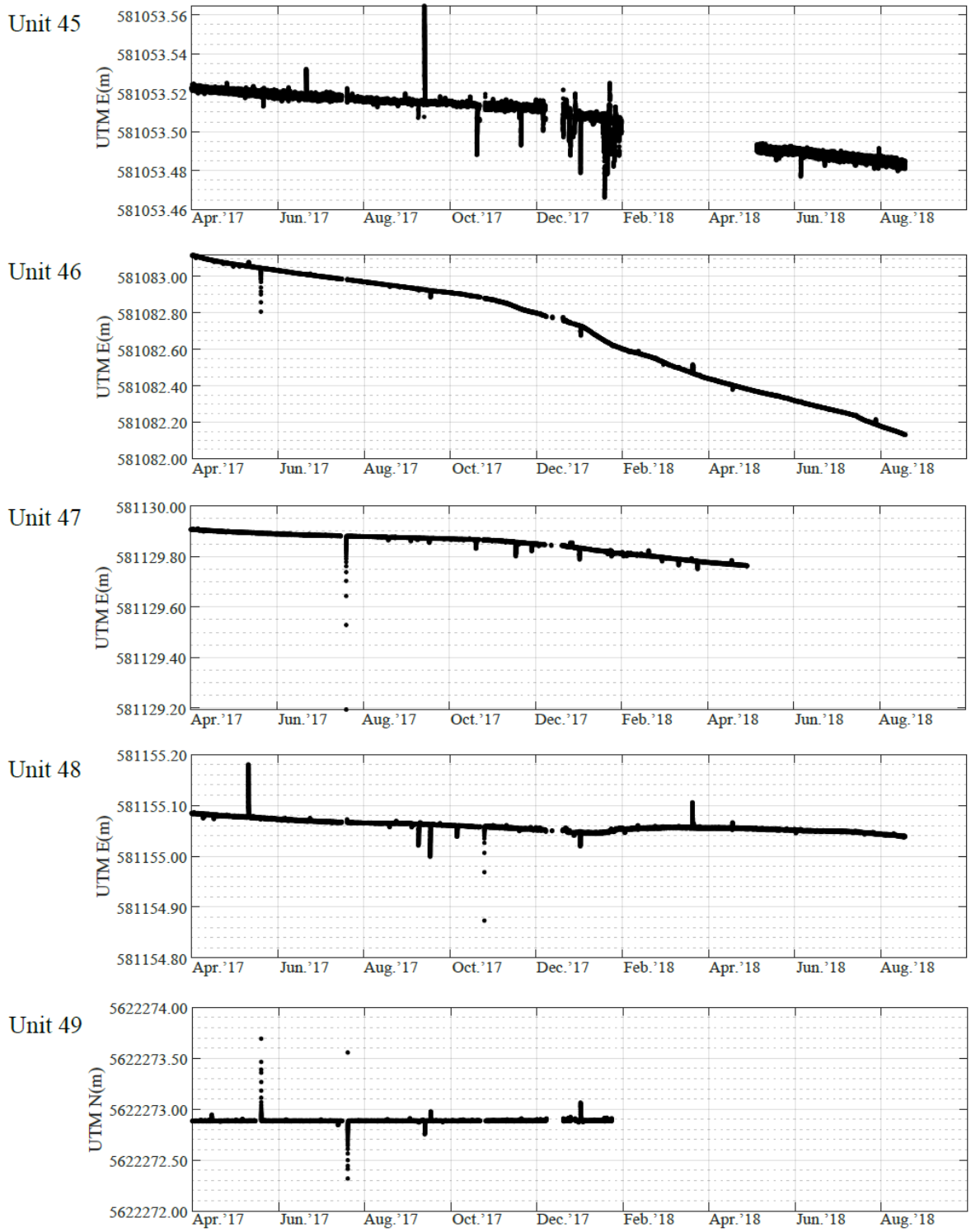


**Figure B-2 Raw data recorded of the changes in the East UTM format for units #45, #46, #47, #48, #49 at the Ten-mile landslide.**

## Appendix B: Results from Geocube instrumentation

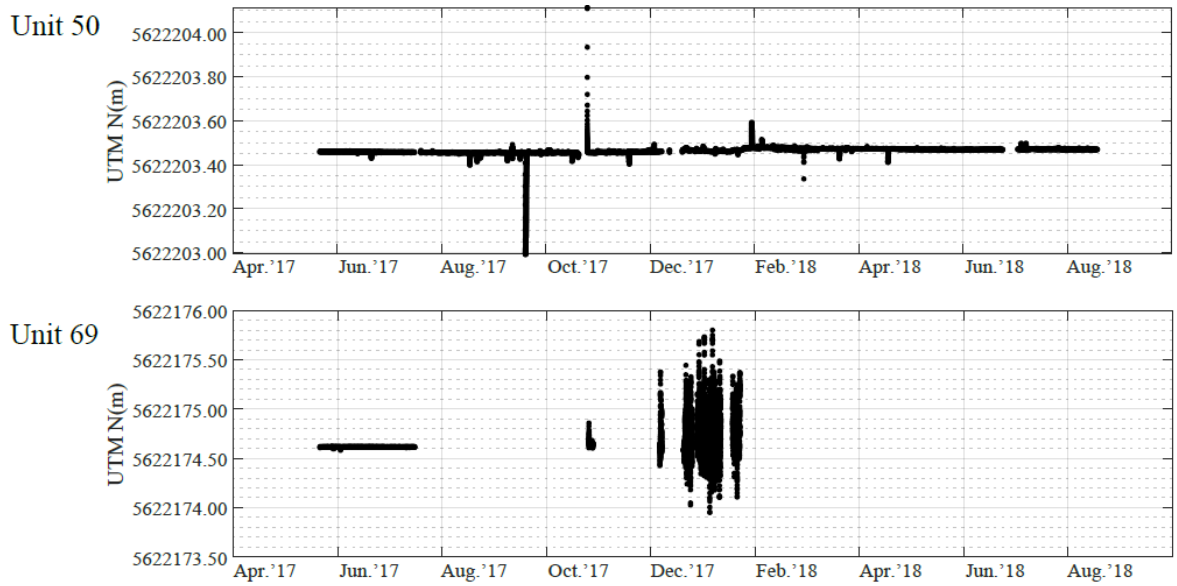


**Figure B-3 Raw data recorded of the changes in the East UTM format for units #50, #69 at the Ten-mile landslide.**

- Changes in the North UTM Coordinates:

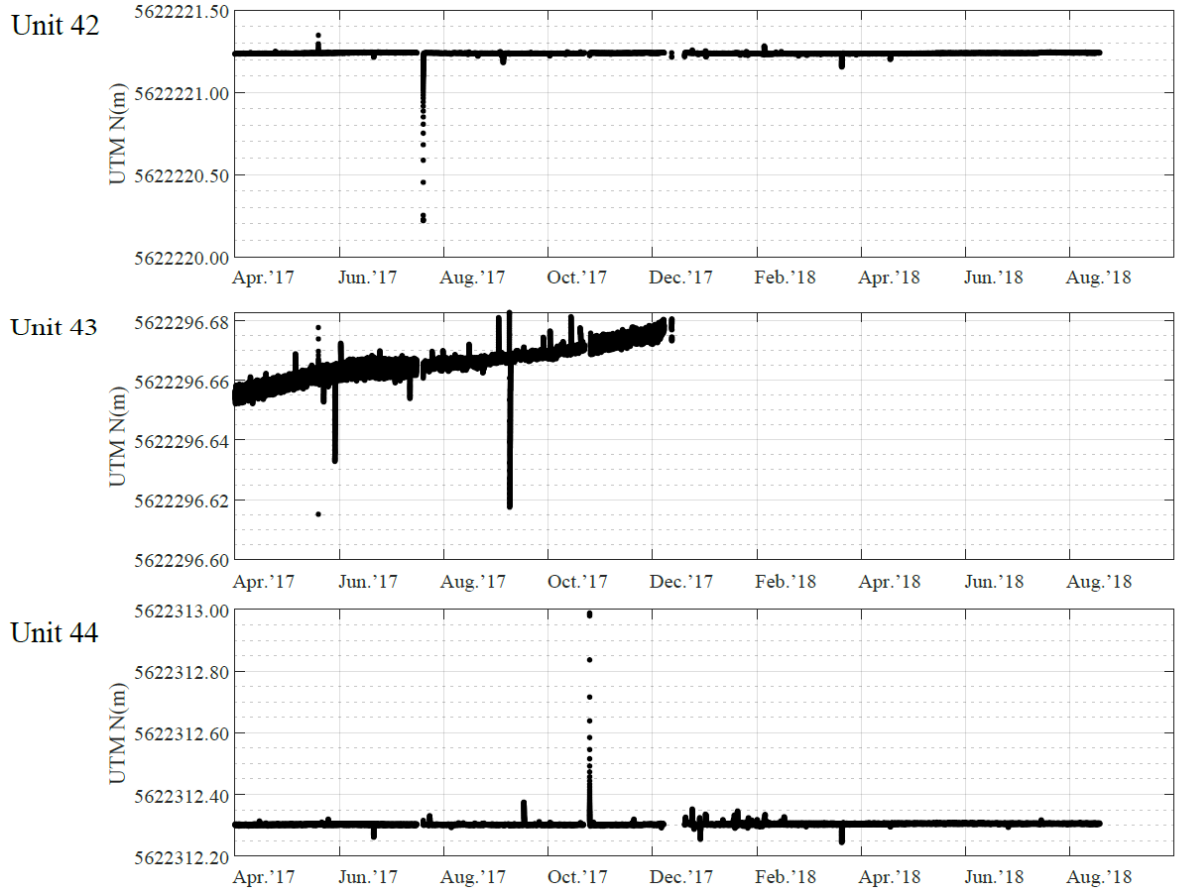


**Figure B-4 Raw data recorded of the changes in the North UTM format for units #42, #43, #44 at the Ten-mile landslide.**

## Appendix B: Results from Geocube instrumentation

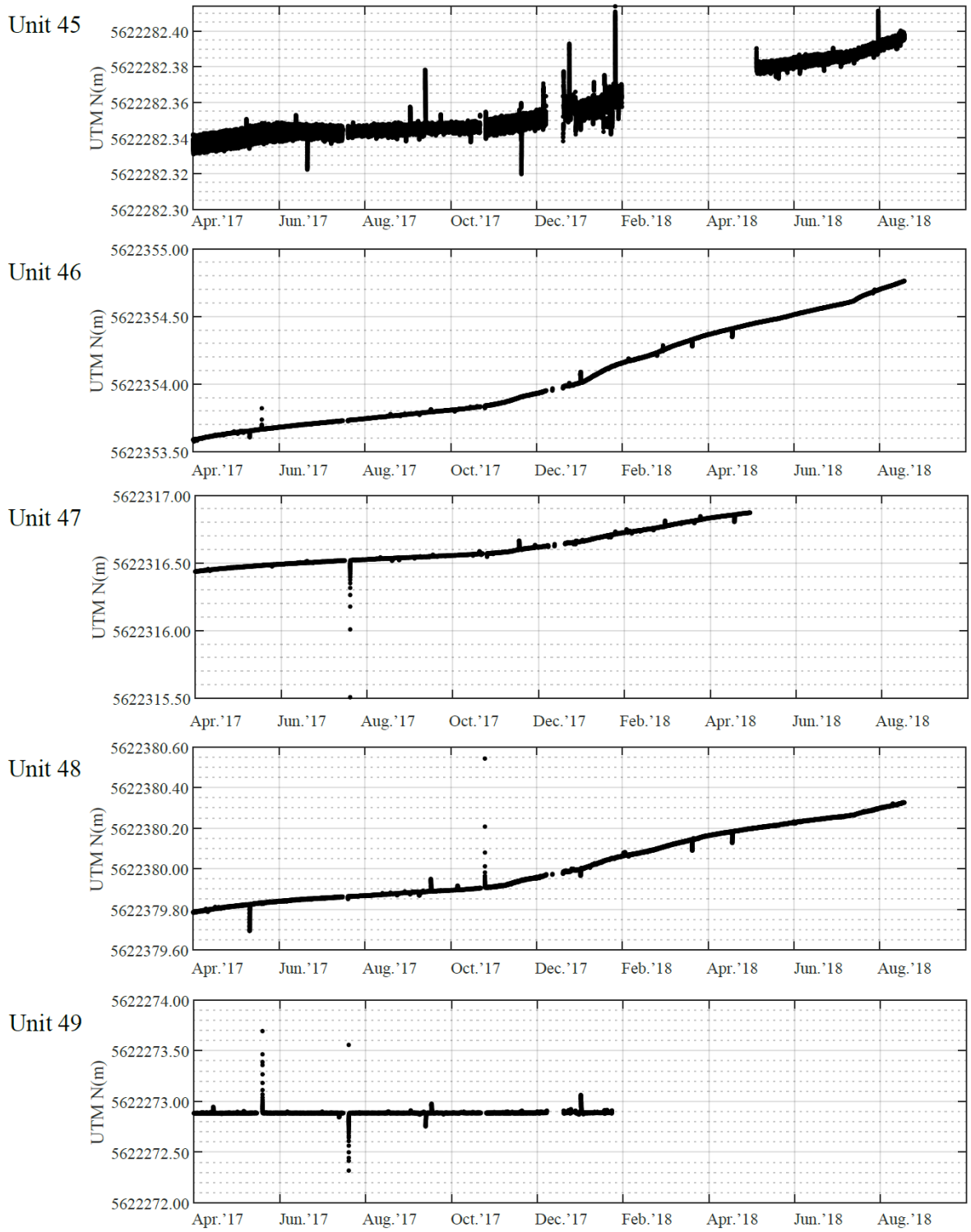


**Figure B-5 Raw data recorded of the changes in the North UTM format for units #45, #46, #47, #48, #49 at the Ten-mile landslide.**

## Appendix B: Results from Geocube instrumentation

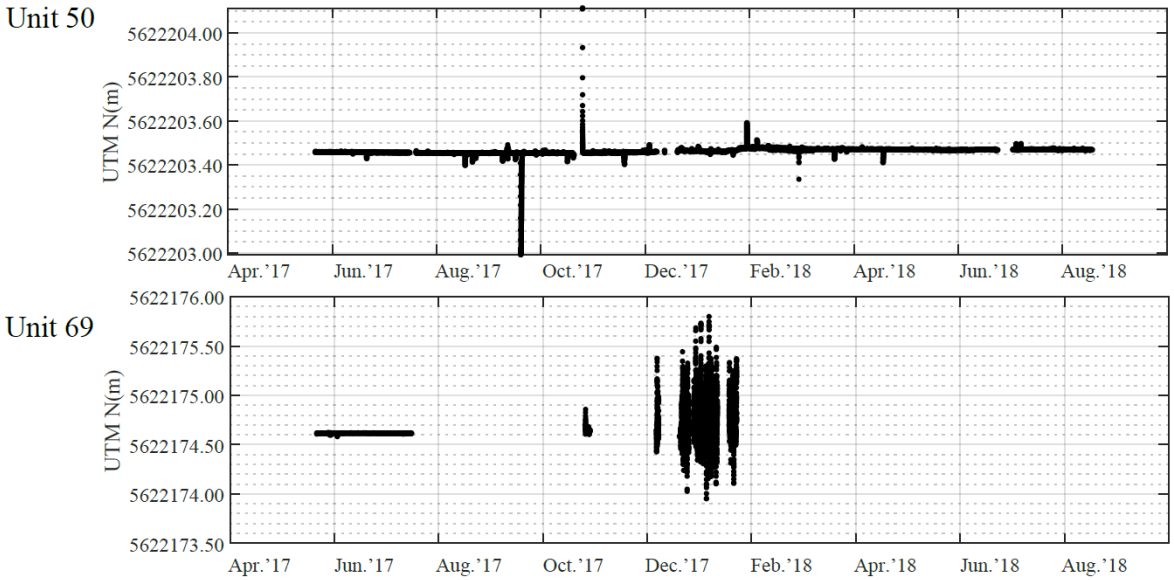


**Figure B-6 Raw data recorded of the changes in the North UTM format for units #50, #69 at the Ten-mile landslide.**

- Changes in the Elevation:

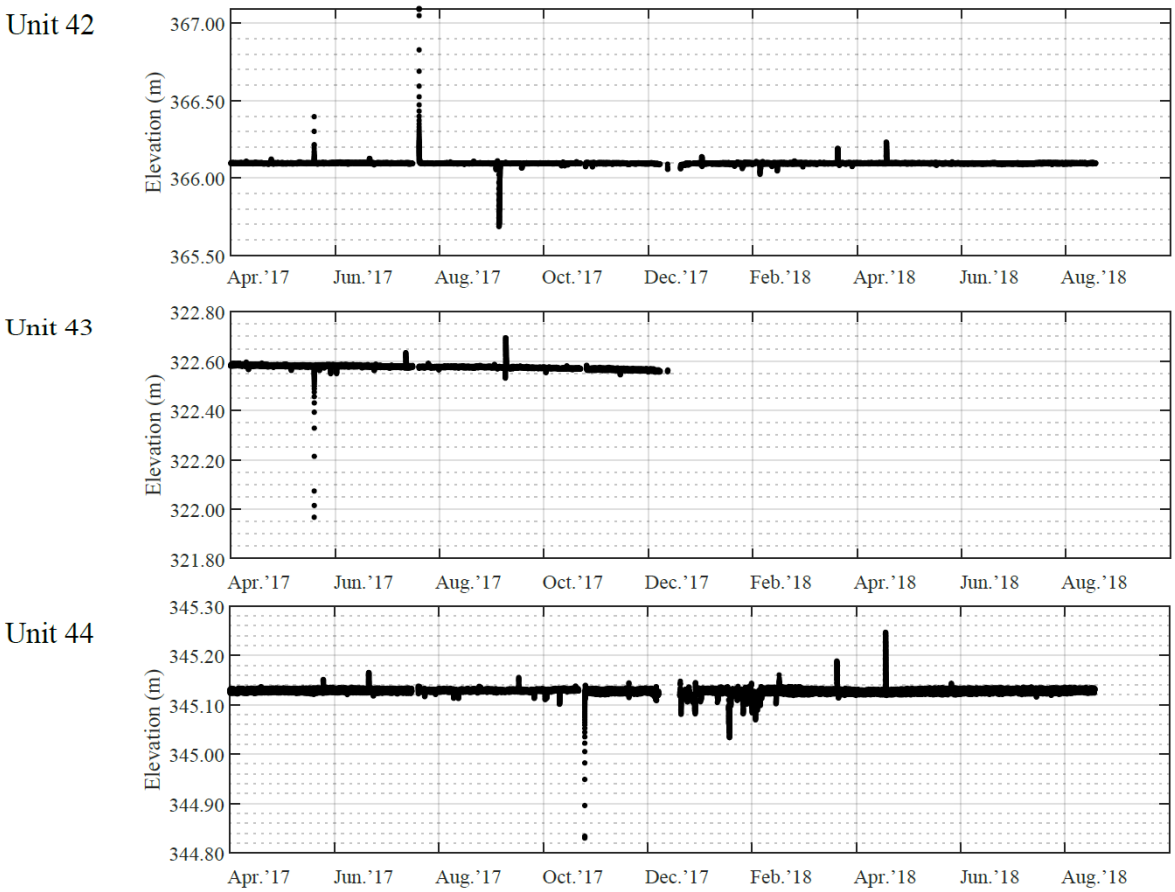


**Figure B-7 Raw data recorded of the changes in elevation for units #42, #43, #44 at the**

## Appendix B: Results from Geocube instrumentation

**Ten-mile landslide.**

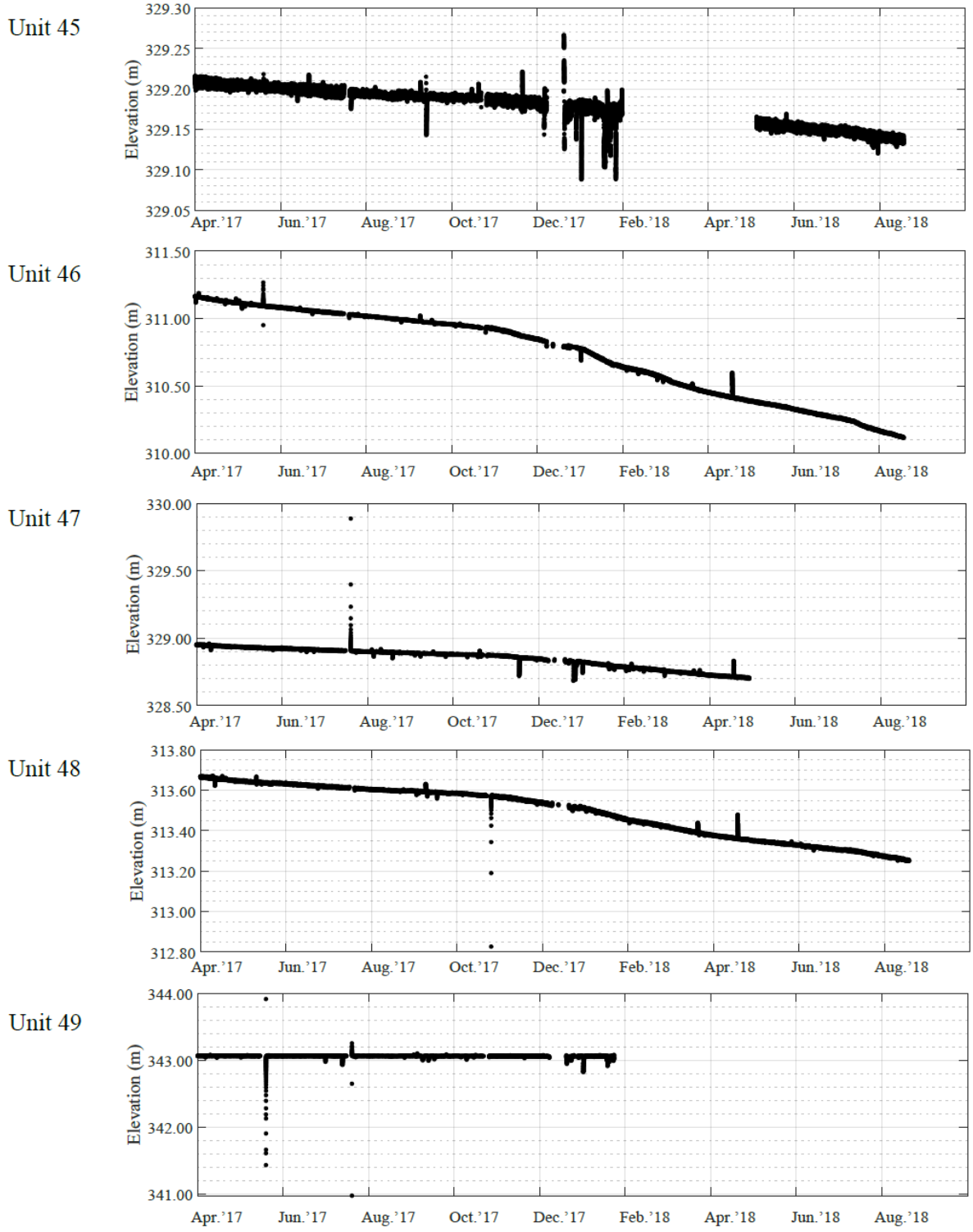


**Figure B-8 Raw data recorded of the changes in elevation for units #45, #46, #47, #48, #49 at the Ten-mile landslide.**

## Appendix B: Results from Geocube instrumentation

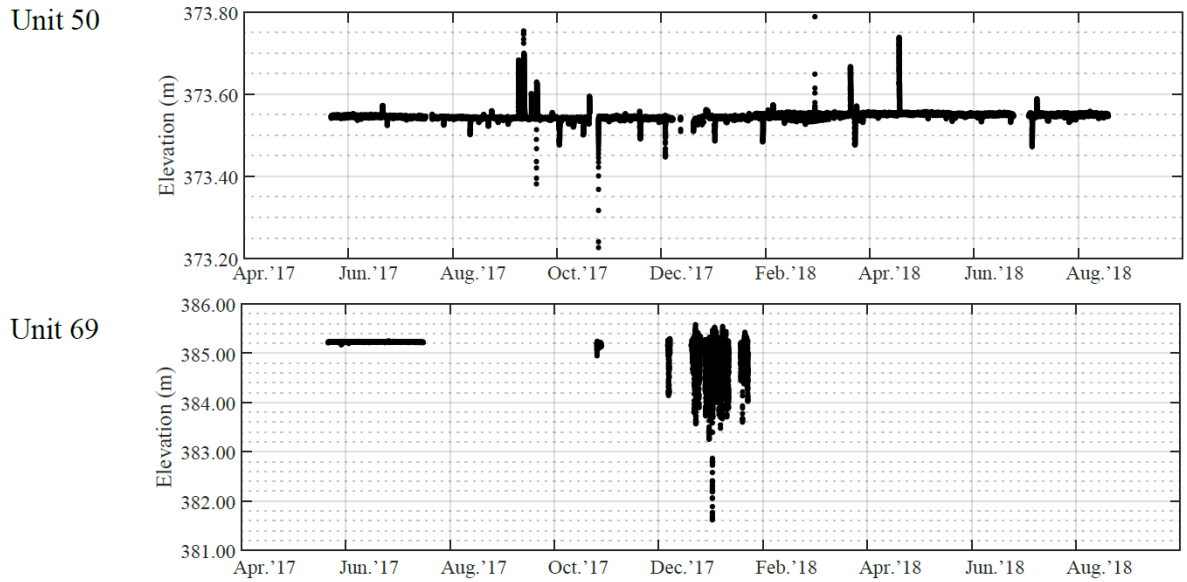


**Figure B-9 Raw data recorded of the changes in elevation for units #50, #69 at the Ten-mile landslide.**

- Summary plots:

The following plots shows the trends of displacement, displacement rate, and angle of movement based on a 15-day moving average that filters out most variations in the data.

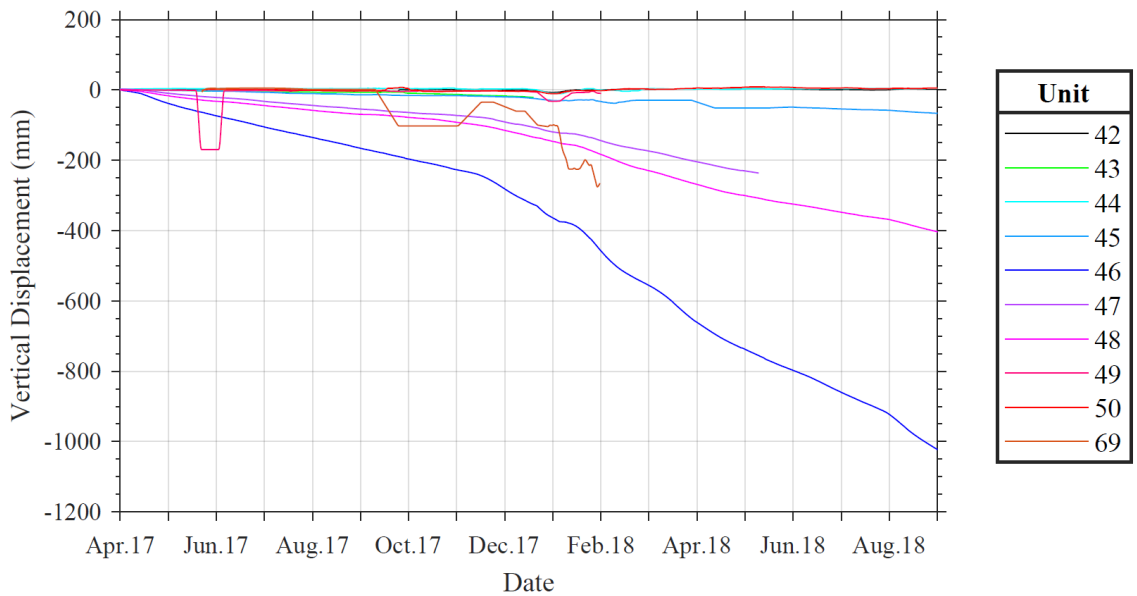


**Figure B-10 Cumulative change in elevation from all the dGNSS units located at the Ten-mile landslide.**

## Appendix B: Results from Geocube instrumentation

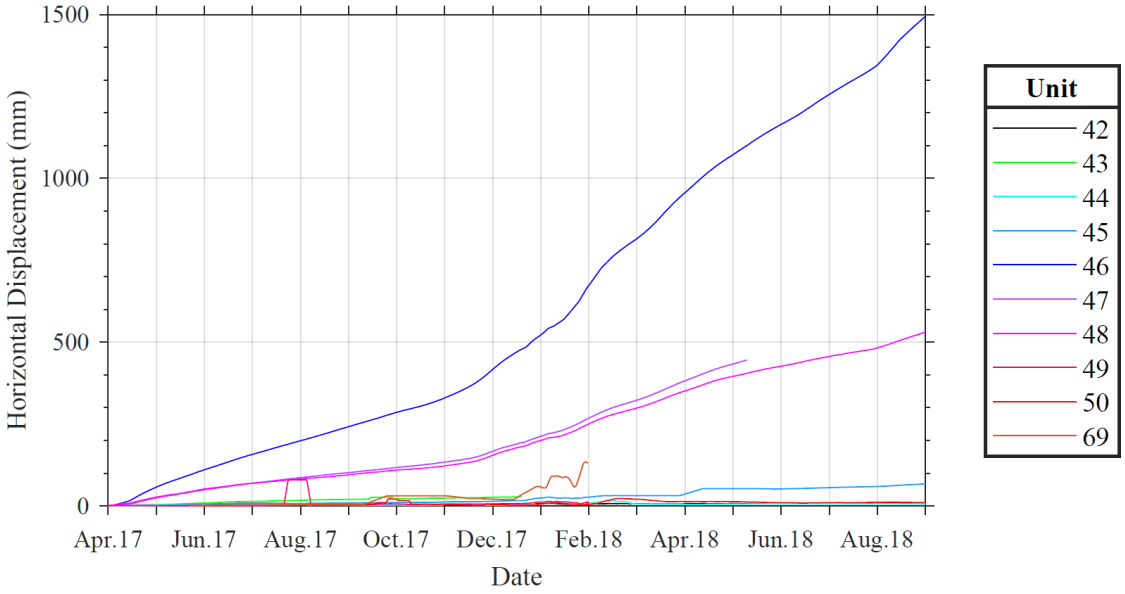


**Figure B-11 Cumulative change in horizontal displacement from all the dGNSS units located at the Ten-mile landslide.**

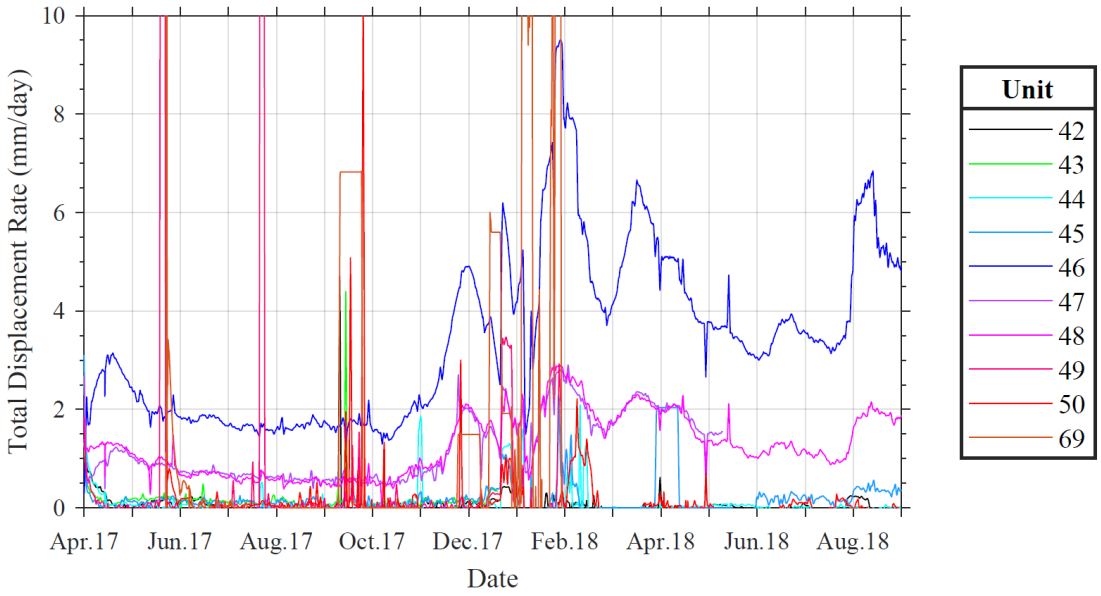


**Figure B-12 Change in displacement rate from all the dGNSS units located at the Ten-mile landslide.**

## Appendix B: Results from Geocube instrumentation

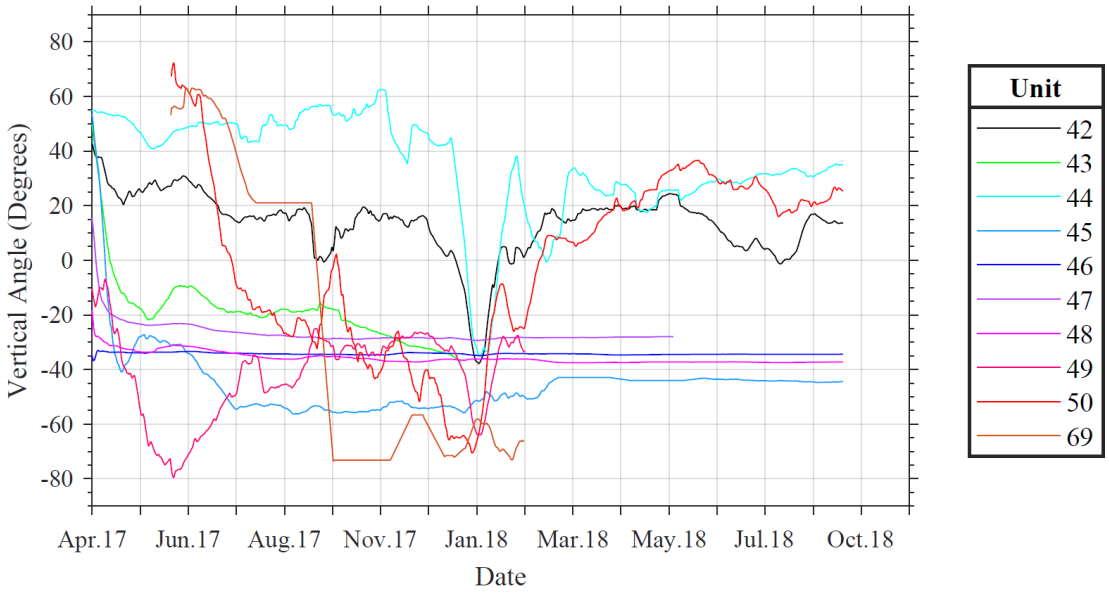


**Figure B-13 Change in the vertical angle of movement from all the dGNSS units located at the Ten-mile landslide.**

## Appendix B: Results from Geocube instrumentation

### Chin-Coulee

- Changes in the East UTM Coordinates:

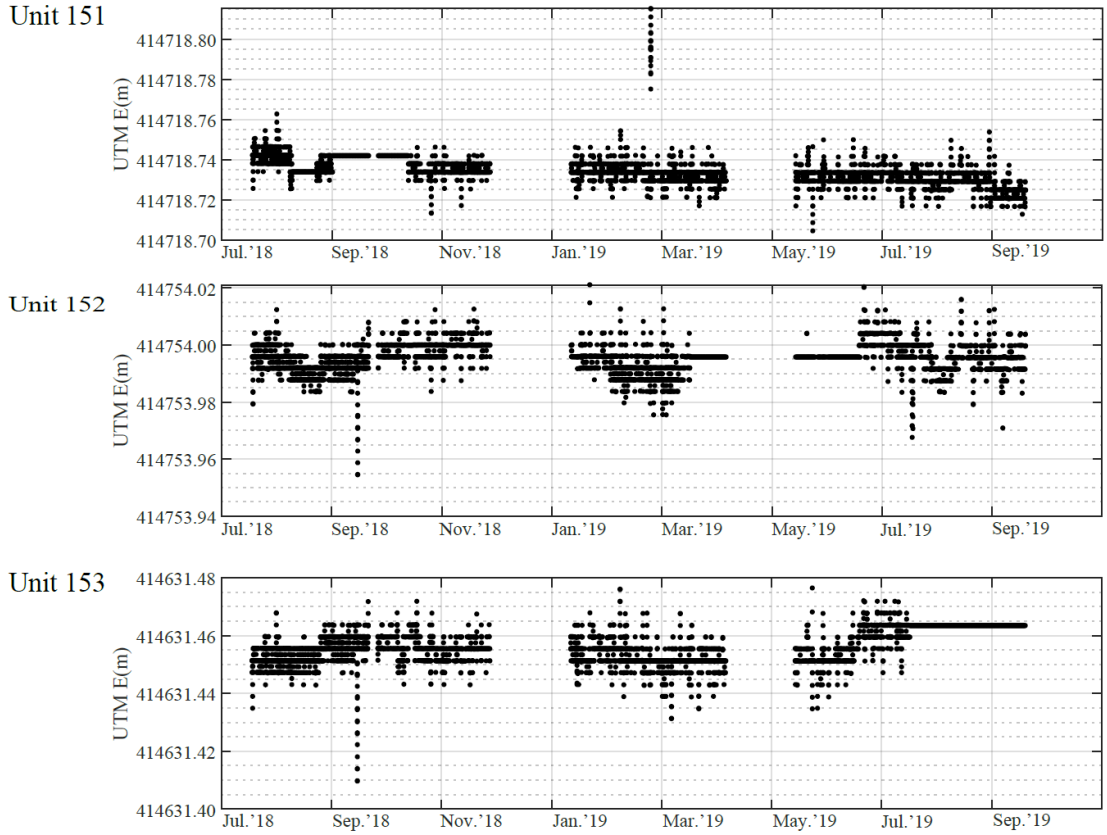


**Figure B-14 Raw data recorded of the changes in the East UTM format for units #151, #152, #153 at the Chin-Coulee landslide.**

## Appendix B: Results from Geocube instrumentation

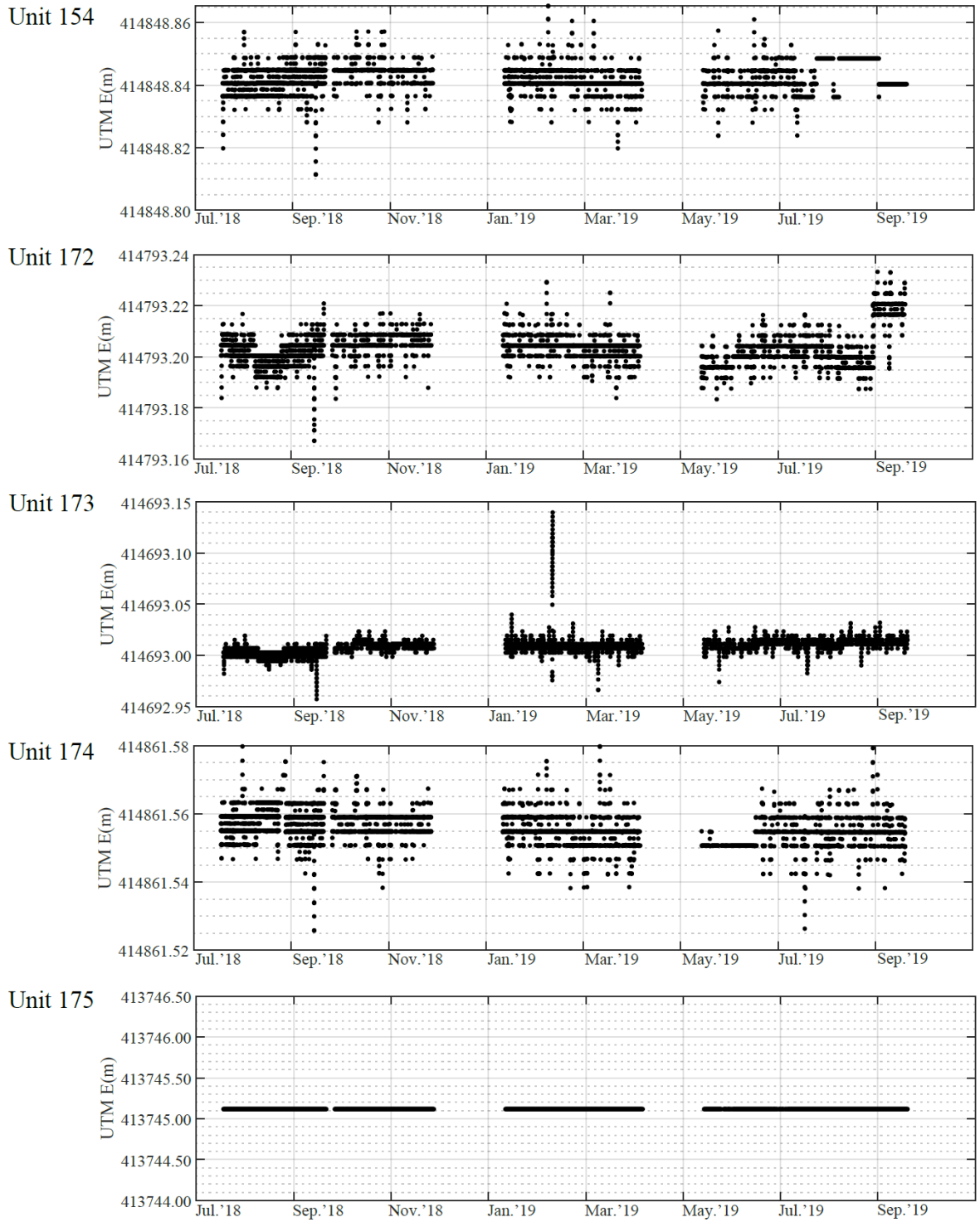


**Figure B-15 Raw data recorded of the changes in the East UTM format for units #154, #172, #173, #174, #175 at the Chin-Coulee landslide.**

## Appendix B: Results from Geocube instrumentation

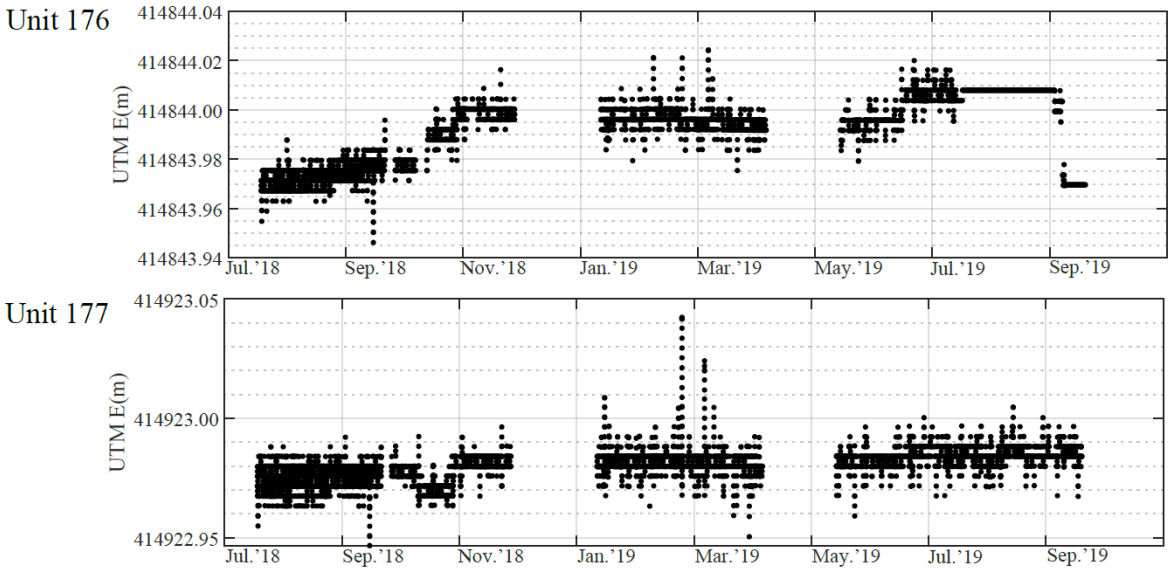


**Figure B-16 Raw data recorded of the changes in the East UTM format for units #176, #177 at the Chin-Coulee landslide.**

- Changes in the North UTM Coordinates:

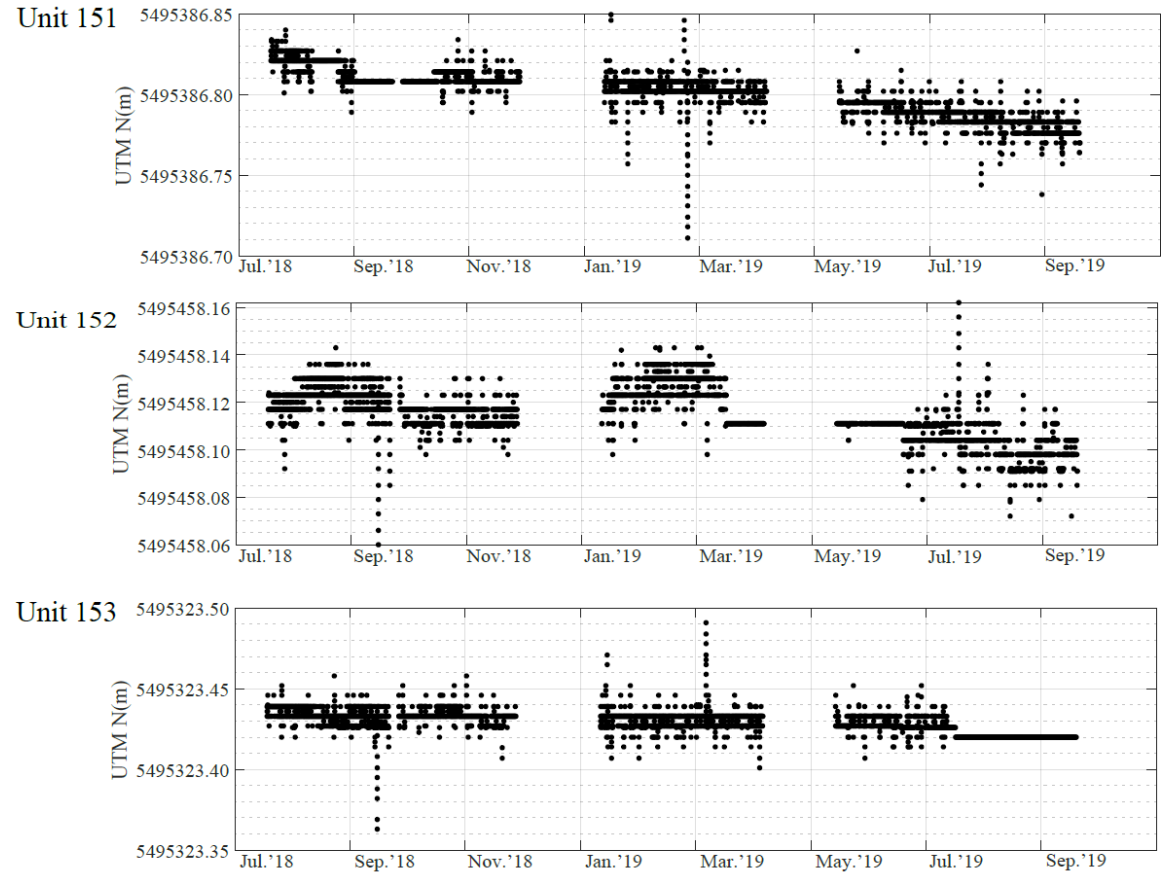


**Figure B-17 Raw data recorded of the changes in the North UTM format for units #151, #152, #153 at the Chin-Coulee landslide.**

## Appendix B: Results from Geocube instrumentation

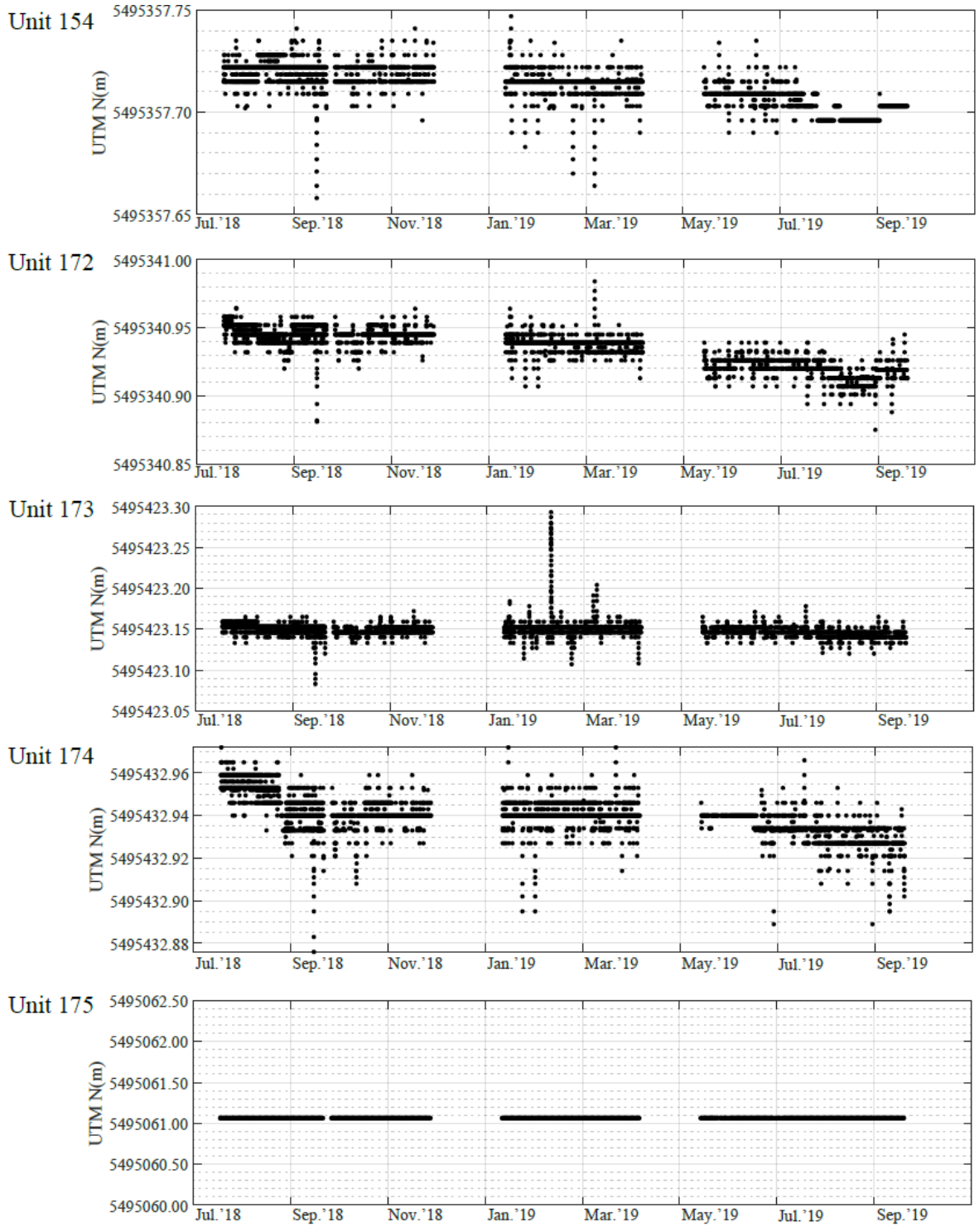


**Figure B-18 Raw data recorded of the changes in the North UTM format for units #154, #172, #173, #174, #175 at the Chin-Coulee landslide.**

## Appendix B: Results from Geocube instrumentation

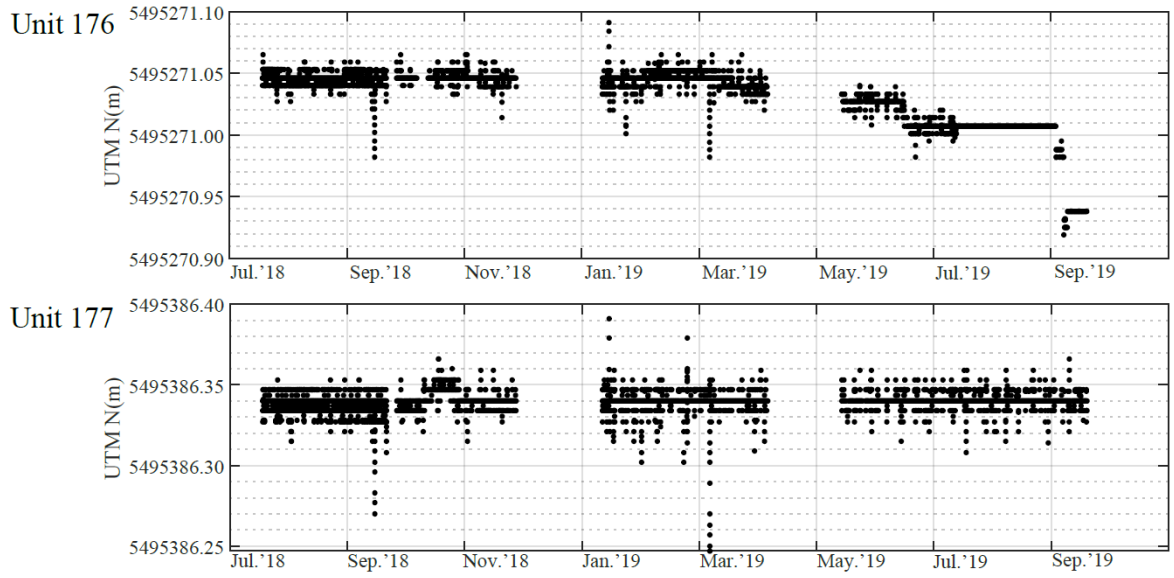


**Figure B-19 Raw data recorded of the changes in the North UTM format for units #176, #177 at the Chin-Coulee landslide.**

- Changes in the Elevation:

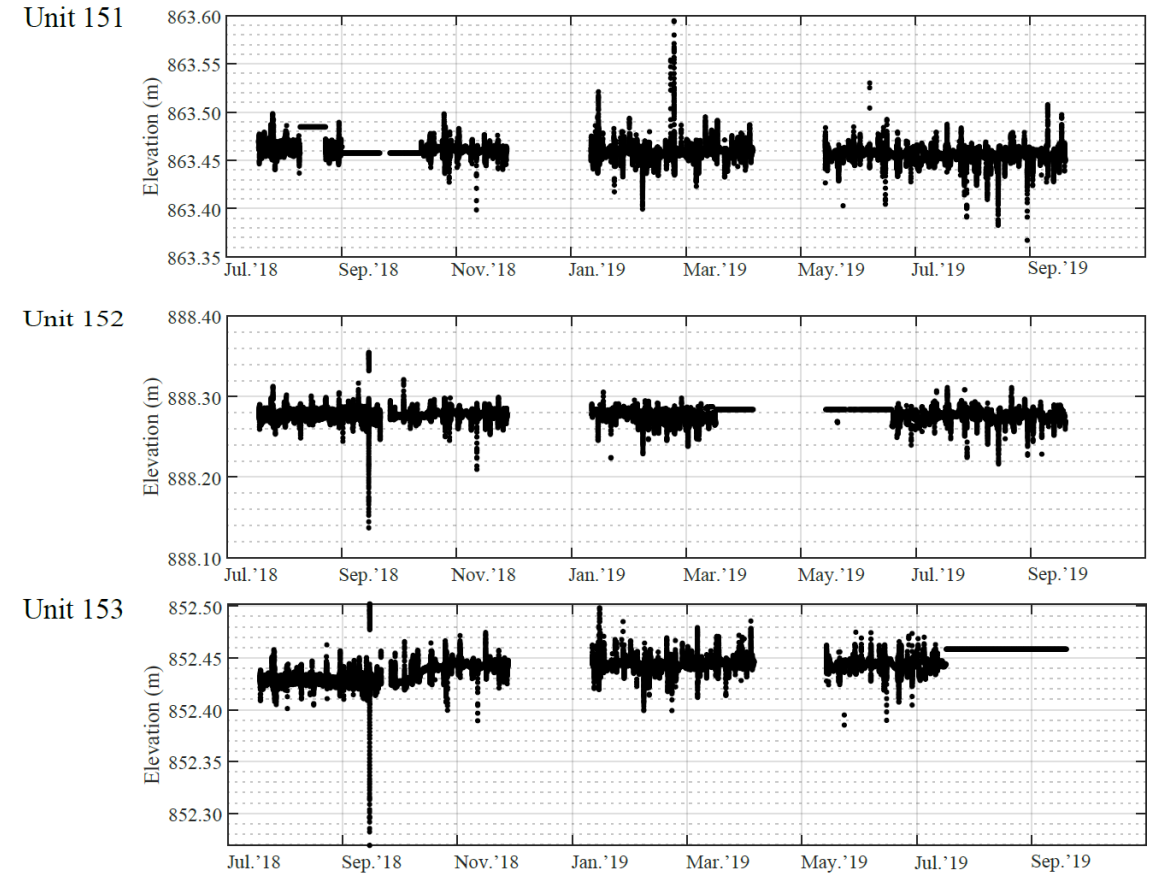


**Figure B-20 Raw data recorded of the changes in Elevation for units #151, #152, #153 at the Chin-Coulee landslide.**

## Appendix B: Results from Geocube instrumentation

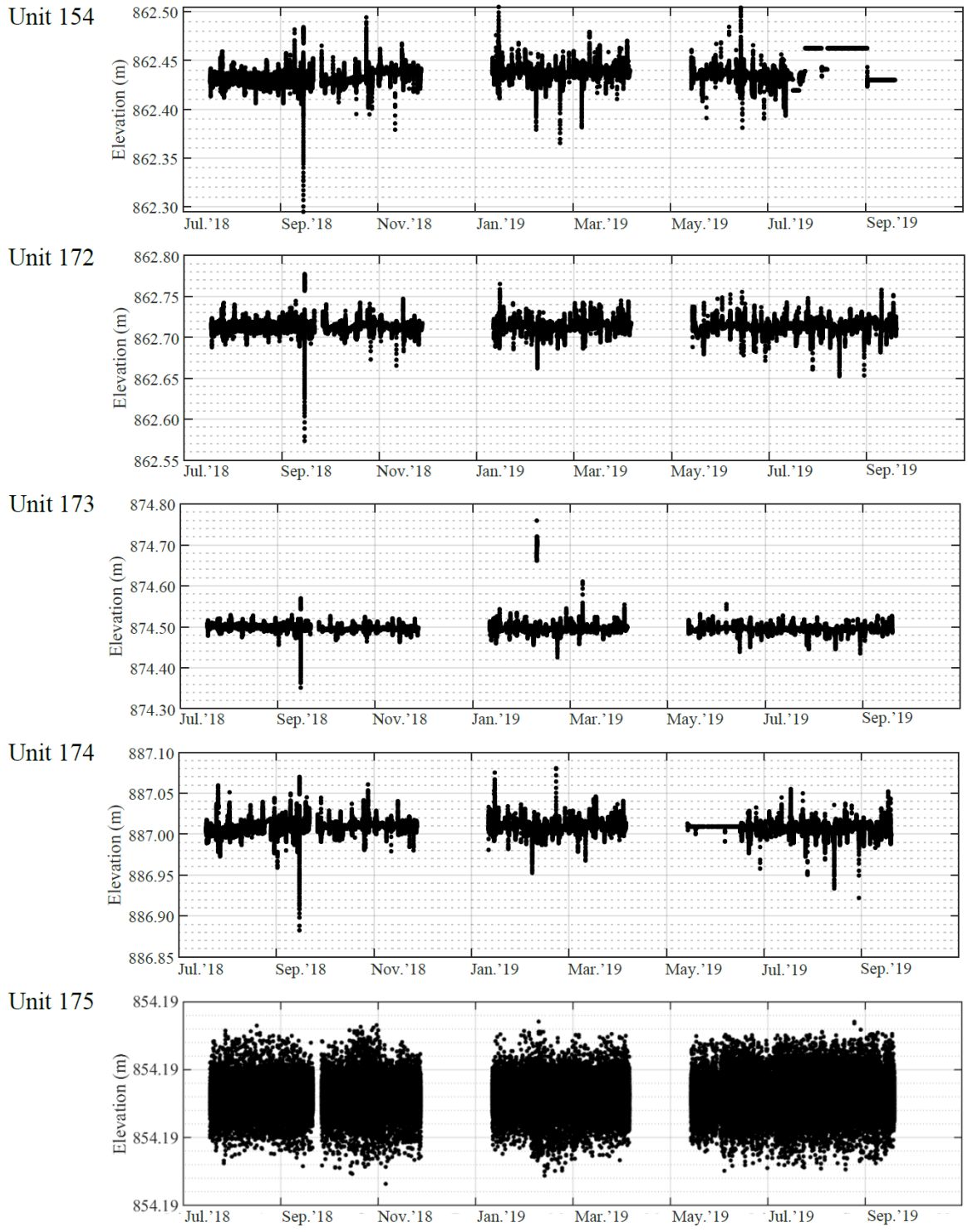


**Figure B-21 Raw data recorded of the changes in Elvevation for units #154, #172, #173, #174, #175 at the Chin-Coulee landslide.**

## Appendix B: Results from Geocube instrumentation

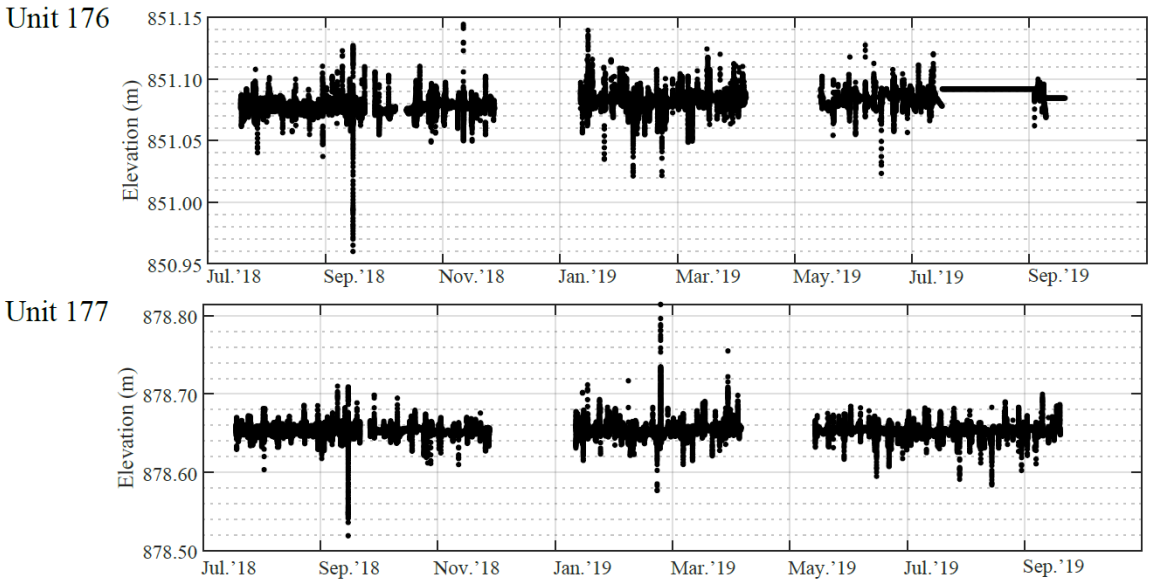


**Figure B-22 Raw data recorded of the changes in Elevation for units #176, #177 at the Chin-Coulee landslide.**

- Summary plots:

The following plots shows the trends of displacement, displacement rate, and angle of movement based on a 15-day moving average that filters out most variations in the data.

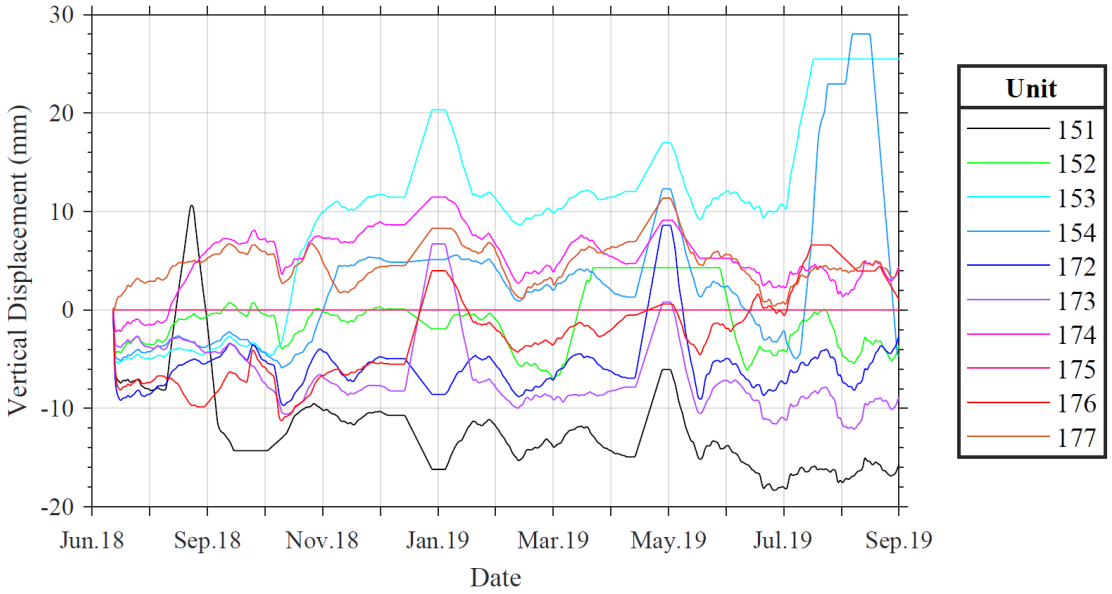


**Figure B-23 Cumulative change in elevation from all the dGNSS units located at the Chin-Coulee landslide.**

## Appendix B: Results from Geocube instrumentation

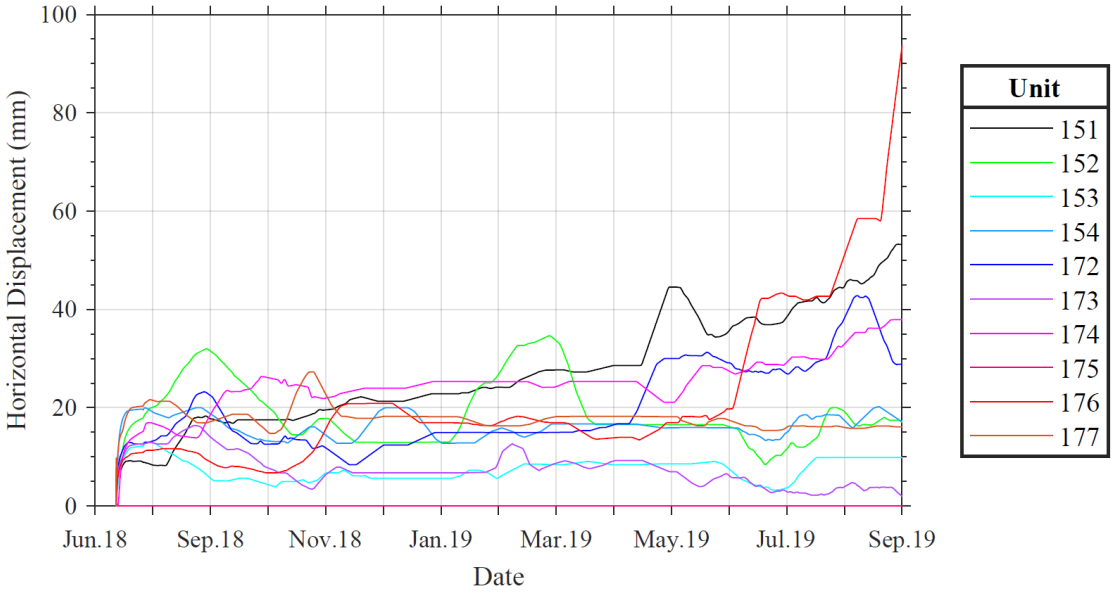


**Figure B-24 Cumulative change in horizontal displacement from all the dGNSS units located at the Chin-Coulee landslide.**

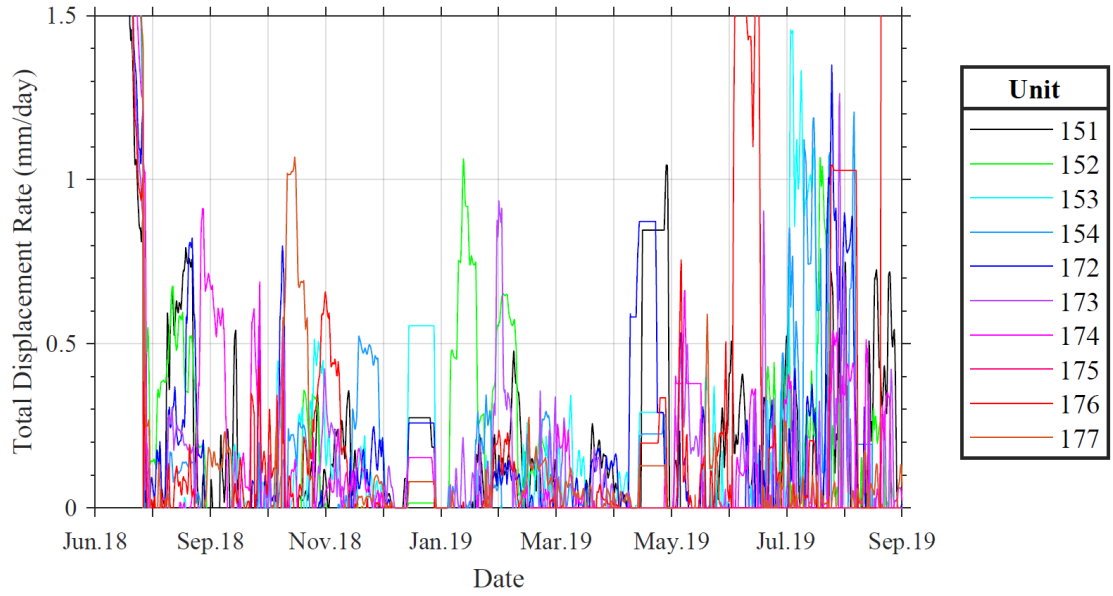


**Figure B-25 Change in displacement rate from all the dGNSS units located at the Chin-Coulee landslide.**

## Appendix B: Results from Geocube instrumentation

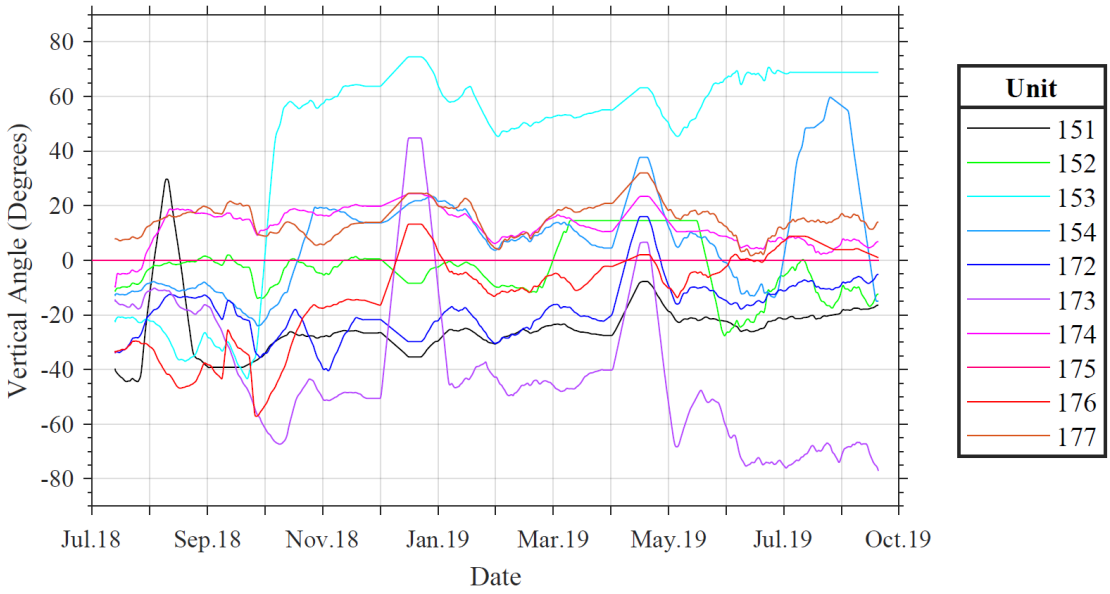


**Figure B-26 Change in the vertical angle of movement from all the dGNSS units located at the Chin-Coulee landslide.**

# APPENDIX C: RESULTS FROM LABORATORY TESTING OF EARTHFLOW DEPOSIT SAMPLES

This appendix includes the details of the laboratory test results conducted during this research on recovered samples of the earthflow deposit at the Ten-mile. The samples were taken from borehole BH-BGC15-01 provided the Canadian National Railways. The borehole was located next to the railway with coordinates 581,339E, 5,624,334N. The laboratory tests were performed following ASTM standards, including:

- Moisture content (ASTM D2216)
- Sieve analysis, Hydrometer test and Atterberg limits (ASTM D 421 – 85, D422 – 63, D7928 and D4318 − 10)
- Direct Shear Testing CD (ASTM D3080)
- Soil Water Characteristic curve measures (ASTM D6836)

## APPENDIX C: RESULTS FROM LABORATORY TESTING OF EARTHFLOW DEPOSIT SAMPLES

### Moisture Content

The borehole samples were maintained in a control moisture room at the University of Alberta until testing. The selected samples from the borehole were place on the oven for 24 hours to estimate the gravimetric water content. The results of moisture content were compared to the results from test made on different boreholes by BGC engineering (2016).

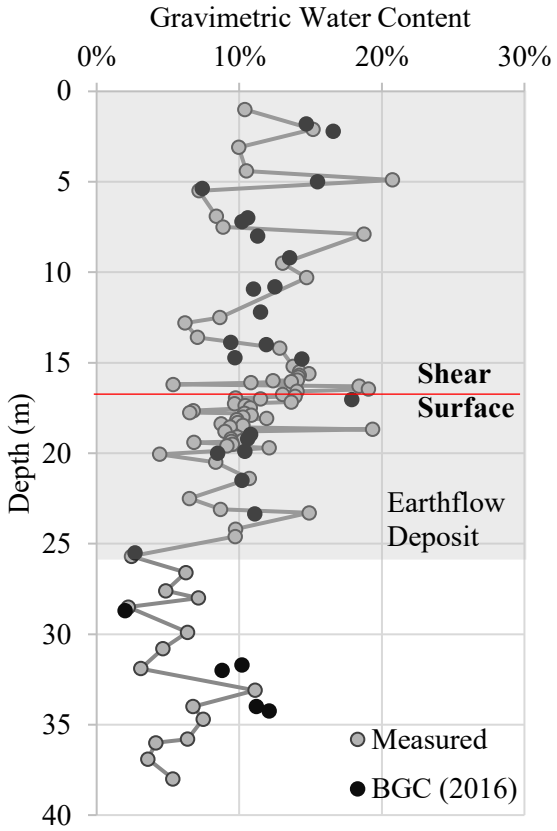


**Figure C-1 Changes in the gravimetric water content from earthflow deposit samples at the Ten-mile landslide (including testing carried by BGC Eng.,2016).**

## APPENDIX C: RESULTS FROM LABORATORY TESTING OF EARTHFLOW DEPOSIT SAMPLES

### Sieve analysis, Hydrometer test and Atterberg limits

The grain size distribution was focused on representative samples of the earthflow close to the location of the shear surface.

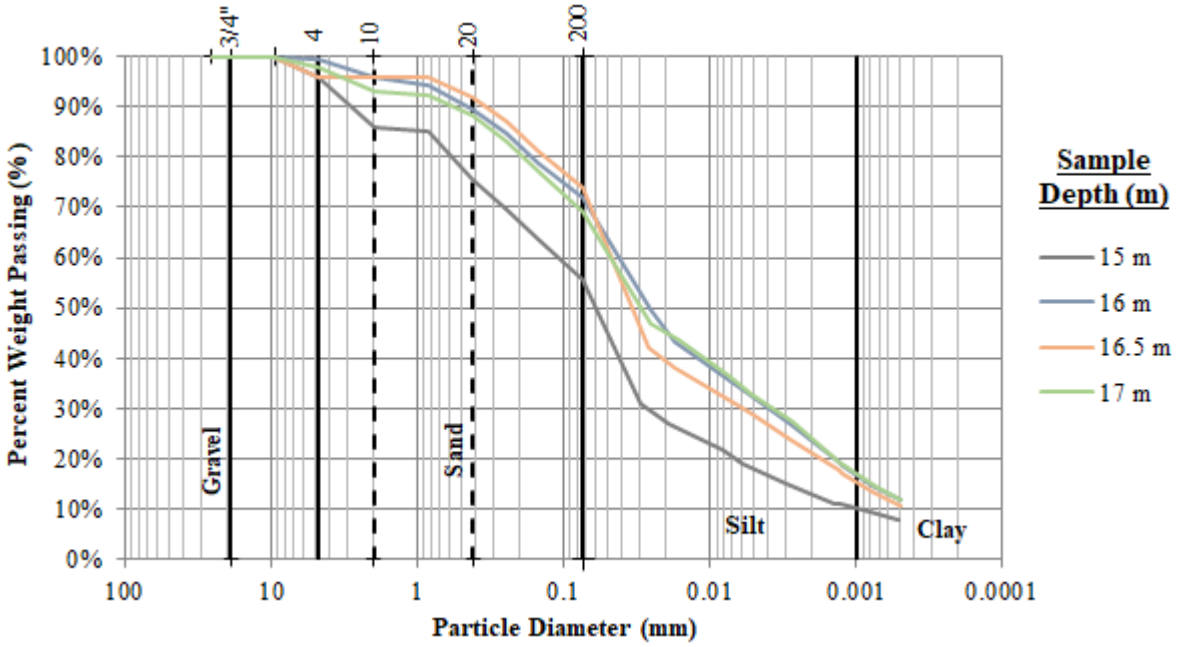


**Figure C-2 Particle size distribution of four samples from the earthflow deposit at the Ten-mile landslide.**

**Table C-1 Gradation summary of Ten-mile samples**

| Sample Depth (m) | 17 | 16.5 | 16 | 15 |
|---|---|---|---|---|
| Gravel % | 2% | 4% | 0% | 4% |
| Sand % | 29% | 22% | 28% | 40% |
| Silt/Clay % | 69% | 74% | 72% | 56% |
| Silt % | 50% | 56% | 53% | 45% |
| Clay % | 19% | 18% | 19% | 11% |
| D60 (mm) | 0.045 | 0.045 | 0.045 | 0.045 |
| D30 (mm) | 0.0035 | 0.0035 | 0.0035 | 0.0035 |
| D10 (mm) | 0.0003 | 0.0003 | 0.0003 | 0.0003 |
| Cc: | 0.91 | 0.91 | 0.91 | 0.91 |
| Cu: | 150 | 150.00 | 150 | 150 |

## APPENDIX C: RESULTS FROM LABORATORY TESTING OF EARTHFLOW DEPOSIT SAMPLES

**Table C-2 Atterberg limits**

| Sample Depth (m) | Plastic Limit (%) | Liquid Limit (%) | Plastic Index (%) |
|---|---|---|---|
| 15 | 14% | 25% | 11% |
| 16 | 23% | 32% | 9% |
| 17 | 18% | 27% | 9% |
| 18 | 23% | 33% | 10% |
| 18.5 | 17% | 25% | 8% |
| 19 | 19% | 29% | 10% |
| 19.5 | 17% | 27% | 10% |
| 19.8 | 19% | 29% | 10% |

### Direct Shear Test

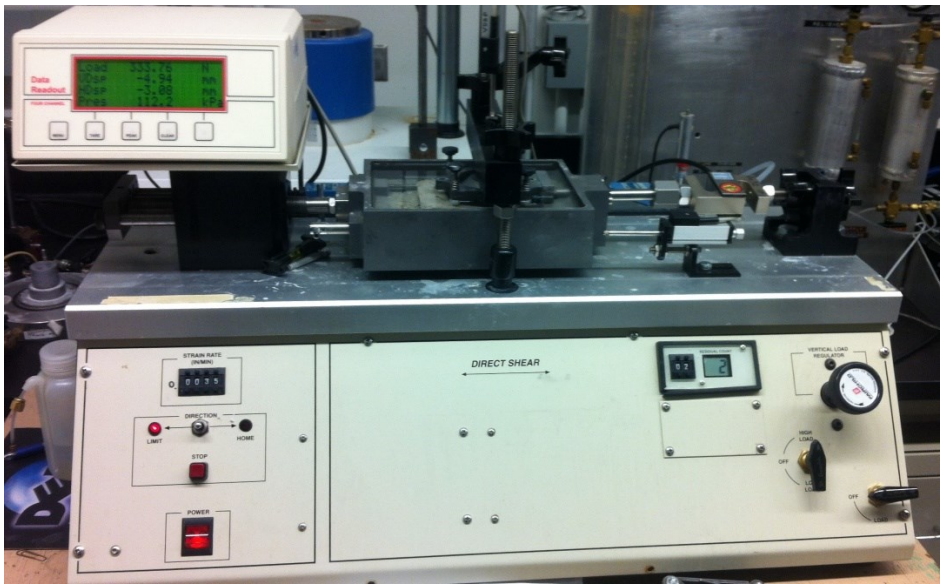


**Figure C-3 Direct shear box apparatus at the University of Alberta used for testing samples.**

## APPENDIX C: RESULTS FROM LABORATORY TESTING OF EARTHFLOW DEPOSIT SAMPLES

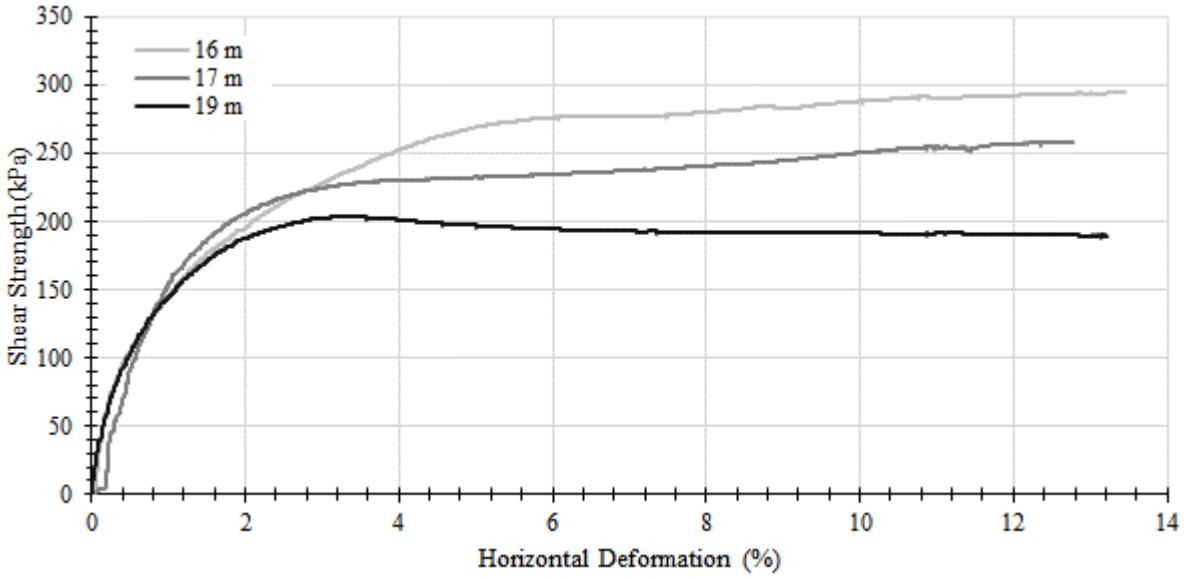


**Figure C-4 Peak measurement of shear strength of the earthflow deposit from three samples at 16 m, 17 m, and 19 m from the surface.**

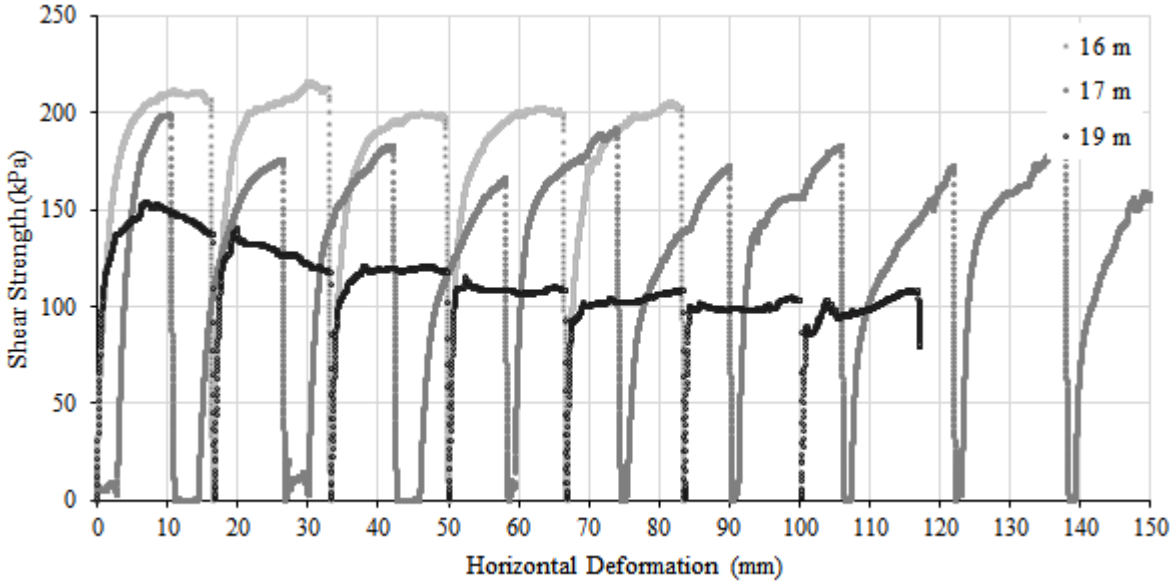


**Figure C-5 Multiple reversal measurements of shear strength of the earthflow deposit from three samples at 16 m, 17 m, and 19 m from the surface.**

Figure C-6 shows the measured peak and residual shear strength under different magnitudes of confiding stress for the earthflow matrix.

## APPENDIX C: RESULTS FROM LABORATORY TESTING OF EARTHFLOW DEPOSIT SAMPLES

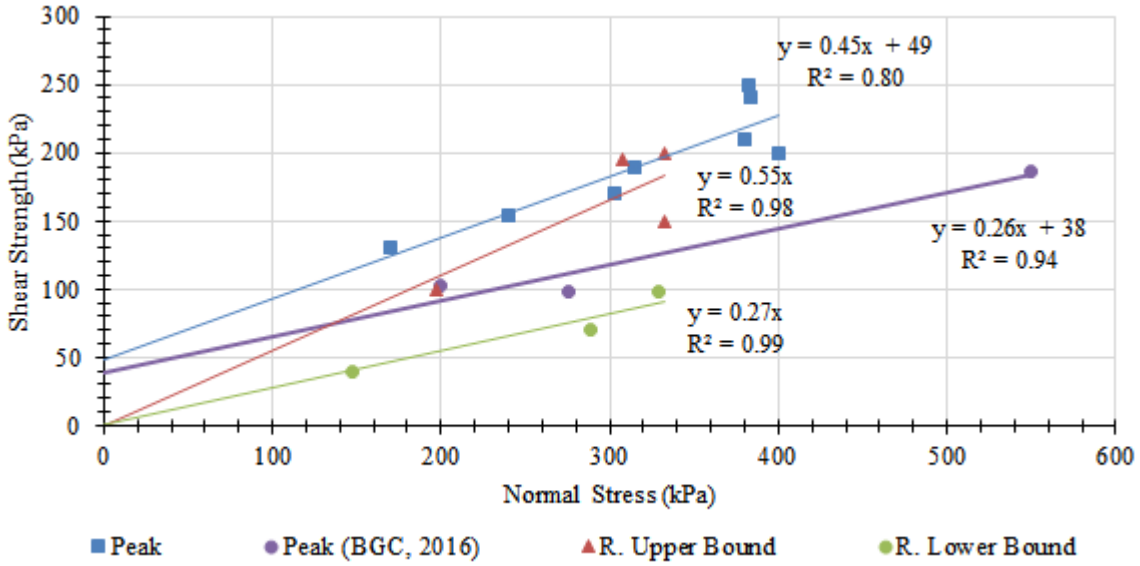


**Figure C-6 Linear regression of shear strength envelope of earthflow deposit from direct shear box test for the peak strength from samples tested at the University of Alberta and by BGC (2016); and estimation of the upper and lower bound of residual strength through multiple reversals of the direct shear box at the University of Alberta.**

## APPENDIX C: RESULTS FROM LABORATORY TESTING OF EARTHFLOW DEPOSIT SAMPLES

**Table C-3 Summary of Direct shear testing results.**

| Depth (m) | Density (kN/m3) | GWC (%) | Saturation (%) | Porosity | Strain Rate (in/min) | Normal Stress (kPa) | Peak Shear Stress* (kPa) | Normal Stress (kPa) | Residual Shear Stress (kPa) |
|---|---|---|---|---|---|---|---|---|---|
| 10 | 20.50 | 20% | 98% | 36% | 0.0030 | 240 | 154 | 197 | 100 |
| 16 | 21.90 | 11% | 88% | 25% | 0.0004 | 315 | 190 | ** | * * |
| 16.5 | 20.98 | 16% | 92% | 32% | 0.0010 | 170 | 130 | 147 | 40 |
| 16.5 | 21.00 | 16% | 93% | 32% | 0.0009 | 355 | 290 | 308 | 195 |
| 17 | 21.57 | 14% | 95% | 29% | 0.0002 | 382 | 250 | 333 | 150 |
| 17 | 20.91 | 14% | 85% | 31% | 0.0005 | 303 | 170 | 289 | 70 |
| 18 | 21.65 | 14% | 95% | 28% | 0.0008 | 380 | 210 | 332 | 200 |
| 19 | 22.42 | 9% | 85% | 22% | 0.0008 | 400 | 200 | 329 | 98 |

*The peak shear strength was taken as 10% of the shear strain as the material displayed a strain hardening response at a strain rate below 3.3 mm/hour.

**Error in measuring the residual shear strength.

**Table C-4 Mohr-Coulomb mechanical properties for earthflow deposit at the Ten-mile.**

| Strength Type | Cohesion (kPa) | Phi' (grad) |
|---|---|---|
| Peak | 49 | 24 |
| Peak (BGC, 2016) | 38 | 15 |
| Residual Max | 0 | 29 |
| Residual Min | 0 | 15 |

## APPENDIX C: RESULTS FROM LABORATORY TESTING OF EARTHFLOW DEPOSIT SAMPLES

### Soil Water Characteristic curve

Soil suction is affected by the pore size distribution, grain size distribution, density, organic material content, clay content, and mineralogy on the pore-water retention behavior. Measurement of the soil-water-characteristic-curves (SWCC) allows relating the changes in moisture content and the suction within the soil (Fredlund and Xing 1994). Three remolded samples extracted from sonic drilling boreholes were used to measure the SWCC for the earthflow. The SWCC was measured on a Tempe cell (Fredlund et al. 2012), for sample 1 and sample 2, and Hyprop 2 meter (METER Group AG 2018), for sample 3, through the drying process (Figure C-7a). The hydraulic conductivity curve (Figure C-7b) was fitted with the Mualem model (Mualem 1976; Pertassek et al. 2011) from measured k values using two tensiometers in the Hyprop 2 meter.

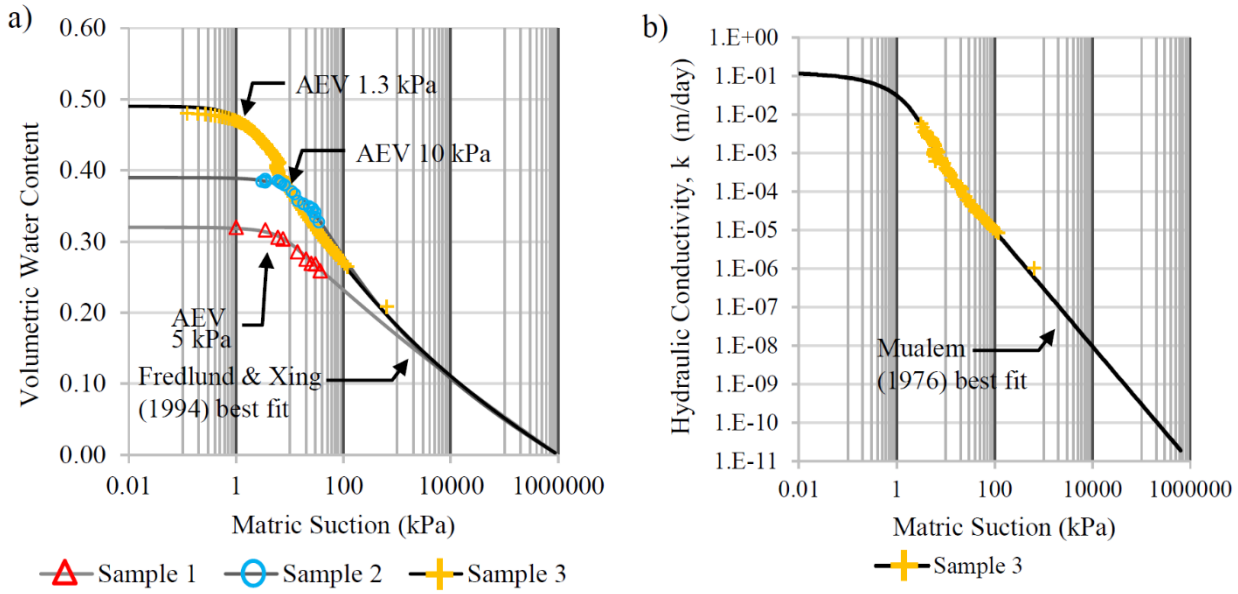


**Figure C-7 Unsaturated soil properties of the active earthflow deposit at the Ten-mile landslide: (a) SWCC and curve fitting using Fredlund and Xing (1994)'s model for three earthflow samples; (b) hydraulic conductivity curve from sample 3 and curve fitting using Mualem (1976)'s model.**

# APPENDIX D: ESTIMATION OF MATRIC SUCTION THROUGH EARTHFLOW DEPOSIT

Precipitation events on unsaturated slopes can result in changes in the moisture content that reduces the matric suction of the soil. Changes in moisture in unsaturated slopes are frequent in the upper zone due to the waterfront at the surface from precipitation events (Fredlund et al. 2012). However, the ground surface at the Ten-mile has large and depth cracks and fissures from the continuous movement that allows water to infiltrate deep into the earthflow deposit. Water infiltration can cause changes in moisture along with the active material and reach the shear zone. Variations of moisture along the earthflow deposit (Figure D-1a) would result in changes in matric suction. However, limitation in instrumentation to measure moisture or suction along the active material requires to estimate the shear strength changes after precipitation events. The use of the SWCC would give an estimate of the maximum soil suction (Figure D-1b) for the corresponding moisture content. Estimating the suction levels of the earthflow based on in-situ moisture measurement and the SWCC is limited by the accuracy of the laboratory testing and range of suction with the natural moisture content of the ground (Fredlund et al. 2012).

**Appendix D: Estimation of Matric Suction Through Earthflow Deposit**

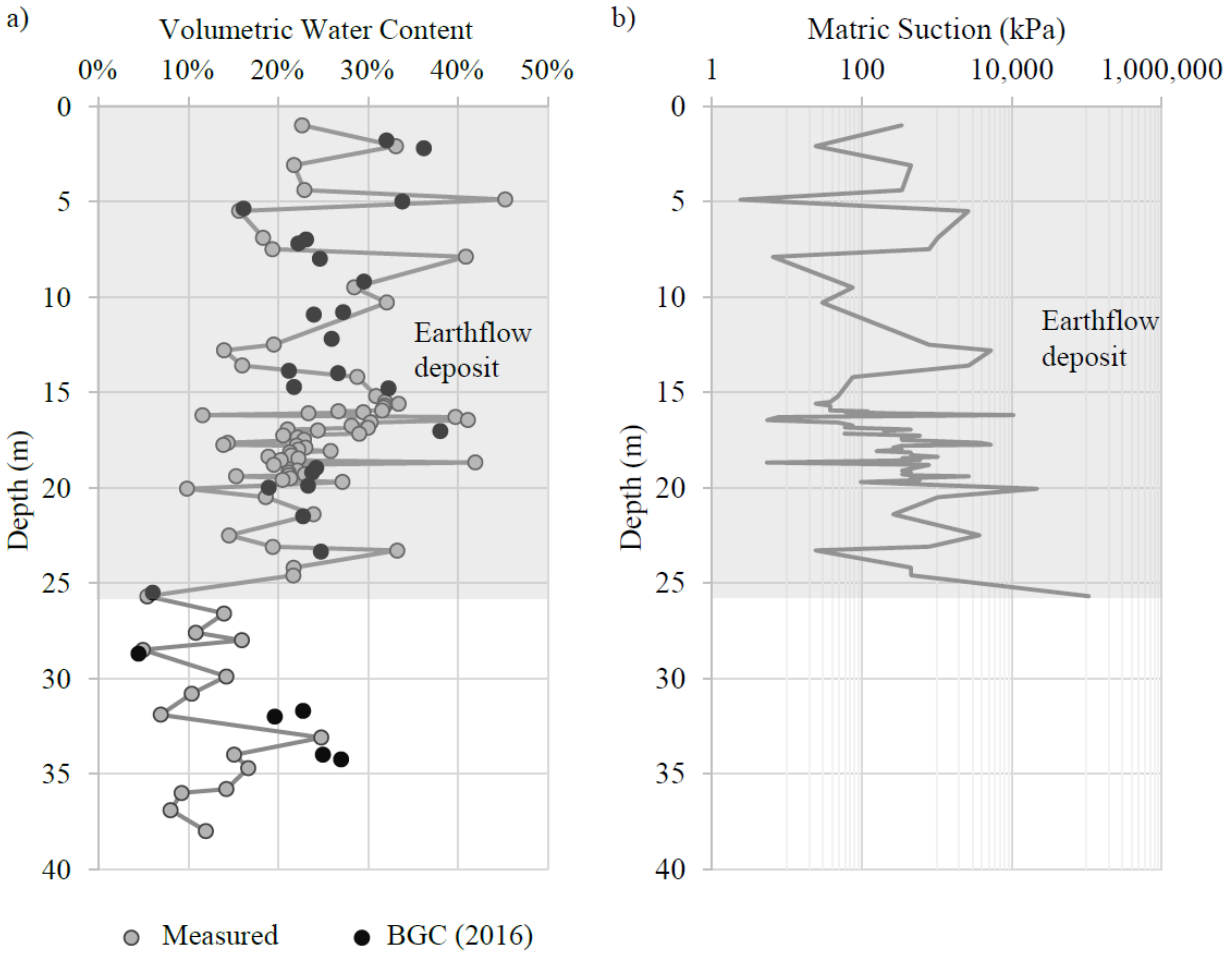


**Figure D-1 Changes in the moisture of the earthflow deposit from samples of different boreholes and collected during different periods at the Ten-mile landslide. a) changes in depth of measured volumetric water content (including testing carried by BGC Engineering Inc.,2016). b) estimation of matric suction along with the earthflow deposit.**

# APPENDIX E: CORRELATION ANALYSIS BETWEEN ANTECEDENT PRECIPITATION AND DISPLACEMENT RATE MEASURES AT THE TEN-MILE LANDSLIDE

The correlation between antecedent precipitation and displacement rates was assessed numerically by determining the spearman rank correlation coefficient (SCC). The SCC measures the degree to which both variables have a monotonic relationship according to equation (11):

$$SCC = 1 - \frac{6}{n(n^2-1)} \sum d_i^2 \,, \qquad (11)$$

Where n is the number of observations from the precipitation and displacement rate in each unit, and $d_i$ is the difference between the ranks of the displacement rate and the antecedent precipitation. The Spearman coefficients are computed from the ranks of the data values rather than from the values themselves. Consequently, the correlation would be less sensitive to outliers than other conventional methods such as the Pearson coefficients method used by Macciotta et al. (Macciotta et al. 2015). Table E-1 shows Spearman rank correlations between displacement rate and the antecedent precipitation. These correlation coefficients range between -1 (negative correlation) and +1 (positive correlation) and measure the strength of the association between the variables. Each correlation was tested through a null hypothesis test to validate the significant of the correlation. A probability of the significant level of correlation less than 5% was selected to reject the null hypothesis. (i.e., a P-value less than 0.05). The test hypotheses are defined as:

- Null-Hypothesis: Correlation Geocube and antecedent precipitation is Insignificant (NO RELATIONSHIP) then the Geocube does not move with the period of antecedent precipitation.
- Alternative-Hypothesis: Correlation Geocube and antecedent precipitation is Significant (THERE IS A RELATIONSHIP) then the Geocube does move with the period of antecedent precipitation.

The correlation coefficient values highlighted in green on Table E-1 satisfy the conditions of a P-Value<5%.

## Appendix E: Correlation coefficient between antecedent precipitation and displacement rate measures at the Ten-mile landslide

**Table E-1 Correlation coefficient between displacement rate and antecedent precipitation rates for all geocube units**

| Unit | Horizontal Displacement (mm) | Total of recorded days | SCC for Days of Antecedent Precipitation | | | | | | | |
|---|---|---|---|---|---|---|---|---|---|---|
| | | | 1 | 7 | 15 | 30 | 60 | 70 | 80 | 90 |
| **42** | 9 | 536 | -0.09 | 0.02 | 0.08 | 0.08 | 0.11 | 0.11 | 0.09 | 0.07 |
| **43** | 29 | 271 | 0.00 | 0.09 | 0.08 | 0.07 | 0.18 | 0.20 | 0.24 | 0.26 |
| **44** | 6 | 536 | -0.03 | 0.00 | -0.01 | 0.09 | 0.10 | 0.07 | 0.06 | 0.06 |
| **45** | 71 | 536 | 0.03 | -0.03 | 0.08 | 0.17 | 0.17 | 0.17 | 0.18 | 0.17 |
| **46** | 1530 | 536 | 0.12 | 0.30 | 0.46 | 0.55 | 0.67 | 0.70 | 0.75 | 0.78 |
| **47** | 456 | 418 | 0.11 | 0.28 | 0.38 | 0.44 | 0.59 | 0.62 | 0.68 | 0.73 |
| **48** | 545 | 536 | 0.12 | 0.29 | 0.42 | 0.51 | 0.63 | 0.67 | 0.72 | 0.75 |
| **49** | 8 | 315 | 0.08 | 0.04 | 0.05 | -0.03 | 0.00 | -0.02 | 0.01 | -0.03 |
| **50** | 10 | 480 | -0.07 | -0.10 | -0.02 | -0.04 | -0.01 | -0.01 | -0.02 | -0.02 |

# APPENDIX F: CORRELATION ANALYSIS BETWEEN DISPLACEMENT RATES MEASURES AT THE TEN-MILE LANDSLIDE

The data recorded from the dGNSS units within the active sliding mass were used to determine the changes in displacement rates during the monitoring period. The correlation of movement between the Geocube units was calculated based on the displacement rates measured, as discusses in section 5.4. The correlation analysis of the displacement rates was assessed numerically by determining the spearman rank correlation coefficient, similarly to Appendix E. This appendix presents:

- Summary of the correlation coefficient of the displacement rates measured between April 2017 and November 2018.
- Summary of the sliding correlation coefficient of the displacement rates between October 2017 and March 2018 as described in Chapter 5.

The correlation analysis allowed identifying the dGNSS units with similar changes in the displacement rates over the monitoring period; thus, correlated dGNSS units are considered a moving block. The correlation must satisfy two conditions; first, the correlations should have a confidence level above 95% (or P-value <5%); second, the correlated dGNSS units must have a logical cluster (i.e., a block of movement can not have an uncorrelated dGNSS unit). The test hypotheses to validate the significant of the correlation are:

- Null-Hypothesis: Correlation Geo 1 and Geo 2 is Insignificant (NO RELATIONSHIP) then Geo 1 and Geo 2 do not move together
- Alternative-Hypothesis: Correlation Geo 1 and Geo 2 is Significant (THERE IS A RELATIONSHIP) then Geo 1 and Geo 2 do not move together

For example, Figure F-1 shows dGNSS units #46, #47, and #48 with a strong correlation and a P-value <5%.

The sliding correlation analysis allowed identifying the sequence of the moving blocks, as described in section 5.4. Table F-1 to Table F-7 show the correlation coefficients for the dGNSS units within sliding mass at 0 days, 1 day, 2 days, 3 days, 7 days, and 15 days after registering an

initial acceleration between October 2017 and March 2018. The period with the strongest correlation and P-value<5% indicates the lag time for two dGNSS units to experience a similar change in the displacement rate.

## Correlations in displacement rate

Figure F-1 shows the correlation matrix of the displacement rates from the dGNSS units within the sliding mass at the Ten-mile. The values presented in each grid represent the spearman rank correlation coefficient. The correlation coefficient values in red satisfy the conditions of a P-Value<5%.

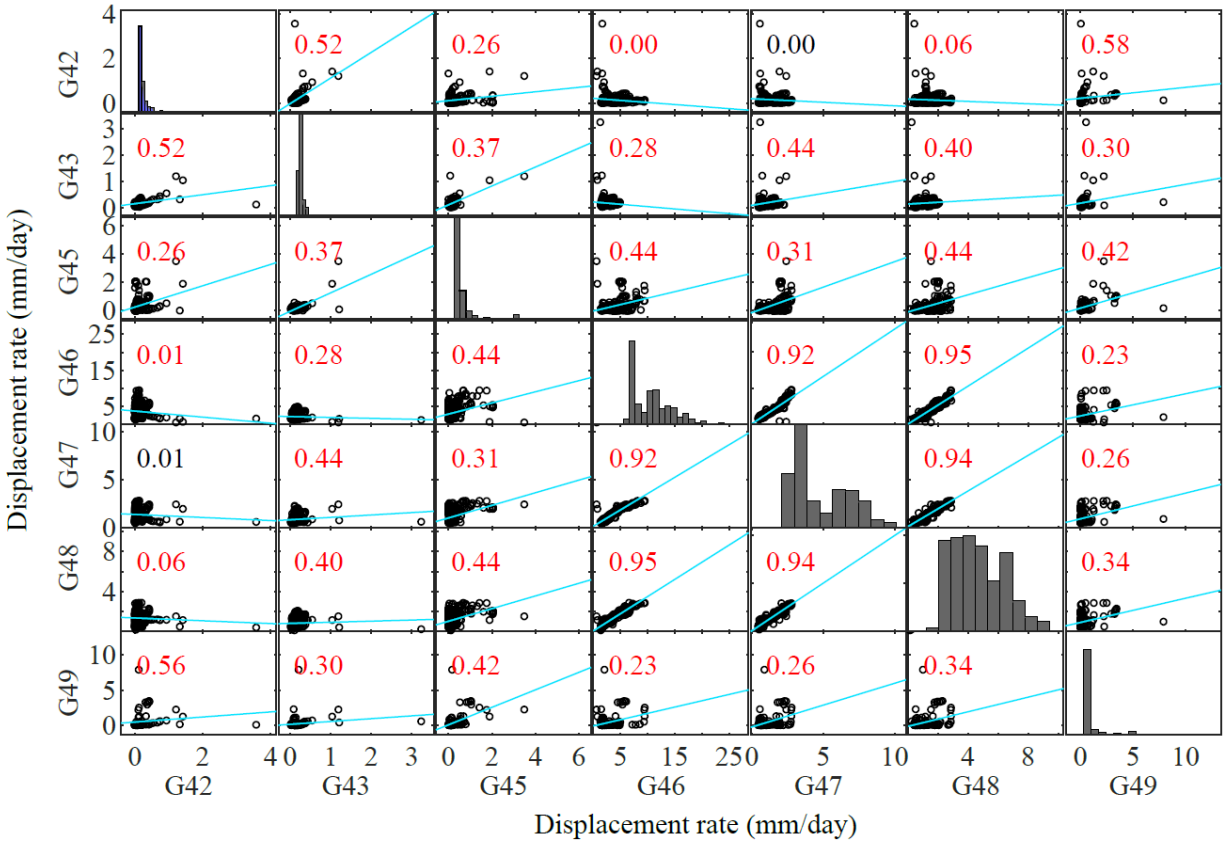


**Figure F-1 Correlation matrix of displacement rate between dGNSS units within the sliding mass.**

## Appendix F: Correlation analysis between displacement rates measures at the Ten-mile landslide

### Sliding correlations in displacement rate

The correlation coefficient values highlighted in green satisfy the conditions of a P-Value<5%.

**Table F-1 Sliding correlation coefficient between the displacement rate of unit #42 and other dGNSS units.**

| Unit | Days after registering acceleration in unit #42 | | | | | |
|---|---|---|---|---|---|---|
| | 0 | 1 | 2 | 3 | 7 | 15 |
| 42 | 1.00 | 1.00 | 1.00 | 1.00 | 1.00 | 1.00 |
| 43 | 0.54 | 0.52 | 0.49 | 0.33 | 0.21 | -0.12 |
| 45 | -0.04 | 0.01 | 0.06 | 0.08 | 0.19 | 0.16 |
| 46 | 0.33 | 0.29 | 0.26 | 0.22 | 0.02 | -0.23 |
| 47 | 0.26 | 0.25 | 0.21 | 0.19 | 0.11 | -0.14 |
| 48 | 0.32 | 0.28 | 0.24 | 0.21 | 0.06 | -0.19 |
| 49 | 0.37 | 0.36 | 0.39 | 0.37 | 0.18 | 0.05 |

**Table F-2 Sliding correlation coefficient between the displacement rate of unit #43 and other dGNSS units.**

| Unit | Days after registering acceleration in unit #43 | | | | | |
|---|---|---|---|---|---|---|
| | 0 | 1 | 2 | 3 | 7 | 15 |
| 42 | 0.54 | 0.53 | 0.57 | 0.49 | 0.53 | 0.23 |
| 43 | 1.00 | 1.00 | 1.00 | 1.00 | 1.00 | 1.00 |
| 45 | 0.18 | 0.09 | 0.05 | 0.05 | -0.01 | 0.13 |
| 46 | 0.39 | 0.40 | 0.37 | 0.33 | 0.25 | 0.09 |
| 47 | 0.57 | 0.48 | 0.45 | 0.46 | 0.29 | 0.02 |
| 48 | 0.43 | 0.44 | 0.42 | 0.41 | 0.32 | 0.12 |
| 49 | 0.14 | 0.07 | -0.10 | -0.08 | 0.11 | 0.13 |

## Appendix F: Correlation analysis between displacement rates measures at the Ten-mile landslide

**Table F-3 Sliding correlation coefficient between the displacement rate of unit #45 and other dGNSS units.**

| Unit | Days after registering acceleration in unit #45 | | | | | |
|---|---|---|---|---|---|---|
| | 0 | 1 | 2 | 3 | 7 | 15 |
| 42 | -0.04 | -0.06 | -0.07 | -0.10 | 0.10 | 0.20 |
| 43 | 0.18 | 0.23 | 0.20 | 0.08 | 0.24 | 0.37 |
| 45 | 1.00 | 1.00 | 1.00 | 1.00 | 1.00 | 1.00 |
| 46 | 0.28 | 0.26 | 0.27 | 0.28 | 0.34 | 0.34 |
| 47 | 0.39 | 0.39 | 0.38 | 0.35 | 0.38 | 0.26 |
| 48 | 0.34 | 0.32 | 0.30 | 0.29 | 0.32 | 0.32 |
| 49 | 0.13 | 0.03 | -0.04 | -0.04 | 0.00 | -0.04 |

**Table F-4 Sliding correlation coefficient between the displacement rate of unit #46 and other dGNSS units.**

| Unit | Days after registering acceleration in unit #46 | | | | | |
|---|---|---|---|---|---|---|
| | 0 | 1 | 2 | 3 | 7 | 15 |
| 42 | 0.33 | 0.36 | 0.37 | 0.38 | 0.39 | 0.21 |
| 43 | 0.39 | 0.38 | 0.40 | 0.42 | 0.47 | 0.23 |
| 45 | 0.28 | 0.27 | 0.26 | 0.26 | 0.33 | 0.27 |
| 46 | 1.00 | 1.00 | 1.00 | 1.00 | 1.00 | 1.00 |
| 47 | 0.87 | 0.87 | 0.86 | 0.85 | 0.84 | 0.64 |
| 48 | 0.97 | 0.97 | 0.95 | 0.94 | 0.88 | 0.67 |
| 49 | 0.09 | 0.04 | 0.02 | 0.02 | 0.02 | 0.07 |

**Table F-5 Sliding correlation coefficient between the displacement rate of unit #47 and other dGNSS units.**

| Unit | Days after registering acceleration in unit #47 | | | | | |
|---|---|---|---|---|---|---|
| | 0 | 1 | 2 | 3 | 7 | 15 |
| 42 | 0.26 | 0.27 | 0.30 | 0.32 | 0.23 | 0.12 |
| 43 | 0.57 | 0.61 | 0.58 | 0.56 | 0.29 | -0.12 |
| 45 | 0.39 | 0.36 | 0.34 | 0.30 | 0.25 | 0.13 |
| 46 | 0.87 | 0.85 | 0.84 | 0.83 | 0.74 | 0.59 |
| 47 | 1.00 | 1.00 | 1.00 | 1.00 | 1.00 | 1.00 |
| 48 | 0.90 | 0.87 | 0.85 | 0.83 | 0.76 | 0.60 |
| 49 | -0.10 | -0.10 | -0.12 | -0.14 | -0.09 | 0.02 |

## Appendix F: Correlation analysis between displacement rates measures at the Ten-mile landslide

**Table F-6 Sliding correlation coefficient between the displacement rate of unit #48 and other dGNSS units.**

| Unit | Days after registering acceleration in unit #48 | | | | | |
|---|---|---|---|---|---|---|
| | 0 | 1 | 2 | 3 | 7 | 15 |
| 42 | 0.32 | 0.34 | 0.35 | 0.35 | 0.38 | 0.23 |
| 43 | 0.43 | 0.43 | 0.48 | 0.50 | 0.46 | 0.26 |
| 45 | 0.34 | 0.31 | 0.29 | 0.28 | 0.32 | 0.22 |
| 46 | 0.97 | 0.95 | 0.94 | 0.92 | 0.85 | 0.64 |
| 47 | 0.90 | 0.89 | 0.87 | 0.85 | 0.82 | 0.59 |
| 48 | 1.00 | 1.00 | 1.00 | 1.00 | 1.00 | 1.00 |
| 49 | 0.03 | 0.01 | 0.00 | 0.00 | 0.06 | 0.08 |

**Table F-7 Sliding correlation coefficient between the displacement rate of unit #49 and other dGNSS units.**

| Unit | Days after registering acceleration in unit #49 | | | | | |
|---|---|---|---|---|---|---|
| | 0 | 1 | 2 | 3 | 7 | 15 |
| 42 | 0.37 | 0.44 | 0.45 | 0.38 | 0.29 | -0.03 |
| 43 | 0.14 | 0.05 | -0.09 | -0.18 | -0.11 | -0.06 |
| 45 | 0.13 | 0.06 | -0.01 | -0.01 | 0.12 | -0.01 |
| 46 | 0.09 | 0.07 | 0.04 | 0.01 | -0.05 | -0.24 |
| 47 | -0.10 | -0.12 | -0.14 | -0.12 | -0.01 | -0.04 |
| 48 | 0.03 | 0.02 | 0.00 | -0.04 | -0.02 | -0.19 |
| 49 | 1.00 | 1.00 | 1.00 | 1.00 | 1.00 | 1.00 |

## APPENDIX G: DRAINAGE NETWORK AT THE TEN-MILE LANDSLIDE

The detail point clouds from photogrammetry process using the UAV photos surveys allowed overcoming the limitations of using LiDAR in terms of shadow areas. A point cloud is used to estimate the drainage network of the Ten-mile, using the same methodology discussed on Chapter 3 for the C018 site.

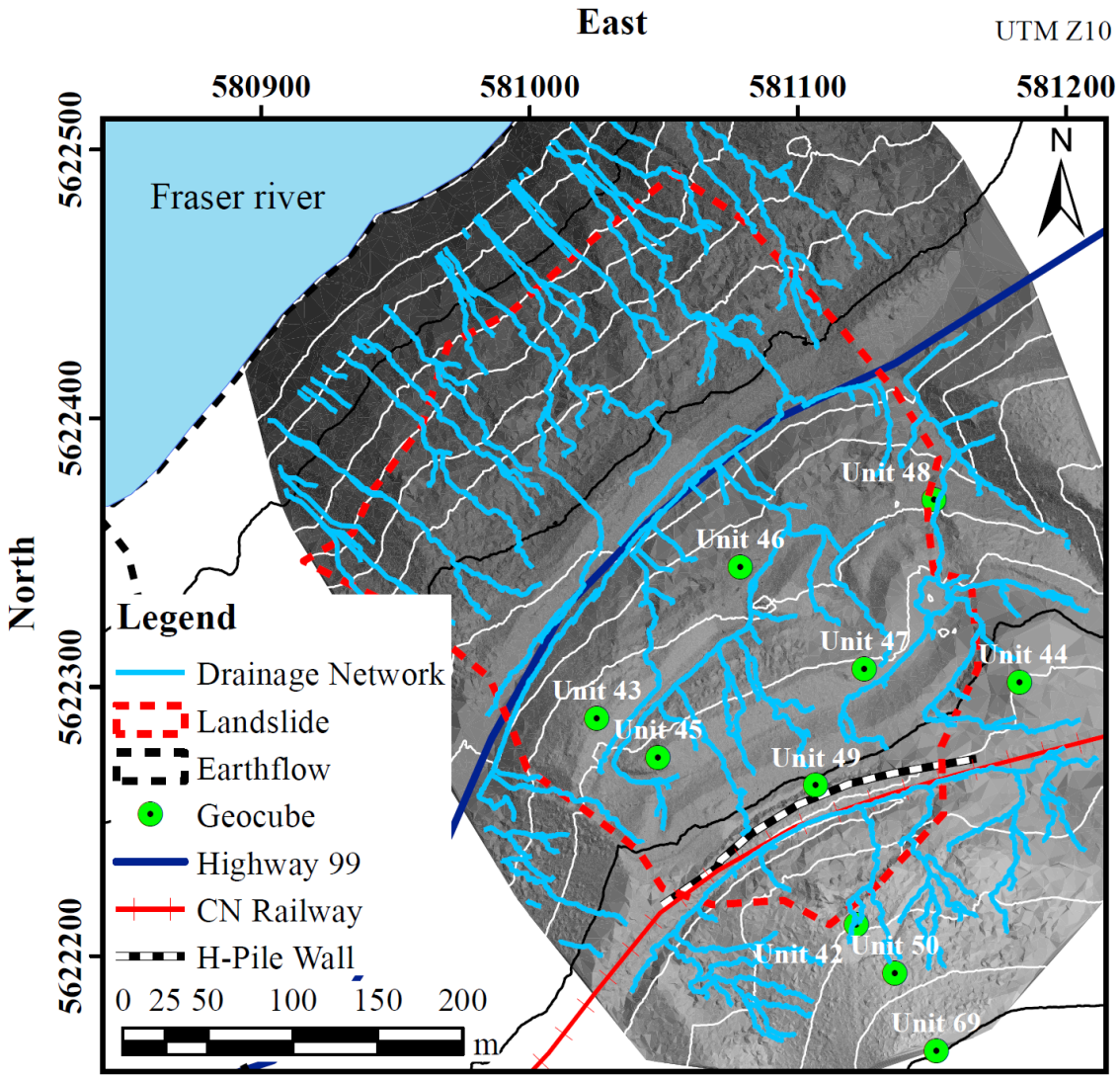


**Figure G-1 Drainage network of the Ten-mile landslide from point cloud generated from UAV flights in March 2018.**

The drainage network shows the highest concentration of contributing area of runoff water towards the northern section of the slide that coincides with areas of highest movement.

## APPENDIX H: UAV MONITORING AND CHANGE DETECTION ANALYSIS AT THE TEN-MILE LANDSLIDE

The processing of the information has been made by using several commercial software with private and open sources algorithms. The processing of UAV photos to generate a reconstruction of the topography is been made by using Pix4D (Pix4D S.A. 2018b). The comparison of point cloud to estimate displacement changes is calculated using Cloudcompare V2.9 (LGPL 2011). Figure H-1 shows the detail methodology process to followed in to calculate the changes between point cloud from UAV surveys at the Ten mile performed during the investigation of this research.

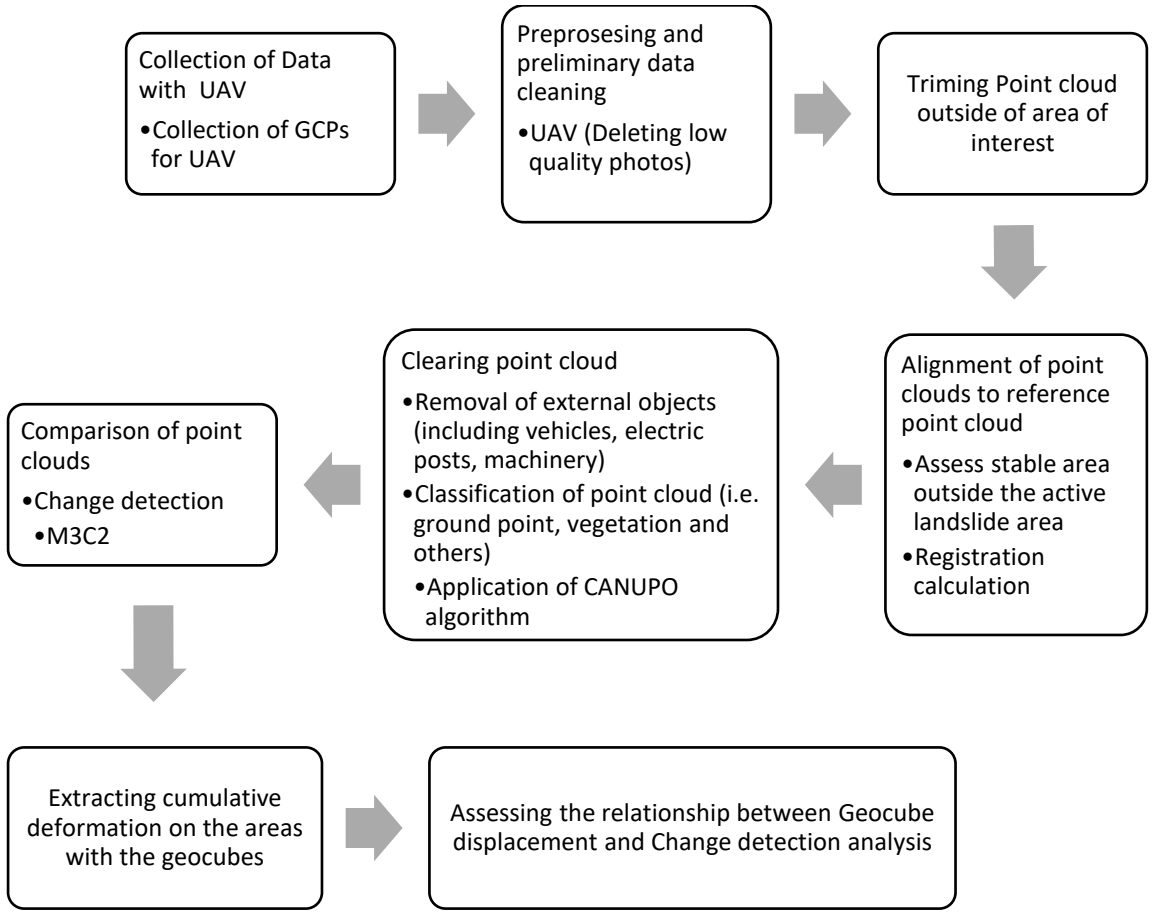


**Figure H-1 Methodology implemented to assess the kinematics of the 10-mile slide using the data from the monitoring campaign between 2017 to 2018.**

The results of change detection calculation at the Ten-mile between March 29, 2017 and September 21, 2018 are shown in Figure H-2. The change detection has significant noise due difficulties from filtering out vegetation from point clouds generated through photogrammetry.

## APPENDIX H: UAV MONITORING AND CHANGE DETECTION ANALYSIS AT THE TEN-MILE LANDSLIDE

The change detection was compared with the 18 blocks in the active zone of the landslide shown by Lato et al. (2016).

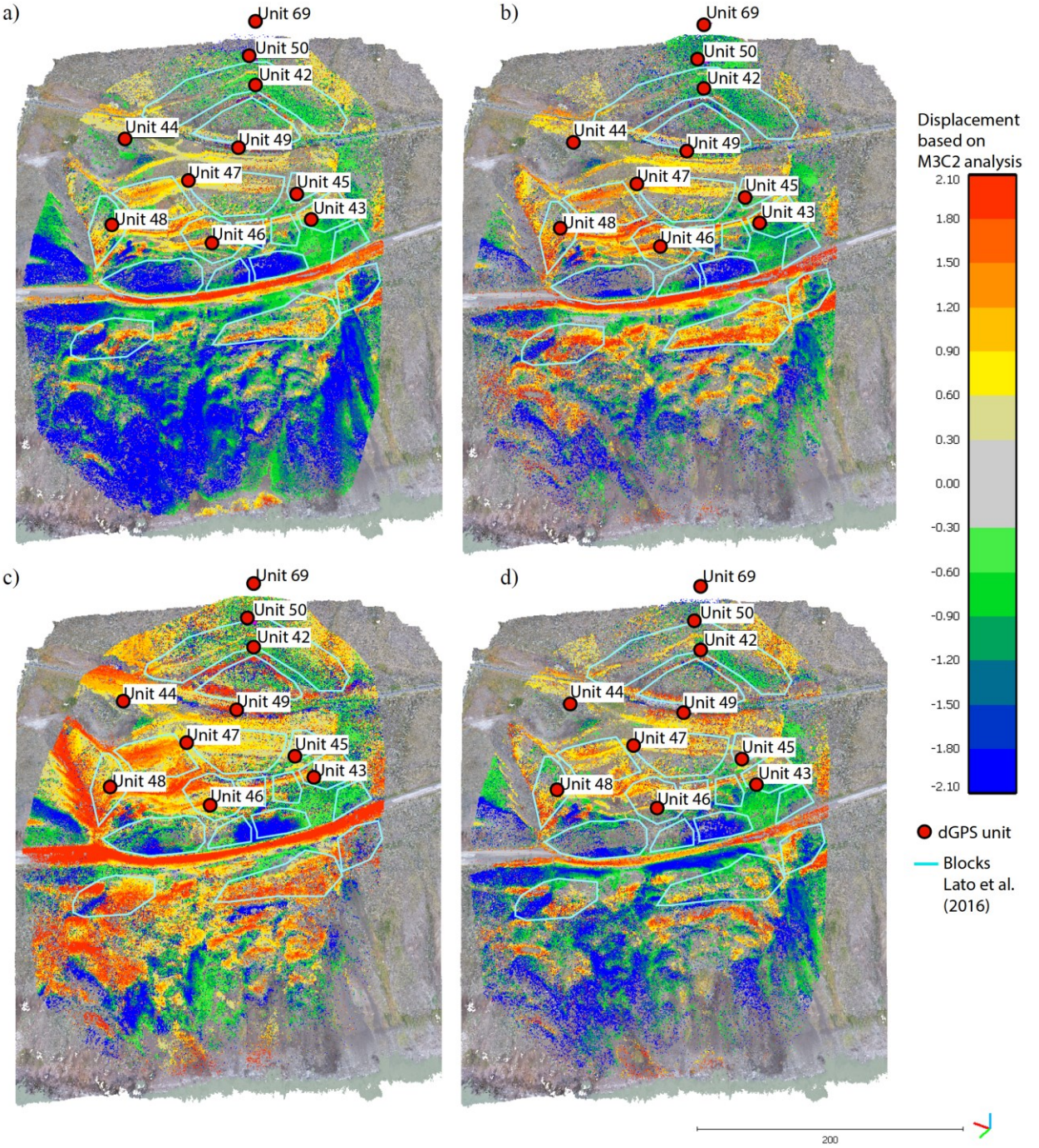


**Figure H-2 Change detection results between UAV flight on March 29, 2017 and UAV flights on July 24, 2017, November 5, 2017, March 23, 2018 and September 21, 2018.**

# APPENDIX I: PROPOSED METHOD FOR DEVELOPING AN EARLY WARNING SYSTEM FOR LANDSLIDE DEFORMATIONS NEXT TRANSPORTATION CORRIDORS USING SINGLE-FREQUENCY GNSS RECEIVERS

Stablishing a warning system for landslide requires assessing the error in data that are instrument and site related. Early warning systems based on dGNSS measures are exposed to generate false positive and false negatives due to the signal error from each raw data point. Different landslide would also require having warning settings that fit its kinematics behaviour (e.g., displacement, velocity, and acceleration). For example, setting a warning system at the Ten-mile using a network of dGNSS system should consider four objectives:

I. Early warning against excessive *cumulative deformation* of the landslide that exceeds the serviceability of the railway or the highway.

II. Early warning against an *accelerating trend* of the landslide that could suggest it is evolving towards collapse (e.g., inverse velocity approaches).

III. Early warning against a *collapse of the landslide*. Warning aims to prevent users of the highway or railway to encounter the blocked/missing section of the corridor.

IV. "warning" against a change in the *displacement trend* that could indicate the landslide kinematics are evolving (e.g., retrogression, the development of a through-going shear zone, etc.).

The "noise" (error) from the monitoring system would need to be assessed to detect specific changes in each objective. The errors from the dGNSS system installed at the Ten-mile and Chin-Coulee that allows assessing the previous four objectives can be established by:

1. Collecting location from each unit at the maximum frequency provided by instrument to provide a significant sample size to assess the errors of the measurements.

2. Assessing the direction or azimuth of movement using the collected data or estimate initial direction based on the orientation.

3. Defining a baseline of each coordinate component by filtering outliers of the data and using low-pass filters such as moving average with 24 hours window to reduce the data noise.

4. Assessing kinematic similarities between units based on time of data, location, weather changes (such as precipitation and temperature).

5. Assessing the "noise" from system "raw" measurements in each unit by calculating the difference to the baseline from each coordinate component and direction.

6. Defining specific magnitudes and trend of the cumulative deformation, changes in velocities, and acceleration that would warn against the monitoring system exceeding a tolerance criterion for the individual objectives. The four objectives for the Ten-mile would need to consider:

    I. Tracking the cumulative deformation in expected direction of movement from a starting date that adds the noise level. This cumulative deformation would need to be compared with a defined tolerance criterion based on the serviceability of the infrastructure. An "event" could be associate to a measurement that exceeds the tolerance deformation. The cumulative deformation would be validated based on the number of events generated outside the noise frequency, thus limiting the number of "false positives". Ultimately, the stakeholders can establish different hazard levels based on the proximity cumulative deformation to the maximum tolerance and the proximity of the units to the infrastructure.

    II. Tracking high frequency measures in the displacement allows to detect quick acceleration trends. Slow moving landslide allows assessing the increments in the rate of displacement that has been filtered. Counting the increments in the rate of displacement would provide indication of a faster evolution at different landslide sections. Furthermore, the information allows using forecasting techniques, such as "inverse velocity method" (Carlà et al., 2017), to estimate the time of potential collapse at different landslide sections.

    III. Identifying sudden signal loss between units or sudden accelerations that exceed the maximum noise to determine a possible blockage/missing section of the infrastructure. In the later case, a sudden acceleration should be validated with respect to the cumulative deformation in the expected direction to determine that movement is outside the noise of the system.

IV. A similar approach from tracking the cumulative deformation in objective I) can be considered on units located outside the active zone of the landslide. Examining the increase in displacement between consecutive measurement on outer units provide warning against retrogression of the landslide.

7. Reassessing the monitoring system for changes in the measured errors.